



Ministério da  
Ciência e Tecnologia



INPE-13269-MAN/45 - version 1

**A STUDY OF SHOCK WAVE FRONT'S AND  
MAGNETIC CLOUD'S EXTENT IN THE INNER  
HELIOSPHERE USING OBSERVATIONS FROM  
MULTI-SPACECRAFT**

Aline de Lucas

Ph.D. Thesis in Space Geophysics, supervised by Drs. Alisson Dal Lago and Alcía L. Clúa de Gonzalez, and Prof. Rainer Schwenn, presented on May 15, 2009.

Original document registry:

[<http://urlib.net/>](http://urlib.net/)

INPE  
São José dos Campos  
2009

**PUBLICADO POR:**

Instituto Nacional de Pesquisas Espaciais - INPE

Gabinete do Diretor (GB)

Serviço de Informação e Documentação (SID)

Caixa Postal 515 - CEP 12.245-970

São José dos Campos - SP - Brasil

Tel.:(012) 3945-6911/6923

Fax: (012) 3945-6919

E-mail: [pubtc@sid.inpe.br](mailto:pubtc@sid.inpe.br)

**CONSELHO DE EDITORAÇÃO:****Presidente:**

Dr. Gerald Jean Francis Banon - Coordenação Observação da Terra (OBT)

**Membros:**

Dra. Maria do Carmo de Andrade Nono - Conselho de Pós-Graduação

Dr. Haroldo Fraga de Campos Velho - Centro de Tecnologias Especiais (CTE)

Dra. Inez Staciarini Batista - Coordenação Ciências Espaciais e Atmosféricas (CEA)

Marciana Leite Ribeiro - Serviço de Informação e Documentação (SID)

Dr. Ralf Gielow - Centro de Previsão de Tempo e Estudos Climáticos (CPT)

Dr. Wilson Yamaguti - Coordenação Engenharia e Tecnologia Espacial (ETE)

**BIBLIOTECA DIGITAL:**

Dr. Gerald Jean Francis Banon - Coordenação de Observação da Terra (OBT)

Marciana Leite Ribeiro - Serviço de Informação e Documentação (SID)

Jefferson Andrade Ancelmo - Serviço de Informação e Documentação (SID)

Simone A. Del-Ducca Barbedo - Serviço de Informação e Documentação (SID)

**REVISÃO E NORMALIZAÇÃO DOCUMENTÁRIA:**

Marciana Leite Ribeiro - Serviço de Informação e Documentação (SID)

Marilúcia Santos Melo Cid - Serviço de Informação e Documentação (SID)

Yolanda Ribeiro da Silva e Souza - Serviço de Informação e Documentação (SID)

**EDITORAÇÃO ELETRÔNICA:**

Viveca Sant´Ana Lemos - Serviço de Informação e Documentação (SID)



Ministério da  
Ciência e Tecnologia



INPE-13269-MAN/45 - version 1

**A STUDY OF SHOCK WAVE FRONT'S AND  
MAGNETIC CLOUD'S EXTENT IN THE INNER  
HELIOSPHERE USING OBSERVATIONS FROM  
MULTI-SPACECRAFT**

Aline de Lucas

Ph.D. Thesis in Space Geophysics, supervised by Drs. Alisson Dal Lago and Alcía L. Clúa de Gonzalez, and Prof. Rainer Schwenn, presented on May 15, 2009.

Original document registry:

<http://urlib.net/>

INPE  
São José dos Campos  
2009

Cataloging in Publication Data

---

Cutter de Lucas, Aline.

A STUDY OF SHOCK WAVE FRONT'S AND MAGNETIC CLOUD'S EXTENT/ Aline de Lucas. – São José dos Campos: INPE, 2009.

??p. ; (INPE-13269-MAN/45 - version 1)

Thesis () – Instituto Nacional de Pesquisas Espaciais - INPE/MCT, São José dos Campos, 2009.

1. Shock Waves. 2. Interplanetary Coronal Mass Ejections. 3. Magnetic Clouds. 4. Helios mission. 5. Longitudinal Extension 1. Ondas de Choque 2. Ejeções Coronais de Massa Interplanetárias 3. Nuvens Magnéticas 4. Missão Helios 5. Extensão Longitudinal I. Shock wave front's and magnetic cloud's extent in the inner heliosphere.

CDU

---

Copyright © 2009 do MCT/INPE. Nenhuma parte desta publicação pode ser reproduzida, armazenada em um sistema de recuperação, ou transmitida sob qualquer forma ou por qualquer meio, eletrônico, mecânico, fotográfico, microfílmico, reprográfico ou outros, sem a permissão escrita da Editora, com exceção de qualquer material fornecido especificamente no propósito de ser entrado e executado num sistema computacional, para o uso exclusivo do leitor da obra.

Copyright © 2009 by MCT/INPE. No part of this publication may be reproduced, stored in a retrieval system, or transmitted in any form or by any means, electronic, mechanical, photocopying, microfilming, recording or otherwise, without written permission from the Publisher, with the exception of any material supplied specifically for the purpose of being entered and executed on a computer system, for exclusive use of the reader of the work.



**ATENÇÃO! A FOLHA DE  
APROVAÇÃO SERÁ INCLU-  
IDA POSTERIORMENTE.**



*“Têm coisas que tem seu valor,  
Avaliado em quilates, em cifras e fins  
E outras não têm o apreço  
Nem pagam o preço que valem pra mim*

*Tenho uma velha saudade  
Que levo comigo por ser companheira  
E que aos olhos dos outros  
Parecem desgostos por ser tão caseira*

*Não deixo as coisas que eu gosto  
Perdidas aos olhos de quem procurar  
Mas olho o mundo na volta  
Achando outra coisa que eu possa gostar  
Tenho amigos que o tempo  
Por ser indelével, jamais separou  
E ao mesmo tempo revejo  
As marcas de ausência que ele me deixou...  
Carrego nas costas meu mundo  
E junto umas coisas que me fazem bem  
Fazendo da minha janela  
Imenso horizonte, como me convém*

*Das vozes dos outros eu levo a palavra  
Dos sonhos dos outros eu tiro a razão  
Dos olhos dos outros eu vejo os meus erros  
Das tantas saudades eu guardo a paixão*

*Sempre que eu quero, revejo meus dias  
E as coisas que eu posso, eu mudo ou arrumo  
Mas deixo bem quietas as boas lembranças  
Vidinha que é minha, só pra o meu consumo...”*

GUJO TEIXEIRA/LUIZ MARENCO  
em “Pro meu Consumo”



*To my parents Elio and Reni and my sisters Andrea and  
Luisa for the constant presence in all moments of this "journey"*

...



## ACKNOWLEDGEMENTS

First, I would like to thank God for my life, my family, everything and everyone who shared something with me or supported me during this hard time, but a very fruitful period of new experiences. For staying with me, even during the several times I ignored His presence in my life - times when I did not want to admit I needed Him, because I could not understand the reasons why things had an end like they did. Times when I felt I needed to believe in something - just believe in something - to be able to follow my way.

Second, I am extremely grateful to my family for their love, attention, and patience in all moments, faith, inspiration, power, example of life, everything that contributed a lot or a little in my personality, in my way of seeing the world and living in it. They were also responsible for my persistence especially during the hardest times of my life, when the personal losses seemed to be so hard that one could not stand to the sorrow. They were my support during all this sorrow and believed in me even though I did not do the same. I thought I could not go longer than I had reached.

Not only have my parents and sisters contributed to all this work with their support and patience, but all my family, including grandparents, cousins, aunts, uncles, great-aunts and uncles, and those more than third degree relatives with their prayers, cheers, and positive thoughts.

How could I forget you, granny? The moments were so many and intense that is impossible not remember all of them, each detail of our conversations, the stories and experiences of your life, and so many other things that remind me of the wonderful and precious person you were. Your personality and determination contributed a lot to what I became as an individual. I am extremely grateful to you because I feel that you have “followed my steps” in this long journey.

A very special thanks goes out to my supervisors during my internship in Germany, Profs. Drs. Rainer Schwenn - who is so humble that he prefers to be called just Rainer - and Eckart Marsch. I am really grateful to all that I improved in my understanding of the physics and statistics behind the data I was analyzing. I thank especially Rainer for everything I learned about being a good and exemplary researcher. For sure, I learned a lot from his humbleness, simplicity, honesty, and utmost competence.

To my official supervisors Drs. Alisson Dal Lago and Alícia L. Clúa de Gonzalez, and to my non-official - but very considerate - supervisor Dr. Walter Gonzalez for all their support and understanding during the four years of difficulty. I would like to express my gratitude to them for the times of discussion of the results, for the moments that we stopped in front of the results without knowing what to do afterwards - these were times of patience and reflection. For the moments of difficulty, desperation, lack of faith, hard times that helped to enrich the experience.

To those old and more experienced friends and colleagues, Ezequiel, Luís Eduardo, Jean and Fernando whose help contributed a lot to the content of this thesis with new ideas how to analyze and treat the data. For the ideas that made me think again about the techniques and ways I was handling my dataset.

To my friend and sister - not the blood one, but a friend who shares similar feelings, who sees the world in a comparable way like I do, a friend who can understand me even though I cannot find words to explain how I feel, or why I act in such way sometimes - Amita, who has supported me during this period of four years even when I was in the “other side of the world”. How many times I have not understood the way of using the tools to reach the final results I expected. She with her patience was always giving me hints for use of the correct commands in MatLab. I do appreciate her vast knowledge in solving problems by the shortest way.

To all those friends that came to my office with fruitful ideas and discussions, who brought good feelings and thoughts during a “roda de mate”. These moments were and continue to be very important to me, not only because they remind me of the good times with my family and at the university when the time for drinking the mate was almost sacred. These moments are so precious due to the inspiration they bring with them once we take time to think, stop, relax, and realize things that we did not notice before. Without their companion, friendship, and assistance, I would not have been able to finish this thesis. A special thanks goes out to Gi, Marlos, Zé, Rosângela, Ale, Vandoir, Vir, Fábio, Daiki, Paulito, among many others.

I could not forget those friends whose friendship goes through time and space and does not lose its power. The friends who do not follow the same steps like you, but, even not fully understanding what you do, they support you along the way. Besides, they understand your disappearance and the times you are extremely stressed racing the clock. Thanks Cá, Rica, Sãn, Jú, Égi, Régis!



I recognize that this research would not have been possible without the technical and structural support of the Instituto Nacional de Pesquisas Espaciais (INPE) and Max-Planck-Institute für Sonnensystemforschung (MPS) during my respective Ph.D. studies and “Sandwich” internship. I am grateful for the opportunity to study in these institutions and collaborate with renowned researchers.

Another special thanks goes to those public employees at INPE for their help, especially to Filomena, an exemplary secretary who was always available to solve any problem we had. To the INPE staff for all the instances in which their assistance helped me along the way.

To CNPq for the fellowship received and the encouragement in doing research in our country with the certainty that our work is going to be recognized by the government and its institutions. Without its financial assistance it would have been hard to finish the thesis on time.



## ABSTRACT

The two Helios probes traveled at variable longitudinal and radial separations (from 0.3 to 1 AU distance from the Sun) through the inner heliosphere from the end of 1974 until the beginning of 1986. In this way, they collected high resolution plasma and magnetic field data for an entire solar cycle. More than 390 shock waves driven by Interplanetary Coronal Mass Ejections (ICMEs) could be detected. Combining the data from both probes, we made a statistical study of the spatial extent of shock fronts in the interplanetary medium. We determine the dependence of the probability for shocks to be observed by both probes as a function of the spacecraft separation. We found that for a longitudinal separation of about  $90^\circ$  a shock has 50% chance to be observed by both probes. Including plasma and magnetic field data from the near-Earth ISEE-3 and IMP-8 spacecraft improved our statistical evaluation substantially. Thus, we found a few cases where the observation points were located on almost opposite sides of the Sun and yet observed shock fronts within reasonable timely context. However, due to the absence of simultaneous coronal observations we can no longer uniquely decide whether these shocks originated at one and the same solar event. Among the large set of shocks identified by H1 and H2, many of them were driven by Magnetic Clouds (MCs). Some of these MCs were observed by multi-spacecraft, while most part of them constituted the group of single-spacecraft observation of MCs. On the other hand, we found that the longitudinal extent of MCs can be as large as  $90^\circ$ . We found one event where the two probes were separated by about  $15^\circ$ , and only one of the probes observed the MC and the shock wave driven by the cloud. We used the local Minimum Variance Analysis (MVA) to determine the direction of rotation of the magnetic field inside the MCs and the orientation of the MC axis. Highly-inclined MCs are less likely to be observed by two space probes even if they are very close to each other. In general, as observations from multi-spacecraft, MCs behave as well-organized structures in the inner heliosphere.



# ESTUDO DA EXTENSÃO DAS FRENTES DE CHOQUE E DAS NUVENS MAGNÉTICAS NA HELIOSFERA INTERNA USANDO OBSERVAÇÕES DE MÚLTIPLAS ESPAÇONAVES

## RESUMO

As duas sondas Helios viajaram na heliosfera interna do final do ano de 1974 até o início do ano de 1986, variando sua posição em longitude e distância radial (de 0,3 a 1 AU). Elas coletaram dados de plasma e campo magnético de alta resolução durante um ciclo solar completo. Mais de 390 ondas de choque interplanetárias guiadas por Ejeções Coronais de Massa Interplanetárias (ICMEs) foram identificadas pelas duas sondas, H1 e H2. Associando-se os dados de plasma e campo magnético de ambas as sondas, fazemos um estudo estatístico da extensão espacial de frentes de choque no meio interplanetário. Determinamos a dependência da probabilidade de choques serem vistos por ambas as sondas como uma função da separação longitudinal das espaçonaves. Como resultado, encontramos que, para um ângulo de separação entre as sondas de aproximadamente  $90^\circ$ , um choque tem 50% de chance de ser visto por ambas as sondas. A inclusão de dados dos satélites ISEE-3 e IMP-8 orbitando nas proximidades da Terra melhorou nossa estatística consideravelmente. Dentre os choques estudados, encontramos alguns casos em que as sondas estavam em direções praticamente opostas ao Sol e ainda assim observaram frentes de choque dentro de um contexto temporal aceitável. No entanto, devido à falta de observações simultâneas da coroa, não pudemos decidir univocamente se tais choques têm a mesma origem solar. Dentre o grande grupo de ondas de choque identificadas por H1 e H2, muitas delas foram guiadas por Nuvens Magnéticas (MCs). Algumas destas MCs foram observadas por múltiplas espaçonaves, enquanto que a maioria delas constituiu o grupo das MCs observadas por uma única espaçonave. Por outro lado, encontramos que a extensão longitudinal das MCs pode ser tão grande quanto  $90^\circ$ . Dentre as nuvens estudadas, encontramos um evento em que as sondas estavam separadas por apenas  $15^\circ$  e somente uma delas observou a MC e o choque guiado pela mesma. Usamos a técnica de Análise da Mínima Variância (MVA) para determinar a direção de rotação do campo magnético dentro das MCs e a orientação do eixo das mesmas. Nuvens magnéticas que são altamente inclinadas em relação ao plano da eclíptica têm menos chance de ser observadas por duas espaçonaves mesmo se elas estiverem próximas uma da outra. Em geral, como indicado pelas observações através de múltiplas espaçonaves, MCs comportam-se como estruturas bem organizadas na heliosfera interna.



# CONTENTS

Pág.

## LIST OF FIGURES

## LIST OF TABLES

## LIST OF ABBREVIATIONS

## LIST OF SYMBOLS

<b>1 INTRODUCTION</b> . . . . .	<b>43</b>
1.1 Outline of the Thesis . . . . .	45
<b>2 REVIEW ON SOLAR ACTIVITY, INTERPLANETARY MEDIUM PROPERTIES AND STRUCTURES, AND SPACE WEATHER</b> . . . . .	<b>47</b>
2.1 The Sun . . . . .	47
2.2 Solar Atmosphere and Energy . . . . .	49
2.3 Coronal Mass Ejections . . . . .	54
2.3.1 Flares and CMEs . . . . .	54
2.4 Propagation in the Interplanetary Medium . . . . .	60
2.5 CIRs and Shocks . . . . .	62
2.6 ICMEs and Shocks . . . . .	63
2.7 Magnetic Clouds . . . . .	66
2.7.1 Definition and Properties of Magnetic Clouds . . . . .	66
2.7.1.1 Flux Tube Model for Magnetic Clouds . . . . .	67
2.7.1.2 Magnetic Cloud Polarities . . . . .	68
2.7.1.3 Expansion of Magnetic Clouds . . . . .	70
2.8 Propagation of shock waves in the IP medium . . . . .	71
2.9 Formation of a Hydrodynamic Shock . . . . .	72
2.10 Interplanetary Shocks . . . . .	74
2.11 The Rankine-Hugoniot Equations . . . . .	74
2.11.1 The Shock Normal . . . . .	76
2.11.2 Mach Number . . . . .	78

2.11.3	Types of MHD Shocks	79
2.11.3.1	Parallel Shocks	79
2.11.3.2	Perpendicular Shocks	80
2.11.3.3	Oblique Shocks	80
2.12	Concluding Remarks	81
<b>3</b>	<b>GETTING THE CLOSEST TO THE SUN WITH HELIOS MISSION</b>	<b>83</b>
3.1	The launch	85
3.2	Scientific Objectives of the Mission	85
3.3	Instrumentation	87
3.3.1	Plasma Experiment	89
3.3.2	Fluxgate Magnetometers	89
3.3.3	Induction Magnetometer	90
3.3.4	Plasma Wave Experiment	90
3.3.5	Cosmic Radiation Experiment	91
3.4	Results Obtained with Helios	91
3.4.1	Technological Development	92
3.4.2	Scientific Development	92
<b>4</b>	<b>LONGITUDINAL EXTENSION OF SHOCK WAVES IN THE INNER HELIOSPHERE</b>	<b>95</b>
4.1	Overview of the Chapter	95
4.2	Introduction	95
4.3	Event Selection and Data Analysis	96
4.3.1	Shocks observed by multi-spacecraft	101
4.3.1.1	Shock on DOYs 28-29/1977	109
4.3.1.2	Shock on DOY 075/1977	113
4.3.1.3	Shock on DOY 148/1979	116
4.3.1.4	Shock on DOY 89/1980	119
4.3.2	Shock Events observed by only one of the probes	123
4.3.2.1	Shock on DOY 078/1977	123
4.3.2.2	Shock on DOY 327/1977	126
4.3.2.3	Shock on DOY 333/1978	129
4.3.2.4	Shock on DOY 312/1978	133
4.3.2.5	Shock on DOY 131/1981	136



4.4	The Statistical Analysis	139
4.4.1	Results	139
4.5	Conclusions	145
<b>5</b>	<b>EXTENSION OF MAGNETIC CLOUDS IN THE INNER HELIOSPHERE BY MULTI-SPACECRAFT OBSERVATIONS</b>	<b>149</b>
5.1	Introduction to the Chapter	149
5.2	Observation of Magnetic Clouds	149
5.3	Magnetic Clouds seen by Multi-Points	154
5.3.1	MC observed on DOY 29/1977 by H1 and H2	155
5.3.2	MC observed on DOY 76/1977 by H1 and H2	162
5.3.3	MC observed on DOY 327/1977 by H2 and IMP-8	169
5.3.4	MC observed on DOY 335/1977 by H1 and H2	176
5.3.5	MC observed on DOY 003/1978 by H1 and H2	183
5.3.6	MC observed on DOY 046/1978 by H1 and H2	193
5.4	Shock Wave observed by Multi-spacecraft where the Magnetic Cloud was observed by a single-spacecraft	201
5.4.1	MC observed on DOY 106/1978 only by H2	202
5.4.2	MC observed on DOY 058-059/1979 only by H1	207
5.4.3	MC observed on DOY 175/1979 by H1	211
5.5	Magnetic Clouds and Shock Observed by a Single-Spacecraft	216
5.5.1	MC observed on DOY 78/1977 only by H1	216
5.6	Discussion	221
5.7	Conclusions	222
<b>6</b>	<b>SUMMARY AND CONCLUSIONS</b>	<b>225</b>
	<b>REFERENCES</b>	<b>229</b>
<b>A</b>	<b>APPENDIX A - LIST OF SHOCKS AS SEEN BY HELIOS MISSION</b>	<b>245</b>
<b>B</b>	<b>APPENDIX B - CONFIDENCE INTERVAL FOR PROPORTIONS</b>	<b>285</b>
B.1	Estimate of the Error Margin for the "Safe" Events	286
<b>C</b>	<b>APPENDIX C - MINIMUM VARIANCE ANALYSIS</b>	<b>293</b>



## LIST OF FIGURES

	<u>Pág.</u>
1.1 Some effects of solar activity over aerospace technology systems and human activities in space, human being health and life. Astronauts are susceptible to the radiation threat when they are in orbit. Furthermore, spacecrafts can be damaged and their systems disrupted what can change their orbits. . . . .	44
2.1 The God Sun, Ra, worshiped by the Egyptians, with the body of a man, a hawk or falcon head, over it a disc representing the Sun is involved by a serpent. . . . .	48
2.2 Solar interior and atmosphere. The energy is generated in the core, then transferred to the radiative zone through photons, and then to the convective zone by convection, corresponding to the solar interior. In the outer part of the solar structure, one finds the atmosphere that comprises the photosphere, the chromosphere, and the corona, the outermost layer of the atmosphere. . . . .	50
2.3 A disappearing filament seen in H- $\alpha$ by HASTA telescope. . . . .	51
2.4 EIT 195 Å image from SoHO. Over the CHs (dark regions) the configuration of the magnetic field is represented by open field lines, while over the bright regions (active regions) the predominant field is the one characterized by closed field lines. . . . .	53
2.5 Drawing of the corona as it appeared to Tempel at Torreblanca, Spain, during the total solar eclipse of 18 July 1860 that may be the first register of a CME (EDDY, 1974). . . . .	55
2.6 Solar flare observed by HINODE on DOY 347/2006. . . . .	56
2.7 CME observed by the HAO coronagraph onboard Solar Maximum Mission (SMM) spacecraft on DOY 231/1980 (August 18, 1980), at 13:09 UT. . . . .	57
2.8 Model for interpretation of the energy release through magnetic reconnection. The filament emerges and is broken out forming new loops as well releasing energy through flares. . . . .	58

2.9	The three-parts <i>light bulb</i> CME that was observed by LASCO-C3 coronagraph onboard SoHO satellite on February 27, 2000. The bright kernel is the innermost part of the CME, followed by the “dark void” and the bright loops. . . . .	59
2.10	Height-time diagram for the leading edge of the CME observed on DOY 001/2005 as provided by LASCO/C2 and C3 observations. . . . .	61
2.11	Schematic representation of an ICME observed at 1 <i>AU</i> . Two satellites, T1 and T2, cross the structure, observing different parts of it. In front of the ICME, a very turbulent region, composed by an intense southward magnetic field, is formed between the ejecta - in this case, a MC is identified due to the rotation of $\vec{B}$ - and the shock. . . . .	62
2.12	Schematic and idealized representation of a CIR flowing out from the Sun with a “rectangular” speed profile that suffers a gradual increase in its speed at 1 <i>AU</i> . The angular separation between the stream interfaces and the sector boundaries decreases significantly with the increase of the heliospheric distance. . . . .	64
2.13	Voyager 2, Helios A (Helios 1) and B (2), and IMP-8 identified a structure similar to a magnetic tube flux just after a shock wave was observed by their instruments. These observations served as the confirmation of the existence of magnetic clouds, a special group of the ICMEs. The probes identified the front boundaries, as marked by the “x” tick marks, and the rear parts of the MC, as represented by the “o” tick marks. The rotation of the magnetic field, as identified by the probes, is represented by the arrows. . . . .	67
2.14	Magnetic Configuration of MCs parallel to the ecliptic plane. Their magnetic helicity (left-handed (LH), right-handed (RH)) based on the magnetic flux tube concept and the rotation that a spacecraft would observe during the cloud’s passage are also illustrated. . . . .	69
2.15	Magnetic polarity of MCs whose axes are perpendicular to the ecliptic plane. . . . .	70
2.16	Representation of the steepening of a compressional wave resulting in a shock wave at $t = t_3$ . . . . .	73
3.1	The God of the Sun: Helios. From this Greek god that the inspiration for the name of the mission comes from. . . . .	83

3.2	Out of scale view of the Solar System. The probes Helios traveled around the Sun, at distances ranging from around 0.3 to 1 <i>AU</i> , inside Mercury and Earth's orbits. H1 was launched from Earth at the position marked by 'A'. In the opposite side, one identifies the probe describing an elliptic orbit. The representation shows the terrestrial magnetosphere ('1'), the bow shock ('2'), and the solar wind flowing from the sun ('3'). On the solar surface, one observes the sunspots ('4'), filaments extending out from the surface ('5'), and the outermost atmosphere, the corona ('6'), coronal arches ('7'), streamers of magnetic loops ('8'), and the coronal arches ('9'). In the interplanetary medium, the IMF ('10'), and Alfvén and shock waves ('11') are identified. The mark '12' corresponds to the flares, while the solar radiation propagation is defined by the mark '13'. The galactic cosmic rays are identified by '15', while the scattering of sunlight and the zodiacal light are identified by '16' and '17', respectively.	84
3.3	Helios 1 and 2 orbits around the sun, describing elliptic orbits. Earth's orbit is also shown. The tick marks refer to calendar days in 1976. . . . .	85
3.4	The launcher vehicle of satellites, Titan IIIE Centaur, with H1 probe (1974). . . . .	86
3.5	Visit to the Helios third probe in the Deutsches Museum, Munich. . . . .	88
4.1	Helios probes orbits in a top view. H1 and H2 described ecliptic orbits around the sun, traveling from 0.3 to 1 <i>AU</i> (in the inner heliosphere). . .	97
4.2	View from the Earth of the Helios 1 orbit in the inner heliosphere. Note that the probe's orbit is half of the Earth's orbit. . . . .	98
4.3	Annual shock frequency during the operation of the two Helios probes. On the right-hand side of the plot, the identification of the sunspots number showing that the frequency of shocks does follow the variation of sunspots number over the solar cycle. The error bars show the the correspondence between the expected number of shocks for each year and the number of shocks identified by the two probes. . . . .	99
4.4	Estimate of the arrival time of the shock waves as a function of the radial distance from the Sun according to Helios observation. The circles (o) that fill the plot are the result of the shock speed measurements of Helios probes. Each circle corresponds to a shock speed calculated when the shock was detected at a determined radial distance ( <i>AU</i> ), based on the remaining distance. . . . .	101

4.5	Correlation between the difference on the shock speeds of H1 and H2 and the predicted time for the shock arrival. Note that $\Delta t_{H12}$ comes from the measurements of H1 and H2, while $t_p$ is predicted based on $V_S = constant$ .	105
4.6	Correlation between the shock speed difference measured at H1 and H2 ( $\Delta V$ ) and the time predicted ( $t_p$ ) considering a constant speed as the propagation speed of the shock. . . . .	106
4.7	Correlation between the longitudinal separation between H1 and H2 and the predicted time for the shock arrival. . . . .	106
4.8	Number of days of observation from H1 and H2, for angular separation $\Delta\Phi$ between the probes. . . . .	107
4.9	Days of separation between all the points of observation: H1, H2, and IMP-8/ISEE-3. One gets the idea of the number of days the probes remained with the same angular opening. . . . .	108
4.10	H1 observation of a shock on the DOY 29/1977, at 1:03 UT, as identified by the vertical line. The plots give, from top to bottom, the magnetic field strength and angular components, followed by the solar wind proton speed, density, temperature, and the plasma beta, respectively. A magnetic cloud drives the shock, observed by H1 at 0.952 AU, 37° away from Sun-Earth line. At the top of the figure, the position of the two probes H1 and H2 is shown, as well as the radial distance and longitude (in the counterclockwise direction in relation to the Sun-Earth line) of H1/H2. Earth is schematically represented on the upper plot, as well as the Sun and H1 and H2 positions at the period of the shock. The Sun is the central point of the circumference sector from where the location lines of H1 and H2 for the period of the shock originate. The thicker solid line connects the center (Sun) to Earth. Note that on the top of the top panel there is also information about the probe that observed the shock (H1), the radial distance (0.952 AU), the Sun-Earth angle (323.3°), and the Number of Shock (NS=26). . . . .	110
4.11	H2 observation of a shock on DOY 28/1977, at 21:07 UT. The plots are organized similarly to Figure 4.10. This is the same shock as seen in H1, however, the signatures for a MC are not visible as they are in H1. . . .	111

4.12	Interplanetary shock observed by IMP-8 on DOY 28/1977, at 22:40 UT, identified by the vertical line. This is the same shock previously observed by H2 and later on by H1. The plots are given in the same sequence as the one in Figure 4.10. IMP-8 was in the solar wind near Earth during the period of observation of this shock. . . . .	112
4.13	A shock wave was detected by H1 on DOY 75 of 1977, at 11:33 UT, as identified by the vertical line. Plots are organized similarly as in Figure 4.10.	114
4.14	H2 observation of a shock wave on DOY 75/1977, at 19:47 UT. The plots are given in the same sequence as in Figure 4.10. The shock is identified by the vertical line. It is driven by an ICME/MC, like the low plasma beta and density show. . . . .	115
4.15	H2 observation of a shock wave on DOY 148/1979, at 10:28 UT, as identified by the vertical line. The plots are given in the same sequence as in Figure 4.10. Even with gaps on the data, one can identify some of the features for a possible MC. . . . .	117
4.16	H1 observation of the shock wave on DOY 148/1979, at 18:41 UT, as identified by the vertical line. The plots are given in the same sequence as in Figure 4.10. A MC drove the shock wave, identified by the vertical line, as one can see in the plot. . . . .	118
4.17	ISEE-3 observation of a shock wave driven by a MC on DOY 149/1979 at 18:24 UT, identified by the vertical line. From top to bottom, one can find the magnetic field strength, angles (inclination and azimuthal), and components $B_x$ , $B_y$ , and $B_z$ , and, finally, the plasma beta characterizing the period of the shock. There is no plasma data during the period of interest. . . . .	119
4.18	H1 observation of a shock wave on DOY 89/1980, at 11:53 UT, identified by the vertical line. The plots are given in the same sequence as in Figure 4.10. . . . .	120
4.19	IMP-8 observation of the shock wave on DOY 90/1980, at 23:45 UT, represented by the vertical line, near Earth. The plots are given in the same sequence as in Figure 4.10. . . . .	121
4.20	H1 measurements for the event on DOY 78 of the year 1977, at 7:48 UT, as identified by the vertical line. From top to bottom, one can see the magnetic field strength and angles (inclination and azimuthal), the protons speed, temperature, and density, and, finally, the plasma beta profiles. . . . .	124

4.21	H2 solar wind and magnetic field profiles for the period from DOY 76 to 80/1977. The plots are given in the same sequence as in Figure 4.10. No shock (NS) signatures are registered for the considered period. . . . .	125
4.22	IMP-8 magnetic field and plasma parameters from DOY 76 to 82/1977. The plots are given in the same sequence as in Figure 4.10. As one can see in the parameter profiles, there is no signature for a shock during the corresponding period. . . . .	126
4.23	H2 observation of a shock wave on DOY 327/1977, at 16:09 UT, as identified by the vertical line. The plots are given in the same sequence as in Figure 4.10. . . . .	127
4.24	H1 observation of the period of interest: from DOY 327 to 331/1977. The plots are given in the same sequence as in Figure 4.10. No shock (symbol “NS”, on top of the figure) is detected by the instruments onboard H1. . . . .	128
4.25	H1 observation of a shock wave on DOY 333/1978, at 03:17 UT, as identified by the vertical line. The plots are given in the same sequence as in Figure 4.10. . . . .	130
4.26	H2 monitoring of the period of interest: from DOYs 331 to 335/1978. The plots are given in the same sequence as in Figure 4.10. There is no shock registered by the probe, although it was operating during the corresponding period. . . . .	131
4.27	IMP-8 monitoring of the period from DOYs 331 to 336/1978. The sequence of plots is the same presented in Figure 4.10. No shock was registered during the considered period by the spacecraft. . . . .	132
4.28	H2 observation of a shock wave on DOY 312/1978, at 7:26 UT. The plots are given in the same sequence as in Figure 4.10. The shock is identified by the vertical line. . . . .	133
4.29	H1 observation from 310 to 314 DOYs of 1978. The plots are given in the same sequence as in Figure 4.10. No shock was registered by the probe during the corresponding period. . . . .	134
4.30	ISEE-3 plasma and magnetic field monitoring of the period from DOYs 310 to 317/1978. The plots are given in the same sequence as in Figure 4.10. Two shock waves were identified during the period. . . . .	135
4.31	H1 observation of a shock wave observed on DOY 131/1981, at 7:09 UT, as identified by the vertical line. The plots are given in the same sequence as in Figure 4.10. Note that a MC is the driver of the shock wave, as shown in the plasma and magnetic field parameter profiles. . . . .	137



4.32	ISEE-3 monitoring of the solar wind from DOY 129 to 135/1981. The plots are given in the same sequence as in Figure 4.10. No shock associated to the one at H1 was registered by the spacecraft during the corresponding period. . . . .	138
4.33	Rate of “safe” events observed by H1 (dark blue) and H2 (dark red) probes as a function of the angular separation between them. In the upper panel, the multi-spacecraft observations represent the distribution of the shocks inside each angle, while the lower panel shows that most events are distributed in this class of shock (seen by a single-spacecraft in space). . . . .	140
4.34	Percentage of “safe” registered events by H1 (dark blue) and H2 (dark red). Again, the multi-spacecraft observations are located in the upper panel, while the single-spacecraft ones are represented by the upside down histogram (lower panel). . . . .	141
4.35	Rate of shock waves observed from 1974 to 1985 (Table A.1) by at least two spacecraft (upper panel), or only one of the spacecraft (lower panel) according to the longitudinal separation ( $\Delta\Phi$ ) between the probes. The constellations are divided in three groups according to each two probes: Helios 1 and 2 (dark blue), Helios 1 and IMP-8/ISEE-3 (green), and Helios 2 and IMP-8/ISEE-3 (dark red). A total of 308 entries for the single and multi-spacecraft observations was collected. Note that increasing the angular distance between two different observational points diminishes the number of events observed by each of the constellations during the period of observation. At the top (upper panel) and at the bottom (lower panel) of each bar, one finds the total number of events in each bar according to each type of observation, multi or single-spacecraft. . . . .	143
4.36	Number of safe shocks distributed according to the angular extension and year of observation. At the ascending phase and maximum of the solar cycle, the number of shocks is bigger compared to the years of minimum or descending phase. . . . .	144

4.37	The percentage of shock waves observed into a longitudinal angle of separation between different probes shows that there is a bigger tendency for observing shocks in smaller angles ( $\Phi$ ). Helios 1 and 2 were not separated in more than $120^\circ$ of longitude between them. In $\Delta\Phi = 90^\circ$ , the same percentage is found for observing or not the shocks in two different points. This means that there is a cutoff value at this angle, so one can expect with the same likelihood a shock expanding in longitude until $90^\circ$ or not expanding until this angle. . . . .	145
4.38	This is the same plot as shown before in the percentage of shocks (upper panel of Figure 4.37). The error margin for the percentage of shocks observed by multi-spacecraft into each longitudinal separation as seen by Helios-1,2 and IMP-8/ISEE-3. As $\Delta\Phi$ increases, the uncertainty also does. Observe that in $\Delta\Phi = 110^\circ$ the biggest error for our estimate is found. That is because only two events, as seen in Figure 4.35, were registered for that angle: one was detected by a pair of probes, and the other by a single probe. . . . .	146
5.1	Number of shock waves detected at two spacecraft, where MCs were identified at minimum one spacecraft (upper panel) and shocks detected by only one spacecraft and MC as well (lower panel). The three different constellations are separated by colors: H1 and H2 (dark blue), H1 and IMP-8/ISEE-3 (green), and H2 and IMP-8/ISEE-3 (dark red). . . . .	151
5.2	Percentage of shock waves driven by MCs in multi-spacecraft (upper panel) and single-spacecraft (lower panel) observations. The legend corresponds to the same presented in Figure 5.1. . . . .	152
5.3	Rate of Magnetic Clouds seen by at least two spacecraft according to the separation $\Delta\Phi$ between the probes/spacecraft. The legend corresponds to the same presented in Figure 5.1. . . . .	153
5.4	H1 observation of a MC from DOY 29/1977, at 10:22 UT, to DOY 030, at 11:16 UT. The plots give, from top to bottom, the profiles of the magnetic field strength, and inclination and azimuthal angles, the protons speed, temperature and density, and the plasma beta, respectively. The vertical continuous line identifies the shock wave, driven by the MC whose boundaries are represented by the dotted lines. Note that at the first half of DOY 026 a HSS is identified by the plasma and magnetic field parameters. . . . .	156

5.5	H2 observation of a MC from DOY 029/1977, at 18:11 UT, to DOY 030/1977, at 06:31 UT. Meaning similar to Figure 5.4. . . . .	157
5.6	H2 magnetic field data for the MC observed on DOY 29-30/1977. The plots give, from top to bottom, the magnetic field strength, inclination and azimuthal angles, and components $B_x$ , $B_y$ and $B_z$ , followed by the plasma beta, respectively. The vertical continuous line identifies the shock wave, driven by the MC whose boundaries are represented by the dotted lines. . . . .	158
5.7	IMP-8 observation of a MC from DOY 30/1977, at 01:00 UT, to DOY 31, at 13:00 UT. Meaning similar to Figure 5.4. . . . .	159
5.8	Plane of Maximum Variance for the MC on DOY 029-030/1977 as observed by H1. The angles for the direction of the cloud's axis are represented by $\theta_2$ and $\phi_2$ in the figure. In addition, the error criteria ( $\lambda_2/\lambda_3 > 2$ ) is satisfied. The arrow indicates the initial points and gives the direction of the rotation of the magnetic field. . . . .	160
5.9	Plane of Maximum Variance for the MC observed by H2 on DOY 029-030/1977. Meaning similar to Figure 5.8. . . . .	162
5.10	Plane of maximum variance for the MC observed on DOYs 030-031/1977. The meaning is similar to Figure 5.8. . . . .	163
5.11	H1 observation of a MC on DOY 75/1977, from 16:15 UT to 23:43 UT. Meaning similar to Figure 5.4. . . . .	164
5.12	H1 magnetic field data for the period from DOY 75 to 77/1977. Meaning similar to Figure 5.6. . . . .	165
5.13	Plane of maximum variance for the MC observed by H1 on DOY 75/1977. Cloud's axis is directed according to the angles $\theta_2$ and $\phi_2$ . The criterion for the MVA technique is satisfied because $\lambda_2/\lambda_3 = 5.4$ . The arrow indicates the initial points and gives the direction of the rotation of the magnetic field. . . . .	166
5.14	H2 observation of the same MC observed by H1 on DOY 76/1977, from 05:06 UT to 20:09 UT. Meaning similar to Figure 5.4. . . . .	167
5.15	Magnetic field data by H2 for the period from DOY 75 to 77/1977. Meaning similar to Figure 5.6. . . . .	168
5.16	Plane of maximum variance for the MC observed by H2 on DOY 76/1977. The meaning is similar to Figure 5.8. . . . .	169
5.17	H2 observation of a MC from DOY 327/1977, at 21:01 UT, to DOY 328/1977, at 03:52 UT. Meaning similar to Figure 5.4. . . . .	170

5.18	H2 observation for the period between 327-329/1977. Meaning similar to Figure 5.6. . . . .	171
5.19	Maximum variance plane for the MC observed on DOY 327/1977. Meaning similar to Figure 5.8. . . . .	172
5.20	IMP-8 observation of a MC on DOY 329/1977, at 17:55 UT, to DOY 330/1977, at 12:10 UT. Meaning similar to Figure 5.4. . . . .	173
5.21	IMP-8 magnetic field data for the period from 329 to 331/1977. Meaning similar to Figure 5.6. . . . .	174
5.22	Maximum Variance plane for the MC observed on DOY 329/1977. Meaning similar to Figure 5.8. . . . .	175
5.23	H1 observation of a MC on DOY 335/1977, from 14:01 UT to 15:39 UT. Meaning similar to Figure 5.4. . . . .	177
5.24	H1 magnetic field data for the period from DOY 334 to 337/1977. Meaning similar to Figure 5.6. . . . .	178
5.25	Maximum Variance plane for H1 observation of a MC on DOY 335/1977. Through intermediate variance, the angles $\theta_2$ and $\phi_2$ that represent the direction of the cloud's axis are obtained. The arrow indicates the initial points and gives the direction of the rotation of the magnetic field. . . . .	179
5.26	H2 magnetic field data for the period from DOY 334-337/1977. Meaning similar to Figure 5.4. . . . .	180
5.27	H2 observation of a MC on DOY 335/1977, from 06:26 UT to 12:00 UT. Meaning similar to Figure 5.6. . . . .	181
5.28	H1 observation of a MC from DOY 003/1978, at 14:19 UT, to 004/1978, at 17:05 UT. Meaning similar to Figure 5.4. . . . .	184
5.29	H1 observation for the period between 003-005/1978. Meaning similar to Figure 5.6. . . . .	185
5.30	Plane of maximum variance analysis for the MC observed on DOYs 003-004/1978. Meaning similar to Figure 5.25. . . . .	186
5.31	H2 observation of a MC from DOY 004, at 07:36 UT, to DOY 005/1978, at 15:04 UT. Meaning similar to Figure 5.4. . . . .	187
5.32	H2 magnetic field data for the period from 003-006/1978. The plots give, from top to bottom, the profiles of the magnetic field strength, inclination and azimuthal angles, the components $B_x$ , $B_y$ and $B_z$ , and the plasma beta, respectively. The vertical continuous line identifies the shock wave, driven by the MC whose boundaries are represented by the dotted lines. . . . .	188
5.33	Plane of maximum variance for the MC observed by H2 on DOYs 003-004/1978. Meaning similar to Figure 5.25. . . . .	189

5.34	IMP-8 observation of a MC on DOY 004/1978, at 11:00 UT, to DOY 005/1978, at 20:00 UT. Meaning similar to Figure 5.4. . . . .	191
5.35	IMP-8 magnetic field data for the period from 003 to 007/1977. The plots give, from top to bottom, the profiles of the magnetic field strength, inclination and azimuthal angles, the $B_x$ , $B_y$ and $B_z$ components, and the plasma beta, respectively. The vertical continuous line identifies the shock wave, driven by the MC whose boundaries are represented by the dotted lines. . . . .	192
5.36	Plane of maximum variance for the MC observed by IMP-8. Meaning similar to Figure 5.25. . . . .	193
5.37	Intense geomagnetic storm ( $Dst_p = -121 \text{ nT}$ ) registered on DOY 005/1978, at 00:00 UT. . . . .	194
5.38	H1 observation of a MC from DOY 046, at 12:46 UT, to DOY 047/1978, at 21:50 UT. Meaning similar to Figure 5.4. . . . .	195
5.39	H1 observation of a MC from DOY 046/1978, at 12:46 UT, to 047/1978, at 21:50 UT. The plots give, from top to bottom, the profiles of the magnetic field strength, inclination and azimuthal angles, the components $B_x$ , $B_y$ and $B_z$ , and the plasma beta, respectively. The vertical continuous line identifies the shock wave, driven by the MC whose boundaries are represented by the dotted lines. . . . .	196
5.40	Plane of maximum variance analysis for the cloud on DOY 046-047/1978. Meaning similar to Figure 5.25. . . . .	197
5.41	H2 observation of a MC from DOY 046, at 09:58 UT, to DOY 048/1978, at 16:51 UT. Meaning similar to Figure 5.4. . . . .	198
5.42	H2 magnetic field data for the period from 045 to 049/1977. The plots give, from top to bottom, the profiles of the magnetic field strength, inclination and azimuthal angles, the components $B_x$ , $B_y$ and $B_z$ , and the plasma beta, respectively. The vertical continuous line identifies the shock wave, driven by the MC whose boundaries are represented by the dotted lines. . . . .	199
5.43	Plane of maximum variance for the MC observed on DOYs 046-048/1978. Meaning similar to Figure 5.25. . . . .	200
5.44	Intense magnetic storm ( $Dst_p = -108 \text{ nT}$ ) registered on DOY 047/1978 at the terrestrial magnetosphere. . . . .	201

5.45	H1 plasma and magnetic field data for the period from DOY 105 to 109/1978. The plots are given in the same sequence as in Figure 5.41. The vertical continuous line identifies the shock wave. There is no visible signatures for a MC. . . . .	203
5.46	H2 observation of a MC from DOY 106/1978, at 18:37 UT, to DOY 107/1978, at 01:08 UT. Meaning similar to Figure 5.4. . . . .	204
5.47	H2 magnetic field data for the period from 105-109/1978. Meaning similar to Figure 5.6. . . . .	205
5.48	Plane of Maximum variance for the MC observed on DOY 106-107/1978 by H2. Meaning similar to Figure 5.8. . . . .	206
5.49	H1 observation of a MC on DOY 058/1979, at 15:00 UT, to 059/1979, at 15:00 UT. Meaning similar to Figure 5.4. . . . .	208
5.50	H1 magnetic field data for the period from 057-060/1979. Meaning similar to Figure 5.6. . . . .	209
5.51	H2 monitoring of the period from DOY 057 to 060/1979. The plots give, from top to bottom, the profiles of the magnetic field strength, and inclination and azimuthal angles, the protons speed, temperature, and density, and the plasma beta, respectively. . . . .	210
5.52	H1 observation of a MC on DOY 176/1979, from 06:32 to 12:54 UT. Meaning similar to Figure 5.5. . . . .	212
5.53	H1 magnetic field data for the period from DOY 175-178/1979. Meaning similar to Figure 5.6. . . . .	213
5.54	Plane of Maximum Variance for the MC observed on DOY 176/1979 by H1. Meaning similar to Figure 5.8. . . . .	214
5.55	H2 observation of a shock wave on DOY 175/1979. The plots are given in the same sequence as in Figure 5.41. The same MC was not observed by the solar wind instruments. From the magnetic field instruments we do not have any data provided by them, so differentiating the structures in the IP medium becomes more difficult. Nevertheless, a HSS precedes the shock arrival on DOY 175/1979. . . . .	215
5.56	H1 observation of a MC from DOY 78/1977, at 21:20 UT, to DOY 079/1978, at 08:21 UT. Meaning similar to Figure 5.4. . . . .	217
5.57	H1 magnetic field data for the period from 078-081/1977. Meaning similar to Figure 5.6. . . . .	218
5.58	Plane of maximum variance for the MC observed from DOY 78/1977, at 21:20 UT, to 79/1977, at 08:21 UT. Meaning similar to Figure 5.8. . . . .	219

5.59	H2 magnetic field and plasma data for the period from DOY 076 to 081/1977. The plots are given in the same sequence as in Figure 5.41. There is nor shock neither MC identified through the parameter profiles. However, at the beginning of DOY 80/1977 a HSS is identified. . . . .	220
B.1	Rate of shock waves observed from 1974 to 1985 by at least two spacecraft (upper panel), or a single-spacecraft (lower panel) according to the longitudinal separation ( $\Delta\Phi$ ) between the probes. At the top (upper panel) and bottom (lower panel) of each bar, one finds the total number of events in each bar according to each type of observation: multi or single-spacecraft, respectively. . . . .	288
B.2	The percentage of “safe” events as a function of the longitudinal separation among the probes. In the upper panel, one can see the observations from multi-spacecraft (H1, H2, and IMP-8/ISEE-3), and in the lower panel one finds the sample of single-spacecraft observed events. . . . .	289
B.3	Percentage of shocks observed by multi-spacecraft and the error margin estimated for the percentage of shock waves observed in each angular separation $\Delta\Phi$ based on the test for proportions. . . . .	291
C.1	Representative sketch of a magnetic flux tube (approximation for a MC) traveling in the IP medium. Note that the original coordinate system is changed due to the application of the MVA technique, resulting in the components of maximum ( $B_x^*$ ), intermediate ( $B_y^*$ ), and minimum ( $B_z^*$ ) variance of the magnetic field. . . . .	296





## LIST OF TABLES

	<u>Pág.</u>
4.1 Arrival time of shocks when Helios 1 and 2 observed the same event. . .	102
A.1 Shock Waves Driven by ICMEs observed by Helios 1 and 2. . . . .	247
A.2 Classification of the type of observation done by Helios missions and IMP-8/ISEE-3 . . . . .	258
B.1 Student-t Distribution with the correspondent critical $t_{\alpha_c/2}$ values and the degrees of freedom ( $df$ ). . . . .	287



## LIST OF ABBREVIATIONS

AU	–	Astronomical Unit
CH	–	Coronal Hole
CIR	–	Corotating Interaction Region
CLASS	–	Classification of the Shocks
CLAT	–	Carrington Latitude
CLONG	–	Carrington Longitude
CME	–	Coronal Mass Ejection
CORR	–	Spacecraft for the comparison of the shock observation
DOY	–	Day of the Year
EIT	–	Extreme Ultraviolet Imaging Telescope
GSE	–	Geocentric Solar-Ecliptic
GSM	–	Geocentric Solar-Magnetospheric
H1	–	Helios 1
H2	–	Helios 2
HAO	–	High Altitude Observatory
HCS	–	Heliospheric Current Sheet
HH	–	Hour
HSE	–	Helios Sun-Earth angle
HSS	–	High-Speed Stream
ICME	–	Interplanetary Coronal Mass Ejection
IMF	–	Interplanetary Magnetic Field
IMP-8	–	Interplanetary Monitoring Platform 8
IP	–	Interplanetary
ISEE-3	–	The International Sun-Earth Explorer 3
LASCO	–	The Large Angle Spectrometric Coronagraph
MC	–	Magnetic Cloud
MHD	–	Magnetohydrodynamics
MLSO	–	Mauna Loa Solar Observatory
MM	–	Minute
MVA	–	Minimum Variance Analysis
N	–	North
OAFA	–	Observatorio Astronómico Félix Aguilar
OSO-7	–	7th Orbiting Solar Observatory
<i>p.f.</i>	–	Probability Function
<i>p.d.f.</i>	–	Probability Distribution Function
RAD	–	Radial Distance
RH	–	Rankine-Hugoniot
S	–	South
SC	–	Spacecraft

SEP – Solar Energetic Particles  
SMM – Solar Maximum Mission  
SN – Shock Number  
SoHO – Solar and Heliospheric Observatory  
YY – Year  
WDC – World Data Center

## LIST OF SYMBOLS

$X$	–	Sequence of observations
$\xi(\phi)$	–	Prior Distribution before the observations $x$
$\xi(\phi x)$	–	Posterior Distribution after the observations $x$
$df$	–	Degrees of Freedom
$R_{\odot}$	–	Solar radius
$R_E$	–	Earth radius
$d$	–	Radial distance
$B_S$	–	Southward Component of the Interplanetary Magnetic Field
$u$	–	Solar wind speed
$B_x$	–	Component-x of the IMF
$B_y$	–	Component-y of the IMF
$B_z$	–	Component-z of the IMF
$B$	–	Magnetic Field Strength
$Dst$	–	Disturbance Storm Time Index
$Dst_p$	–	Dst peak value
$\beta$	–	Plasma Beta
$J$	–	Current density
$\sigma$	–	Electrical Conductivity
$L1$	–	Lagrangian point
$\gamma$	–	Ratio of specific heats
$c_v$	–	Specific heat at constant volume
$\rho$	–	Mass density
$p$	–	Plasma pressure
$N_p$	–	Protons Density
$T_p$	–	Protons Temperature
$V_p$	–	Protons Velocity
$p_S$	–	Population Proportion
$\hat{p}_S$	–	Sample success estimator
$\hat{q}_S$	–	Sample failure estimator
$P$	–	Proportion of success from the sample of size N
$S$	–	Sample of size N
$\mu_S$	–	Mean of the sample S
$\sigma_S$	–	Variance of the sample S
$\mu$	–	Magnetic Permeability
$\mu_0$	–	Magnetic Permeability of the Free Space
$\rho_{SW}$	–	Solar Wind Mass Density
$\rho_1$	–	Upstream Mass Density
$\rho_2$	–	Downstream Mass Density
$B_1$	–	Upstream Magnetic Field

$B_2$	–	Downstream Magnetic Field
$B_{1n}$	–	Upstream Magnetic Field in the Normal Direction
$B_{2n}$	–	Downstream Magnetic Field in the Normal Direction
$n_1$	–	Upstream Solar Wind Density
$n_2$	–	Downstream Solar Wind Density
$v_1$	–	Upstream Solar Wind Velocity
$v_2$	–	Downstream Solar Wind Velocity
$p_1$	–	Upstream Solar Wind Pressure
$p_2$	–	Downstream Solar Wind Pressure
$\vec{B}_t$	–	Tangential Magnetic Field Vector
$B_{1t}$	–	Upstream Tangential Component of the Magnetic Field
$B_{2t}$	–	Downstream Tangential Component of the Magnetic Field
$v_{1n}$	–	Upstream Normal Component of the Solar Wind Velocity
$v_{2n}$	–	Downstream Normal Component of the Solar Wind Velocity
$v_{1t}$	–	Upstream Tangential Component of the Solar Wind Velocity
$v_{2t}$	–	Downstream Tangential Component of the Solar Wind Velocity
$u_1$	–	Upstream Radial Speed of the Shock
$u_2$	–	Downstream Radial Speed of the Shock
$R_N$	–	Ratio between the down and upstream values of the solar wind density
$R_B$	–	Ratio between the down and upstream values of the magnetic field strength
$\hat{n}$	–	Normal Unit Vector
$\hat{n}_{VC}$	–	Velocity Coplanarity Shock Normal
$\hat{n}_{MX1}$	–	First Mixed Mode Shock Normal
$\hat{n}_{MX2}$	–	Second Mixed Mode Shock Normal
$\hat{n}_{MX3}$	–	Third Mixed Mode Shock Normal
$\vec{B}_n$	–	Normal Magnetic Field Vector
$B_n$	–	Normal Component of the Ambient Magnetic Field
$\theta_{B_n}$	–	Angle between the shock normal and the upstream magnetic field
$\sigma^2$	–	Mean Quadratic Deviation
$\langle B^i \rangle$	–	Mean value of $\vec{B}$
$\lambda_1$	–	Eigenvalue for the direction of maximum variance
$\lambda_2$	–	Eigenvalue for the direction of intermediate variance
$\lambda_3$	–	Eigenvalue for the direction of minimum variance
$ e $	–	Magnitude of the unitary eigenvector
$e_1$	–	Eigenvector for the direction of maximum variance
$e_2$	–	Eigenvector for the direction of intermediate variance
$e_3$	–	Eigenvector for the direction of minimum variance

$\phi_k$	– Azimuthal Angle of the minimum variance plane
$\theta_k$	– Elevation Angle of the minimum variance plane
$x^*$	– Axis of the Maximum Variance
$y^*$	– Axis of the Intermediate Variance
$z^*$	– Axis of the Minimum Variance
$B_k^{i*}$	– Components of $\vec{B}$ in the minimum variance system
$B_1^*$	– Component of Maximum Variance
$B_2^*$	– Component of Intermediate Variance and orientation of the cloud axis
$B_3^*$	– Component of Minimum Variance
$B_{\alpha,\beta}$	– Cartesian Components of $\vec{B}$ for a single measurement
$M_{\alpha,\beta}$	– Covariance Matrix
$B^i$	– Individual Field Measurements
$N$	– Number of Data Points
$M_A$	– Alfvén Mach Number
$V_A$	– Alfvén Speed
$C_S$	– Speed of Sound
$V_S$	– Shock Speed
$M_{MS}$	– Magnetosonic Mach Number
$M_c$	– Critical Mach number
$V_{MS}$	– Magnetosonic Speed
$\alpha$	– General Scalar Function for the direction of the shock wave
$\theta$	– Elevation Angle out of the ecliptic plane
$\phi$	– Azimuthal Angle in the ecliptic plane
$r$	– Radial Distance in AU
$\Delta\Phi$	– Longitudinal Separation
$\vec{\Phi}$	– Zenith Direction
Y	– Yes for multi-point observation
N	– No for multi-point observation
D	– Discarded event
X	– Non-excluded event
$f(X \phi)$	– Distribution function of $\phi$ based on the observations $X = X_1, \dots, X_n$
$z_c$	– Confidence Coefficients
$\alpha_c$	– Significance Level
$\varsigma$	– Constant for the force-free magnetic field model
$\vec{H}$	– Magnetic Helicity
$\vec{A}$	– Potential Vector
$V$	– Volume that contains $\vec{B}$
$B_0$	– Magnetic field at the cloud's axis
$J_n$	– n-order Bessel functions

- $J_0$  – zeroth-order Bessel function
- $J_1$  – first-order Bessel function
- $p$  – distance from the cloud's axis



## 1 INTRODUCTION

The Sun is the star of the Solar System, extending its domain over the whole Heliosphere, the region dominated by the solar wind. As the center of the Solar System, the Sun contributes to several phenomena happening in the Heliosphere. Some of these phenomena can affect the terrestrial environment and human beings.

The study of space weather is an upcoming field in expansion worldwide because it combines the academic aspect with the observation (practical), giving the possibility of several applications. Certainly, with the increasing dependence of our society in the new and sensitive technologies, the necessity of studying and predicting the occurrence of geomagnetic disturbances and other atmospheric effects will increase. Satellite communication, sub-orbital flights, oil ducts among others that have an utmost dependence on understanding and being able to predict phenomena, such as magnetic storms. The solar sources and the dynamics of the IP structures are not completely understood so far. [Figure 1.1](#) is an illustration of the solar activity impact on satellites and astronauts in orbit. At Earth, depending on the latitude, some of the effects can threaten electric power grids that might cause extensive blackouts. Furthermore, colorful curtains of light, the so-called auroras, are seen from Earth in the poles as a result of solar wind particles precipitation and collision with other constituents of the terrestrial atmosphere.

Among other Space Weather phenomena, shock waves are very important mechanisms responsible for the dissipation of energy and acceleration of particles into the interplanetary medium. Their main drivers are the interplanetary counterparts of the Coronal Mass Ejections (CMEs), huge amounts of plasma released from the solar surface to the interplanetary space. Among the CMEs, a special class has features that differentiate them from the whole group, the so-called Magnetic Clouds (MCs). When traveling into space, Interplanetary Coronal Mass Ejections (ICMEs) are generally associated to shock waves formation due to the high speed they propagate.

As it was pointed out by [Schwenn \(2006\)](#), every fifth transient shock or ICME or isolated geomagnetic storm is not caused by an identifiable partial or full halo CME on the front side of the sun. This can be due to the fact that these CMEs are so narrow that they cannot be seen in the field of view of coronagraphs. Another possibility is that their solar sources are in the far side of the sun, and the shock's

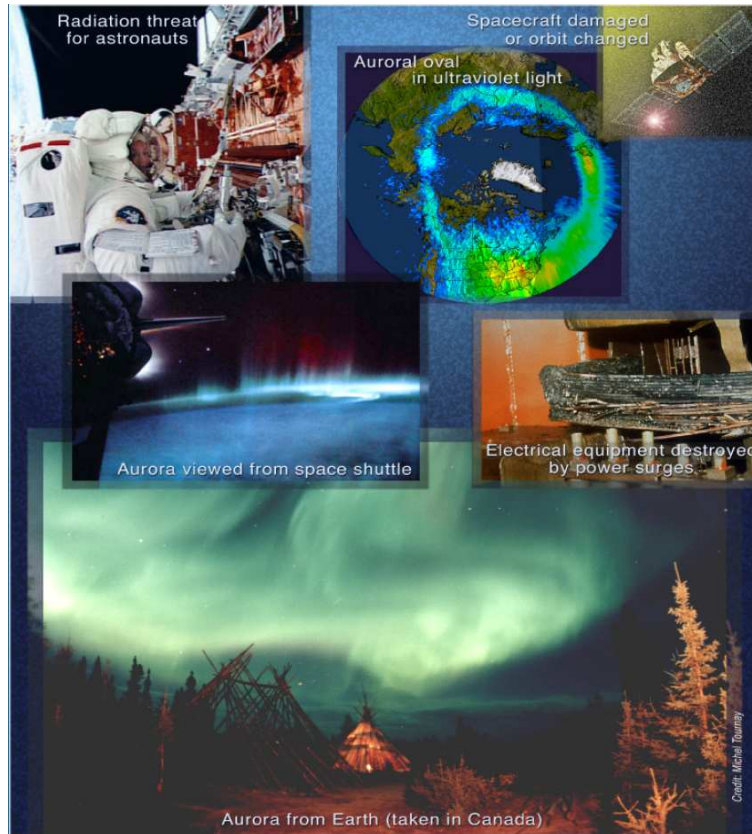


FIGURE 1.1 - Some effects of solar activity over aerospace technology systems and human activities in space, human being health and life. Astronauts are susceptible to the radiation threat when they are in orbit. Furthermore, spacecrafts can be damaged and their systems disrupted what can change their orbits.

SOURCE: SOHO Portfolio (2001). Access by <http://sohowww.nascom.nasa.gov>.

front extends into a large angle and reaches the Earth. In this sense, we emphasize the importance of the study of shock and ICMEs extension in the interplanetary medium, as a way of predicting their possible angular range. By using data from the end of 1974 until the beginning of the year 1986, provided by Helios mission and IMP-8/ISEE-3 spacecraft, we present some statistical results for the shock front's and magnetic cloud's extent.

Once we have the full coverage of the solar disc, one can improve space weather prediction models, such as CME travel time models. Based on the potential angular extent of geoeffective structures originated at the solar surface, such as ICMEs and the shock waves they drive, one can better correlate the solar activity with the space weather phenomena. Newly space missions have been providing several findings for the understanding of some phenomena in solar physics and space weather, and

probably the forthcoming space missions will answer many of the still open questions. Nevertheless, we cannot forget the diversity of findings some of the older missions provided and continue contributing to the space science. This is the case of Helios mission whose data this thesis will be profiting the most.

The Helios mission allowed unique associations between limb CMEs and their radial propagation toward an “in-situ” observer. Taking advantage on these findings and the several others due to the recent space missions (Ulysses, Yohkoh, SoHO, Wind, ACE), in addition to the more accurate simulation models, we can improve our understanding of the space weather phenomena. Furthermore, the Helios data can be useful for other missions like STEREO.

With STEREO mission, scientists are able to look at the Sun from two distant points in space and reconstruct the three dimensional form of CMEs and other interplanetary structures. Unfortunately, since STEREO was launched in late 2006, the sun is at minimum activity and there has been no events to include in this work.

## 1.1 Outline of the Thesis

The thesis consists of six chapters, divided according to our conception of better understanding of the present study. The *second chapter* introduces the solar environment inside 1 *AU* (inner heliosphere) and some of the main features observed in this region. Furthermore, some of the structures permeating the interplanetary medium will be addressed in this chapter, as well as their dynamics and main characteristics. The *third chapter* introduces the Helios mission, presenting the main tasks of the Helios project and its orbital characteristics. In the same chapter, the principal instruments composing the scientific payload of the project are described in conjunction with the involved institutions. The *fourth chapter* describes the shocks observed during Helios mission, estimating their extent in the inner heliosphere. This is done based on solar wind and magnetic field data at different radial and longitudinal distances in the inner heliosphere. Many magnetic clouds have been observed as the drivers of these shock waves, and Helios provided solar wind and magnetic field data for many of the events seen at least at two different points. Based on the dataset, one can also make some studies related to the magnetic cloud’s extent in the inner heliosphere, as it will be addressed in the *fifth chapter*. Finally, the *last chapter* summarizes the conclusion drawn at the end of each chapter with the results obtained in each of them, as well as the suggestions for future work related to the

present subjects.

## 2 REVIEW ON SOLAR ACTIVITY, INTERPLANETARY MEDIUM PROPERTIES AND STRUCTURES, AND SPACE WEATHER

In this chapter, we present a review on the theoretical and observational aspects of the solar wind with its different types, which are still under debate. Furthermore, a review on the first images and drawing of coronal mass ejections, followed by the observations through coronagraph, and their counterparts in the interplanetary (IP) medium will be presented. In particular, shock waves driven by these structures will be addressed. Their connection with solar flares is also taken into account during the discussion on the solar activity. A special section describes the particular class of the interplanetary coronal mass ejections: the magnetic clouds. Some of their interesting aspects are detailed in the sequence of the section “Magnetic Clouds”. Corotating Interaction Regions (CIRs) drive shock waves when traveling into space, however, these shocks are not usually formed in the inner heliosphere inside 1  $AU$ . A short description of this group of structures is going to be presented in the sequence of the present chapter. Later on, a theoretical review on the shock waves gives an idea of the main physical conservation laws governing this type of interplanetary structure.

### 2.1 The Sun

Ancient civilizations worshiped the Sun as one of the main gods of their cultures. Among the numerous cultures that considered the Sun as a god, the Egyptians called their Sun god Ra (or Re) and regarded him as the creator of light and all things. Ra was usually depicted in human form with a falcon head, crowned with the Sun disc and encircled by a serpent (REDFORD, 2002). The Sun itself was taken to be either his body or eye. Figure 2.1 is a representation of this god as worshiped by the Egyptians during their ancient empire.

Different ways of adoring the Sun along the history made him the god of intellect, honesty, virtue, truth, fertility, prophecy, and vitality. Sometimes, the divine also manifested in the form of a dark disc. They were the solar eclipses, adored by very old civilizations, and interpreted in different forms depending on the culture. The Babylonians, for instance, were the responsible for the discovery of the long cycle of 6,585.3 days (the so-called *Saros* cycle of eclipses). This cycle has been used in a large scale as an attempt to go back on time and fix the exact dates for old notable events.



FIGURE 2.1 - The God Sun, Ra, worshiped by the Egyptians, with the body of a man, a hawk or falcon head, over it a disc representing the Sun is involved by a serpent.

SOURCE: Adapted from (<http://www.uwm.edu/Course/egypt/Pyr/horus.jpg>). Access in: February 2009.

All the observations that were carried out during those periods did not use sophisticated instrumentation. Most of them were naked-eye observations, but did not have a very scientific meaning like nowadays they do. With the modernization and evolution of the observational techniques, the resources became diverse and made possible to better understand the phenomena occurring in the solar corona. Astronomers have achieved recently the use of sophisticated equipment and innovatory techniques in the study of solar eclipses. By virtue of the advent of these instruments, discoveries, such as the finding of Helium (He) in the solar eclipse of August 16<sup>th</sup> 1868, were achieved. The discovery of a non-static Sun led to the development of the coronagraph (LYOT, 1931). Through them, artificial eclipses would be simulated in order to obtain images from the solar corona, improving the dataset for the study of this phenomenon. Later on, scientists launched satellites to space with appropriate telescopes onboard them. In such way, spectral lines in wavelengths absorbed by Earth's atmosphere could also be observed. The result of these studies was a deeper understanding of the Sun and its 11-years cycle. Nevertheless, new discoveries and theories are needed in order to reach a more complete understanding of the whole mechanisms that take place in the Sun.

## 2.2 Solar Atmosphere and Energy

When we observe the Sun near Earth, at 1  $AU$  (Astronomical Unit, 1  $AU = 1.49 \times 10^8 \text{ km}$ ) distance, the Sun seems a giant sphere of gas whose radius ( $R_{\odot}$ ) is approximately  $6.96 \times 10^5 \text{ km}$  and mass around  $1.99 \times 10^{30} \text{ kg}$ . The mean density of our star is  $1.4 \text{ g/cm}^3$  and the radiation emitted is  $3.86 \times 10^{26} \text{ W}$  (PRIEST, 2000).

The energy emanating from the Sun is the main source playing an important role in geospace. The origin of this energy is supposed to be in the core of the Sun, where extremely high temperatures - more than  $15 \text{ MK}$  - and a very condensate material dominate the region (PRIEST, 2000). Both these features represent very important generators of energy in the core once they create an appropriate environment for the occurrence of nuclear fusion reactions. From the core, the energy propagates to the solar surface through the photons that are found in the radiative zone. In its way, the energy, in form of radiation, transfers itself by interaction with the atoms found in this region. Crossed the radiative zone ( $d < 0.7R_{\odot}$ ), the energy continues to be transferred outward, this time by convection. All these regions are shown in Figure 2.2 that is a representation of the solar atmosphere and internal structure. As one can see, the energy is first generated in the core, the innermost region, propagating to the outer layers of the interior, and then reaching the solar atmosphere.

In the convective region, a thin visible surface layer of approximately  $550 \text{ km}$ , known as photosphere, represents the transition between the interior and the outer atmosphere of the Sun. In this region, the energy is transferred through radiation and reaches further regions from the core. When observing with naked eye, it represents the only visible region of the solar atmosphere. Sunspots, faculae and granules are characteristic structures of this layer, all of them easily observed by using a telescope. In terms of temperature, the photosphere is characterized by temperature decreasing with increasing height.

Just above the photosphere, the region known as chromosphere is characterized by its irregularity and temperatures around  $20,000 \text{ K}$ . At these temperatures, the hydrogen emits reddish light ( $H_{\alpha}$  emission), mainly visible in prominences that project themselves above the solar limb during the occurrence of total solar eclipses. For this reason, the chromosphere receives the name of *color-sphere*. When observed through a spectrometer or a filter, elements of the magnetic field, bright plages around sunspots, filaments in the disc, and prominences above the solar limb can



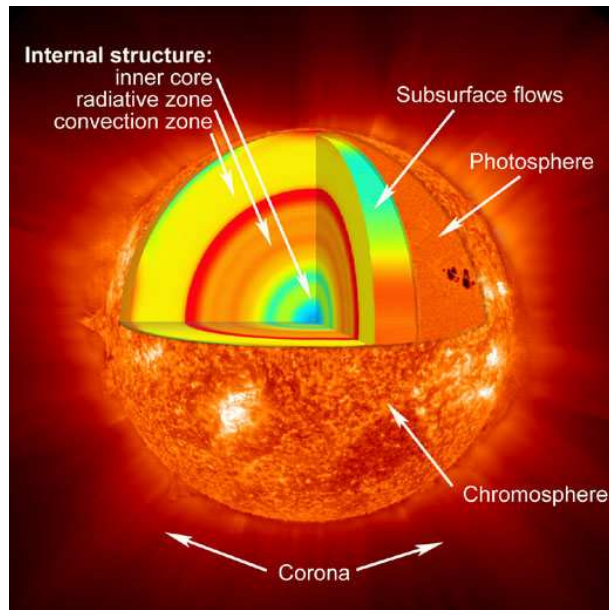


FIGURE 2.2 - Solar interior and atmosphere. The energy is generated in the core, then transferred to the radiative zone through photons, and then to the convective zone by convection, corresponding to the solar interior. In the outer part of the solar structure, one finds the atmosphere that comprises the photosphere, the chromosphere, and the corona, the outermost layer of the atmosphere.

SOURCE: SoHO (2006).

be visualized. [Figure 2.3](#) is an image taken from HASTA ground-based telescope in Argentina, showing darker regions in the solar surface, the prominences seen in  $H_{\alpha}$ . In addition to the  $H_{\alpha}$  emission, the chromosphere is also visible in the wavelength of the light emitted by neutrons and ionized atoms, such as Ca II, in the violet part of the spectrum ( $3934 \text{ \AA}$ ), corresponding to the K Ca emissions.

Described by an extreme change in temperature, from  $20,000 \text{ K}$  in the top of the photosphere to temperatures higher than  $2 \text{ MK}$ , the transition region, just above the chromosphere, emits light basically by a few times ionized ions (C III-IV, O IV-VI, Si IV-VI, N III-V). They radiate mainly in the region of the ultraviolet solar spectrum, only accessible from space. In the sequence, the most external region of the solar atmosphere is known as corona due to its appearance during solar eclipses. It extends into the IP medium and forms the solar wind as a result of the magnetic and dynamic pressures disequilibrium and gravity ([PARKER, 1958](#)). This region is thin and tenuous, being visible from earth only during the occurrence of solar eclipses or by using images taken from coronagraphs. Dominated by the solar magnetic field,



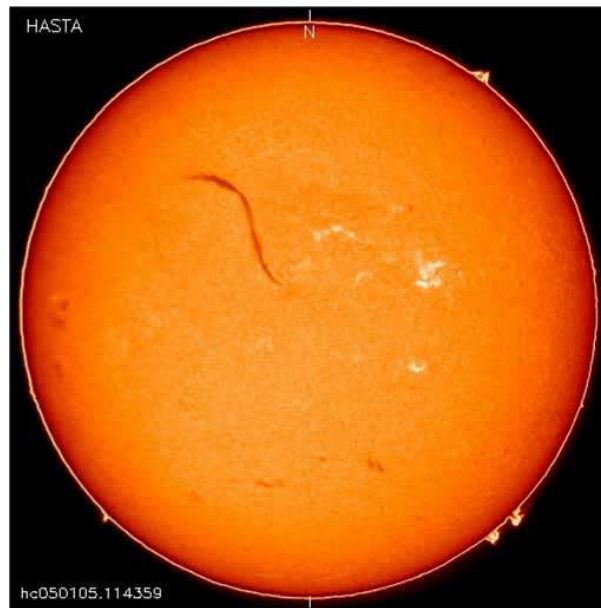


FIGURE 2.3 - A disappearing filament seen in H- $\alpha$  by HASTA telescope.

SOURCE: Oafa (2005).

the corona suffers the influence of its high temperatures. The kinetic pressure is then increased in this medium to values higher than the pressure of the medium outside it. As a result, plasma in the corona flows into the IP space carrying with it part of the magnetic field (PARKER, 1958; HUNDHAUSEN, 1972) whose name in that region is Interplanetary Magnetic Field (IMF).

The name “solar wind” was proposed by Parker (1958) and its confirmation came with the advent of the Soviet probes Lunik 2 and 3 in 1960, after they left the magnetosphere. The probe Mariner, in 1962, during its 4 months around the planet Venus, have also confirmed the existence of a continuous flow of plasma from the Sun (PARKS, 1991). The solar wind is now recognized as a mixture of elements found in the solar plasma, such as ionized hydrogen (protons and electrons), helium (He) (alpha particles), and trace amounts of heavy ions and atomic nuclei: C, N, O, Ne, Mg, Si, S, and Fe ripped apart by heating of the Sun’s outer atmosphere, that is, the corona (FELDMAN et al., 1998). In the corona, the flux of particles is dominated by the Sun’s magnetic field pressure and the thermal pressure of the fluid. At certain distances, some of the features of the solar wind, particularly in the case of the high-speed streams (HSSs) (KRIEGER et al., 1973; NOCI, 1973), can be identified with

features of the large-scale corona, the so-called coronal holes (CHs). Coronal holes are usually located above inactive parts of the Sun, where “open” magnetic field lines prevail, e.g., at the polar caps around activity minima (WOO; HABBAL, 2002; GONZALEZ et al., 1999).

In the IP medium, the solar wind is composed by two basic types: the slow and fast solar winds. The former has typical speeds around  $400 \text{ km/s}$  while in the latter the speeds are about  $750\text{--}800 \text{ km/s}$ . Ulysses and Helios (SCHWENN, 1990) missions both contributed to the confirmation of the existence of these two different types of solar wind. Ulysses described orbits over the solar poles and observed more the fast solar wind. On the other hand, Helios with its orbit mostly in the ecliptic plane, detected the features of the slow solar wind commonly found in the equatorial region. In fact, the existence of sharp boundaries between solar wind streams (in longitude as well as in latitude) had already been noticed by Rosenbauer et al. (1977) and Schwenn et al. (1978). Their assumptions were supported by the “in situ” measurements from the Helios solar probes that went as close as  $0.3 \text{ AU}$  of distance from the Sun. These two basic types of quasi-steady solar wind differ markedly in their main properties and by the location and magnetic topology of their sources in the corona. They are probably distinct in relation to their acceleration mechanisms.

It is important to note that both the CHs as well as the HSSs, which emerge from the CHs, are representatives of the inactive or “quiet” Sun. In this sense, the fast solar wind stream may deserve the label “quiet” rather than the slow solar wind, originating from above active regions. Feldman et al. (1976) and Bame et al. (1977) were the first to propose this nomenclature, which caused a major paradigm change. No longer could the slow wind be considered the “quiet” or “ground state” type, although it would fit much better to the famous model of a thermally driven solar wind as derived by Parker (1958).

On the other hand, the more active near-equatorial regions on the Sun are most often associated with “closed” magnetic structures, such as bipolar loop systems and helmet streamers on top (SCHWENN, 2006). From there, the more turbulent slow solar wind emerges. Figure 2.4 exhibits these two sources of the respective states of the solar wind. The dark regions are the CHs, a result of the observation in hot lines once the open field lines does not confine the plasma that is free to flow into the IP medium. One can also observe structures in form of arcades that are formed over lines of magnetic polarity inversion on the photosphere (STURROCK;

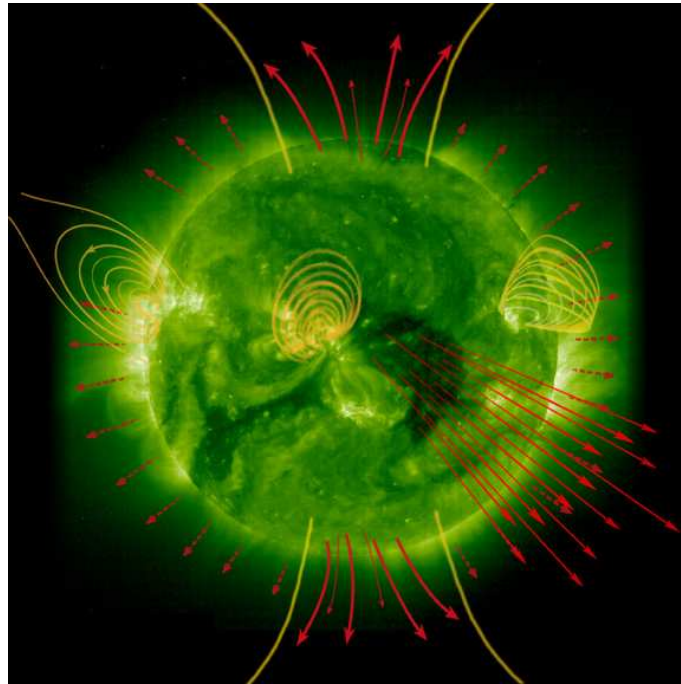


FIGURE 2.4 - EIT 195 Å image from SoHO. Over the CHs (dark regions) the configuration of the magnetic field is represented by open field lines, while over the bright regions (active regions) the predominant field is the one characterized by closed field lines.

SOURCE: SoHO (2006).

SMITH, 1968; PNEUMAN, 1968). Such structures are normally located over sunspots and active regions, the so-called helmet streamers (HOWARD et al., 1985; ILLING; HUNDHAUSEN, 1986; STEINOLFSON; HUNDHAUSEN, 1988). In their base, generally filaments or prominences are observed. The magnetic configuration formed by a set of closed loops contributes to the suspension of the prominence material over the solar surface. These closed magnetic field lines trap the electrically charged coronal gases to form these relative dense structures. At these regions, close to the solar equator, the majority of Coronal Mass Ejections (CMEs) is observed (HOWARD et al., 1985; ST. CYR et al., 2000).

In addition to these two basic states of solar wind typical of the solar minimum, the slow solar wind that fills most of the heliosphere during high solar activity can be considered as a third category. It emerges from above active regions distributed over large parts of the Sun, far from the Heliospheric Current Sheet (HCS), and in a highly turbulent state. It differs in some aspects from the slow solar wind at solar

minimum. Finally, we regard the plasma expelled from the Sun during huge CMEs as a category on its own, because of some fundamental differences (SCHWENN, 2006).

Recent studies have considered CMEs as a third category of solar wind (MARSCH *et al.*, 2003). However, the difficulties to understand the mechanisms involved in their acceleration, as well as the mechanism related to the generation of these structures, reveal that there is still a lot to be investigated. It is observed that around 30% of the CMEs have associated to their sources an enormous eruptive prominence (WANG; ZHANG, 2008) whose features can be observed even after the eruption. The plasma behavior is very different when CMEs are involved once we deal with densities in general higher than the typical solar wind density. Furthermore, CMEs are generally associated to propagation speeds that can reach more than 2000 *km/s*.

### 2.3 Coronal Mass Ejections

About forty years ago, before the first space-borne white-light coronagraph observations started, our knowledge of the solar corona was limited to observations made by a very few ground-based coronagraph or during total solar eclipses (HUNDHAUSEN, 1999; GOSLING, 1999). Before that, scientists used to make drawing of what was observed in the corona. One example is Figure 2.5, a drawing of the eclipse of 18 July 1860, probably the most thoroughly observed eclipse up to that time. In all the drawings found from these events, it is possible to observe a peculiar feature in the corona regarding a CME.

At the time of the first observations, the corona was considered very quiet, almost static, with a very slow evolution in its appearance over the 11-years solar activity cycle. With the advent of the new technologies and the improvement on the observation techniques, the corona was recognized by its very dynamic behavior, with activity occurring over a wide range of temporal and spatial scales. Perhaps the most spectacular manifestations of the coronal activity are the CMEs (PLUNKETT; WU, 2000).

#### 2.3.1 Flares and CMEs

Carrington, in 1859, was the first to suggest the association between a flare he observed and a geomagnetic storm, detected 17 hours later, as he reported to the Royal Society. Carrington's report in 1860 was reprinted in Meadows (1970).

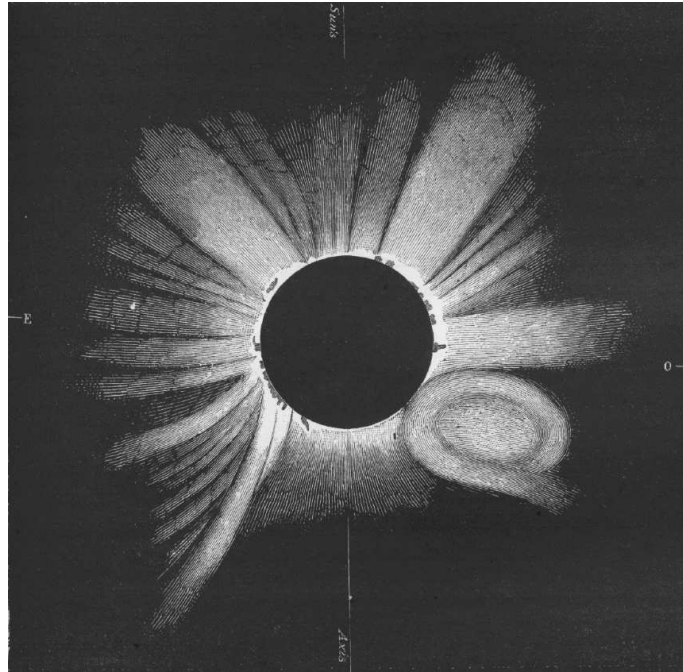


FIGURE 2.5 - Drawing of the corona as it appeared to Tempel at Torreblanca, Spain, during the total solar eclipse of 18 July 1860 that may be the first register of a CME (EDDY, 1974).

SOURCE: Adapted from Eddy (1974).

The release of the magnetic energy accumulated in the solar atmosphere is named “flare”. Solar flares are certainly among the most dramatic and energetic fast processes in our solar system that we know of. They can be identified by a sudden (within seconds to minutes) and intense variation in brightness. The flashes of electromagnetic radiation released may cover a wavelength range of as much as 17 orders of magnitude: from kilometric radio waves through the infrared, visible and UV ranges down to X-rays and even Gamma-rays (SCHWENN, 2006). Figure 2.6 is an example of a X3-category solar flare occurred on DOY 347/2006, at precisely 02:34 UT. The explosion hurled a CME into space which drove a shock wave later on. Particles were accelerated during the flare because of the magnetic energy release.

Flares were considered during decades the responsible for the geomagnetic activity until the first observations of CMEs were available through the coronagraph onboard the seventh Orbiting Solar Observatory (OSO-7). After that, the real importance of the flares and their association with the geomagnetic activity were discussed again (Gosling (1993), Schwenn (1996), and references therein). With the improve-

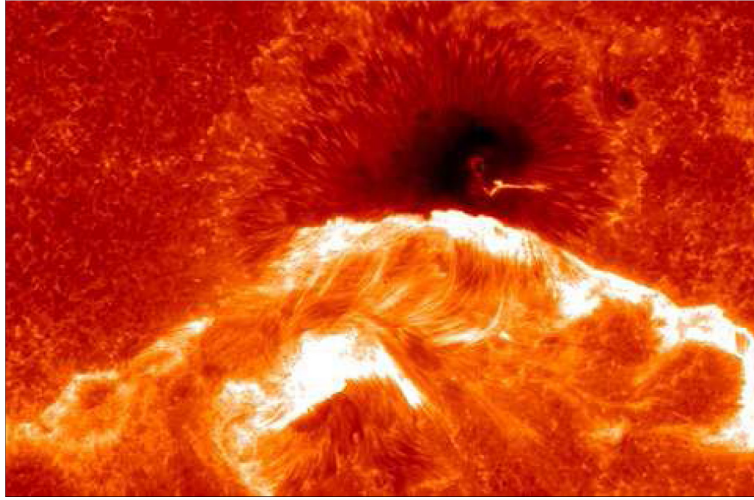


FIGURE 2.6 - Solar flare observed by HINODE on DOY 347/2006.

SOURCE: HINODE JAXA/NASA (2006).

ment on the coronagraph observations, it was shown that the CMEs are generally associated to solar flares ([KAHLER, 1992](#)). However, there are some CMEs observed without flares, and flares with no observation of CMEs in the coronagraph. Nevertheless, when both flare and CME are produced they share in their sources the same energetic processes for accelerating the CME and setting free the energy from the flare ([ZHANG et al., 2004](#)).

Related to the magnetic configuration of the solar surface when CMEs are released, it is known that there is a strong connection between the magnetic field lines opening and the solar material ejected to IP space ([GONZALEZ et al., 1996](#)). This connection is recognized through radio wave measurements when intense solar flares are observed in the high corona. Only after the advent of the first coronagraph OSO-7 and with Skylab/ATM and P78-1 at the beginning of the 1970's ([TOUSEY, 1973](#); [HILDNER et al., 1976](#)) came the first observation of a CME at the solar surface. The white light that appeared in the coronagraph images onboard OSO-7 gave birth to the knowledge of a new type of solar eruption ([TOUSEY et al., 1973](#)), later denominated Coronal Mass Ejections (CMEs) ([GOSLING et al., 1975](#); [BURLAGA et al., 1982](#)). [Hundhausen et al. \(1984\)](#) and [Schwenn \(1996\)](#) have defined a CME as “an observable change in coronal structure that 1) occurs on a time scale of a few minutes and several hours and 2) involves the appearance (and outward motion) of a new, discrete, bright, white light feature in the coronagraph field of view”.



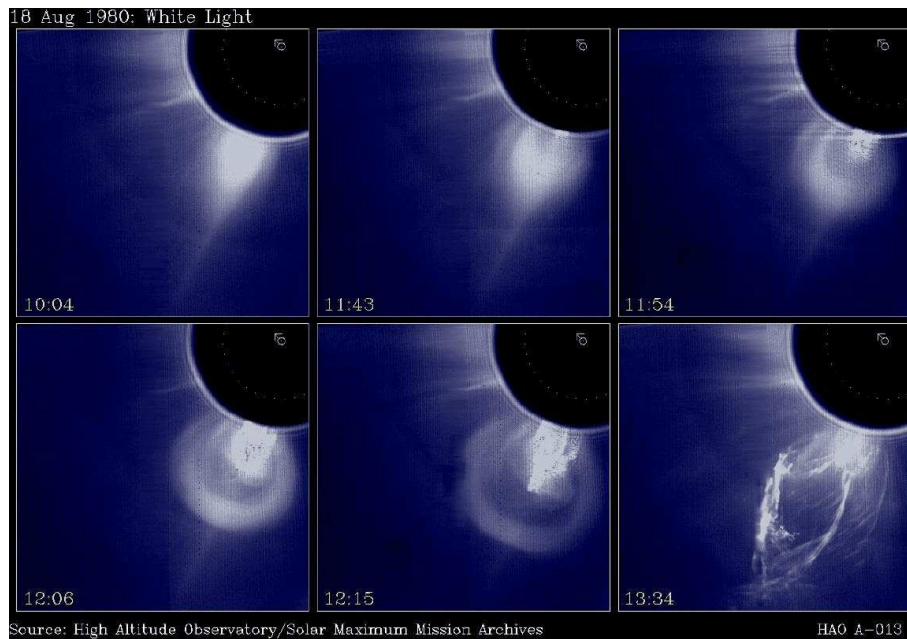


FIGURE 2.7 - CME observed by the HAO coronagraph onboard Solar Maximum Mission (SMM) spacecraft on DOY 231/1980 (August 18, 1980), at 13:09 UT.

SOURCE: MLSO (1980).

In the 1980's, the High Altitude Observatory's (HAO) coronal observations onboard Solar Maximum Mission (SMM) observatory contributed to the study of the dynamics of solar flares and their relationship with the corona. The observation of CMEs was also possible through the HAO coronagraph, as it is shown in [Figure 2.7](#) for the CME observed on DOY 231/1980, at 13:09 UT.

Among the phenomena that are responsible for the opening of the magnetic field lines, eruptive flares are only a set - and apparently the more energetic - when a very intense magnetic field inside an active region is involved in the process. The opening of the magnetic field lines is visible in most part of the events through a filament activation, observed in the  $H_{\alpha}$  images. This happens because the inversion lines inside active regions are generally characterized by dark filaments. [Figure 2.8](#) shows a model for a filament that goes up slowly to the corona being accelerated until the filament disrupts. When the open magnetic field lines start reconnecting again (flares), particles are accelerated to space and also inside the new loops that are formed. When the collision with a denser material takes place, bright bands and loops start appearing at the same time that the material is ejected and propagates

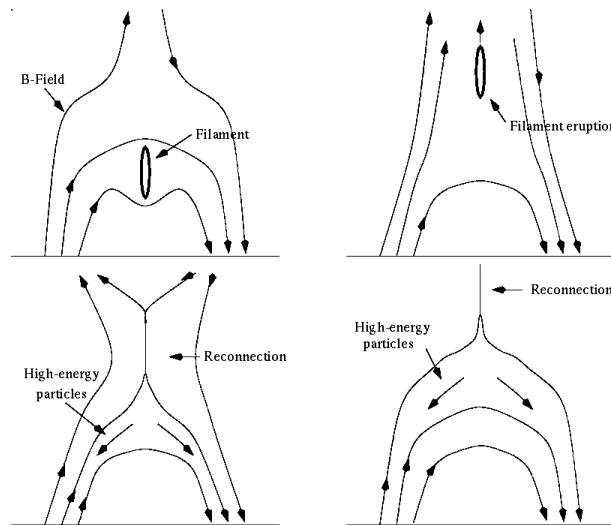


FIGURE 2.8 - Model for interpretation of the energy release through magnetic reconnection. The filament emerges and is broken out forming new loops as well releasing energy through flares.

SOURCE: TRACE webpage  
 (<http://soi.stanford.edu/results/SolPhys200/Schrijver/images/tworibbonflaremodel.gif>).  
 Access on January 2009.

with a speed of hundreds of  $km/s$  in the high corona toward the IP medium. In general, quiescent filaments are observed far away from active regions and dominate the solar surface during the quiet Sun, being able to become active and break down. The first time the activity of this type of filament was observed through X-rays was in the 1970's, revealing the effects of these phenomena, also important in terms of the impact at Earth and in the IP medium (KAHLER, 1977).

The image obtained from a coronagraph, like the one shown in Figure 2.9, is a result of the projection of the structure in the plane of sky, showing the light scattered by electrons in the corona. Due to the projection effect, a large diversity of CME shapes is obtained (BURKEPILE et al., 2004; CREMADES; BOTHMER, 2004). The brightness in a given point is the result of the integration over the scattered light along the line of sight from the telescope. The integral is known as the scattering of the light close to the plane of sky, where the photospheric radiation and the scattering on the electron density are higher.

CMEs are gigantic plasma clouds ejected from the Sun to the IP space that normally are associated to high propagation speeds. This later property leads to large scale



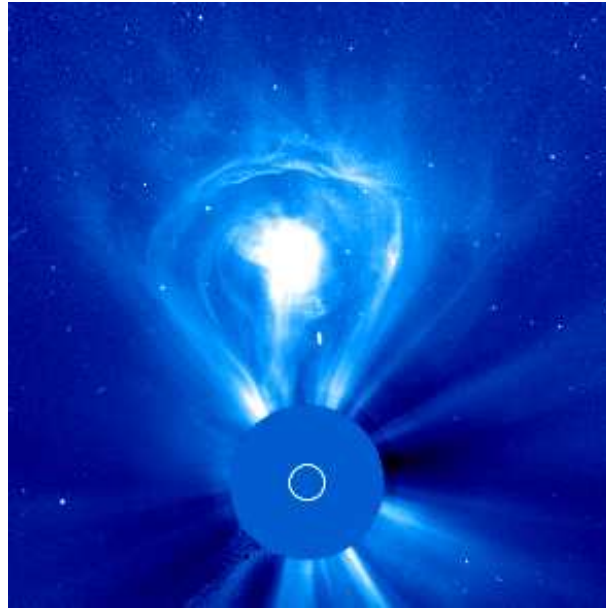


FIGURE 2.9 - The three-parts *light bulb* CME that was observed by LASCO-C3 coronagraph onboard SoHO satellite on February 27, 2000. The bright kernel is the innermost part of the CME, followed by the “dark void” and the bright loops.

SOURCE: SoHO (2000).

shock waves generated due to the difference between the speed of the medium and the speed of the CME. [Figure 2.9](#) is an image of a CME obtained by the Large Angle Spectrometric Coronagraph (LASCO) C3 onboard SoHO. From the figure one can clearly identify the noteworthy 3-part structure of the CME (a bright outer loop, followed by a dark void, and finally by a bright kernel). The CME, released at high latitudes, was named *light bulb* due to its light bulb shape.

By using images from LASCO, [Cremades et al. \(2006\)](#) found that CMEs’ central Position Angles (PAs) have been sorted in two categories : eastern PAs (0-180°) and western PAs (180-360°). The PA is an angular attribute of a feature projected in the plane of the sky, measured counterclockwise from the solar north. Because of their position in the solar disc and the place they are ejected in the field of view of the coronagraph, CME may be classified as limbs, halos or partial halos. The so-called “halo” CMEs extend themselves over the full solar disc, an their brightening occurs simultaneously all around the coronagraph occulting disk ([HOWARD et al., 1982](#)).

[Cremades and Bothmer \(2004\)](#) have corrected the effect of CME’s projection for 200

events observed between years 1996 and 2002 by determining their real latitudinal centers. During solar minimum the solar equator was pointed out as the center of the ejections. They found that the CME sources were centered in two belts around  $25^\circ$  latitude North and South. Furthermore, the deflection on the structured CME was mostly caused by the fast solar wind from the CHs in the solar poles. CHs block the CME expansion to higher latitudes, however, this has a dependence on the solar cycle and on the complexity of the corona. For instance, when larger CHs are absent, the CMEs would not suffer such deflection.

## 2.4 Propagation in the Interplanetary Medium

The combination of observations from LASCO and the Extreme Ultraviolet Imaging Telescope (EIT) allowed the determination of the origin of the CME, whether it is in the far side or in the visible disk (earthward). In addition to the images obtained from the instruments onboard the satellites, magnetic field and plasma data complement the understanding of the relations between the IP structures and their solar sources.

When propagating in the IP medium, together with the solar wind that constantly flows from the solar atmosphere, the CMEs are named Interplanetary Coronal Mass Ejections (ICMEs). The frequency of their occurrence is a function of the 11-years solar activity cycle. During the maximum of the solar activity the frequency is higher than 6 CMEs/day, while in the minimum this frequency decreases to 0.5 CMEs/day (GOPALSWAMY, 2006). Gopalswamy et al. (2003) studied the solar cycle variations of various properties of CMEs for cycle 23 (1996-2002) and they found an increase of the mean and median speeds of CMEs from minimum to maximum by a factor of 2.

The mass that is driven out from the Sun during CMEs may vary from  $10^{12}$  to  $10^{13}$   $kg$  of material, with speeds ranging from 200 to 2,000  $km/s$ . Due to the extremely high speeds, they are associated with shock waves as they propagate in the IP medium (GOSLING et al., 1991). Traveling with the continuous solar wind, a slow CME might be accelerated in this medium, and a fast one, decelerated (LOW, 1990; LINDSAY et al., 1999). To explain this variation on the speed of the ICMEs as they travel away and encounter different plasma environments in their ways, a height-time diagram of the characteristic movement is constructed for each CME. From these diagrams, it is possible to follow the acceleration/deceleration of the CMEs, and the speed of each propagating structure is determined.

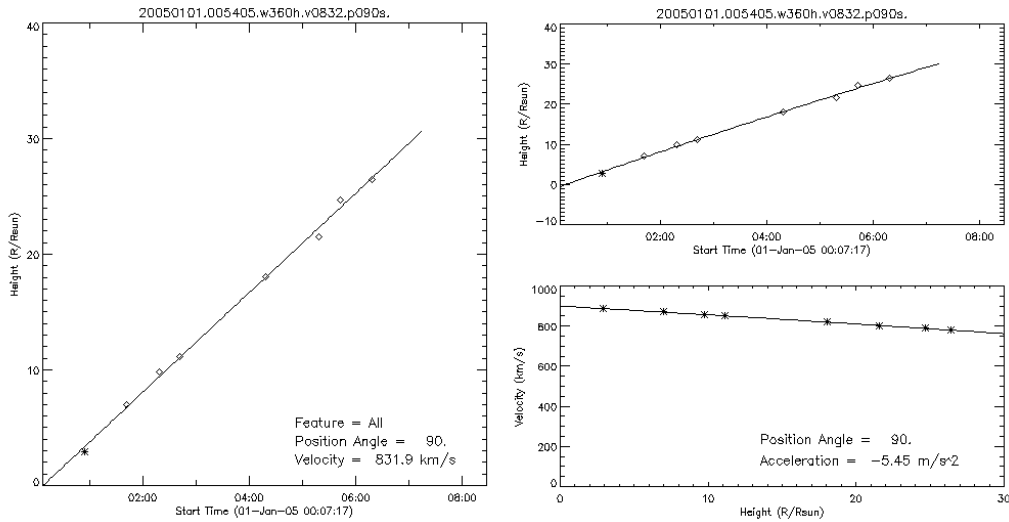


FIGURE 2.10 - Height-time diagram for the leading edge of the CME observed on DOY 001/2005 as provided by LASCO/C2 and C3 observations.

SOURCE: SoHO (<http://sohowww.nascom.nasa.gov/home.html>). Access on November 2008.

Yashiro et al. (2004) built a catalog with more than 10,000 CMEs observed by the instruments onboard SoHO during 10 years of the mission. The on-line catalog (<http://cdaw.gsfc.nasa.gov/CME list/>) documents the observed properties of all CMEs observed by LASCO, such as central position angle, angular width in the plane of sky, heliocentric distance with time, average speed, and acceleration. For each event, images from EIT telescope and the two LASCO coronagraph, C2 and C3, contributed to the composition of the CMEs height-time diagrams. Figure 2.10 shows the height-time diagram for the CME on DOY 001/2005. On the left panel, one finds that the average front edge speed (the first fit) was 831.9 km/s, while the acceleration was negative and equal to  $-5.45 \text{ m/s}^2$  (right panel at the bottom). In this case, the CME was decelerated as it moved outwardly from the Sun. Figure 2.11 is a schematic representation of a ICME propagating in the IP space. Two spacecraft, T1 and T2, go through the structure crossing different parts of it, showing that not always we have a complete view of the structure that is traveling earthward. Besides the influence of the solar activity and the dynamics of the corona on the evolution of the structures, the position of the spacecraft when it crosses the traveling structure influences the study of the propagation and features of those structures. As the scheme shows, the speed of the ICME is higher than the speed of the medium.

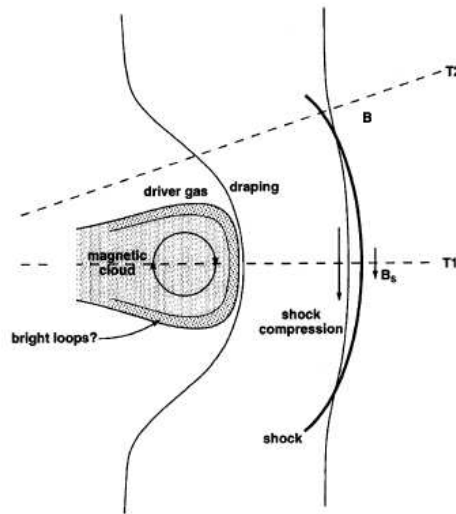


FIGURE 2.11 - Schematic representation of an ICME observed at 1  $AU$ . Two satellites, T1 and T2, cross the structure, observing different parts of it. In front of the ICME, a very turbulent region, composed by an intense southward magnetic field, is formed between the ejecta - in this case, a MC is identified due to the rotation of  $\vec{B}$  - and the shock.

SOURCE: Adapted from [Gonzalez et al. \(2002\)](#).

That is the reason why the shock wave is formed in front of the structure. Behind the shock driven by the ICME, a turbulent region of compressed plasma and magnetic field is formed. There, the plasma temperature is very high, and the oscillation on the magnetic field direction is also intense due to the compression of the structure against the shock wave. This region is named “sheath region”. As one can see, the rotation on the magnetic field is observed inside the “ejecta” characterizing a special class of ICMEs: the Magnetic Clouds (MCs), to be discussed in Section 2.5. Around one third of the total ICME events belong to this class ([BURLAGA et al., 1981](#); [GOSLING, 1990](#)).

## 2.5 CIRs and Shocks

When flowing from higher latitude regions, the solar wind is normally faster than the one closer to the solar Equator. This is because its source is associated to the CHs, regions characterized by an open magnetic field line configuration. At the CHs, particles are free to flow as they are accelerated due to the presence of the magnetic field. The fast wind can encounter the slow solar wind in the way to the IP medium and form compression regions. The region of interaction between these two flows

with different speeds, density and magnetic field topologies suffers an influence of the solar rotation as it is decelerated due to the presence of the slow solar wind (GOSLING *et al.*, 1976; GOSLING; PIZZO, 1999; BALOGH *et al.*, 1999). That is the reason for the name Corotating Interaction Region (CIR).

The existence of CIRs had been suggested based on the observation of their geomagnetic effects (PARKER, 1963). The hypothesis of the existence of CIRs played an important role on the theory and practice for some studies carried out by using the “in situ” measurements from these probes (PARKER, 1958; PARKER, 1963). On the other hand, the corotating shocks at CIRs were first identified between 1 and 5  $AU$  by the probes *Pioneer 10* and *11* through the magnetic field and plasma data collected by them during their operation.

After the launch of Helios mission, important information related to the features of such structures in the inner heliosphere were available. From these data, it was possible to compare two different regions in the heliosphere, the inner and the outer heliosphere. The observations made by Helios served as a link between what was known about CIRs at distances between 1 and 5  $AU$ , and their evolution in the inner heliosphere. The interaction regions observed in distances of the order of 0.3  $AU$  are very small compared to those from distances very far from the Sun.

Figure 2.12 (SCHWENN, 1990) is a schematic representation of the idealized evolution of a CIR in the inner heliosphere (inside 1  $AU$ ). The speed whose profile is initially near the Sun “rectangular” suffers the action of compression and deflection in both sides of the interface between the two types of solar wind. When one increases the heliocentric distance the result is that the open field lines of the faster wind (with a smaller Parker angle) start making pressure on the slower solar wind against the more curved magnetic field lines. For this reason, inside 1  $AU$ , the compression region that extends over some  $30^\circ$  in longitude has plasma content that has emerged from a coronal source at  $70^\circ$  of longitudinal extension. As a result, sector boundaries at 1  $AU$  are found sometimes inside these compressed regions even though they are well separated and independent of a stream interface (SCHWENN, 1990).

## 2.6 ICMEs and Shocks

Transient shocks are often formed during the passage of large scale structures, such as the ICMEs, in the IP medium (SHEELEY JR. *et al.*, 1985; SCHWENN, 1986; CANE

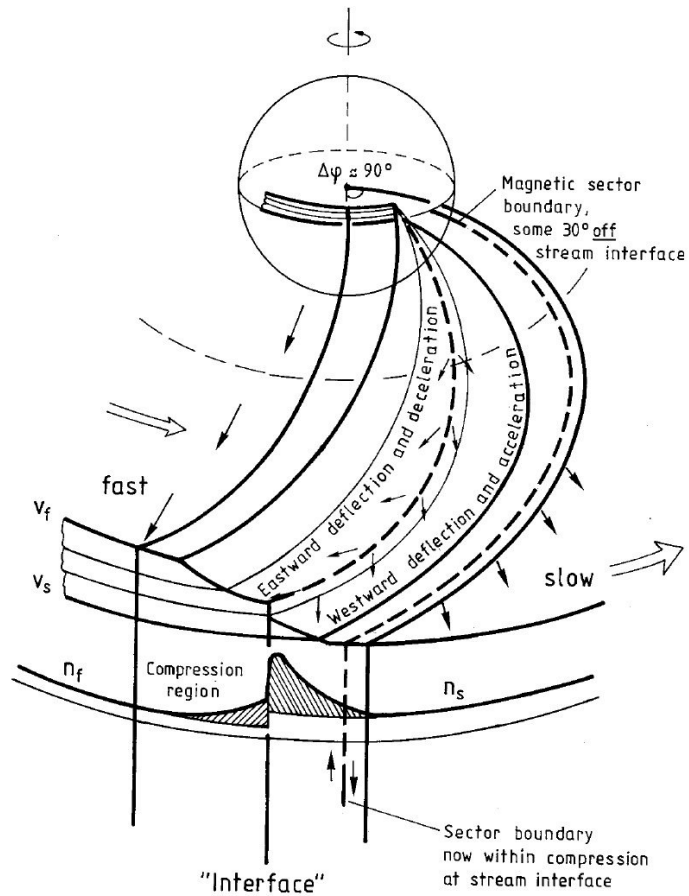


FIGURE 2.12 - Schematic and idealized representation of a CIR flowing out from the Sun with a “rectangular” speed profile that suffers a gradual increase in its speed at 1 AU. The angular separation between the stream interfaces and the sector boundaries decreases significantly with the increase of the heliospheric distance.

SOURCE: Adapted from Schwenn (1990).

et al., 1986). The IP shock is the result of the difference between the propagating structure (upstream) and the medium (downstream) speeds. Normally, ICMEs are associated to speeds higher than the magnetosonic speed of the solar wind, resulting in shock waves from ICMEs. They are also very often associated to the occurrence of geomagnetic storms, because they are generally associated to the compression and intensification of the magnetic field between the “ejecta” and the shock waves (TSURUTANI et al., 1988; TSURUTANI et al., 1992; GONZALEZ et al., 1999; HUTTUNEN; KOSKINEN, 2004). Thus, the field orientations in the sheath region, behind the shock driven by the ICMEs, can start an energy transfer depending on the  $B_z$  component direction. In some events, a southward  $B_z$  component ( $B_S$ ), which leads to magnetic reconnection (DUNGEY, 1961), never occurs, while in others it lasts for several hours. The compressed and high-density sheath plasma puts the magnetosphere under additional pressure. If a  $B_S$  is present in the high pressure episode, the result is a geomagnetic storm that may become particularly severe (SCHWENN, 2006). On the other hand, Srivastava and Venkatakrishnan (2002), Gonzalez et al. (2002), Yurchyshyn et al. (2004) found that the very fast ICMEs are often responsible for the most intense geomagnetic storms, apparently because they build up extreme ram pressure on the Earth’s magnetosphere.

As shown in Figure 2.11, when a CME travels in the IP medium it is normally constituted by three parts: a shock wave, just after the sheath region, followed by the “ejecta” material. Characterized by a region of heated and compressed plasma, the sheath region is described by turbulent magnetic field that commonly leads to the injection of solar wind energy into the magnetospheric cavity. Note that T1 and T2 represent two satellites crossing the ICME during its travel. T2 only observes the shock wave and the sheath region, while T1 is located in the propagation line of the ICME and it sees the “ejecta” and its features as it evolves in the medium. When a satellite crosses the shock region, it registers the jumps in the plasma and magnetic field parameters.

Due to the large quantities of mass expelled from the Sun and the high propagation speed, CMEs form a group of the main solar phenomena leading to geomagnetic storms occurrence (GOSLING, 1990; GOSLING et al., 1991). This is the main reason why studies to understand those structures have been extensively encouraged. Making predictions about their arrival time at terrestrial environment is of extreme importance for space weather.

## 2.7 Magnetic Clouds

The existence of MCs propagating toward the Earth from the Sun in the IP medium had been proposed as a cause of geomagnetic disturbances even before the observations of the solar wind were made (LINDEMANN, 1919; CHAPMAN; FERRARO, 1929). Such magnetic structures are commonly observed in the solar wind mainly during the solar maximum. The magnetic field in front of a MC is normally turbulent (MORRISON, 1956), and in the driver gas its configuration is of a very smooth magnetic field in the form of a loop or a tongue, where the tongue long-extended fields are still connected to the Sun (COCCONI et al., 1958). Later on, it was also supposed that MCs are disconnected from the Sun (PIDDINGTON, 1958) by the reconnection process (DUNGEY, 1961; PUDOVKIN et al., 1979).

### 2.7.1 Definition and Properties of Magnetic Clouds

The term Magnetic Cloud was first used by Morrison (1954) referring to plasma and magnetic field ejections from solar active regions (KLEIN; BURLAGA, 1982). From Helios 1 and 2, Voyager 2 and IMP-8 observations, Burlaga et al. (1981) were the first to confirm the existence of a turbulent region behind a shock wave that was followed by a region where the rotation direction of the magnetic field was consistent with the passage of a magnetic flux tube. Figure 2.13 represents the position of the 4 space probes when the MC was observed (BURLAGA et al., 1981). Note that dotted lines represent the uncertainty related to the connection of the structure to the solar surface or its complete disconnection.

Considered as a special set of the ICMEs, MCs have some special features that differentiate them from the rest of the ICMEs. They are regions of increased magnetic field whose orientation varies slowly during their propagation in the IP medium. The proton temperature is very low inside the structure (BURLAGA et al., 1981; KLEIN; BURLAGA, 1982; BURLAGA, 1995). On the other hand, magnetic field strength is higher than average. The plasma pressure, dependent on the plasma temperature and density, is normally smaller than the magnetic pressure inside such structures. The ratio between the two pressures (thermal and magnetic) is represented by the plasma beta ( $\beta$ ) (BURLAGA, 1991). Plasma beta is characteristically low (lower or equal to 0.1) in MCs due to the dominance of the magnetic field and the low proton temperature and the non-enhanced proton density, typical of MCs.



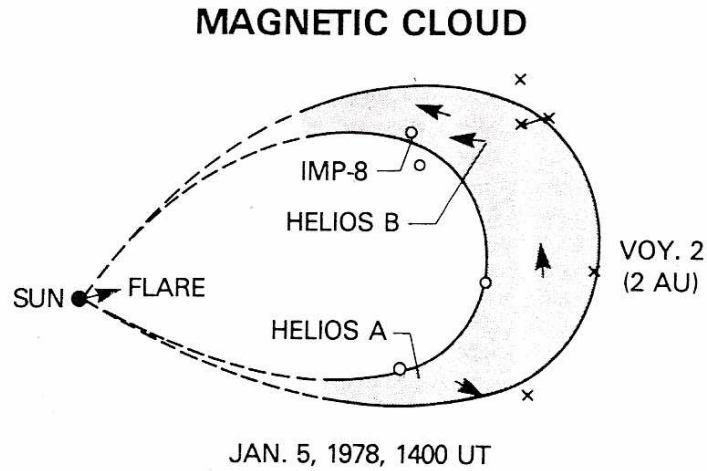


FIGURE 2.13 - Voyager 2, Helios A (Helios 1) and B (2), and IMP-8 identified a structure similar to a magnetic tube flux just after a shock wave was observed by their instruments. These observations served as the confirmation of the existence of magnetic clouds, a special group of the ICMEs. The probes identified the front boundaries, as marked by the "x" tick marks, and the rear parts of the MC, as represented by the "o" tick marks. The rotation of the magnetic field, as identified by the probes, is represented by the arrows.

SOURCE: Adapted from [Burlaga \(1995\)](#).

### 2.7.1.1 Flux Tube Model for Magnetic Clouds

In the solar wind, MCs are identified through a model first established by [Burlaga et al. \(1990\)](#), and further by [Mulligan et al. \(1998\)](#). In a one-day time scale, the magnetic field vector rotates by a large angle in the IP medium. [Goldstein \(1983\)](#) proposed that this variation in the magnetic field vector, characteristic of MCs, is consistent with the configuration of a force-free magnetic field in a flux tube.

To describe the configuration of a flux tube, [Goldstein \(1983\)](#) considered a cylindric force-free configuration, where the magnetic field  $\vec{B}$  is represented by  $\nabla \times \vec{B} = \zeta \vec{B}$ , with  $\vec{B} = (0, B_\phi(r), B_z(r))$ , and  $\zeta$  is a constant. In a force-free magnetic field,  $\vec{J} \times \vec{B} = 0$ , that results in  $\mu_0 \vec{J} = \zeta \vec{B}$ , i.e., the currents are aligned with the field. Based on these considerations and taking into account some arithmetic properties, the expression that describes a force-free magnetic field is given by:

$$\nabla^2 \vec{B} = -\zeta \vec{B} \quad (2.1)$$

whose solutions are given by [Lundquist \(1950\)](#) in the following forms:

$$B_\rho = 0, \tag{2.2}$$

$$B_\phi = \pm B_0 J_1(\zeta r), \tag{2.3}$$

$$B_z = B_0 J_0(\zeta r), \tag{2.4}$$

where  $\rho$ ,  $\phi$ , and  $z$  are cylindrical coordinates;  $B_0$  is the amplitude of the maximum value of the magnetic field;  $J_n$  are the  $n$ th-order Bessel functions; and the  $\pm$  signs refer to the magnetic helicity. The helicity is related to the structural properties of the magnetic field in a helicoidal form. In a mathematic interpretation, the helicity can be expressed as  $\vec{H} = \int_V \vec{A} \cdot \vec{B} dV$ , where  $V$  is the volume that contains the magnetic field, and  $\vec{A}$  is the vector potential that satisfies  $\vec{B} = \nabla \times \vec{A}$ . In the case of a MC, the helicity can be understood as the form in which the magnetic field is rolled up around itself in a flux tube (MC).

### 2.7.1.2 Magnetic Cloud Polarities

Within a MC, the magnetic field fluctuations are very small due to the smooth rotation of  $\vec{B}$  and its components. From the rotation direction of the main magnetic field in a cloud, it is possible to define the MC polarity. In a study of MCs observed during Helios mission, [Bothmer and Schwenn \(1998\)](#) interpreted the magnetic clouds in terms of flux tube model. The structure of the MCs was classified into 4 distinct categories, based on the magnetic field lines orientation in the boundaries of the cloud and its axis. According to this assumption, MCs would be classified into SEN (SWN) clouds, where the magnetic field vector first turns south (S) to east (E) (west (W)) in the cloud axis, and, finally, to north (N) in a region behind the cloud, and vice-versa in the case of NES (NWS) clouds. [Figure 2.14](#) presents sketches of these classifications, where the rotation of the magnetic field in the direction north-south determines the change in the sign of  $B_z$ .

Besides the configuration of the cloud axis in the ecliptic plane, MCs are also classified when their main axes are perpendicular to the ecliptic plane, as illustrated in [Figure 2.15](#). MCs whose main axes are perpendicular to the ecliptic plane are classified as unipolar MCs S or N ([MULLIGAN et al., 1998](#)). Similarly to the clouds

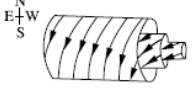



MC Type	Magnetic helicity	Variation of magnetic field vector	Direction of magnetic field on flux tube axis
SEN Number of MCs during 1974–1981	Left-handed  17	South $(-B_z) \rightarrow$ north $(+B_z)$	East $(+B_y)$
SWN	Right-handed  17	South $(-B_z) \rightarrow$ north $(+B_z)$	West $(-B_y)$
NES	Right-handed  6	North $(+B_z) \rightarrow$ south $(-B_z)$	East $(+B_y)$
NWS	Left-handed  6	North $(+B_z) \rightarrow$ south $(-B_z)$	West $(-B_y)$
Orientations for high inclinations to the ecliptic SEN, NWS, SWN, NES		East $(+B_y) \rightarrow$ west $(-B_y)$ West $(-B_y) \rightarrow$ east $(+B_y)$	North $(+B_z) \rightarrow$ south $(-B_z)$ South $(-B_z) \rightarrow$ north $(+B_z)$

FIGURE 2.14 - Magnetic Configuration of MCs parallel to the ecliptic plane. Their magnetic helicity (left-handed (LH), right-handed (RH)) based on the magnetic flux tube concept and the rotation that a spacecraft would observe during the cloud's passage are also illustrated.

SOURCE: Adapted from [Bothmer and Schwenn \(1998\)](#).

**Magnetic Rope Types Perpendicular to Ecliptic Plane**





Magnetic Cloud Type				
	WNE	ESW	ENW	WSE
Leading Field	West (-By)	East (+By)	East (+By)	West (-By)
Axial Field	North (+Bz)	South (-Bz)	North (+Bz)	South (-Bz)
Trailing Field	East (+By)	West (-By)	West (-By)	East (+By)
Helicity	RH	RH	LH	LH

FIGURE 2.15 - Magnetic polarity of MCs whose axes are perpendicular to the ecliptic plane.

SOURCE: Adapted from [Mulligan et al. \(1998\)](#).

whose axes are parallel to the ecliptic plane, the classification of the unipolar clouds is given by WNE, ESW, ENW, and WSE. Note that this time we start by the orientations E or W (see [Figure 2.15](#)), since the magnetic field in these clouds turns from West (East) to East (West). During a spacecraft passage, the  $B_z$  component does not change its signal, what explains the name unipolar.

### 2.7.1.3 Expansion of Magnetic Clouds

As many other IP structures, MCs suffer expansion when traveling in a medium filled with plasma and magnetic field. At approximately 1 AU away from the Sun, they modify significantly their dimensions as “in situ” observations indicate. This can be verified, for instance, when a spacecraft traverses the front part of a MC and the speed values is higher compared to the rear parts of the cloud ([DASSO et al., 2005](#)).

When dynamical interactions are absent in a magnetic cloud that propagates in the IP medium, the magnetic field strength is higher inside than outside it, at 1 AU. This means that the magnetic pressure  $B^2/2\mu_0$  is higher than the plasma pressure inside the structure. A gradient in pressure would make the MC expand unless an external force prevents the expansion ([BURLAGA, 1991](#)).

Coronal Mass Ejections are often associated with flares and disappearing filaments

(STEINOLFSON; HUNDHAUSEN, 1988). But there is not a complete understanding whether the relationship among these events follows a magnetic field configuration in the corona or not. The only way to associate the CME/MC occurrence with the solar source is through the combination of solar data, coronagraph images of CMEs, and “in situ” measurements of the solar wind and IP magnetic field.

At 1  $AU$ , MCs represent a good example of IP magnetic flux ropes (LEPPING et al., 1990; FARRUGIA et al., 1995; MARUBASHI, 1997). Another important feature of these structures is that they are long duration (meaning cross-sectional transit times) ranging from about 10 hours up to 2 days at 1  $AU$ . Every observed MC is believed to have a solar origin, not only because of their large sizes, but also for numerous other reasons including their often apparently successful direct linkage to solar events (MARUBASHI, 1986; MARUBASHI, 1997; HUNDHAUSEN, 1987; GOSLING, 1990).

## 2.8 Propagation of shock waves in the IP medium

Interplanetary shock waves involve non-linear processes that take place in the IP space with non-collisional plasmas. Collisionless shock waves in the solar wind result from the interaction of plasma flows of different velocities, densities, and temperatures. They are formed when the difference between the speeds of the interacting plasma flows is greater than the characteristic velocity at which information about dissipation processes propagates. In the classical view of Magnetohydrodynamic (MHD) shock waves, when two plasmas interact, this takes place over a very short distance, and at a sufficient distance away from the shock surface (BALOGH et al., 1995). The two different plasma regimes are governed and related by the Rankine-Hugoniot (RH) jump relations that take into account the conservation of mass, momentum and energy flow across the surface formed between the two plasmas. The boundary conditions at the shock are derived from the Maxwell’s equations.

Through a closer examination one can see that shock waves involve a wide variety of complex plasma phenomena with wave-particle interactions. Such interaction can have a significant spatial extent, affecting the properties of the upstream, as well as the downstream, solar wind flow. Depending on the geometry of the magnetic field in relation to the shock surface, it can play an important role in determining the type of dissipation process that will take place. The angle between the shock normal and the upstream magnetic field,  $\theta_{B_n}$ , is the parameter used to classify the shocks in the upstream region.

The existence of shock waves in collisionless plasmas has been debated over many decades. The first prediction of a shock wave formed in front of Earth’s magnetosphere was done by [Axford \(1962\)](#) and [Kellogg \(1962\)](#). The confirmation came with spacecraft observations in 1963. The shock formed in front of the dayside magnetopause is due to the continuous supersonic solar wind flow that finds an obstacle in its path. The interaction and the difference between the speed of the solar wind and the obstacle speed in the medium forms a shock wave in the IP space that represents an important feature of the solar wind. With the advent of the probe IMP-1/Explorer 18, the so-called bow shock was reported for the first time ([SONETT et al., 1964](#)).

In the same manner as the steady-state shocks, which are formed due to interaction between the solar wind and planets, shocks involving collisions can be formed in the IP space. The presence of electromagnetic fields may alter the dissipation process of the charged particles leading to collisions among them. Finally, these long-range interactions result in collective effects that, among others, form shock waves and other plasma modes ([PARKS, 1991](#)).

In general, shock waves are easily identifiable phenomena by the observation of the local plasma and magnetic field “in situ” measurements. Despite this fact, there is a size distribution of weak shock waves whose identification is not always trivial, but most parts of time questionable because of the difficulty on distinguishing it from a pressure pulse signature ([BALOGH et al., 1995](#)).

Despite the type of shock, there is always a surface associated to this shock that provides the direction of propagation of the wave, as well as the region of the lower entropy. Such surface is defined by the normal vector,  $\hat{n}$ , that forms an angle  $\theta_{B_n}$  with  $\vec{B}_1$ , the upstream magnetic field. By using the kinetic theory, one has more information about the details of these shock surfaces. However, the MHD theory gives enough information about the plasma before (upstream) and after (downstream) the shock surface that enables us to describe the shock ([ECHER et al., 2006](#)).

## 2.9 Formation of a Hydrodynamic Shock

In an ordinary gas with uniform pressure ( $p$ ) and density ( $\rho$ ), the speed of sound is the speed of propagation, given by

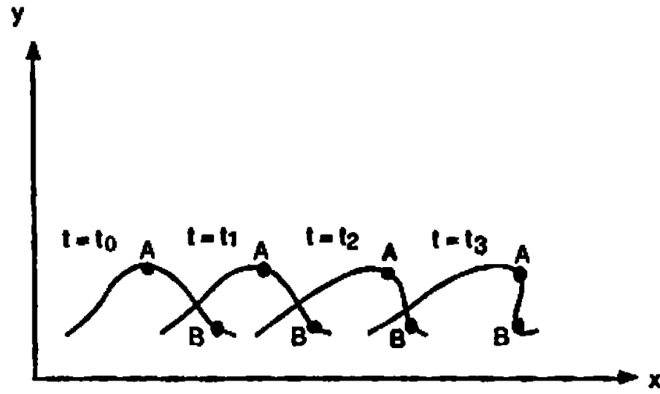


FIGURE 2.16 - Representation of the steepening of a compressional wave resulting in a shock wave at  $t = t_3$ .

SOURCE: Adapted from Parks (1991).

$$C_S = \left(\gamma \frac{p}{\rho}\right)^{1/2}, \quad (2.5)$$

where  $\gamma$  is the ratio of specific heats. If we consider a fully-ionized hydrogen (H) plasma, typically assumed for the solar wind, one gets  $\gamma = 5/3$  (KIVELSON, 1995). In this scenario, there is only one kind of gas dynamic shock wave: the one formed by a surface that propagates faster than the speed of sound in the medium ahead of it. As a consequence, a mass flux is observed through the surface, and temperature, density, and entropy increase across the surface.

In a uniform gas the waves propagate equally in all directions with the same speed: the sound speed. However, when the wave is characterized by a finite amplitude so that non-linear terms become important, the crest of the sound wave moves faster than the leading edge. As a result a steepening of the sound wave is observed with a progressive development until the gradients of pressure, temperature, density, and velocity become so large that dissipative processes, such as viscosity or thermal conduction, are no longer negligible (PRIEST, 2000). Figure 2.16 shows a compressional wave at instants of time  $t = t_{0..3}$ . Note that points A and B represent the crest and the leading parts of the wave, respectively. Point A is at the beginning behind point B, but since the crest moves faster than the leading edge, it reaches point B and the wave steepens forming a shock wave.

## 2.10 Interplanetary Shocks

When the MHD theory is taken into account, three possible speeds are present: the sound, Alfvén, and magnetoacoustic speeds (LANDAU; LIFSHITZ, 1960; BURLAGA, 1971). Consequently there are six possible types of shocks: the fast, the slow, and four other types of intermediate shocks (WU, 1990). However, based on the shock's evolutionary condition of ideal MHD, Taniuti (1962) and Kantrowitz and Petschek (1966) argued that the MHD intermediate shocks are not structurally stable and are physically unrealizable. However, theoretical study and numerical simulations showed that the MHD intermediate shocks are admissible and can be formed by the steepening of nonlinear MHD waves (e.g., Kennel et al. (1989) and Hau and Sonnerup (1999)).

The type of shock is dependent on the propagation speed of the surface in relation to the characteristic speeds of the medium (Parks (1991), Burlaga (1995) and references therein). In space, the most likely type is the fast one, characterized by an increase in the IMF strength, while the slow one is characterized by a decrease in the IMF strength. Both fast and slow shocks that move radially away from the Sun are so-called forward shocks, and the ones that move toward the Sun relatively to the solar wind are named reverse shocks. In the IP space, the forward shocks are normally formed as a consequence of the propagation of structures such as CMEs and identified by the sensors onboard satellites in orbit. In general, when a mass flux through the shock is observed and subsequently the solar wind parameters and the entropy of the system increase abruptly, a shock wave is identified.

## 2.11 The Rankine-Hugoniot Equations

The RH equations represent relations between the up and downstream parameters. Sometimes they are referred to as shock jump conditions although they are physical relations that must be satisfied whichever the type of shock and discontinuity surface is present in the MHD fluid. This surface separates two states of plasma. They are denoted here by subscripts 1 for the undisturbed gas (ahead of the shock) and 2 for the shocked gas (behind the shock). We consider a constant field in both sides of the shock in such a way that no change in the magnetic field happens due to the shock. Besides, both the density  $\rho$  and the total pressure  $p$  are isotropic. In this sense, the equations describe a MHD discontinuity in relation to a surface that is steady or moving. The conservation of mass through the shock surface is given by:



$$\rho_1 v_{1n} = \rho_2 v_{2n}, \quad (2.6)$$

where  $\rho_1$  and  $\rho_2$  are the densities, and  $v_{1n}$  and  $v_{2n}$  are the velocity components in the direction of the normal to the shock surface.

Note that the conservation of the normal component of the magnetic flux results in:

$$B_{1n} = B_{2n} = B_n. \quad (2.7)$$

The condition of the frozen-in field is then valid:

$$B_n(v_{1t} - v_{2t}) = B_{1t}v_{1t} - B_{2t}v_{2t}, \quad (2.8)$$

where  $v_{1t}$  and  $v_{2t}$  are the velocity tangential components, and  $B_{1t}$  and  $B_{2t}$  are the magnetic field tangential components. From the conservation of momentum flux, in the normal direction, the following relation is true:

$$\rho_1 v_{1n}^2 + p_1 + \frac{B_1^2}{2\mu_0} = \rho_2 v_{2n}^2 + p_2 + \frac{B_2^2}{2\mu_0}, \quad (2.9)$$

where  $p_1$  and  $p_2$  are the solar wind pressures;  $B_1$  and  $B_2$ , the magnetic field strengths; and  $\mu_0$  is the magnetic permeability of free space.

In the tangential direction, the flux of momentum is also conserved:

$$\rho_1 v_{1n}v_{1t} - \frac{B_n B_{1t}}{\mu_0} = \rho_2 v_{2n}v_{2t} - \frac{B_n B_{2t}}{\mu_0}, \quad (2.10)$$

where  $v_{1t}$  and  $v_{2t}$  are the tangential components of the velocity. The magnetic field perpendicular to the shock normal is represented by  $B_{1t}$  (upstream) and  $B_{2t}$  (downstream).

The energy conservation is represented by:

$$\left(\frac{\rho_1 v_1^2}{2} + \frac{5p_1}{2} + \frac{B_{1t}^2}{\mu_0}\right)v_{1n} - \frac{B_n B_{1t} v_{1t}}{\mu_0} = \left(\frac{\rho_2 v_2^2}{2} + \frac{5p_2}{2} + \frac{B_{2t}^2}{\mu_0}\right)v_{2n} - \frac{B_n B_{2t} v_{2t}}{\mu_0}, \quad (2.11)$$

for  $\gamma = 5/3$ , with  $v_1$  and  $v_2$  the components of the bulk velocity.

Since the shock moves radially away from the Sun with velocity  $V_S$ , and if the up and downstream velocities are radial with respective speeds  $v_1$  and  $v_2$ , one has that  $v_{1n} = v_1 - V_S$  and  $v_{2n} = v_2 - V_S$  are the respective speeds in the normal direction. From the conservation of mass, the shock speed as it moves from the Sun is:

$$V_S = \frac{(n_2 v_2 - n_1 v_1)}{n_2 - n_1}. \quad (2.12)$$

The determination of the shock normal and speed are both fundamental in the detailed quantitative study and classification of shocks ([BURLAGA, 1995](#)).

### 2.11.1 The Shock Normal

Whichever the shock wave propagating into space, the shock normal needs to be determined because, besides the shock speed, it represents an essential parameter for the analysis of the type of perturbation, mainly in relation to the direction of propagation. As shock normal one understands the vector perpendicular to the surface of discontinuity that gives the direction of propagation of the shock and points to the region of the lowest entropy.

Shock normals can be determined by several different methods, either from observations at a single spacecraft using the magnetic field (magnetic coplanarity), that can be accompanied by solar wind data, or from multi-spacecraft data, with magnetic field and possibly plasma data. All these techniques are generally based on the relationship between the shock normal and the change in a shock parameter considered. On the other hand, some of the techniques use the full set of RH equations.

When one considers only the magnetic field (magnetic coplanarity method described by [Colburn and Sonett \(1966\)](#), [Spreiter et al. \(1966\)](#)), the shock normal is estimated by the observation of only one spacecraft and represented by:

$$\hat{n} = \pm \frac{(\vec{B}_1 \times \vec{B}_2) \times (\vec{B}_2 - \vec{B}_1)}{|(\vec{B}_1 \times \vec{B}_2) \times (\vec{B}_2 - \vec{B}_1)|}, \quad (2.13)$$

where one assumes that the normal component of the magnetic induction  $\vec{B}$  is positive; otherwise a minus sign is used. Furthermore, the RH relations show that the up and downstream magnetic fields are in the same plane as the shock normal so that the cross product of these two vectors is orthogonal to the shock normal. Thus the product of the difference field and the cross product of the up and downstream fields is along the shock normal (COLBURN; SONETT, 1966). This leads to the popular coplanarity normal. Even though one considers only the upstream and downstream magnetic field values that make the estimate easier, this method is not accurate. It fails when one considers parallel and quasi-parallel shocks (BURLAGA, 1995).

Another method was developed by Abraham-Shrauner (1972) and Abraham-Shrauner and Yun (1976) that considers the velocity coplanarity method between  $\vec{v}_1$  and  $\vec{v}_2$ . This method is valid for both isotropic and anisotropic plasmas. When the magnetic field is quite small, the tangential components of the bulk flow velocity are nearly continuous, and the shock normal can be approximated by:

$$\hat{n}_{VC} \cong \frac{\vec{v}_2 - \vec{v}_1}{|\vec{v}_2 - \vec{v}_1|}, \quad (2.14)$$

valid at high Mach numbers and for  $\theta_{B_n}$  near  $0^\circ$  and  $90^\circ$ , angles where the magnetic stresses are not important (SCHWARTZ, 1998).

Across the shock, the change in bulk velocity of the plasma is also coplanar with the shock normal, and the up and downstream magnetic fields. By combining the cross product of either the up and downstream fields with the vector velocity change and with the change in the vector magnetic field, one obtains three mixed modes for the shock normal, which combine both magnetic and velocity coplanarities (ABRAHAM-SHRAUNER, 1972; ABRAHAM-SHRAUNER; YUN, 1976; SCHWARTZ, 1998; RUSSELL et al., 2000), represented by:

$$\hat{n}_{MX1} = \pm \frac{[\vec{B}_1 \times (\vec{v}_2 - \vec{v}_1)] \times (\vec{B}_2 - \vec{B}_1)}{\left| [\vec{B}_1 \times (\vec{v}_2 - \vec{v}_1)] \times (\vec{B}_2 - \vec{B}_1) \right|}, \quad (2.15)$$

$$\hat{n}_{MX2} = \pm \frac{[\vec{B}_2 \times (\vec{v}_2 - \vec{v}_1)] \times (\vec{B}_2 - \vec{B}_1)}{\left| [\vec{B}_2 \times (\vec{v}_2 - \vec{v}_1)] \times (\vec{B}_2 - \vec{B}_1) \right|}, \quad (2.16)$$

$$\hat{n}_{MX3} = \pm \frac{[(\vec{B}_2 - \vec{B}_1) \times (\vec{v}_2 - \vec{v}_1)] \times (\vec{B}_2 - \vec{B}_1)}{\left| [(\vec{B}_2 - \vec{B}_1) \times (\vec{v}_2 - \vec{v}_1)] \times (\vec{B}_2 - \vec{B}_1) \right|} \quad (2.17)$$

$$(2.18)$$

### 2.11.2 Mach Number

The Mach number of a shock in MHD fluid is the ratio of plasma velocity to a particular linear wave speed in a stationary reference frame normal to the shock front. In a magnetized plasma, there are three low frequency modes: the fast and slow magnetosonic waves and the intermediate (Alfvén) wave. From the fast and slow modes of magnetosonic waves, we expect, respectively, fast and slow shocks.

Related to the possible speeds in this magnetized medium, there are several Mach numbers of interest. Thus, an additional Mach number, the Alfvén Mach number,  $M_A$ , is often used to characterize a shock. This Mach number is calculated regardless the propagation direction, but the values of the Alfvén and the structure velocities are considered in the upstream region:

$$M_A = \frac{|V_S - v_1|}{V_A}, \quad (2.19)$$

where  $V_S$  is the shock speed, and  $V_A$  is the Alfvén speed, given by:

$$V_A = \frac{B_1}{\sqrt{\mu_0 \rho_1}}. \quad (2.20)$$

Similarly, for a magnetosonic medium, the Mach number is defined as:

$$M_{MS} = \frac{|V_S - v_1|}{V_{MS}}, \quad (2.21)$$

where the magnetosonic speed is given by:

$$V_{MS} = \left[ \frac{1}{2}(V_A^2 + C_S^2) \pm \left( (V_A^2 + C_S^2)^2 - 4C_S^2 V_A^2 \cos^2 \theta_{B_n} \right)^{1/2} \right]^{1/2}. \quad (2.22)$$

The Alfvén Mach number is an indicator of the shock intensity and characterizes the amount of energy involved in the shock. For those shocks observed at 1 *AU*, Mach numbers can reach values around 7 and 8. However, for the majority of shocks these values range from 2 to 3 (ECHER et al., 2003).

An important feature to identify shocks is the fact that, as they propagate in a medium, there will be a mass flux through their surfaces. However, this is not a sufficient condition to identify a shock because the rotational discontinuities and other non-linear waves can also propagate in this medium and they are not considered shock waves. A necessary condition to identify a shock is that there is an entropy increase through the propagating surface.

### 2.11.3 Types of MHD Shocks

Depending on the direction of the magnetic field in the upstream region of the shock,  $\vec{B}_1$ , in relation to the shock normal,  $\hat{n}$ , shocks are classified as parallel, perpendicular, and obliques. The oblique ones are often found in the solar wind, as we are going to discuss in the sequence.

#### 2.11.3.1 Parallel Shocks

A shock is classified as parallel when the shock normal is parallel to  $\vec{B}$  ( $\vec{B} = B_n \hat{n}$ ). Neither the magnetic field nor its intensity change across a parallel shock. For this type of shock, two speeds can be found: the sound and the Alfvén speeds.

If the speed of sound in the upstream region of the shock is higher than the Alfvén speed, the sound speed is dominant. In this case, the shock is an ordinary gas dynamic shock, faster than the speed of sound, however, slower than the speed of sound as it passes through the surface.

On the other hand, if the Alfvén speed is higher than the speed of sound, there are three different possibilities. If the gas moves super-Alfvénically and supersonically, it might result in a gas that moves super-Alfvénically and subsonically as it crosses the region.

Another possibility is a flow that is supersonic and sub-Alfvénic and results in a subsonic gas and either sub-Alfvénic or super-Alfvénic (BURLAGA, 1995). Super-Alfvénic gases that result in sub-Alfvénic gases as they cross the shock do not exist in nature (JEFFREY; TANIUTI, 1964).

The existence of quasi-parallel shocks has been observed during the outbound passes of *Voyager 1* and *Voyager 2*. Furthermore, their existence has been demonstrated at different parts of the heliosphere (Neubauer; Musmann, 1977; ACUÑA et al., 1981; RICHTER et al., 1984).

### 2.11.3.2 Perpendicular Shocks

A fast forward perpendicular shock is the one with a magnetic field perpendicular to the shock normal before and after the shock occurrence, that means,  $B_n = 0$ . The only possible wave to be formed is the magnetoacoustic wave. The flux initially propagates with a speed higher than the magnetosonic speed and later propagates with a lower speed.

From the conservation of mass flux (Equation 2.6) and the frozen-in theorem (Equation 2.8), the following expression describes a perpendicular shock:

$$\frac{\vec{B}_1}{\rho_1} = \frac{\vec{B}_2}{\rho_2}. \quad (2.23)$$

It is important to note that the field does not change its direction through the shock surface (BURLAGA, 1995).

### 2.11.3.3 Oblique Shocks

The term “oblique shock” is somewhat ambiguous, but it is often used to describe the wide range of shocks that present characteristic neither nearly perpendicular nor nearly parallel. The oblique shocks ( $0^\circ < \theta_{B_n} < 90^\circ$ ) are the most common type of shock found in the IP medium. The magnetic field components  $\vec{B}_n$  and  $\vec{B}_t$  are both

non-zero. The perpendicular component to the normal,  $v_{1t} - v_{2t}$  is parallel to  $\vec{B}_{1t}$  and  $\vec{B}_{2t}$ , considering that  $\hat{n}$ ,  $\vec{B}_1$ ,  $\vec{B}_2$ , and  $\vec{v}_1 - \vec{v}_2$  are coplanar (BURLAGA, 1995).

Hundreds of fast oblique shocks have been observed in the solar wind. They are characterized by an increase in the velocity and at the same time increases in the temperature, density and magnetic field magnitude. Furthermore, changes in the components of the magnetic induction and velocity are visible. For instance, the termination shock, the frontier reached by the supersonic solar wind, is in general considered to be an oblique shock.

## 2.12 Concluding Remarks

Along this chapter we introduced the main features of some of the IP structures and their solar origins. Among them, the ICMEs play an important role in driving forward shock waves in the IP medium. Their subclass, the MCs, has special features that differentiate them from the other structures due to the geoeffectiveness hidden in the strong magnetic field inside such structures. The study of ICMEs/MCs, as well as the shocks they drive as they travel in the IP space is of crucial importance in order to estimate their extension in longitude (so that we know if they will reach Earth) and predict their arrival (when they will reach Earth). On the other hand, the characteristic structures of the “quiet” Sun, the CIRs, are not normally associated to shock wave formation in the inner heliosphere, where the measurements from Helios mission were done.





### 3 GETTING THE CLOSEST TO THE SUN WITH HELIOS MISSION

The name Helios comes from the Greek god who, as people in the Ancient World imagined, drives the chariot across the sky each day (for illustration see [Figure 3.1](#)). At the same time, he is the harbinger of light and warmth but also of heat, which can scorch everything, and influence the Earth ([PORSCHÉ, 1984](#)). There was not a more appropriate name for the most successful German-American project of space exploration that could tell us about the tasks of the mission. According to [Porsche \(1984\)](#), the goal of Helios project was to approach the Sun as near as possible, in order to find out how this body influences not only the Earth, but the rest of space. The first investigation of the solar environment with space probes dates from 1974 and 1976, respectively when two probes (H1 and H2) were launched successfully.

Both Helios probes traveled at variable location in the inner heliosphere, describing orbits around the sun that contributed a lot to the shock identification in different parts of the inner heliosphere. The perihelion was observed inside Mercury's orbit



FIGURE 3.1 - The God of the Sun: Helios. From this Greek god that the inspiration for the name of the mission comes from.

SOURCE: <http://www.theoi.com/Titan/Helios.html>. Access on March 28 2009.

and its aphelion inside Earth's orbit, as one can see in [Figure 3.2](#).

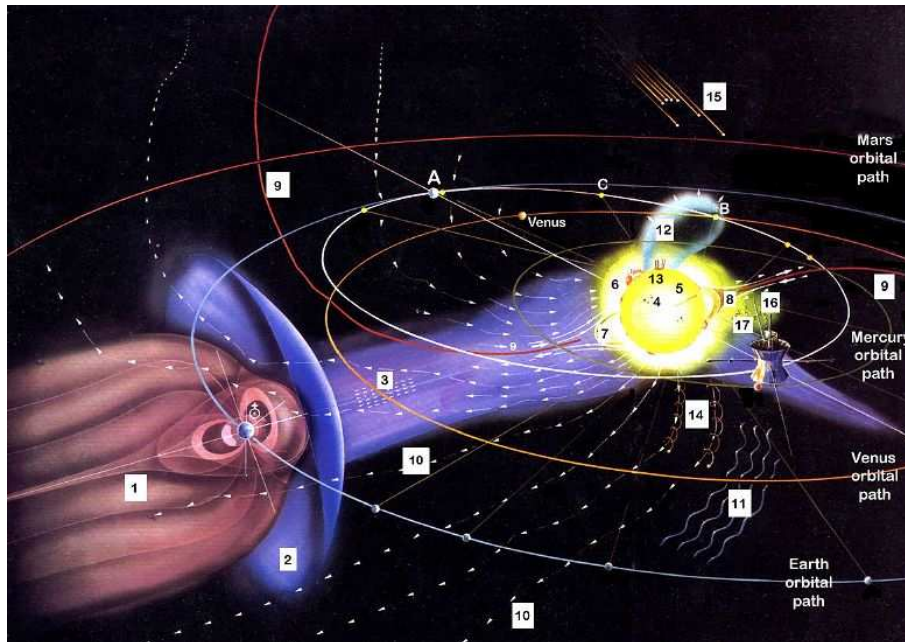


FIGURE 3.2 - Out of scale view of the Solar System. The probes Helios traveled around the Sun, at distances ranging from around 0.3 to 1 *AU*, inside Mercury and Earth's orbits. H1 was launched from Earth at the position marked by 'A'. In the opposite side, one identifies the probe describing an elliptic orbit. The representation shows the terrestrial magnetosphere ('1'), the bow shock ('2'), and the solar wind flowing from the sun ('3'). On the solar surface, one observes the sunspots ('4'), filaments extending out from the surface ('5'), and the outermost atmosphere, the corona ('6'), coronal arches ('7'), streamers of magnetic loops ('8'), and the coronal arches ('9'). In the interplanetary medium, the IMF ('10'), and Alfvén and shock waves ('11') are identified. The mark '12' corresponds to the flares, while the solar radiation propagation is defined by the mark '13'. The galactic cosmic rays are identified by '15', while the scattering of sunlight and the zodiacal light are identified by '16' and '17', respectively.

SOURCE: <http://www.honeysucklecreek.net/dss44/helios.html>. Access on 29 March 2009.

The orbital period was about 190 days, almost the half of the period of Earth's orbit ([PORSCHÉ, 1984](#)). This can be observed by the tick marks in [Figure 3.3](#) that show the number of days H1 and H2 spent in the year 1976 to be in each position of their elliptic orbits. The proximity to the solar environment enabled the probes to be accelerated by the solar gravity, differentiating them from ordinary missions. They reached the still undefeated speed record for spacecraft of 252,000 *km/h*. The high speed they traveled in the inner heliosphere enabled them to describe highly

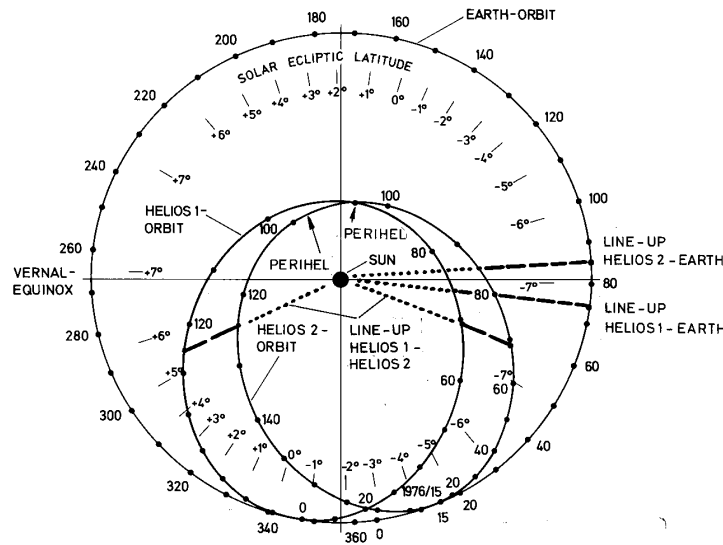


FIGURE 3.3 - Helios 1 and 2 orbits around the sun, describing elliptic orbits. Earth's orbit is also shown. The tick marks refer to calendar days in 1976.

SOURCE: Adapted from [Marsch and Schwenn \(1990\)](#).

accentuated orbits around the Sun in relation to the ecliptic. The eccentricity was of 0.54, and since the Sun's axis is inclined by approximately  $7.25^\circ$  relative to the ecliptic plane (which is also the Helios orbit plane), they covered an interval of heliographic latitude between  $-7.25$  and  $+7.25^\circ$  ([MARSCH; SCHWENN, 1990](#)).

### 3.1 The launch

With the collaboration of the NASA American space agency, the two Helios were launched by the space vehicle Titan-Centaur. [Figure 3.4](#) shows the probe Helios 1 already positioned in the launcher Titan III E Centaur. The launching day of H1 was on December 10 1974, a little bit more than one year in advance of H2 launch, on January 15 1976 ([KUTZER, 1984](#)). As stated previously, they lived through about one solar cycle.

### 3.2 Scientific Objectives of the Mission

Orbital characteristics of the probes were crucial for the studies carried out considering the latitudinal variations of the magnetic field and plasma properties of the solar wind. Besides the fact that the probes were practically identical, another ad-



FIGURE 3.4 - The launcher vehicle of satellites, Titan IIIE Centaur, with H1 probe (1974).

SOURCE: [http://www.absoluteastronomy.com/topics/Titan\\_III](http://www.absoluteastronomy.com/topics/Titan_III). Access on March 29 2009.

vantage came with the configuration of the orbits. During some periods the probes were aligned and the same event could be studied at different radial distances in the inner heliosphere.

Both probes were composed by the same set of instruments, which were calibrated by using the respective instruments on the other. The design and development of the Helios solar probe presented a number of engineering highlights, the most outstanding of which was the design of the thermal control system, essentially valid for a solar mission into a distance closer than  $0.3 AU$  to the Sun (BENOÏT et al., 1977). Similarly to the alignment of the probes, constellations were formed in a way that H1 and H2 were connected by the same magnetic field line along the Parker's spiral. This contributed to the fact that energetic particles from the same magnetic field line could be detected at different longitudinal distances (MARSCH; SCHWENN, 1990). Another important contribution from the advent of the mission is the study of

the solar wind properties with dependence on the radial variation. Near Earth, IMP-8 contributed to the comparison and the understanding of such properties, as well as the measurements in the outer heliosphere, provided by the Voyagers ([MARSCH; SCHWENN, 1990](#)). In this way, the differences among these properties at different locations of the IP medium were noticed.

The mission was successfully completed at the beginning of 1980's decade, however, its observations were extended until 1986. This unexpected and unplanned long period of operation of the probes, as well as the lifetime of essential instruments onboard them, contributed to a complete study of the solar wind properties variation and other phenomena dependent on the solar cycle. Most of the scientific investigations covered basically one solar cycle, what surprised the scientists in face of the technological problems that came into view ([MARSCH; SCHWENN, 1990](#)). Another important contribution comes from the fact that the Helios remained eccentric around the Sun that contributed to the pioneer study of the inner heliosphere as close as 0.3 to the Sun.

### **3.3 Instrumentation**

With the aim of complementing the observations in the inner heliosphere, provided by H1 and H2, a third probe with identical design was built. The initial idea was the observation in front of the magnetosphere, the same type of observation as ISEE-3 and IMP-8 provided. Notwithstanding, this probe was not launched, but sent to the Aeronautics department of the Deutsches Museum ([PORSCHKE, 1984](#)). [Figure 3.5](#) is a picture taken in 2007, during a visit to the Deustches Museum, in Munich.

The scientific payload comprises twelve independent experiments that were sent onboard each probe. They consist in high-energy particles detectors, magnetometers and micrometeorites experiments. Each of the probes had two antennas and an electric dipole 32 meters long. The instruments are listed on [Marsch and Schwenn \(1990\)](#) with their main investigators and affiliations, and described in detail in [Porsche \(1977\)](#). Even though the number of researchers involved in the Helios project was limited, the number of scientists taking part in the data analysis steadily increased due to the success of the project.

The instruments that comprised the payload of the mission were separated into three main groups: the plasma parameters, cosmic rays, and micrometeorites. The



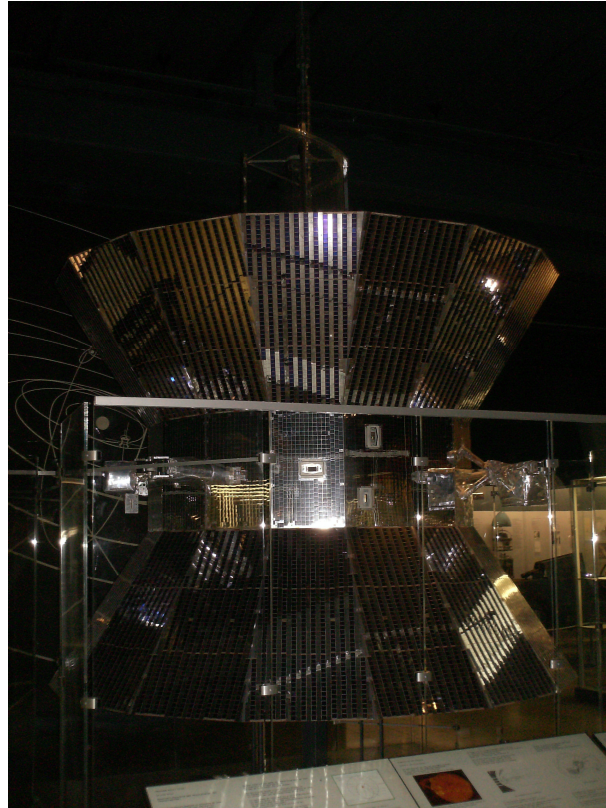


FIGURE 3.5 - Visit to the Helios third probe in the Deutsches Museum, Munich.

first group was composed by seven instruments and designated to the IP medium measurements of the solar wind and magnetic field. In addition to these measurements, the 2D and 3D velocity distributions for the solar wind electrons, protons, and He ions were obtained.

Among the instruments from the first group, there were two fluxgate magnetometers and one induction magnetometer, as well as two plasma wave experiments that measured the electromagnetic field fluctuations over a large interval of frequencies. Another instrument was designed to track radio wave bursts traveling between Sun and Earth.

In the second group, there were three experiments for the observation of mass and directional and spectral energy distributions of galactic and solar cosmic rays. Furthermore, the instruments contributed to the monitoring of the X-ray activity. On H2, there was an additional device whose function was to control the occurrence of

Gamma-ray bursts and their sources.

In the last group, micrometeorites were investigated in order to establish their physical properties in the Solar System. Three photometers were sent onboard each probe. In this sense, the intensity and polarization of the zodiacal light in three directions into space was obtained. Two dust particle analyzers measured the particle fluxes in such a way that the mass distribution and chemical composition of meteorites could be investigated.

Some of the previously mentioned experiments are described in the sequence. Details of their operation, as well as their main investigators and the affiliations involved in their constructions are presented.

### **3.3.1 Plasma Experiment**

This experiment was in charge of the Max-Planck-Institute für Physik und Astrophysik, Munich. Four independent instruments composed the experiment, all of them designated to the investigation of the solar wind plasma. Among the measurements they made, there was the collection of more relevant parameters for the study and analysis of the plasma of the IP medium: temperature, density and speed for different particle populations. Three of these instruments analyzed the positive elements of the solar wind, i.e., heavy ions and protons with energies ranging from 0.155 to 15.32 *keV*. One of the instruments measured electrons in the energy interval of 0.5 to 1,660 *eV* with a unidimensional angular resolution. More details are found in [Schwenn et al. \(1975\)](#).

### **3.3.2 Fluxgate Magnetometers**

Many countries, among them Germany, Italy, and United States, were responsible for the magnetometers onboard the mission. The magnetometers measured the intensities and directions of the magnetic fields of low frequency in the solar atmosphere that extend away from the Sun into the IP medium suffering the influence of the solar rotation. The experiment of the fluxgate magnetometers made use of orthogonal and triaxial 2-meters sensors. The sensitivity range was from  $-100$  to  $+100$  *nT*. Some additional information is found in [Searce et al. \(1975\)](#) and [Mariani and Neubauer \(1990\)](#).

The functionality of these magnetometers was based on the saturation of the mag-

netic material that composed both of them. In the iron core of the electromagnets, a current flows through the coil, and as a result a magnetic field is generated due to the atoms of iron, which are magnetic. In an ordinary iron, the magnetic axes of the atoms are aleatory, totalizing an almost zero contribution. Notwithstanding, when a current flows in the iron, the axes become aligned. The sum of the contribution from each of these axes results in a magnetic field that is larger as compared to the one generated by the electric current.

The position in which the fluxgate magnetometers were disposed was of crucial importance for the correct measurements. A minimum distance between the two magnetometers avoided the interferences caused by currents generated in the spacecraft. These currents, even weak, can generate magnetic fields that, despite the intensity, might affect the magnetic field recording in the sensors.

### **3.3.3 Induction Magnetometer**

In addition to the stationary plasma and the magnetic fields that vary slowly, components with higher frequencies in the IP medium could also be measured. This instrument is complementary to the measurements provided by the fluxgate magnetometer, therefore the magnetic field could be measured between 0 and 3  $kHz$ .

The aim behind this instrument was to analyze and measure shock waves and quickly fluctuating perturbations. The induction magnetometer consisted of three coils positioned at the extremities on the two 2-meter long antennas. At the extremities, the coils were perpendicularly disposed to each other in such a way that the three components were measured.

### **3.3.4 Plasma Wave Experiment**

In order to detect the plasma wave electric component, a bipolar antenna of thirty-two meters from one extremity to the other was used in this experiment.

Several new and important results were generated with the use of this plasma wave detector over a period of ten years. Among the results obtained with this investigation, the presence of Type III bursts was confirmed, twenty-years later in relation to its first supposition. Besides, the presence of advanced levels of ion-acoustic wave turbulences in the solar wind was revealed ([GURNETT; ANDERSON, 1984](#)).



The operation of these instruments provided almost one entire solar cycle “in situ” measurements with a vast temporal and spatial variability. Furthermore, the dataset revealed the complexity of the predominant phenomena in the IP medium, showing that there are still several open questions in Solar Physics.

### 3.3.5 Cosmic Radiation Experiment

High energy particles whose sources can be from billions of stars in our galaxy, Sun, and planetary atmospheres travel with speeds close to the speed of the light in the Solar System. Mainly protons, but also Helium and heavy nuclei constitute the so-called cosmic radiation. The particle experiment for cosmic rays consisted of a telescope containing five detectors that are semiconductor. The instrument was able to measure protons and heavy nuclei of 1.7 to more than 400  $MeV/n$  and  $MeV$  electrons. Besides, the intensity of the solar X-rays was measured by using this experiment. More details can be found in [Kunow and Wibberenz \(1984\)](#) and [Kunow et al. \(1991\)](#).

## 3.4 Results Obtained with Helios

The achievement of all the aimed objectives and even the unexpected long-duration of the Helios mission ran from the date of the launch to the first perihelion passage about 90 days later. It is important to emphasize that the desired mission duration was of 18 months, however, H1 remained operational during an entire solar cycle.

Through Apollo telescope, the interpretation of the solar phenomena in connection with the response in the interplanetary structures through Helios measurements was largely amplified. This improved our understanding of the Sun-Earth connection ([MARSCH; SCHWENN, 1990](#)).

New findings in the solar atmosphere and inner heliosphere were possible with the advent of the two missions. During Skylab era, the coronal holes were identified as the solar sources of the high-speed streams (HSS) ([KRIEGER et al., 1973](#)). At the same time, data from the two Helios probes identified corotating streams and their main characteristics during their propagation in the IP medium. In addition to these discoveries, it was found out that CMEs observed through coronagraph onboard Skylab ([GOSLING et al., 1974](#)) seemed to be associated to erupting filaments, prominences, flares, and radio bursts. The propagation of such CMEs was also studied, and they were associated to the occurrence of shock waves and other perturbations ([SHEELEY](#)

JR. et al., 1985).

### 3.4.1 Technological Development

In addition to the scientific importance of the mission, Helios played an important role on the industrial development. It was intended to advance the managerial or technological expertise of Germany, thus progressing towards more advanced equipments (KUTZER, 1984). Furthermore, there were many facilities for the national and international collaborations.

The project offered many new opportunities to the development of the professional skills that were fundamental in the space science area and the expansion of the space industry. The encouragement given to the implementation of the project counting on highly skilled personnel, the technological facilities, and the institutes of research caused a noticeable development (KUTZER, 1984).

### 3.4.2 Scientific Development

A large number of findings was possible with the advent of Helios mission. Scientists, engaged in the understanding and analysis of the data provided by the instruments onboard each probe, studied large scale phenomena, kinetic and also microscopic aspects of the IP medium and its structures. The kinetic theory was used in the study of plasma waves, turbulences and the individual characteristics of each particle species (MARSCH, 1991).

For the study of the variations occurred in the solar corona, instruments onboard the Helios observed the variations that occurred on the plasma density and the magnetic field configuration. Radio propagation techniques and other similar mechanisms were used to study these variations. Furthermore, these techniques were useful in the detection of CMEs occurrence. The acceleration and heating of the solar wind compared to the temperature in a turbulence were observed. More details of these phenomena can be found in Bird and Edenhofer (1990).

The existence of boundaries between two solar wind streams in longitude as well in latitude was registered by the “in situ” measurements made by the two probes. With the pioneer measurements from the mission, it was possible to differentiate the two basic types of solar wind through their main properties, as well as their location and magnetic topologies of their sources in the solar corona. Based on that,

it was observed that these two types probably differ by the mechanisms involved in their accelerations (SCHWENN, 1990). In addition to the finding of the non-uniform solar wind in the wide extension of the solar corona, the evolution of the solar wind streams was investigated once the probes traveled from distances ranging from 0.29 to 1  $AU$ . Marsch (1991), by using “in situ” measurements of waves from Helios instruments, showed that electrons are generally cold in fast streams.

The magnetic field was deeply investigated by Mariani and Neubauer (1990). Furthermore, they also studied in details the fine structure of the current sheet and its complexity during solar maximum. The sector boundaries complexity was revealed. Sometimes abrupt changes were observed, other times they were smoother in the direction of the magnetic field. On the other hand, the transition to large scale sector occurred uniformly.

Among the CMEs, the MCs subgroup was investigated by the sensors onboard Helios. The first time a magnetic cloud was observed in the IP medium was through the study of shock waves from H1 and H2, Voyagers 2, and IMP-8 spacecraft. A turbulent region with a magnetic field configuration regarding a flux tube magnetic configuration was identified just behind a shock wave (BURLAGA et al., 1981). This identified region presented a magnetic field rotation consisting on the passage of a magnetic loop. From the observations of H1, H2, Voyager 2 and IMP-8 the final proof for the existence of MCs was revealed (see Figure 2.13).



## 4 LONGITUDINAL EXTENSION OF SHOCK WAVES IN THE INNER HELIOSPHERE

### 4.1 Overview of the Chapter

The two Helios probes traveled at variable longitudinal and radial separations through the inner heliosphere. They collected most valuable high resolution plasma and magnetic field data for an entire solar cycle. The mission is still unique in that no other missions will collect the same kind of data in the next 20 years! One of the subjects studied using the Helios mission was the identification of more than 390 shock waves driven by Interplanetary Coronal Mass Ejections (ICMEs). In this chapter, we describe some of the shock events detected by the mission and complement the observations from the Helios 1 and Helios 2 probes with near Earth space probes IMP-8 and ISEE-3. Based on these different points in the IP space, we compare and associate the events at the points of observation. The main idea is to make a statistical study of the extension of the shock waves in the interplanetary medium.

Many shocks were observed from only one of the probes, i.e., single-spacecraft observations. Of course, we had to reject all cases where the second (or third) spacecraft was off-line because of data gaps or other reason of confusion. On the other hand, some shock waves were observed and monitored at different points (multi-spacecraft observations), representing very significant contributions to our statistics. Thus, one can get some idea of the likelihood of the shock's extension in the inner heliosphere based on observations. Some of the cases of multi and single-spacecraft observations are described in details with their time of occurrence, location of the probes, and other interesting features related to them.

### 4.2 Introduction

Interplanetary shock waves are the strongest abrupt perturbation in the solar wind, playing an important role in the solar-terrestrial environment variability. They are large-scale phenomena resultant of the propagation of interplanetary structures, such as ICMEs - the interplanetary counterparts of the coronal mass ejections (CMEs) (see terminology discussion by [Schwenn \(1996\)](#), [Burlaga \(2001\)](#) and [Russell \(2001\)](#)). They are originated due to the fact that the relative speed between a fast stream (downstream the ICME, in this case) and the background solar wind (upstream) is

often greater than the characteristic speed of the medium (magnetosonic speed). In the inner heliosphere (inside 1  $AU$ ), shocks driven by ICMEs are well formed, and the ICME-shock association has been observed since the first images from Solwind coronagraph were available: [Sheeley Jr. et al. \(1985\)](#) were the first to confirm that fast ICMEs were related to the shock formation.

Shocks are interesting phenomena from the solar physics point of view since they are extremely important in the solar wind-terrestrial connection and as a fundamental phenomenon in plasma physics. Hence, they have been studied by using “in situ” measurements of the solar wind and the IMF since the beginning of the space age. Because of their three-dimensional nature, multi-spacecraft observations to study shocks at different locations in the heliosphere have been of particular interest in terms of the macroscopic aspects of the shock propagation in the heliosphere ([DRYER et al., 1976](#); [BURLAGA et al., 1980](#); [BURLAGA et al., 1981](#)). Based on this fact, the purpose of this work is to study the shock extension in the inner heliosphere using Helios, IMP-8, and ISEE-3 observations for the entire solar cycle 21. Section 4.3 presents the event selection with the description of some special shock events. In Section 4.4 the statistical analysis carried out in this work and the results obtained through the statistical analysis are discussed. Finally, Section 4.5 summarizes the conclusions.

### 4.3 Event Selection and Data Analysis

Helios was a solar probe mission composed of two twin probes, Helios 1 (H1) and Helios 2 (H2), that operated simultaneously from 1976 until the beginning of 1981 ([PORSCHÉ, 1984](#)). Both probes spun with one revolution per  $s$ , with the spin axis almost perpendicular to its orbital plane. During the 11-years operation of the H1, the first probe launched in December 1974, registered a large number of shock events. The observations were complemented by Helios 2, the second one, which was in orbit for about 4 years, from January 1976 on. They were bound to the ecliptic plane. The orbits of Helios 1 and 2, shown in [Figure 4.1](#), reached perihelia at 0.31 and 0.29  $AU$ , respectively. They had different orbital periods: 190 days for H1, and 185 days for H2, corresponding to almost half of the period of Earth in the ecliptic plane. As a result, the orbit of H1, as seen from Earth, is represented by [Figure 4.2](#).

From 1976 until the beginning of 1981, H1 and H2 operated at the same time, and during some periods they were aligned between them, or even with the Sun-Earth

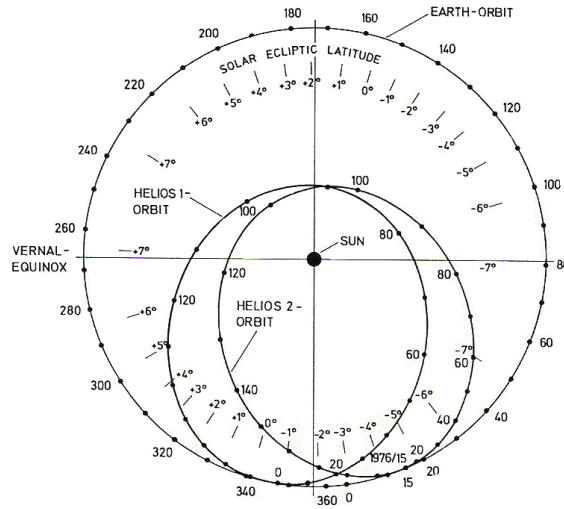


FIGURE 4.1 - Helios probes orbits in a top view. H1 and H2 described ecliptic orbits around the sun, traveling from 0.3 to 1  $AU$  (in the inner heliosphere).

SOURCE: Adapted from [Marsch and Schwenn \(1990\)](#).

line. They have been providing several new inputs for the understanding of the inner heliosphere as well as to several phenomena related to Space Weather. Due to the long life of H1 (1974-1986), it has become possible to collect one of the most complete sets of plasma data over the time span of an entire solar cycle, enabling the study of the solar wind evolution and variation into the inner heliosphere ([SCHWENN; ROSENBAUER, 1984; SCHWENN, 1990](#)). Among the total set of shock waves detected by the instruments onboard Helios, 395 were classified as those driven by ICMEs (see [Table A.1](#)). The majority of these shocks was previously identified by [Khalisi and Schwenn \(1995\)](#) who estimated the expected number of shocks per year (see [Figure 4.3](#)) as a function of the solar cycle, as well as the orbit of the Helios probes.

In this work, a selection of the shock list given by [Khalisi and Schwenn \(1995\)](#) was made. Corotating Interaction Regions (CIRs) were not included in the present work since they are normally related to shocks at distances larger than 1  $AU$  ([HUNDHAUSEN; GOSLING, 1976; SMITH; WOLFE, 1976](#)). However, it is important to emphasize that CIR-shocks were included on the estimate of the total number of shocks seen during the mission, as shown in [Figure 4.3](#).

[Figure 4.3](#) includes already the corrected number of shocks. Considering the orbit of the probes and the solar cycle variation along eleven years, probably many events

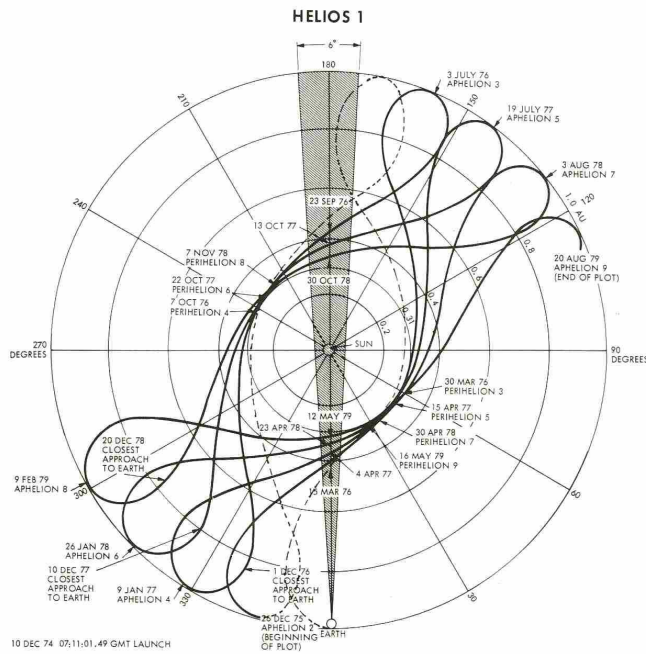


FIGURE 4.2 - View from the Earth of the Helios 1 orbit in the inner heliosphere. Note that the probe's orbit is half of the Earth's orbit.

SOURCE: Adapted from Porsche (1984).

were missed. Another fact is the time they started and stopped operating with a dependence on the solar cycle phase. For example, H1 started operating at the end of 1974, where one finds the largest error bar (see Figure 4.3). Since H1 started operating at the end of 1974, only a few events were detected, nevertheless, the expected number of shocks along the year would have been quite different from the measured one. Thus, the discrepancy between the measured and expected rates of shocks in 1974 is very large.

Each of the shocks driven by ICMEs (Table A.1) was analyzed separately. Data from three spacecraft - more specifically, Helios 1 and 2, and ISEE-3 or IMP-8 - were put together, when available, to contribute to the observational analysis carried out in this work. From three positions in the IP medium, solar wind and magnetic field data were used to observe the evolution of the shock waves. The aim here was the possibility to observe the shock signatures in these distinct points of reference. Then one could estimate the expected total angular distance in longitude that the shock spans.



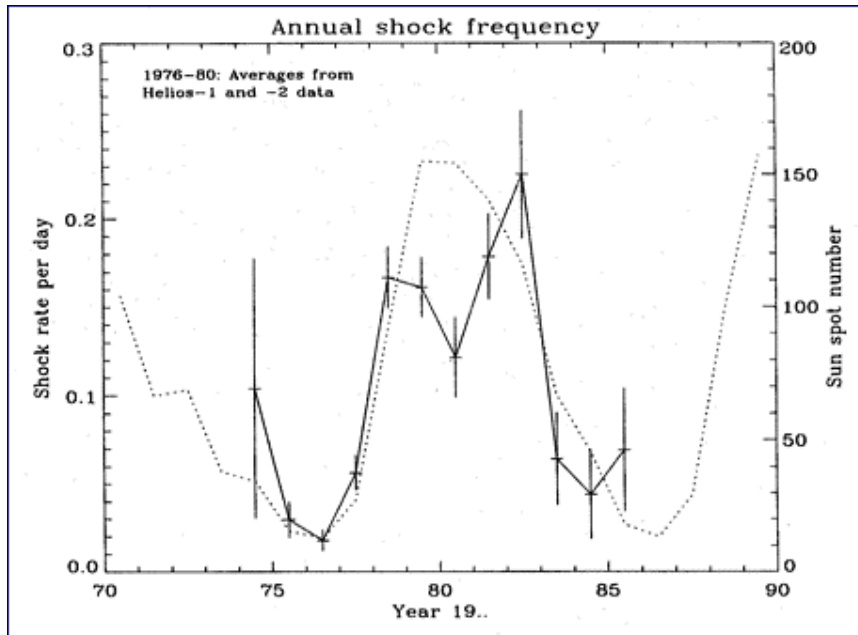


FIGURE 4.3 - Annual shock frequency during the operation of the two Helios probes. On the right-hand side of the plot, the identification of the sunspots number showing that the frequency of shocks does follow the variation of sunspots number over the solar cycle. The error bars show the the correspondence between the expected number of shocks for each year and the number of shocks identified by the two probes.

SOURCE: Adapted from [Khalisi and Schwenn \(1995\)](#).

By using the list of ICME/shock events studied by [Sheeley Jr. et al. \(1985\)](#), we could associate the possible flare locations to limb CMEs when H1 was located close to  $\pm 90^\circ$  of longitude from the Sun-Earth line. This enabled us to correlate the shocks observed by H1 with those observed at the Earth by IMP-8 and/or ISEE-3, because the flare location gives further information about the possible direction the shock wave was driven.

During the time interval covered by the whole set of events, there were periods without observations from the onboard solar wind and/or magnetic field instruments of the three missions. Sometimes a shock was detected by one probe, but gaps were found when the same shock was expected to arrive at the other probes/spacecraft. These cases were not included in the statistical analysis carried out in this study. The “safe events” were defined as those with visible signatures of shocks, i.e., those shocks where plasma and magnetic field signatures of shock waves could be observed without

the interference of data gaps or temporary failure of the instruments onboard each probe. These “safe events” corresponded to the shock waves that made part of the considered sample. We should point out, however, that in some of these cases with gaps, we could see a level enhancement in all solar wind parameters and magnetic field strength before and after the gap. For those cases, we conclude that there was indeed a shock. These cases were considered in our sample “safe events”, even though we could not determine exactly its time of occurrence.

Another difficulty was to determine the periods for which the shocks reached the Earth. There were not many periods for which IMP-8 was in the solar wind. IMP-8’s orbit is near  $35 R_E$  and has a 12+ day period. In this orbit, IMP-8 remains in the solar wind for 7 days, and then it enters into the magnetosphere and remains there for about 5 days/orbit. However, it contributed to improve the estimate, until ISEE-3 appeared in the scenario at the second half of the year 1978 with an orbit around L1 point, constantly immersed in the solar wind. Another aspect that influenced a lot of cases in our sample is the fact that H2 did not operate during the full solar cycle as H1 did. Therefore, for many years we had only one constellation (a pair of probes) as an input to our statistical analysis.

Once the points of observation were located at different longitudinal and radial distances, we used the information in one point to estimate the time for the shock arrival in the other point. The time the shock wave was supposed to reach Earth’s orbit was estimated by using the diagram  $Distance (AU) \times Time (hr)$  as one can see in Figure 4.4. This time was estimated with the information from Table A.1 about the shock speed calculated for each probe, when the shock was observed, and the position of them in the inner heliosphere. Each circle ( $\circ$ ) corresponds to an event in Table A.1, and the straight lines represent the different values of constant speeds. They were used to estimate the arrival time of shock waves traveling without acceleration/deceleration. The time is estimated based on the remaining distance for a shock to reach L1 Lagrangian point. For example, if the shock was detected at  $0.6 AU$  with a speed of  $500 km/s$ , the time it will take to reach IMP-8 and/or ISEE-3 is estimated by considering the remaining distance ( $= 0.4 AU$ ).

The inspection is basically observational, based in the comparison among the different points of reference and their observations. In the following examples, we present some of the shock events seen for more than one probe/spacecraft, and those observed for only one of the probes/spacecraft.

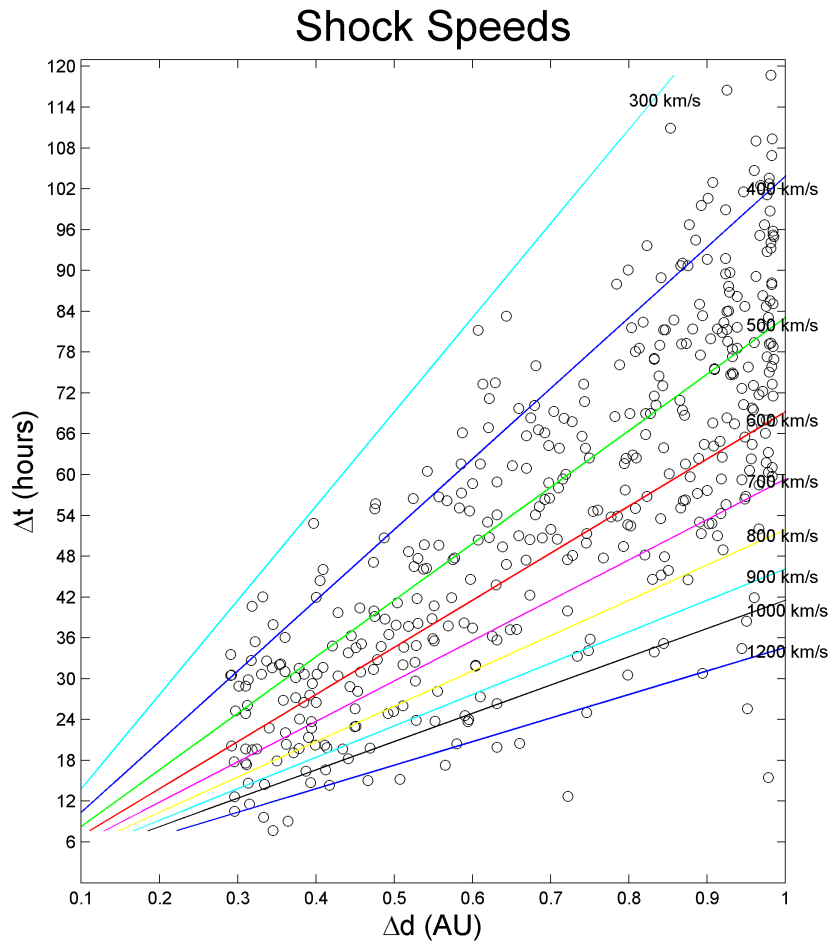


FIGURE 4.4 - Estimate of the arrival time of the shock waves as a function of the radial distance from the Sun according to Helios observation. The circles ( $\circ$ ) that fill the plot are the result of the shock speed measurements of Helios probes. Each circle corresponds to a shock speed calculated when the shock was detected at a determined radial distance (AU), based on the remaining distance.

#### 4.3.1 Shocks observed by multi-spacecraft

Some of the shocks that compose the shock list from Helios ([Table A.1](#)) were observed from multi-spacecraft during their travel in the inner heliosphere. We separated a sample of those events (out of 390 from the total set of shocks) seen by the two Helios probes and put them together into [Table 4.1](#). The first column corresponds to the shock number (SN), followed by the information of the probe (SC) that has observed the event (second column). Represented by YY (third column) is the year; DOY (fourth), the day of the year; HH (fifth column), the hour; and MM (sixth

column), the minutes of the selected events. The seventh column gives the temporal information of the events with the format “dd.mm.yy hh:mm”. The positions of the probes are given by the eighth column (RAD), representing the radial distance, and ninth column (HSE), the Helios Sun-Earth angle. In the sequence, the shock speed ( $V_S$ ), estimated at each probe, is given in the tenth column, followed by the longitudinal separation  $\Delta\phi$  between H1 and H2 (eleventh column), and  $\Delta V_S$  ( $km/s$ ) shock speed difference as measured at H1 and H2 probes (twelfth column). The time difference of the shock arrival at H1 and H2 is given by  $\Delta t_{H12}$  ( $hr$ ) (thirteenth column). The predicted time ( $t_p$ , given in hours) for the shock arrival at the more distant Helios is given in fourteenth column, while the difference between the predicted and the measured time is given by  $\Delta t$  (fifteenth column). The discrepancy between the observed and the predicted times is displayed in the last column by  $\Delta t$ .

TABLE 4.1 - Arrival time of shocks when Helios 1 and 2 observed the same event.

SN	SC	YY	DOY	HH	MM	Date/time	RAD	HSE	$V_S$	$\Delta\phi$	$\Delta V_S$	$\Delta t_{H12}$	$t_p$	$\Delta t$
277	H2	77	28	21	3	28.1.77 21:03	0.978	351.1	489.00	27.80	32.77	4.00	2.00	2.00
26	H1	77	29	1	3	29.1.77 1:03	0.952	323.3	521.77					
279	H2	77	50	17	36	19.2.77 17:36	0.907	345.0	366.18	25.70	11.47	3.07	1.71	4.78
416	H1	77	50	21	40	19.2.77 21:40	0.840	319.3	354.71					
27	H1	77	75	11	33	16.3.77 11:33	0.610	326.3	411.64	18.30	24.54	8.23	6.00	2.23
280	H2	77	75	19	47	16.3.77 19:47	0.717	344.6	436.18					
38	H1	77	268	2	40	25.9.77 2:40	0.580	144.9	1180.73	23.40	609.84	10.00	2.00	8.00
285	H2	77	268	12	51	25.9.77 12:51	0.643	168.3	570.89					
39	H1	77	311	18	15	7.11.77 18:15	0.474	303.2	492.76	22.90	96.75	0.65	5.15	5.80
288	H2	77	311	18	54	7.11.77 18:54	0.400	326.1	396.01					
290	H2	77	328	6	11	24.11.77 6:11	0.620	352.9	385.06	31.40	12.90	16.27	7.02	9.25
40	H1	77	328	22	27	24.11.77 22:27	0.681	321.5	372.16					
293	H2	77	335	1	29	1.12.77 1:29	0.697	356.4	450.84	32.80	14.19	3.73	3.23	0.50
41	H1	77	335	5	13	1.12.77 5:13	0.743	323.6	436.65					
46	H1	78	3	8	39	3.1.78 8:39	0.950	320.4	1027.03	34.20	530.96	6.18	1.00	5.18
295	H2	78	3	14	50	3.1.78 14:50	0.938	354.6	496.07					
48	H1	78	46	1	30	15.2.78 1:30	0.946	307.6	558.98	33.70	95.19	0.38	-	0.38
303	H2	78	46	1	53	15.2.78 1:53	0.954	341.3	654.17					
305	H2	78	60	4	16	1.3.78 4:16	0.892	338.0	722.34	33.80	111.12	8.25	1.00	7.25
49	H1	78	60	12	15	1.3.78 12:15	0.878	304.7	611.22					
306	H2	78	66	23	54	7.3.78 23:54	0.850	337.1	769.50	32.90	320.85	8.83	1.65	7.18
51	H1	78	67	8	44	8.3.78 8:44	0.832	304.2	448.65					
52	H1	78	91	5	30	1.4.78 5:30	0.604	311.7	784.05	30.90	298.87	3.07	0.80	2.27
308	H2	78	91	8	34	1.4.78 8:34	0.619	342.6	485.18					
53	H1	78	92	12	7	2.4.78 12:07	0.589	312.9	641.00	31.50	24.31	11.13	0.71	10.42
309	H2	78	92	23	15	2.4.78 23:15	0.600	344.4	665.31					
310	H2	78	99	7	16	9.4.78 7:16	0.518	351.1	570.62	29.40	61.62	0.03	0.80	0.83
55	H1	78	99	7	18	9.4.78 7:18	0.504	321.7	509.00					
312	H2	78	106	6	20	16.4.78 6:20	0.421	5.4	502.37	26.80	34.09	8.50	1.00	7.50
56	H1	78	106	14	50	16.4.78 14:50	0.409	338.6	536.46					
313	H2	78	108	13	19	18.4.78 13:19	0.390	12.4	759.07	27.30	237.12	0.52	0.40	0.12
58	H1	78	108	13	50	18.4.78 13:50	0.385	345.1	521.95					
314	H2	78	108	18	0	18.4.78 18:00	0.387	13.1	980.21	25.60	481.96	11.77	0.77	11.00
59	H1	78	109	5	46	19.4.78 5:46	0.378	347.5	498.25					
316	H2	78	119	2	56	29.4.78 2:56	0.292	67.4	603.21	28.70	86.05	0.88	0.53	0.35
61	H1	78	119	3	49	29.4.78 3:49	0.310	38.7	517.16					
64	H1	78	127	20	5	7.5.78 20:05	0.361	85.4	680.08	35.90	59.63	2.28	1.40	0.88
317	H2	78	127	22	22	7.5.78 22:22	0.340	121.3	620.45					
65	H1	78	129	9	36	9.5.78 9:36	0.379	91.6	654.39	36.60	99.74	1.82	1.59	0.23
318	H2	78	129	11	25	9.5.78 11:25	0.358	128.2	554.65					
66	H1	78	130	15	2	10.5.78 15:02	0.392	95.8	590.00	35.60	1,685.10	8.40	0.40	8.00
415	H2	78	130	6	28	10.5.78 28:38	0.370	131.4	2275.10					
67	H1	78	132	2	30	12.5.78 2:30	0.411	100.7	842.31	37.70	151.60	2.75	1.02	1.73
319	H2	78	132	5	15	12.5.78 5:15	0.394	138.4	690.71					

TABLE 4.1 - conclusion

SN	SC	YY	DOY	HH	MM	Date/time	RAD	HSE	$V_S$	$\Delta\phi$	$\Delta V_S$	$\Delta t_{H12}$	$t_p$	$\Delta t$
69	H1	78	134	9	24	14.5.78 9:24	0.441	107.1	541.54	38.40	93.51	2.62	1.80	4.42
320	H2	78	134	15	1	14.5.78 15:01	0.428	145.5	448.03					
328	H2	78	268	1	26	25.9.78 1:26	0.721	158.8	631.02	37.40	11.45	1.07	0.55	0.52
75	H1	78	268	2	30	25.9.78 2:30	0.745	121.4	619.57					
417	H2	78	359	2	2	25.12.78 02:02	0.850	351.3	125.65	42.20	581.74	15.47	0.77	14.70
91	H1	78	359	17	30	25.12.78 17:30	0.820	309.1	707.39					
92	H1	78	362	23	1	28.12.78 23:01	0.844	308.9	996.31	41.90	180.09	7.07	1.31	5.76
337	H2	78	363	6	5	29.12.78 6:05	0.875	350.8	816.22					
94	H1	79	2	5	37	2.1.79 5:37	0.872	308.5	643.46	41.50	4.65	7.28	1.81	5.47
338	H2	79	2	12	54	2.1.79 12:54	0.900	350.0	648.11					
340	H2	79	7	10	33	7.1.79 10:33	0.925	348.9	562.14	41.30	92.34	11.43	1.86	9.57
95	H1	79	7	21	59	7.1.79 21:59	0.904	307.6	469.80					
343	H2	79	30	4	10	30.1.79 4:10	0.983	342.0	557.36	40.30	85.03	2.40	0.32	2.08
100	H1	79	30	6	34	30.1.79 6:34	0.978	301.7	642.39					
345	H2	79	41	18	33	10.2.79 18:33	0.979	338.2	541.77	40.20	114.77	7.62	0.39	7.23
103	H1	79	42	2	10	11.2.79 2:10	0.984	298.0	427.00					
412	H1	79	48	10	35	17.2.79 10:35	0.978	296.0	2629.71	40.00	1,943.50	9.03	1.73	7.30
346	H2	79	48	19	37	17.2.79 19:37	0.966	336.0	686.20					
105	H1	79	62	2	2	3.3.79 2:02	0.944	292.2	1139.00	40.20	552.31	7.53	1.98	5.55
349	H2	79	62	9	34	3.3.79 9:34	0.916	332.4	586.69					
118	H1	79	141	11	5	21.5.79 11:05	0.344	63.2	451.89	79.50	57.52	22.88	3.56	19.32
362	H2	79	142	15	58	22.5.79 15:58	0.445	142.7	509.41					
364	H2	79	148	10	28	28.5.79 10:28	0.525	153.0	469.14	62.90	115.49	8.22	6.90	1.32
119	H1	79	148	18	41	28.5.79 18:41	0.428	90.1	584.63					
401	H2	79	162	19	5	11.6.79 19:05	0.698	165.0	512.89	51.90	202.43	1.83	8.52	10.35
120	H1	79	162	20	55	11.6.79 20:55	0.607	113.1	310.46					
416	H1	79	175	20	6	24.6.79 20:06	0.740	119.9	-1.00	47.70	-	1.05	5.77	6.82
367	H2	79	175	21	9	24.6.79 21:09	0.818	167.6	412.55					
405	H1	79	253	13	45	10.9.79 13:45	0.939	0.0	0.00	-	-	-	-	-
411	H2	79	253	20	35	10.9.79 20:35	0.884	151.6	0.00					
377	H2	79	306	3	28	2.11.79 3:28	0.330	207.0	446.80	80.00	87.80	20.43	13.48	6.95
123	H1	79	306	23	54	2.11.79 23:54	0.475	127.0	359.00					
124	H1	79	347	8	53	13.12.79 8:53	0.538	280.9	450.11	61.90	64.89	3.52	6.53	10.05
381	H2	79	347	12	24	13.12.79 12:24	0.685	342.8	515.00					
126	H1	79	357	13	2	23.12.79 13:02	0.659	289.9	536.82	54.10	106.74	12.57	9.99	2.58
382	H2	79	358	1	36	24.12.79 1:36	0.788	344.0	430.08					
384	H2	80	10	20	48	10.1.80 20:48	0.908	343.0	587.57	49.30	89.57	2.35	2.07	4.42
129	H1	80	10	23	9	10.1.80 23:09	0.827	293.7	498.00					
389	H2	80	37	20	40	6.2.80 20:40	0.983	335.1	602.31	46.50	138.16	3.80	1.60	2.20
131	H1	80	38	0	28	7.2.80 0:28	0.982	288.6	464.15					
134	H1	80	65	1	46	5.3.80 1:46	0.976	280.5	524.63	46.20	7.93	12.80	3.53	9.27
390	H2	80	65	14	34	5.3.80 14:34	0.932	326.7	516.70					

SOURCE: Adapted from [Khalisi and Schwenn \(1995\)](#).

Taking into account the arrival time of the shock at each probe, with the predicted time considering a constant speed, we can associate shocks observed at different points into space. The speed considered as constant was the shock speed estimated for the probe closest to the Sun.

Once the shock was detected by the first probe, one can estimate the time to arrive in the other probe with the same propagation speed. After predicting the time for each event, we can compare it with the result from the observation, in case that this shock was seen at more than one point in the inner heliosphere. [Table 4.1](#) is a list of those events, seen at different points in the IP space. Since a few cases were seen by the two probes in space, compared to the whole set of shocks observed by Helios, we had to predict the time the shock was supposed to arrive near Earth. The

constant speed assumption gives us as result the distribution shown in [Figure 4.4](#). In this figure, all the information from the observations of the mission is represented by the circles ( $\circ$ ), representing the shock speed and the remaining distance to travel in the inner heliosphere. For instance, the shock observed by H2 on the 28<sup>th</sup> of 1977, at 21:07 UT, and the one detected by H1 on the 29<sup>th</sup> of 1977, at 01:03 UT are considered as being the same event. This is specially due to the time of occurrence and the positions of the probes. Since H1 is nearer (0.952 AU) to the Sun, even though this probe observed the shock wave after H2 (at 0.978 AU) has detected it, we consider  $V_S = 521.77 \text{ km/s}$ , the shock speed measured by H1. Thus the reference shock speed is the one measured at the probe which is closer to the Sun.

The time delay between the measured time for the shock arrival in each probe and the predicted time was 2 *hr*. This means that one has to consider a 2-hour time window around the time expected when predicting the arrival time based on this instance. However, many other shock events have been associated among them, as it is shown in [Table 4.1](#). In general, the time delay ranged from a few minutes to almost 20 *hr*, as one can see in the column  $\Delta t$  in [Table 4.1](#). There was only one case with this large time window (= 20 *hr*), and the average difference of the time measured and the predicted one was around  $5.5 \pm 4.3 \text{ hr}$ . This means that if we have to take into account a constant speed as the parameter to estimate the time, we have to consider a time window of around  $5.5 \pm 4.3 \text{ hr}$  in average. In this work, we used a  $\pm 20 \text{ hr}$  window centered at the estimated arrival time to look for the corresponding shock in the second probe. However, we have to keep in mind that the medium is filled with other types of structures and magnetic field topologies, that might interact among them and interfere in the shock propagation.

[Figure 4.5](#) is the result of the correlation between the difference on times at which the shocks were detected by H1 and H2 ( $\Delta t_{H12}$ ) and the estimated time ( $t_p$ ) for the shock arrival at a determined point into the inner heliosphere. There is a low correlation ( $r = 0.37$ ) between the time estimated and the time at which the probes measured the shock arrival at variable points into space. This happens probably because, for some cases, the shock speed measured at the positions of H1 and H2 was very different - sometimes they differed from more than 1000 *km/s*. [Figure 4.6](#) shows that the discrepancy in the shock speeds measured is not well correlated with the time predicted. Thus the difference between the shock speed cannot be taken into account as a parameter for the time window selection. On the other hand, when

considering the longitudinal separation between the two probes, as it is shown in [Figure 4.7](#), one notices that the correlation between  $\Delta\phi$ , the separation in longitude of H1 and H2, and the time we expected the shock to arrive to another point into space is medium to large ( $r = 0.57$ ). This means that as the angular separation increases, one has to increase the time window considered for the prediction, building a time-space window.

Larger longitudinal separations involve different features that dominate the IP medium that might contribute to accelerate or decelerate the shock in its path. Such flexibility and dependence on the angular separation of the probes has guided us to the estimate of the time the shock needs to travel from one point in the inner heliosphere to another one, specially for the association of the arrival time at L1. Another aspect that influences our statistics is the fact that, closer to the sun, the probes, on their highly ecliptical orbit, traveled at higher speeds, according to Kepler's second law.

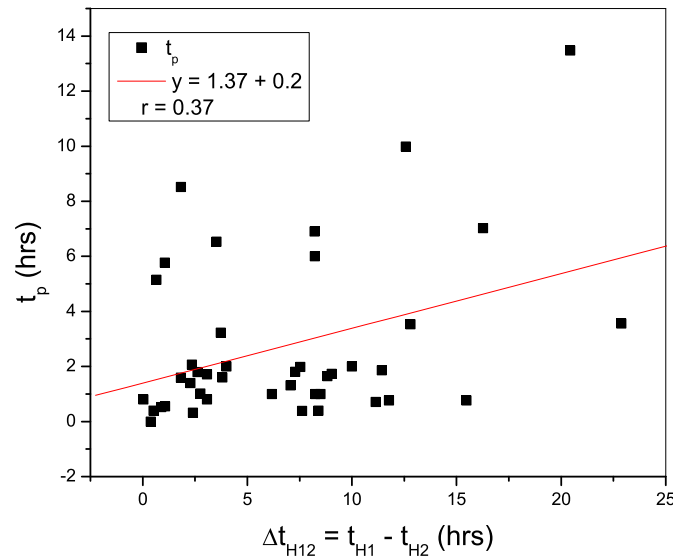


FIGURE 4.5 - Correlation between the difference on the shock speeds of H1 and H2 and the predicted time for the shock arrival. Note that  $\Delta t_{H12}$  comes from the measurements of H1 and H2, while  $t_p$  is predicted based on  $V_S = \text{constant}$ .

[Figure 4.8](#) represents the number of days the probes were separated by  $\Delta\Phi = 10, 20, \dots, 170^\circ$  in the inner heliosphere. Note that from [Figure 4.8](#) we were limited to the angular separation of H1 and H2 that was never bigger than  $130^\circ$ . With the

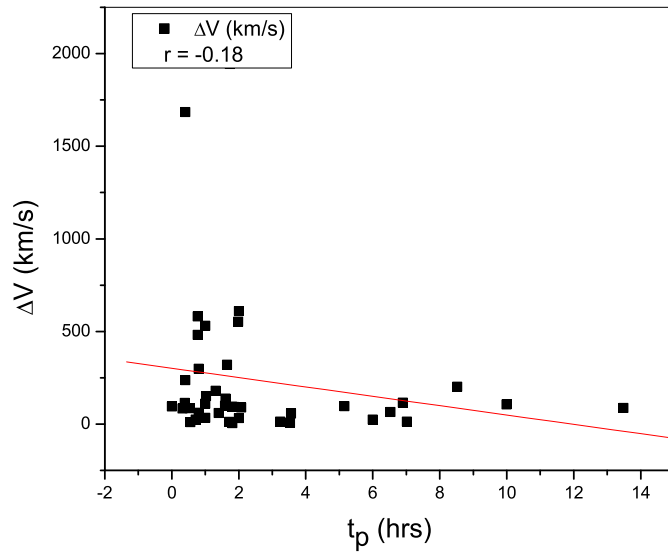


FIGURE 4.6 - Correlation between the shock speed difference measured at H1 and H2 ( $\Delta V$ ) and the time predicted ( $t_p$ ) considering a constant speed as the propagation speed of the shock.

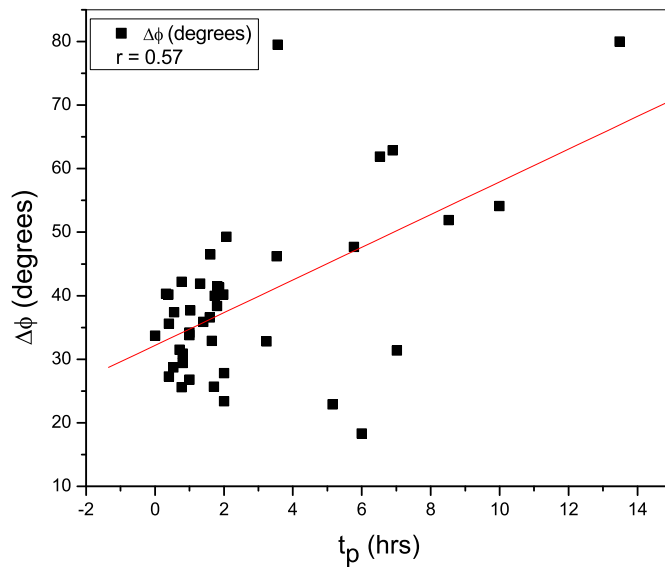


FIGURE 4.7 - Correlation between the longitudinal separation between H1 and H2 and the predicted time for the shock arrival.

inclusion of a third point of observation (Earth, represented by IMP-8 and ISEE-3), one can find larger separation angles and increase the number of days monitored at larger angular separations. The interesting aspect in Figure 4.9 is that for  $\Delta\Phi = 90, 150, 160, 170^\circ$ , that means very large angles, we have around 400 days of



observations. The question that arises is to which angular extensions shock fronts really extend or whether shocks do not expand normally at larger angles or whether there are other parameters that influence and limit their expansion.

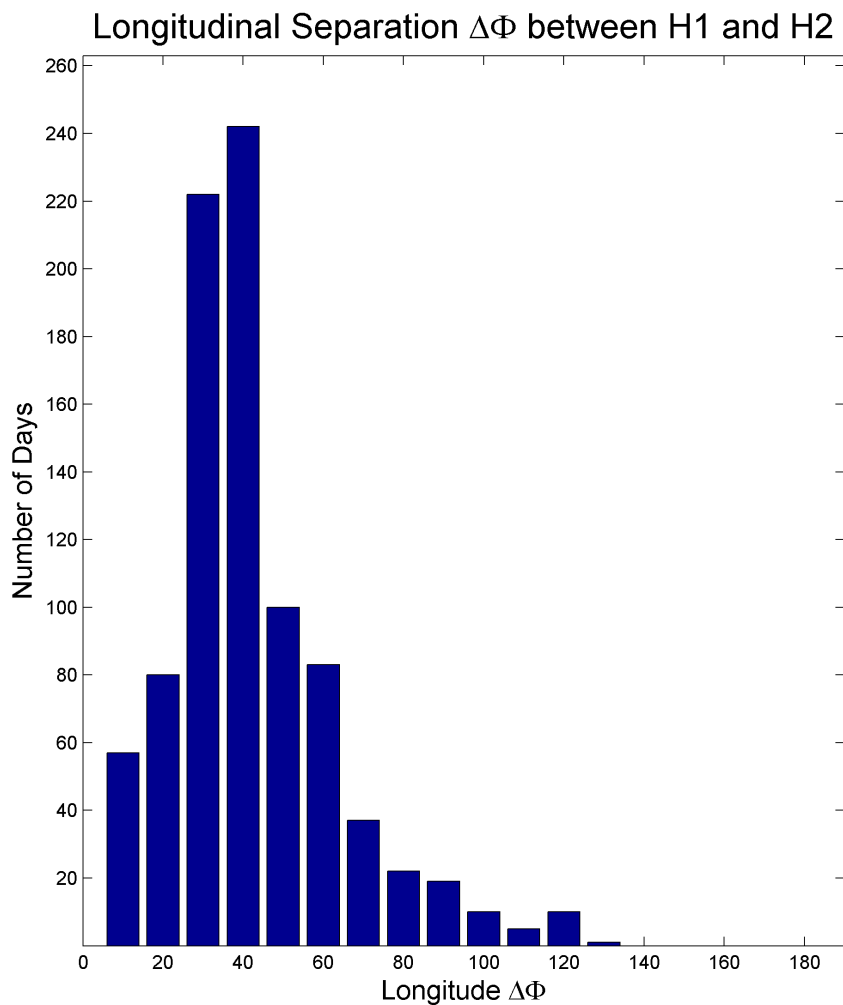


FIGURE 4.8 - Number of days of observation from H1 and H2, for angular separation  $\Delta\Phi$  between the probes.

In the sequence, we describe some special shock events from the Helios shock list (Table A.1) that were analyzed during this study. Furthermore, we discuss some of the features observed in the solar wind and magnetic field profiles in complement with the association we have done among the different points of observation (H1, H2, and IMP-8/ISEE-3). All the information concerning the probe location, the shock arrival at the probes, solar wind and magnetic field data downstream and upstream

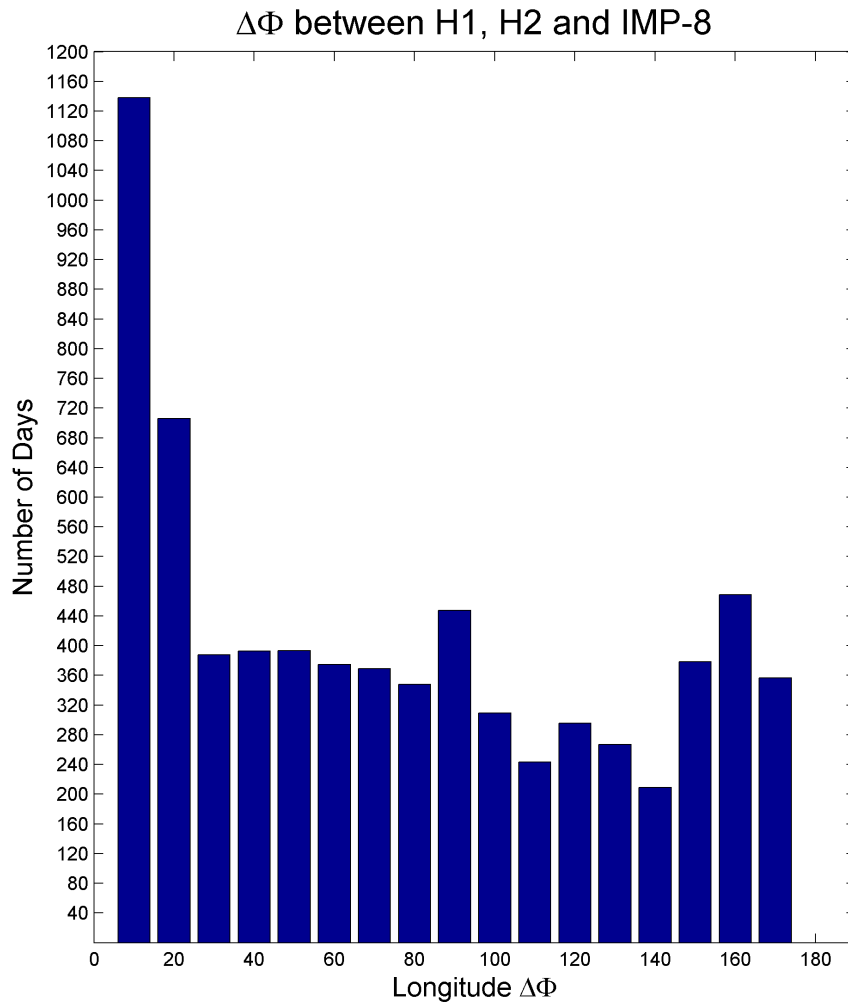


FIGURE 4.9 - Days of separation between all the points of observation: H1, H2, and IMP-8/ISEE-3. One gets the idea of the number of days the probes remained with the same angular opening.

of the shock surface can be found in [Table A.1](#).

#### 4.3.1.1 Shock on DOYs 28-29/1977

Figure 4.10 is one example of a strong shock observed by Helios 1 at 0.952 AU driven by a magnetic cloud in the IP space. The Shock Number ( $SN$ ) referred to this event in Table A.1 is 26. This is the first and one of the best examples of a clear shock/MC pair. This is the famous event where Schwenn et al. (1980) discovered  $H^+$  (i.e., cold prominence material) inside the cloud.

As it is shown in Figure 4.11, interestingly 4 *hr* before H1 has observed it, H2 also detected a shock ( $SN = 277$ ). Even though H2 was further away from the sun, at 0.978 AU, we think that both probes observed the same extended front shock. However, the signatures of the "ejecta" are not clear from the solar wind and magnetic field parameters. This is probably due to the presence of a HSS in the solar wind, identified by H2 around 6:00 UT on DOY 28/1977. The HSS increased the local solar wind speed and the shock wave formed was weakened by this fact. Since the variation in  $\vec{B}$  is very smooth and plasma  $\beta$  is going down after almost one day, counting from the day of the shock, we may conclude that the probe was crossing only the shock wave/sheath region, or maybe the rear part of the magnetic cloud. In the solar surface, no signatures for an eruptive event (flare/CME) were registered that might be related to the CME/MC source.

At the Earth, IMP-8 was the only spacecraft operating during this time interval. Throughout those days, IMP-8 was outside the magnetospheric cavity, thus the solar wind variations could be examined. As one can see in Figure 4.12, the fluctuation on the magnetic field, as identified by  $\theta$  and  $\phi$ , are intense, what would be expected for a HSS as the increase on  $V_p$  and  $T_p$ , and consecutively the decrease in  $N_p$  show us. The abrupt decrease on  $N_p$  was registered before the possible shock was detected, identified by the continuous vertical line on Figure 4.12. The HSS is the same seen by H2, but some hours later due to the longitudinal separation between the two points ( $9^\circ$ ). The time delay between each observation is about 12 *hr*. Around three days before, the same HSS had been observed at H1, which was expected based on the prediction of Schwenn (1990) related to the time a HSS takes to travel a determined angular distance, according to Helios observations.

At the end of DOY 29/1977 the shock was detected by H2, and some hours later by IMP-8. A possible compressed magnetic cloud, according to the signatures discussed on Figure 4.11, is also visible at IMP-8. The HSS, which compressed the MC in its

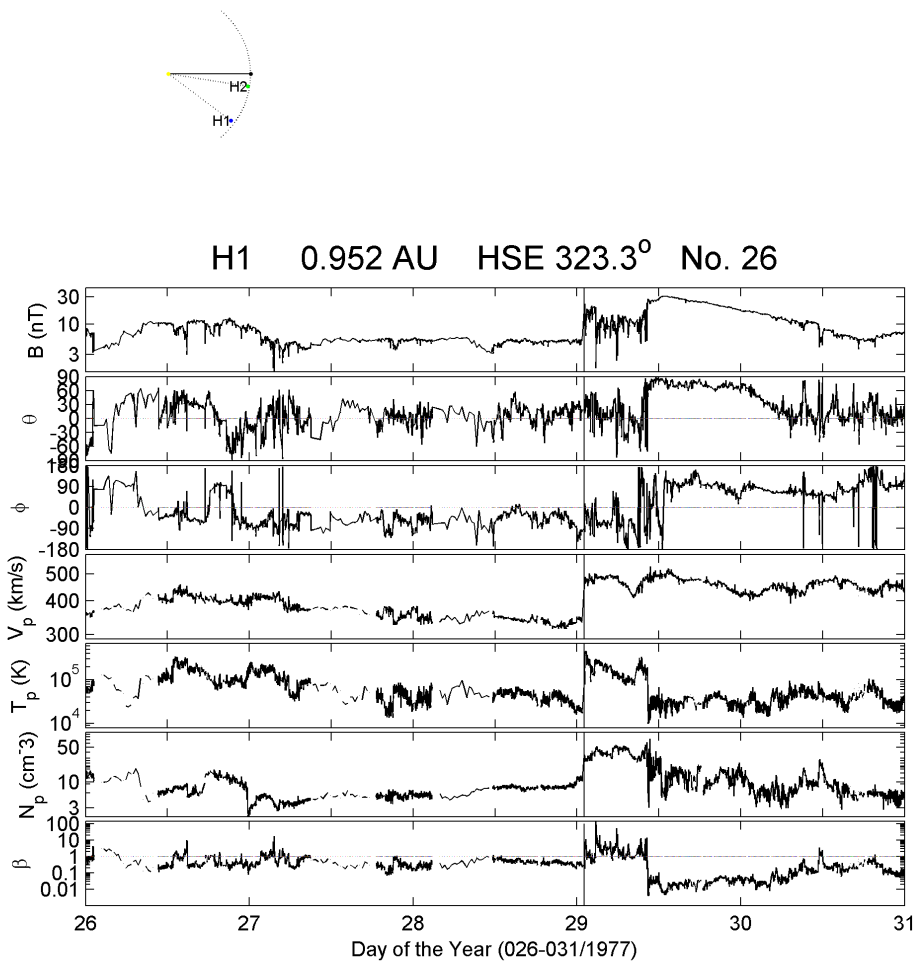


FIGURE 4.10 - H1 observation of a shock on the DOY 29/1977, at 1:03 UT, as identified by the vertical line. The plots give, from top to bottom, the magnetic field strength and angular components, followed by the solar wind proton speed, density, temperature, and the plasma beta, respectively. A magnetic cloud drives the shock, observed by H1 at  $0.952 AU$ ,  $37^\circ$  away from Sun-Earth line. At the top of the figure, the position of the two probes H1 and H2 is shown, as well as the radial distance and longitude (in the counterclockwise direction in relation to the Sun-Earth line) of H1/H2. Earth is schematically represented on the upper plot, as well as the Sun and H1 and H2 positions at the period of the shock. The Sun is the central point of the circumference sector from where the location lines of H1 and H2 for the period of the shock originate. The thicker solid line connects the center (Sun) to Earth. Note that on the top of the top panel there is also information about the probe that observed the shock (H1), the radial distance ( $0.952 AU$ ), the Sun-Earth angle ( $323.3^\circ$ ), and the Number of Shock (NS=26).

west side, increased the speed of the medium and smoothed the shock driven by the MC. Besides, with the compression of the MC caused by the HSS, some of the features of the MC seen at H1 were changed at H2 and IMP-8, probably because the measurements were made in the already compressed MC. At IMP-8, there is a

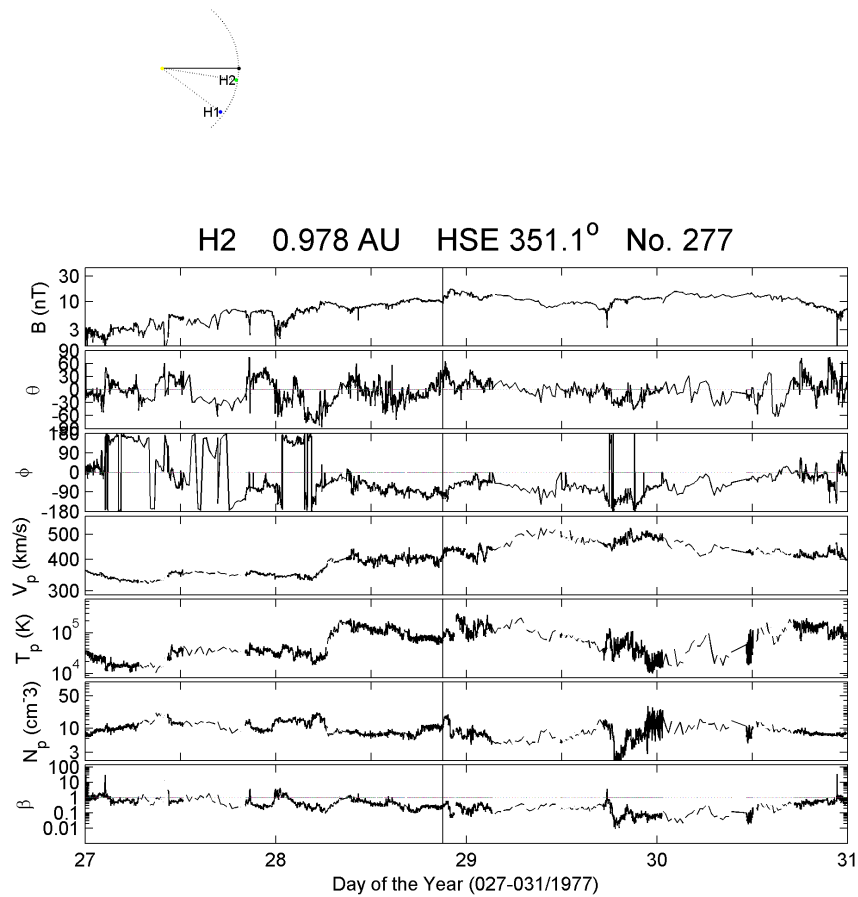


FIGURE 4.11 - H2 observation of a shock on DOY 28/1977, at 21:07 UT. The plots are organized similarly to Figure 4.10. This is the same shock as seen in H1, however, the signatures for a MC are not visible as they are in H1.

mixture between the MC features, the sheath region in front of the structure and the HSS that compressed the MC. The sheath region extension, as detected by H1, is in the order of half a day, while in H2 and IMP-8, if there is really a MC, it seems to extend for almost 1 day.

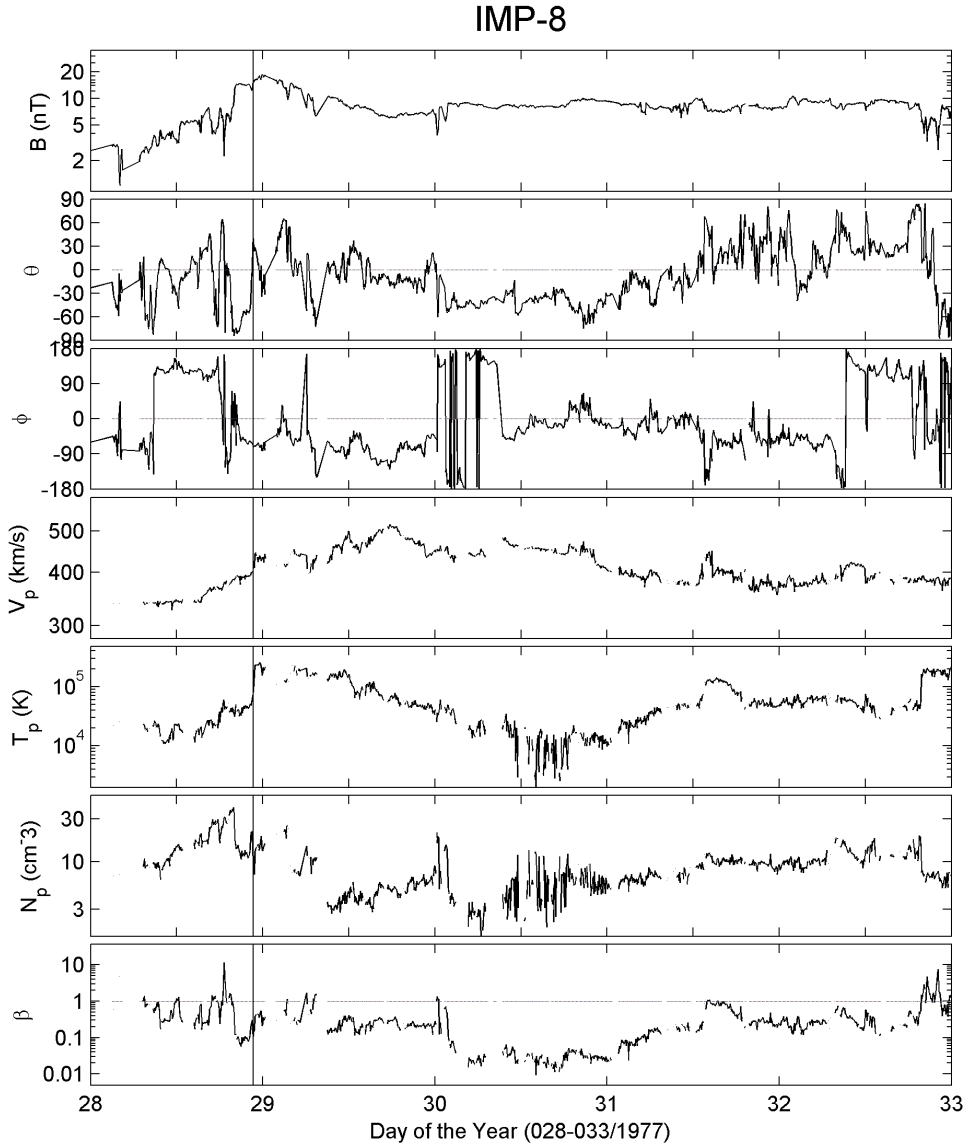


FIGURE 4.12 - Interplanetary shock observed by IMP-8 on DOY 28/1977, at 22:40 UT, identified by the vertical line. This is the same shock previously observed by H2 and later on by H1. The plots are given in the same sequence as the one in Figure 4.10. IMP-8 was in the solar wind near Earth during the period of observation of this shock.

Based on the observations at the considered points, we proceeded to estimate the shock extension in the IP medium. We separated the three points of observation into three “constellations” of two spacecraft each: H1 and H2, H1 and IMP-8/ISEE-3, and H2 and IMP-8/ISEE-3. We associated the shock occurrence on Figure 4.10 with the one on Figure 4.11 which means that the shock was considered the same in both probes. Based on this association, we say that the minimum longitudinal

angular distance reached by the shock was the separation between H1 and H2 - in this case the shock extended at least to  $28^\circ$ . When IMP-8 (Figure 4.12) is included in the statistical analysis a larger angle is considered: H1 and the Sun-Earth line were about  $37^\circ$  of longitude away from each other. Again the minimum distance in longitude the shock reached was that separating IMP-8 and H1, since the shock was crossed by these two spacecraft when traveling in the interplanetary medium outwardly from the Sun. The angular separation between H2 and IMP-8 makes also part of the estimate when we consider the three “constellations” independently.

Note that this is a type of shock where two probes were separated by different radial distances from the Sun, one being closer, the other further. Interestingly, the probe further observed the shock before the closer one, even though the shock speed measured at these different points was almost the same. This means that we cannot expect that a shock always has a spherical shape. In this case, we would suggest a shock with a ripple front. This should be a realistic hypothesis since we have the interaction of distinct parts of the shock with different types of structures in the interplanetary space, changing its shape as it propagates.

#### 4.3.1.2 Shock on DOY 075/1977

From the same active region 14686 two type C flares were observed on DOY 73/1977, one of them at 11:30 UT and the other one at 23:37 UT. They are possibly related to the ICME observed as the driver of the shock wave registered on DOY 75/1977 by H1 and H2, referred as Shock Numbers (*SN*) 27 and 280 (Table A.1, in Appendix A), respectively. As can be observed in the top of Figure 4.13, H1 was located at 0.61 *AU* and  $326.3^\circ$  in longitude (from the Sun-Earth line, in the counterclockwise direction) when it crossed the shock wave driven by this ICME/MC. Eight hours later, the same shock and IP structure were observed by H2, as it is shown in Figure 4.14. At this time, H2 was located at 0.717 *AU*, and  $344.6^\circ$  away from the Sun-Earth line in longitude.

Even though the time difference is large when compared to the arrival time of the shock in two different points, one has to consider the separation between them of almost 0.1 *AU* between them and the shock speed measured at each probe. In both Helios probes, the shock speeds were comparable with the speed of the slow solar wind, explaining possibly why it took longer to reach H2.

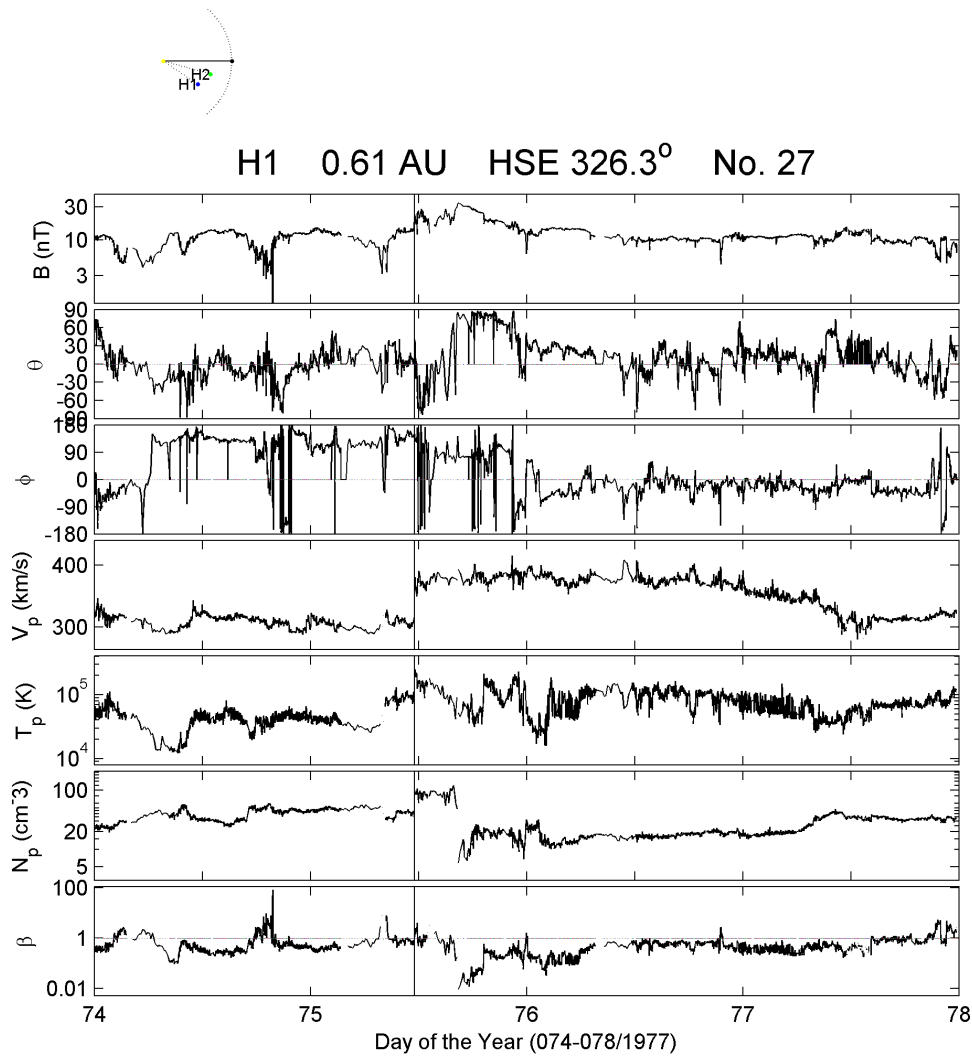


FIGURE 4.13 - A shock wave was detected by H1 on DOY 75 of 1977, at 11:33 UT, as identified by the vertical line. Plots are organized similarly as in [Figure 4.10](#).

The MC that drove the shock crossed H1 and was identified by the low plasma beta and proton temperature, and the rotation in the inclination angle ( $\theta$ ) of the magnetic field, corresponding to the rotation in the  $B_z$  component of the magnetic field, followed by a small increase in the magnetic field strength. The same MC with clearer signatures was observed by H2, as it is shown in [Figure 4.14](#). Note that the MC seems to be compressed in H1 profiles given its short duration. On the other hand, in H2 measurements the structure extends for about fifteen hours.

At this time, IMP-8 was inside the magnetosphere and could not observe IP space. Thus, in the association of the events, since there is no observation near Earth, the



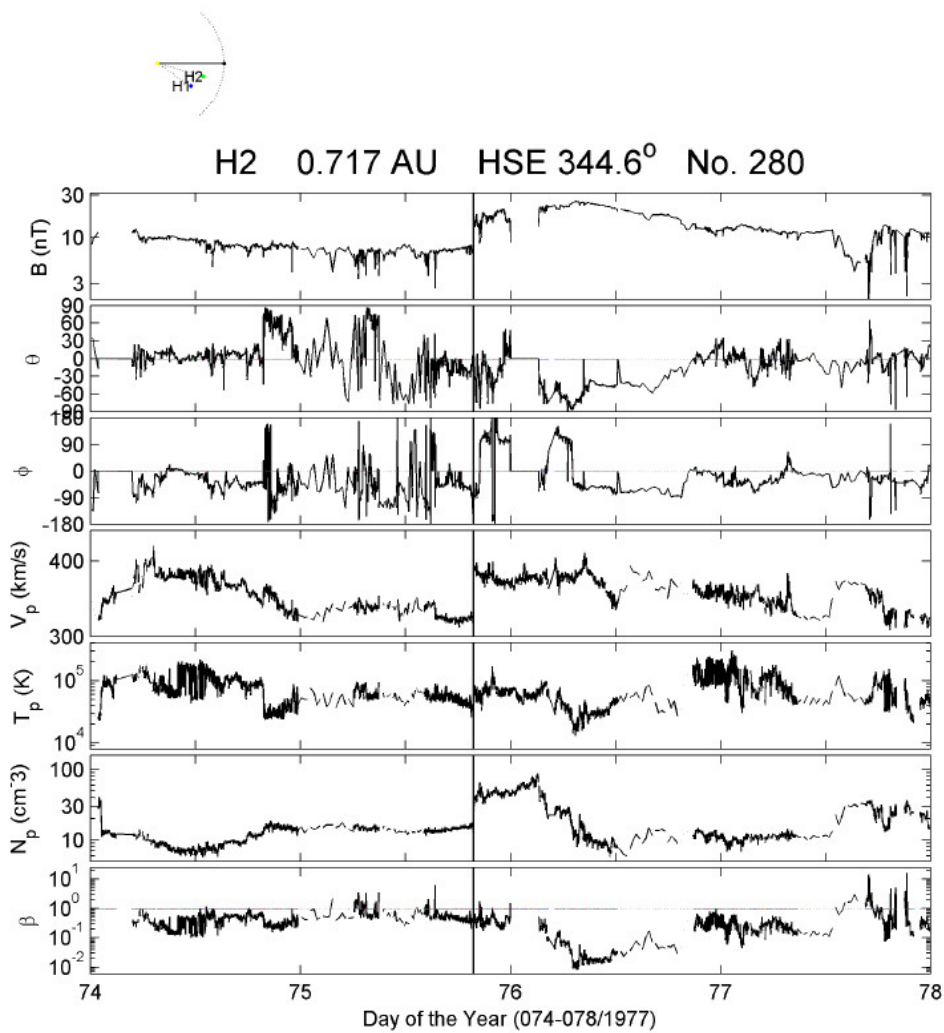


FIGURE 4.14 - H2 observation of a shock wave on DOY 75/1977, at 19:47 UT. The plots are given in the same sequence as in Figure 4.10. The shock is identified by the vertical line. It is driven by an ICME/MC, like the low plasma beta and density show.

only constellation is the one formed by H1 and H2. The angular separation between the two Helios probes was  $18^\circ$ .

### 4.3.1.3 Shock on DOY 148/1979

At 0.525  $AU$ , H2 was the first to see a shock on DOY 148/1979 ( $SN = 364$ ), at 10:28 UT, as it is shown in [Figure 4.15](#). Even though the data are fairly spotty and incomplete, one can see the jumps on the parameters that characterize a shock ([Figure 4.15](#)). Within reasonable timely context, H1 detected a shock ( $SN = 119$ ), at 18:41 UT, and a MC (see [Figure 4.15](#)). This shock was also studied by [Sheeley Jr. et al. \(1985\)](#) in their list of MCs seen at the limb by H1, when the probe was located at about  $90^\circ$ , presenting all the features one would expect to characterize this particular class of ICMEs. At 18:41 UT, in the same day as H2 instruments detected it, H1 sees the shock driven by the MC. Behind the shock wave, the sheath region lasted for a few hours until the MC was visible in H1 data.

According to [Sheeley Jr. et al. \(1985\)](#), no flare signature was visible for the considered period. However, when tracking back to find the solar source at the solar atmosphere, one finds two different onset dates. One of them would be found if we consider the shock speed as being the same as the H1 shock speed, and the other one when considering the shock speed at H2. The former may indicate that no flare was associated to this event, while the latter hints to the class flare observed on DOY 146/1979 at N27W60 with beginning time registered at 20:47 UT, and end, at 21:05 UT. Note though, that the longitudinal separation between the flare site and H1/H2 would be  $30/90^\circ$ , respectively. Such an association appears to be highly improbable, but cannot be ruled out ([YASHIRO et al., 2008](#)).

At the Lagrangian point L1, ISEE-3 sees a shock wave on DOY 149/1979, as shown in [Figure 4.17](#). In spite of the gaps of the plasma data, the shock was confirmed by the printed version of the high-resolution data of ISEE-3 for the corresponding period. From [Figure 4.17](#), a rotation can be seen in the elevation angle and in the components of  $\vec{B}$ , characterizing a MC. Particularly,  $B_z$  shows a smooth rotation in its profile, that follows the same rotation of  $\theta$ . Assuming that this MC is the same one as seen by H1  $90^\circ$  in longitude apart, that would be a really huge solar mass ejection. According to Dr. Russell Howard (private communication during IAU Symposium 257, in Ioannina, Greece, in September 2008), we can expect a shock to extend into even larger distances.

Even though no plasma data are available online for the period, we have confirmed the shock by using the hard copy of ISEE-3 data for the corresponding period.

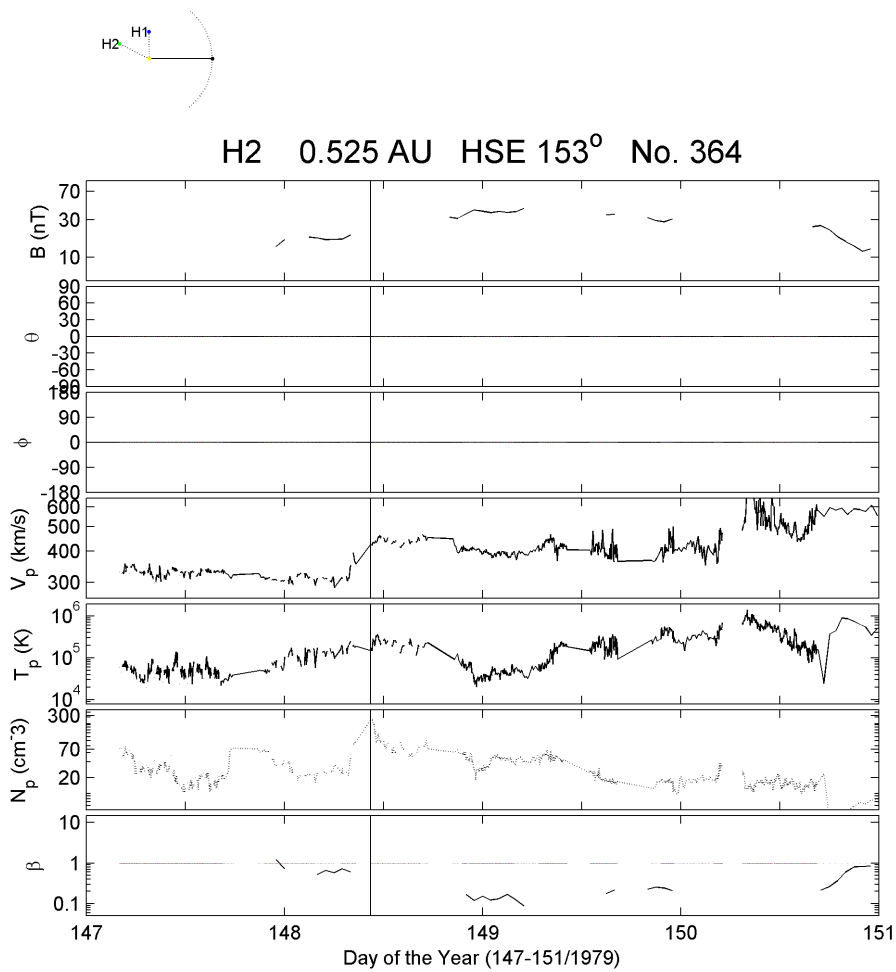


FIGURE 4.15 - H2 observation of a shock wave on DOY 148/1979, at 10:28 UT, as identified by the vertical line. The plots are given in the same sequence as in Figure 4.10. Even with gaps on the data, one can identify some of the features for a possible MC.

Thus, we associate the shock at ISEE-3 with the one observed at H1 and H2, which represents a large longitudinal expansion of the shock wave. To associate the multi-spacecraft observations we use the fact that no other shock was seen by H1 that could be associated to the one at ISEE-3. Second, according to our prediction, the shock should arrive on DOY 150/1979. However, the separation between H1 and ISEE-3 is of almost 90°, that means one needs to consider a space-time window resulting from the big separation of these two points of observation. Inside this time interval, the only shock observed near the Earth by ISEE-3 was the one on DOY 149/1979, at 18:24 UT. According to the ISEE-3 high-resolution data, a MC drove

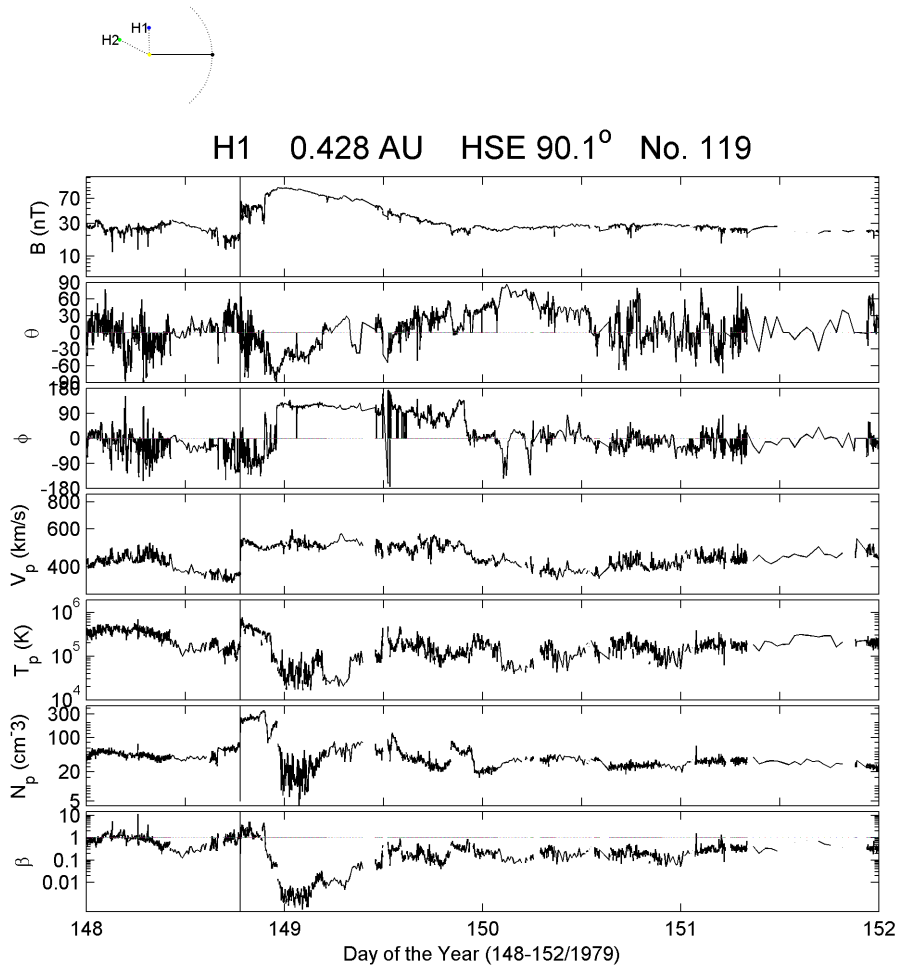


FIGURE 4.16 - H1 observation of the shock wave on DOY 148/1979, at 18:41 UT, as identified by the vertical line. The plots are given in the same sequence as in Figure 4.10. A MC drove the shock wave, identified by the vertical line, as one can see in the plot.

the shock wave identified by H1 and H2 in the IP medium at the considered period of time.

The contribution from this event is very interesting. Based on our assumption around the time occurrence and the flare location, we can say that the shock wave was seen at three different points in space. And they contributed a lot to our sample, since these points are largely separated. From H1 and H2 locations one can say that the shock wave extends inside at least  $62^\circ$ , while from H1 and ISEE-3 the longitudinal extension of this shock is at least  $90^\circ$ , that totalizes  $153^\circ$ , the angle formed between H2 and ISEE-3.

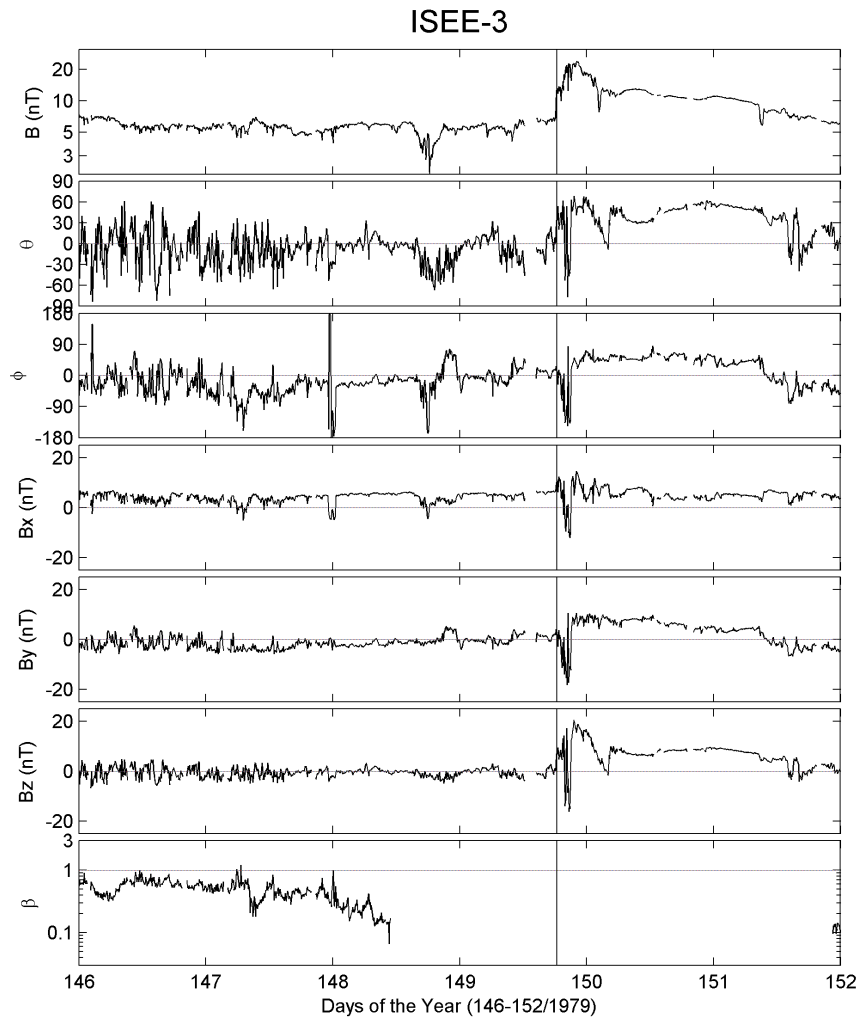


FIGURE 4.17 - ISEE-3 observation of a shock wave driven by a MC on DOY 149/1979 at 18:24 UT, identified by the vertical line. From top to bottom, one can find the magnetic field strength, angles (inclination and azimuthal), and components  $B_x$ ,  $B_y$ , and  $B_z$ , and, finally, the plasma beta characterizing the period of the shock. There is no plasma data during the period of interest.

#### 4.3.1.4 Shock on DOY 89/1980

After H2 ceased its operation in early 1980, we counted with the full time observations of ISEE-3 and H1, and the temporary observations from IMP-8, when this was transiting in the solar wind. One of these cases is the one shown in Figure 4.18 that represents the shock observed by H1 ( $SN = 137$ ) at almost  $90^\circ$  away from the Sun-Earth line in the clockwise direction, i.e, the east limb as sketched in the top of Figure 4.18. The date of the shock was registered on DOY 89/1980 at 11:53 UT,

and the shock is the same studied by [Sheeley Jr. et al. \(1985\)](#). According to [Sheeley Jr. et al. \(1985\)](#), a M2/SB flare occurred on the solar surface at the heliographic location N28E69, at 12:42 UT, and lasted for 5 hours. Associated to this flare, a MC was identified by H1 as the driver of the shock wave.

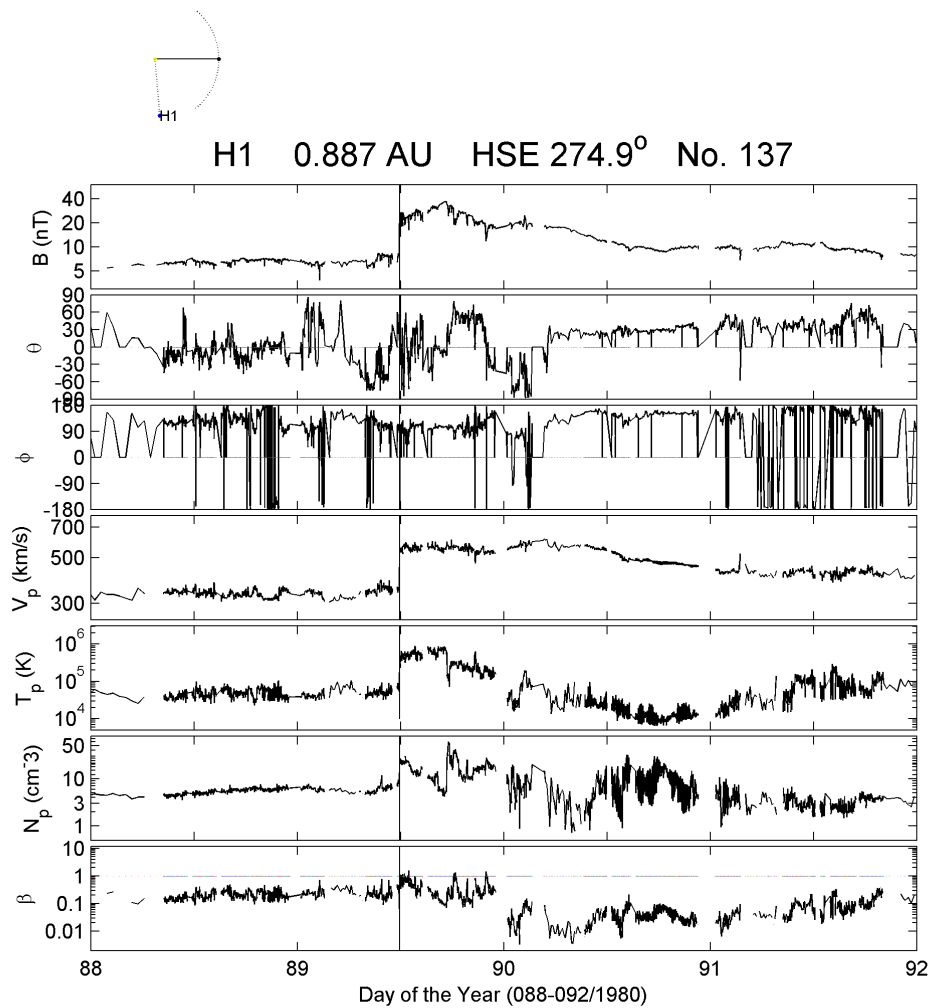


FIGURE 4.18 - H1 observation of a shock wave on DOY 89/1980, at 11:53 UT, identified by the vertical line. The plots are given in the same sequence as in [Figure 4.10](#).

Near the Earth we had data available from IMP-8 and ISEE-3. [Figure 4.19](#) presents the measurements from IMP-8 that was in the solar wind during the corresponding period. Some gaps appeared at the time a shock wave is registered by the solar wind instrument onboard the spacecraft. Nevertheless, one can see the abrupt jumps in

the solar wind parameters. The magnetic field data have no gaps and show a clear profile for a shock wave. There is not enough information to confirm the presence of a MC behind the shock, even though the plasma beta decreases considerably following the decrease in the proton temperature and a smooth rotation in the magnetic field.

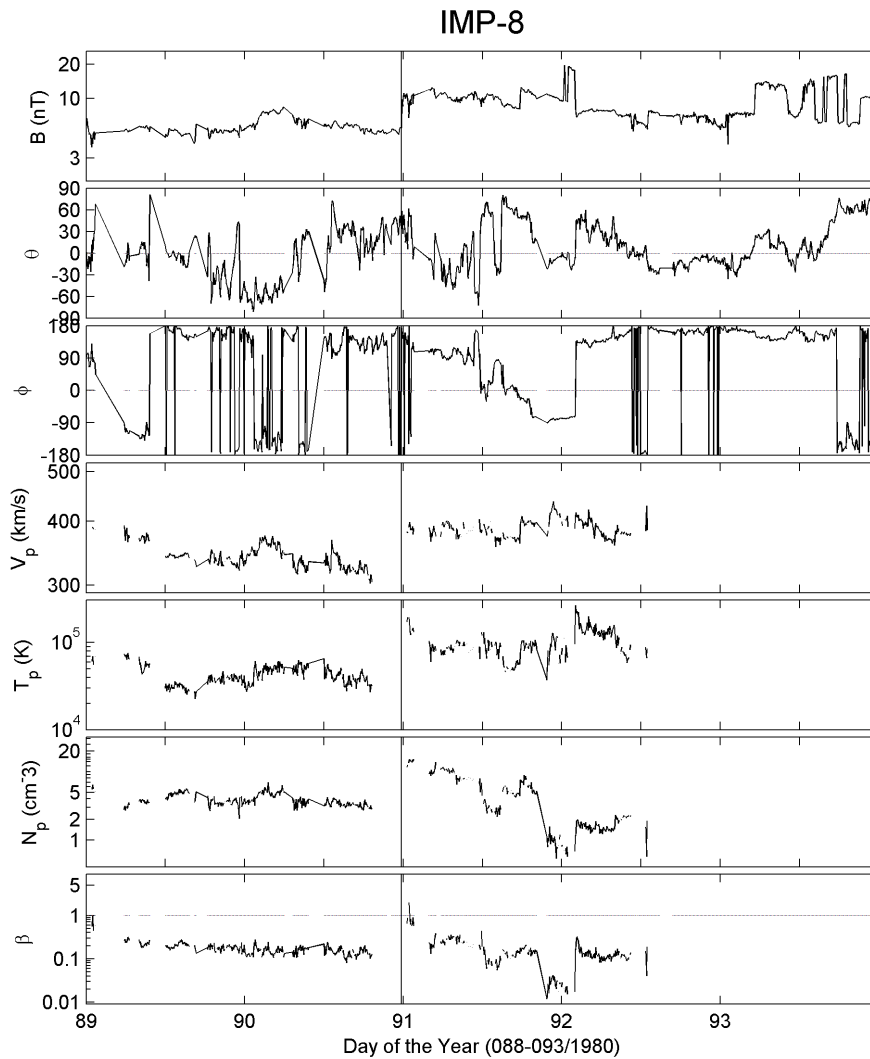


FIGURE 4.19 - IMP-8 observation of the shock wave on DOY 90/1980, at 23:45 UT, represented by the vertical line, near Earth. The plots are given in the same sequence as in Figure 4.10.

Based on the flare location, previously found by [Sheeley Jr. et al. \(1985\)](#), we have an extra information to say that the same shock was seen at two different points of observation, despite the almost 36 *hr* of difference on the time both probes detected the shock arrival. Note that, at H1, the average speed of the propagating structure

was about  $600 \text{ km/s}$ , while, at IMP-8, we identified a speed very close to the one of the slow solar wind. This might explain why the shock arrive first at H1. As a result from the observation of the shock wave at these two spacecraft, the longitudinal separation of about  $90^\circ$  between them corresponds to an expected angular distance into which this shock wave expands.



### 4.3.2 Shock Events observed by only one of the probes

Up to this point we were treating the cases where the probes did observe the same shock wave in different locations of the inner heliosphere. This time, we consider those shocks observed by only one spacecraft, or single-spacecraft observations, although there were other available and operational spacecraft in orbit. When the other probes/spacecraft were operating properly during the considered period, however, the shock was not crossed by it, we consider this event as a single-spacecraft observation. In the sequence, we present and discuss some of these events that represent part of the sample used in the statistics. Of course, we are not interested in cases, where one spacecraft had missed or confused data.

#### 4.3.2.1 Shock on DOY 078/1977

As shown in [Figure 4.20](#), a shock is observed on the DOY 78/1977 by H1 ( $SN = 28$ ), at 7:48 UT. A magnetic cloud drives this shock, as one observes clearly in all the parameters represented in the figure. Based on the magnetic field directions ( $\theta$  and  $\phi$ ), one can notice the rotation of the field, characteristic of the passage of a MC over the probe.

In [Figure 4.21](#), H2 observations are shown, and we notice that at only  $15^\circ$  separation H2 did not observe this shock. Note that for both probes the  $\phi$ -angle of the field was near zero, thus indicating they traveled in the same magnetic sector, i.e., in the same side of the HCS. The HCS consists of a warped magnetic neutral line that separates the two polarities of the global magnetic dipole. It rotates with the Sun and extends throughout the whole heliosphere like a giant ballerina skirt ([ALFVÉN, 1977](#)).

If one considers the speed of the medium, one notices that in both H1 and H2 the upstream speed was around the values of the slow solar wind speed. The shock detected by H1 should be observed by H2 as well, considering the interplanetary conditions for the shock formation, in this case, the difference between the speed of the medium and the propagating structure. However, H2 does not present any variation in its profiles indicating a shock wave formation. The same happened when considering the observations from IMP-8, shown in [Figure 4.22](#). No shock signatures are visible for the considered period.

Based on the observations, one has the contribution from H1 and IMP-8 angular

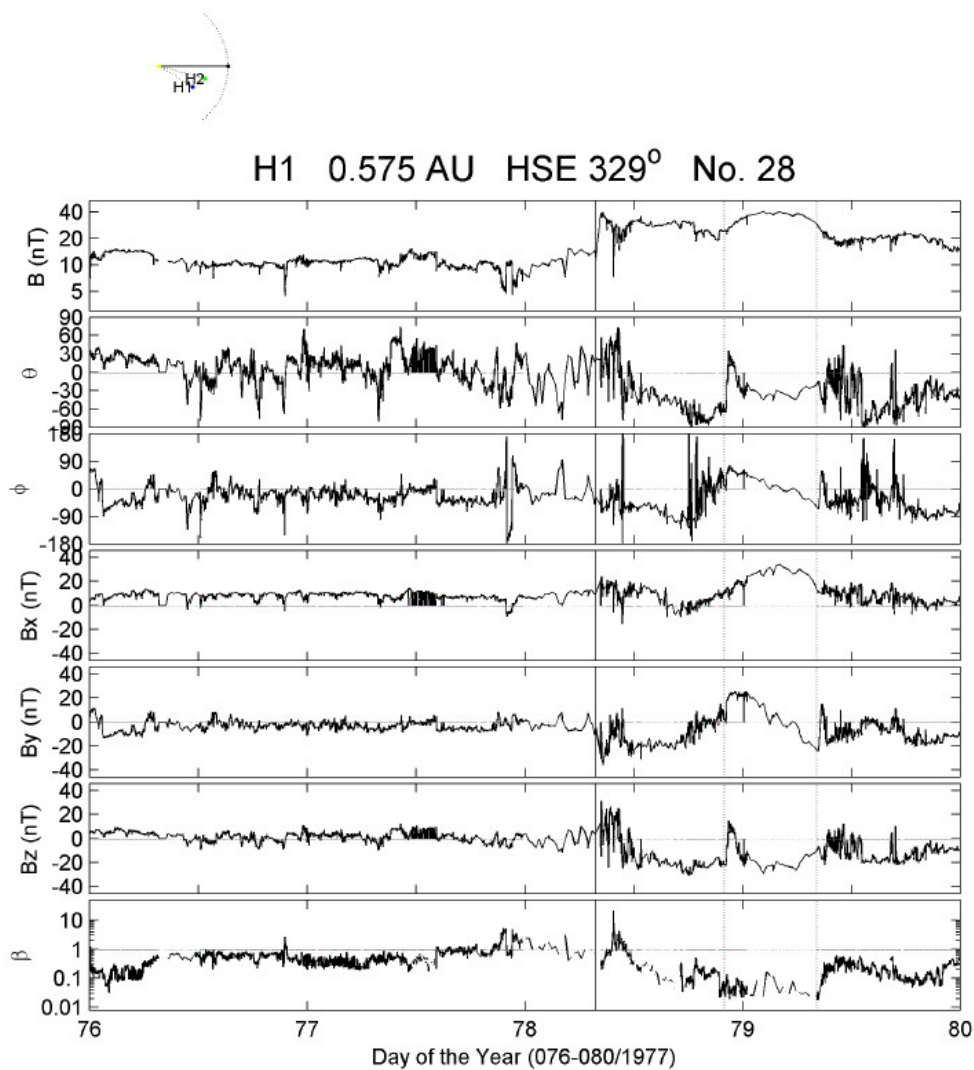


FIGURE 4.20 - H1 measurements for the event on DOY 78 of the year 1977, at 7:48 UT, as identified by the vertical line. From top to bottom, one can see the magnetic field strength and angles (inclination and azimuthal), the protons speed, temperature, and density, and, finally, the plasma beta profiles.

separation. According to our own classification, we consider that the shock did not expand into  $15^\circ$  (H1 and H2 angular separation), neither into  $31^\circ$ , the angular separation between H1 and IMP-8.

This specific case is going to be explored later in Chapter 5, where MVA analysis, a technique used to identify the direction of maximum, intermediate and minimum rotations of the magnetic field, is applied to understand the direction of the cloud axis (intermediate direction). This could also explain why the shock did not occur

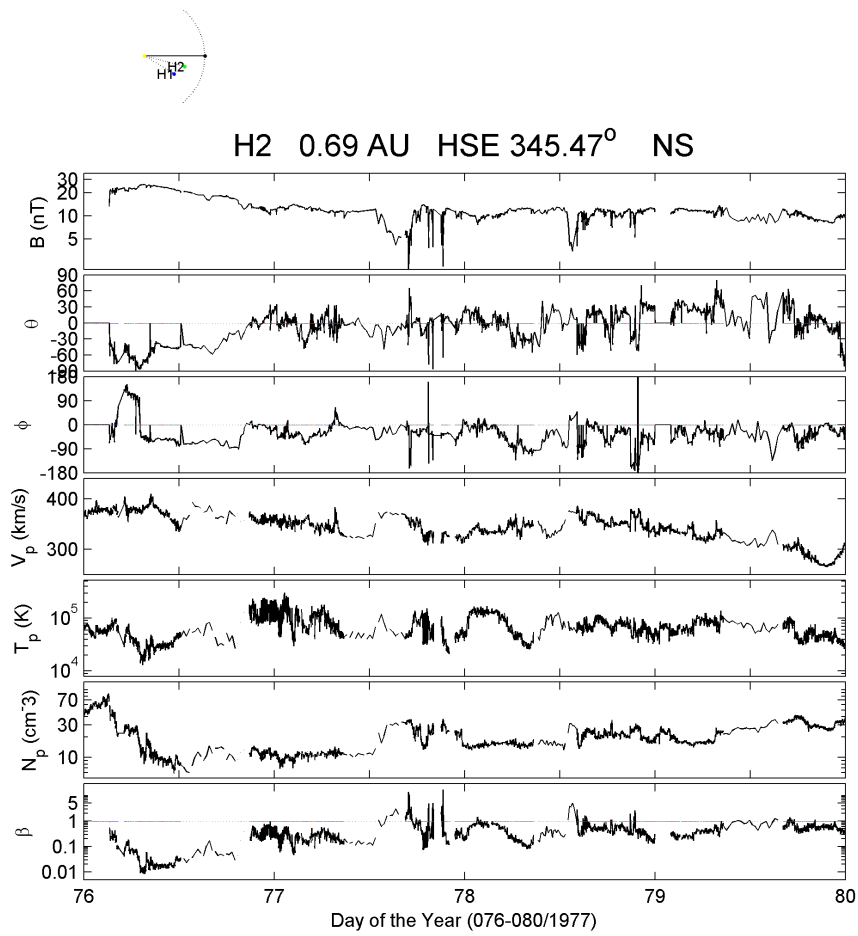


FIGURE 4.21 - H2 solar wind and magnetic field profiles for the period from DOY 76 to 80/1977. The plots are given in the same sequence as in Figure 4.10. No shock (NS) signatures are registered for the considered period.

at H2. If, for instance, the MC was highly inclined in relation to the ecliptic plane, the two probes might not have seen the shock, neither the MC.

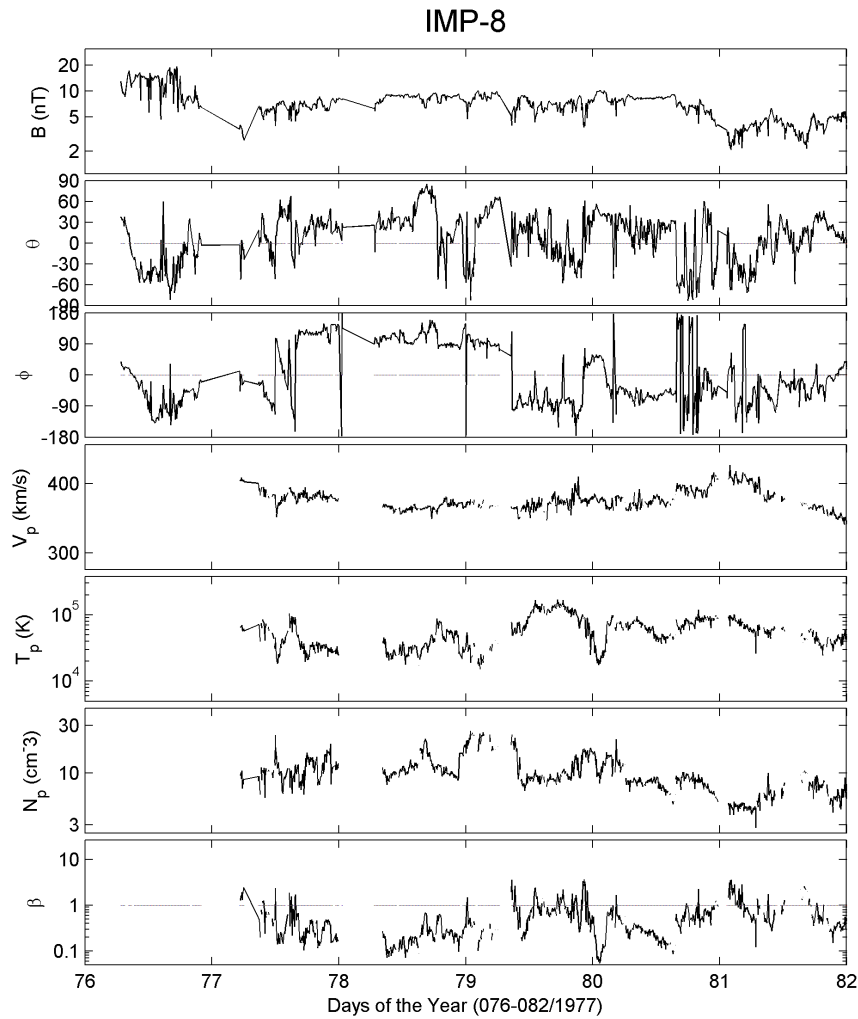


FIGURE 4.22 - IMP-8 magnetic field and plasma parameters from DOY 76 to 82/1977. The plots are given in the same sequence as in Figure 4.10. As one can see in the parameter profiles, there is no signature for a shock during the corresponding period.

#### 4.3.2.2 Shock on DOY 327/1977

A shock wave was detected by the instruments onboard H2 on DOY 327/1977 ( $SN = 289$ ), at 16:09 UT, as shown Figure 4.23. One can identify the shock by the abrupt change in all solar wind values. The vertical line identifies the exact moment of the shock detection by H2, that was in a longitudinal position almost aligned with the Sun-Earth line. After the shock, a sheath region was identified by the high density, due to the compression by the shock wave. The MC is observed afterward through the smooth rotation in the magnetic field azimuthal and elevation angles. The magnetic field strength, high inside the structure, and the plasma beta decrease characterize

the MC that lasted less than one day.

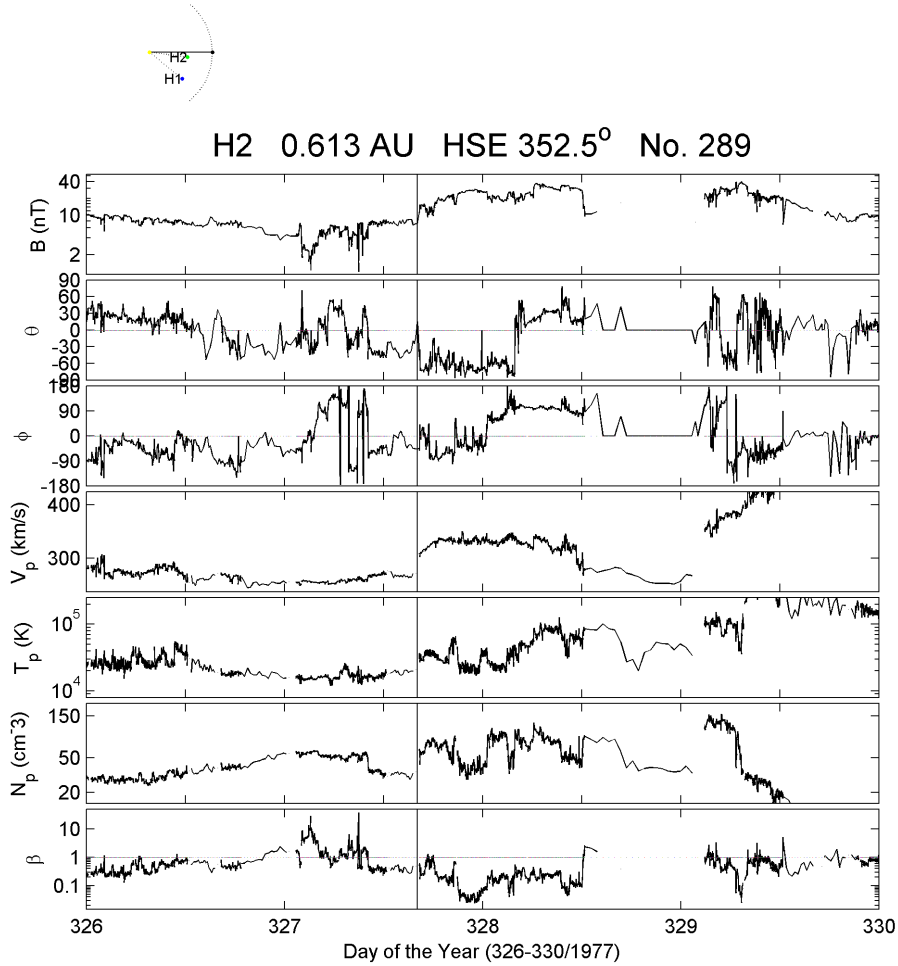


FIGURE 4.23 - H2 observation of a shock wave on DOY 327/1977, at 16:09 UT, as identified by the vertical line. The plots are given in the same sequence as in Figure 4.10.

At about  $39^\circ$  away from the Sun-Earth line, H1 does not observe any feature of a shock wave, as shown in Figure 4.24. However, at the end of DOY 326/1977, the solar wind profiles identify a HSS by the increase in the proton speed and temperature at the same time as the proton density decreases. Fluctuations on the magnetic field vector are identified by the elevation and azimuthal angles, as one observes specially at the beginning of DOY 327/1977. Since there was no shock observation from H1, one can say that a single-spacecraft observation described the event.

Near Earth, IMP-8 was inside the magnetospheric cavity providing no measure-

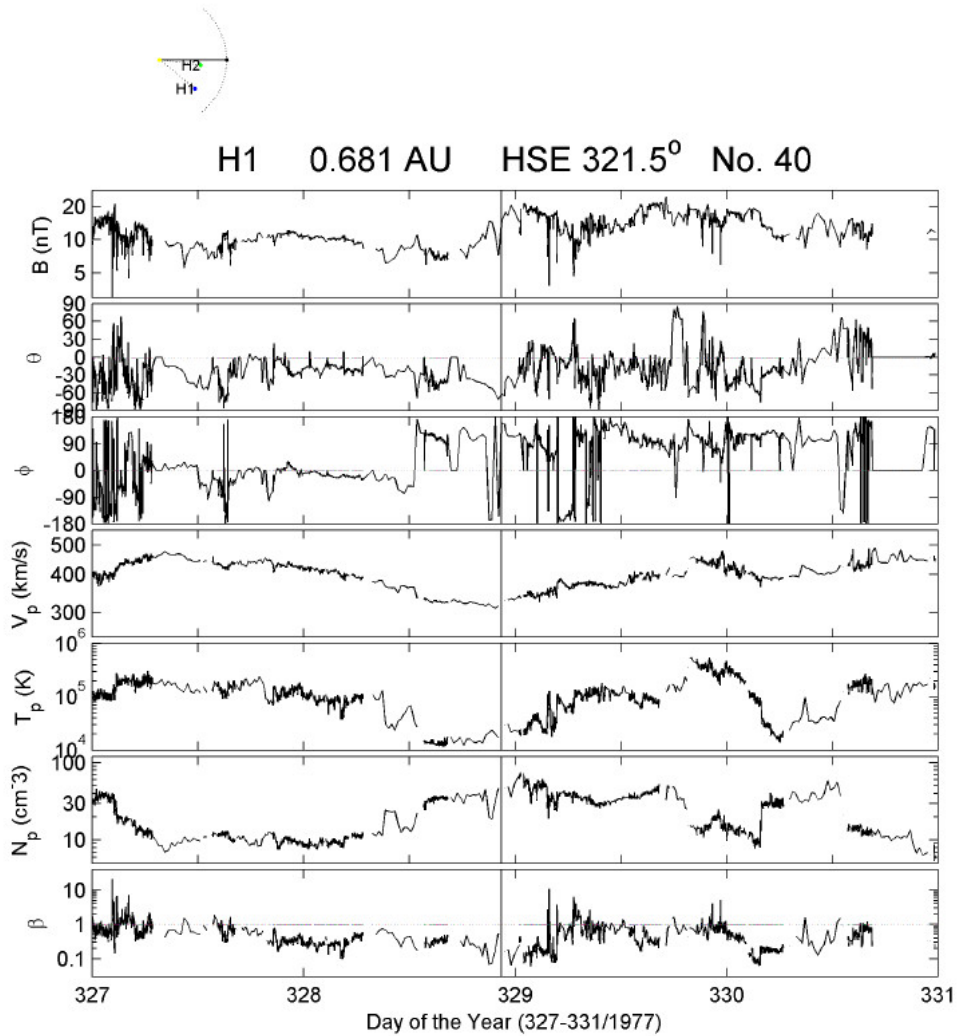


FIGURE 4.24 - H1 observation of the period of interest: from DOY 327 to 331/1977. The plots are given in the same sequence as in Figure 4.10. No shock (symbol “NS”, on top of the figure) is detected by the instruments onboard H1.

ments for the MC that caused a moderate magnetic storm at the beginning of DOY 330/1977. According to the World Data Center (WDC) from Kyoto, the peak reached by the  $Dst$  index was of the order of  $-87 nT$ . Probably, the smooth rotation of the MC contributed to the formation of a southward  $B_z$  component that led to the plasma injection into the magnetosphere.

In relation to the estimate of the longitudinal extension of shock waves, the information we consider from this event is that inside an angular distance of  $39^\circ$  the shock did not extend, what means that we have another type of entry in this case:

a single-spacecraft observation.

#### 4.3.2.3 Shock on DOY 333/1978

Another example is the shock detected by H1 on DOY 333/1978 ( $SN = 82$ ), at 3:17 UT, as one observes in [Figure 4.25](#). H1 was located at 0.552 AU, and  $297.6^\circ$  away from the Sun-Earth line in the counterclockwise direction, shown at the top of the plot. [Figure 4.26](#) shows that, at the same period, H2 did not observe any characteristics of a shock wave. Both twin Helios were separated by about  $47^\circ$ , with H2 closer to the Sun-Earth line. Since H2 did not show any variations on the parameters that characterize a shock, the same is expected from IMP-8/ISEE-3. [Figure 4.27](#) complemented the observations for the shock period. At this time, IMP-8 was measuring in the outer magnetosphere environment and had the most complete data set of the solar wind in front of the magnetosphere compared with ISEE-3. Through the analysis of the solar wind parameters, we conclude that there is no shock between 331-336/1978 near Earth.

The contribution from this event comes from the three points that were monitoring the inner heliosphere during the period of interest. Among these points, we have three entries for our statistics, concerning the considered angular distances into what we do not consider a shock to expand to. From H1 and H2 we have that this shock did not expand more than  $31.4^\circ$ . It is no surprise that at Earth, at  $38.5^\circ$  away from H1, there was also no shock.

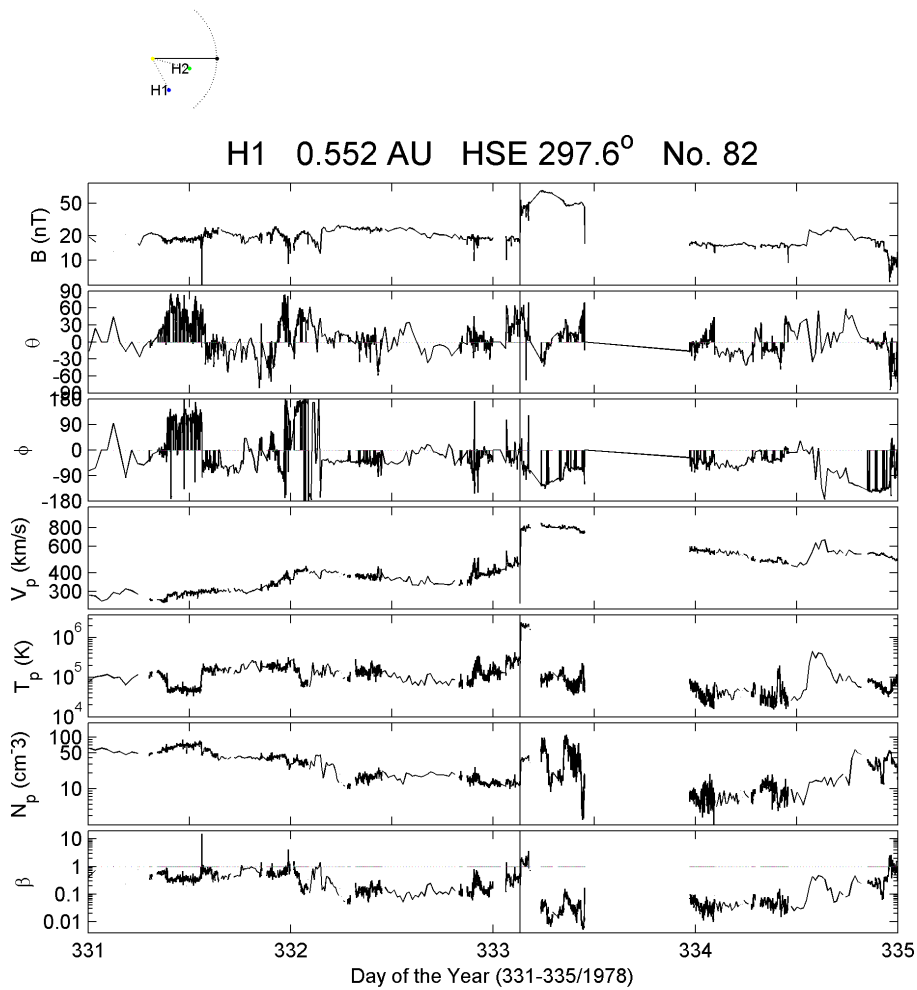


FIGURE 4.25 - H1 observation of a shock wave on DOY 333/1978, at 03:17 UT, as identified by the vertical line. The plots are given in the same sequence as in [Figure 4.10](#).



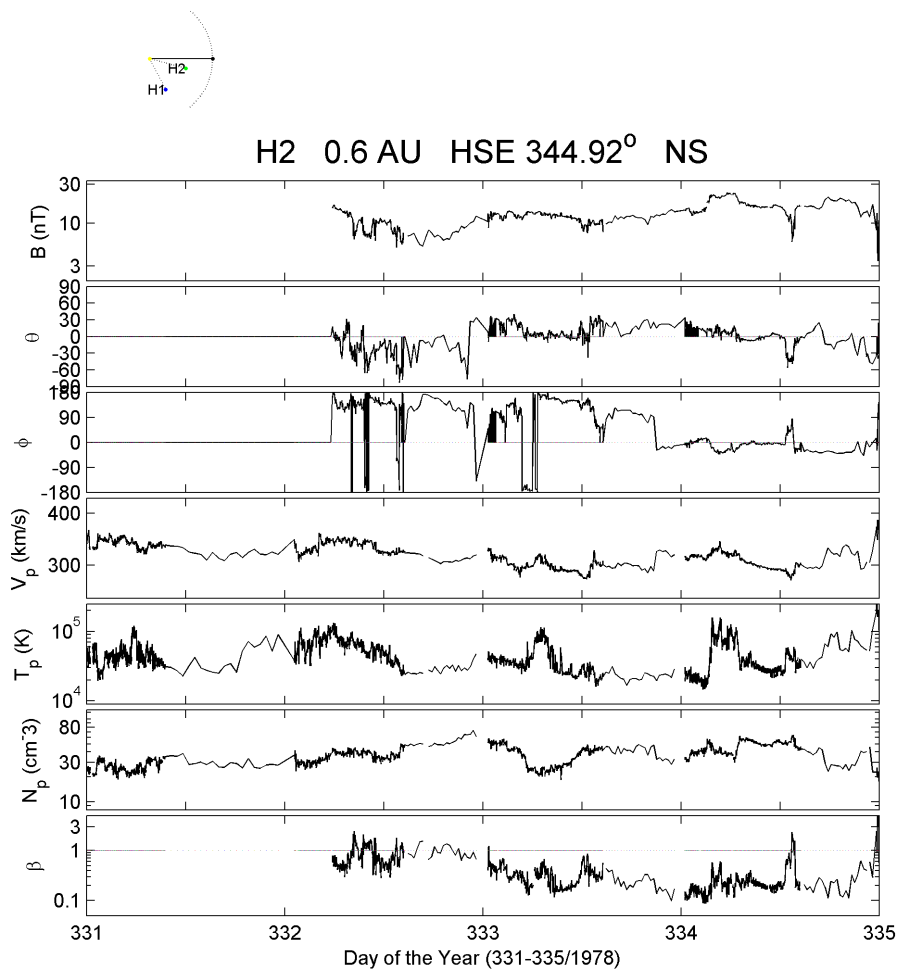


FIGURE 4.26 - H2 monitoring of the period of interest: from DOYs 331 to 335/1978. The plots are given in the same sequence as in [Figure 4.10](#). There is no shock registered by the probe, although it was operating during the corresponding period.

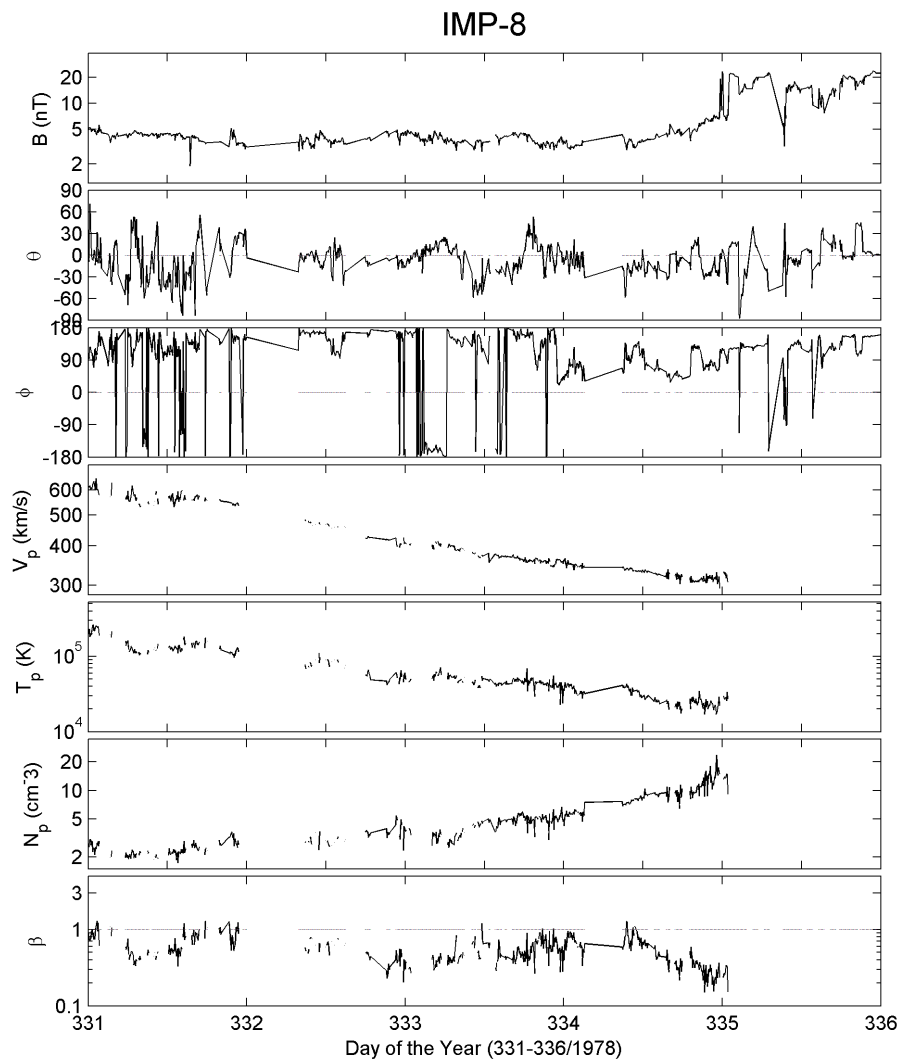


FIGURE 4.27 - IMP-8 monitoring of the period from DOYs 331 to 336/1978. The sequence of plots is the same presented in Figure 4.10. No shock was registered during the considered period by the spacecraft.

#### 4.3.2.4 Shock on DOY 312/1978

This event is another case of a single-spacecraft observation, since the only probe detecting the shock wave on DOY 312/1978 ( $SN = 331$ ), at 07:26 UT, was H2, at 0.324 AU radial distance from the Sun, and  $293.9^\circ$  in longitude from the Sun-Earth line, as shown at the top of Figure 4.28. Near the Sun, a MC was detected by the instruments onboard H2 as the driver of the shock wave. Although the time resolution for this period was quite low, the signatures for the shock and the MC are visible in all profiles of Figure 4.28.

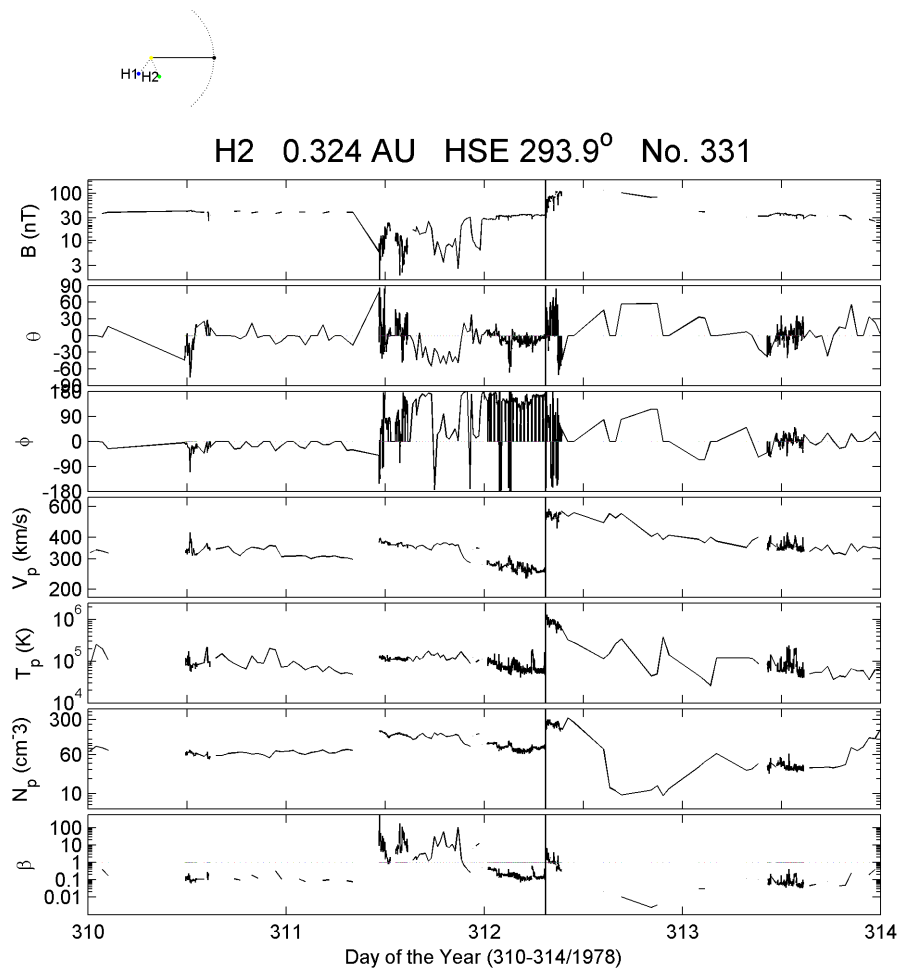


FIGURE 4.28 - H2 observation of a shock wave on DOY 312/1978, at 7:26 UT. The plots are given in the same sequence as in Figure 4.10. The shock is identified by the vertical line.

At about  $61^\circ$  in longitude away from H2 toward the far side of the sun, H1 does not register any perturbation regarding a shock wave, as it is shown in Figure 4.29. Again, a HSS is observed and seems to extend along the entire period of observation.

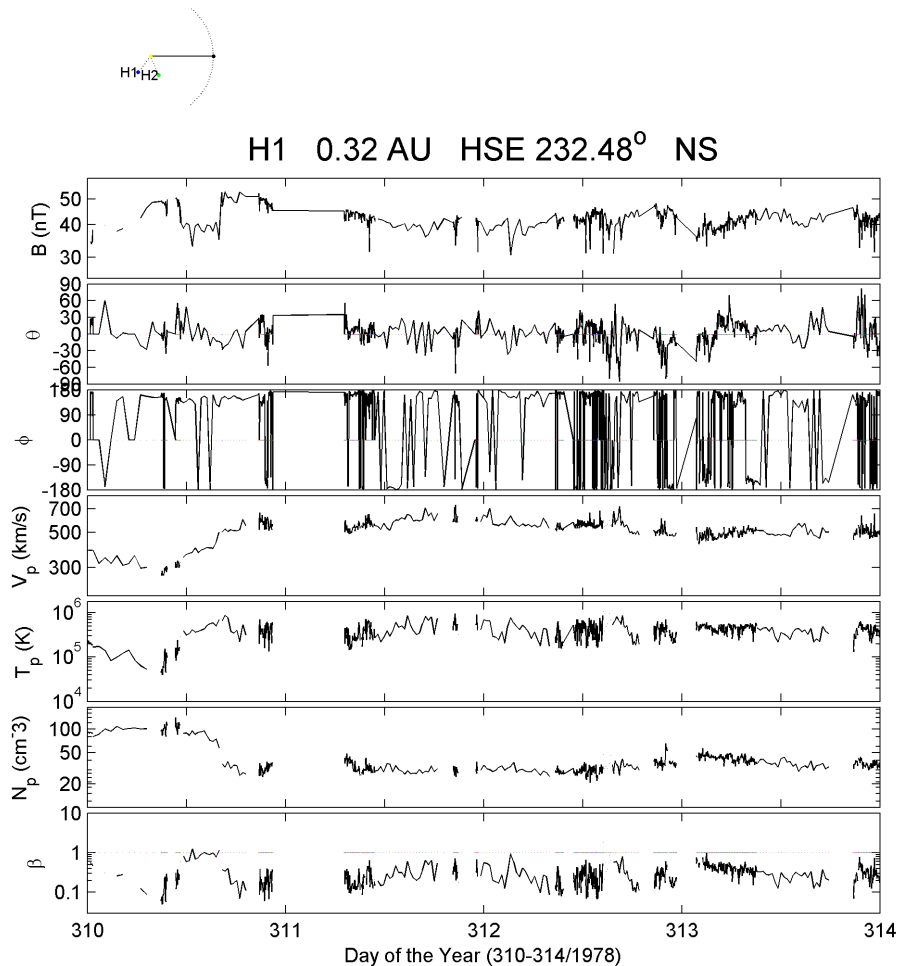


FIGURE 4.29 - H1 observation from 310 to 314 DOYs of 1978. The plots are given in the same sequence as in Figure 4.10. No shock was registered by the probe during the corresponding period.

In front of the magnetosphere, ISEE-3 was the only spacecraft available for the monitoring of this region. As one observes in Figure 4.30, there are two shocks identified for the corresponding period. However, none of them is related to the criterion we considered in the time prediction for the shock arrival. The first shock was identified at the beginning of DOY 312/1978, before H2 has detected the shock wave. Since H2 is closer to the Sun, it is not possible to establish a correspondence

between these two events. Around 4 days later, another shock was registered by ISEE-3 instruments (Figure 4.30). Nevertheless, this shock is not associated to the shock occurrence at H2 on DOY 312, at 7:26 UT, because the travel time for that shock wave would be around 2 days (considering the shock speed at H2 equal to  $683.05 \text{ km/s}$ , and  $\Delta d = 0.68 \text{ AU}$ ). The arrival time does not correspond to the observed shock at ISEE-3. In this case, we did not associate the events.

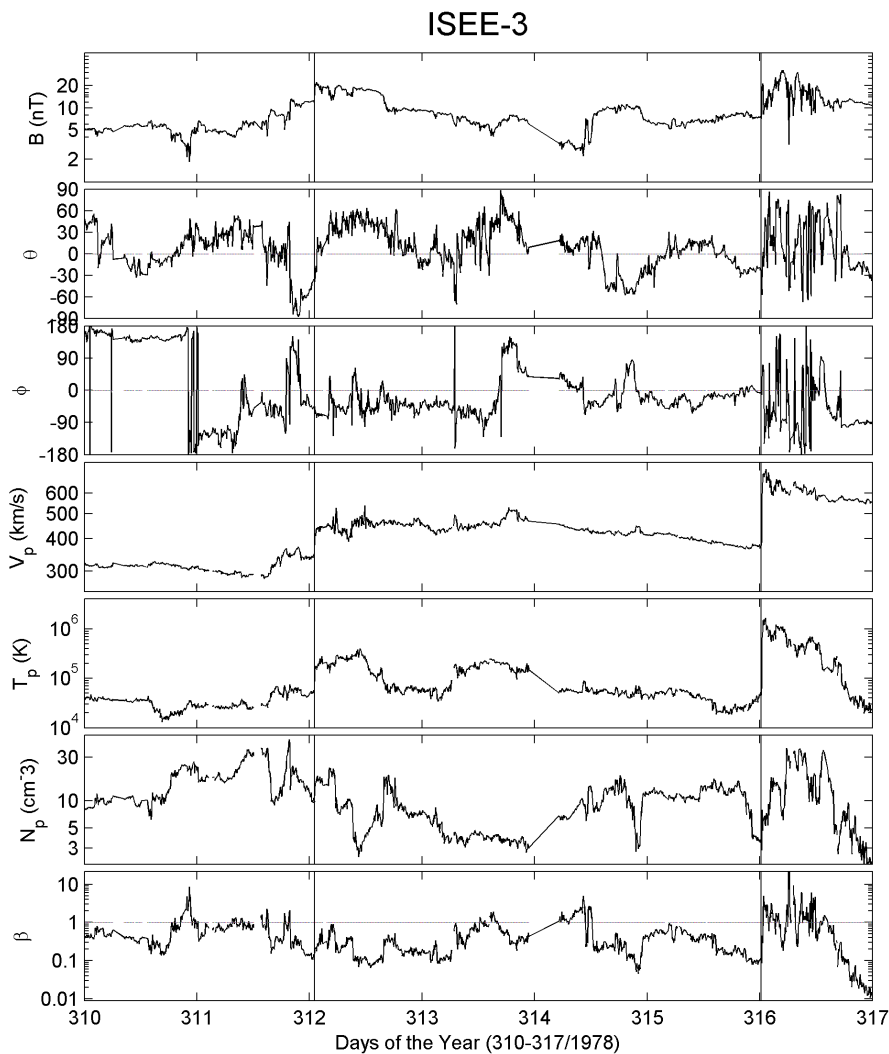


FIGURE 4.30 - ISEE-3 plasma and magnetic field monitoring of the period from DOYs 310 to 317/1978. The plots are given in the same sequence as in Figure 4.10. Two shock waves were identified during the period.

A single observation was performed during this period with the available probes/spacecraft. Based on that, the contribution from this event comes from the non-observation inside the angular distance between H1 and H2, separated by  $61^\circ$ . From the point of view of the statistics, a shock wave is not considered as expanding over more than this angle.

#### 4.3.2.5 Shock on DOY 131/1981

We will now inspect the shock wave that crossed H1 on DOY 131/1981 ( $SN = 199$ ), at 7:09 UT. It was the result of a fast MC (approximately  $1330 \text{ km/s}$ ) propagating from the Sun, as represented in [Figure 4.31](#). According to [Sheeley Jr. et al. \(1985\)](#), on the solar surface at N11E90, a M3 flare was observed one day before, at 12:08 UT, and lasted for about 7 hours. This flare was probably associated to the CME observation by H1 afterwards (DOY 130/1981, at 12:39 UT).

From [Figure 4.31](#), one can identify a very strong field inside the MC, with peak value around  $80 \text{ nT}$ . The proton speed, already high before the structure, increased considerably afterward, with the passage of the MC. In spite of the gaps presented by the data in the sheath region behind the shock, the signatures corresponding to an ICME are visible on the profiles shown in [Figure 4.31](#). These gaps do not hide the rotation on the magnetic field vector and the increase on its strength inside the MC, as well as the low values of the proton density and temperature that contribute to the low plasma beta registered.

Near Earth, as it is shown in [Figure 4.32](#), no signatures of a shock are visible in ISEE-3 magnetic field dataset. The solar wind instrument was not operating during this period. However, the magnetic field does not register any perturbation regarding a shock wave during the expected interval of time. Based on that, we conclude that the shock wave did not expand into the angular distance between H1 and ISEE-3 ( $=95.9^\circ$ ).

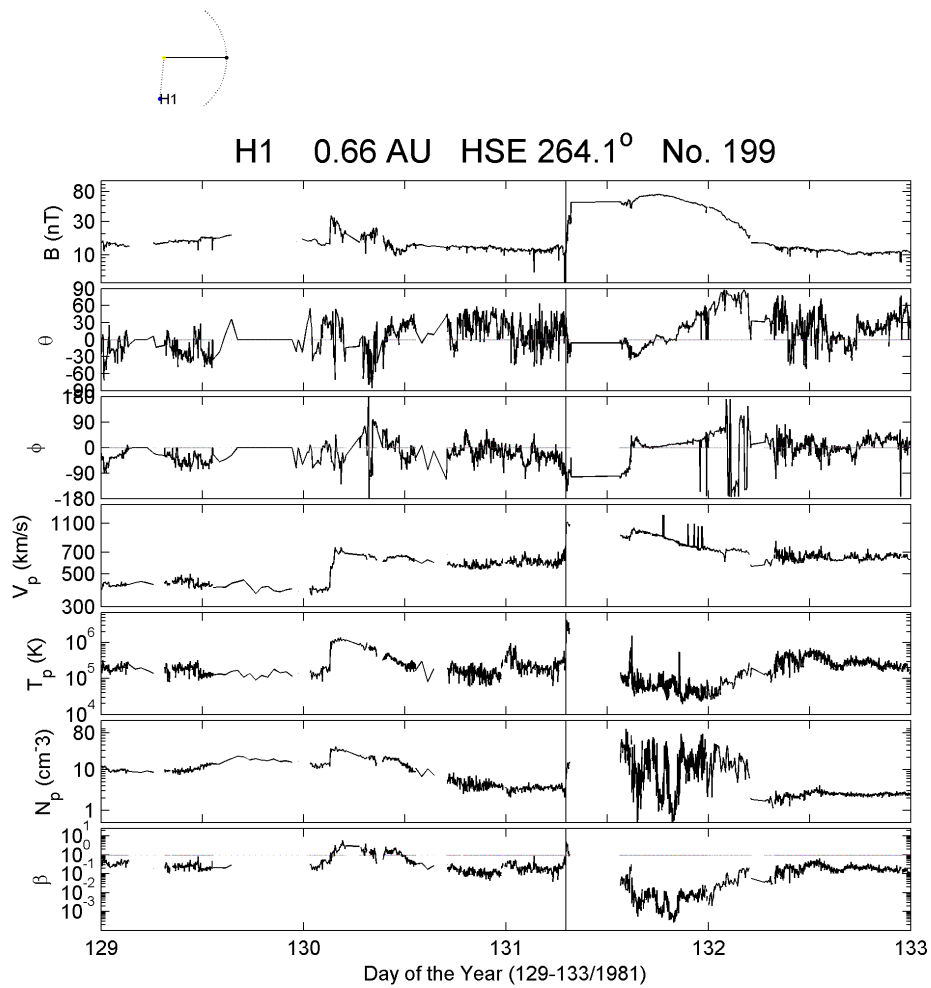


FIGURE 4.31 - H1 observation of a shock wave observed on DOY 131/1981, at 7:09 UT, as identified by the vertical line. The plots are given in the same sequence as in Figure 4.10. Note that a MC is the driver of the shock wave, as shown in the plasma and magnetic field parameter profiles.

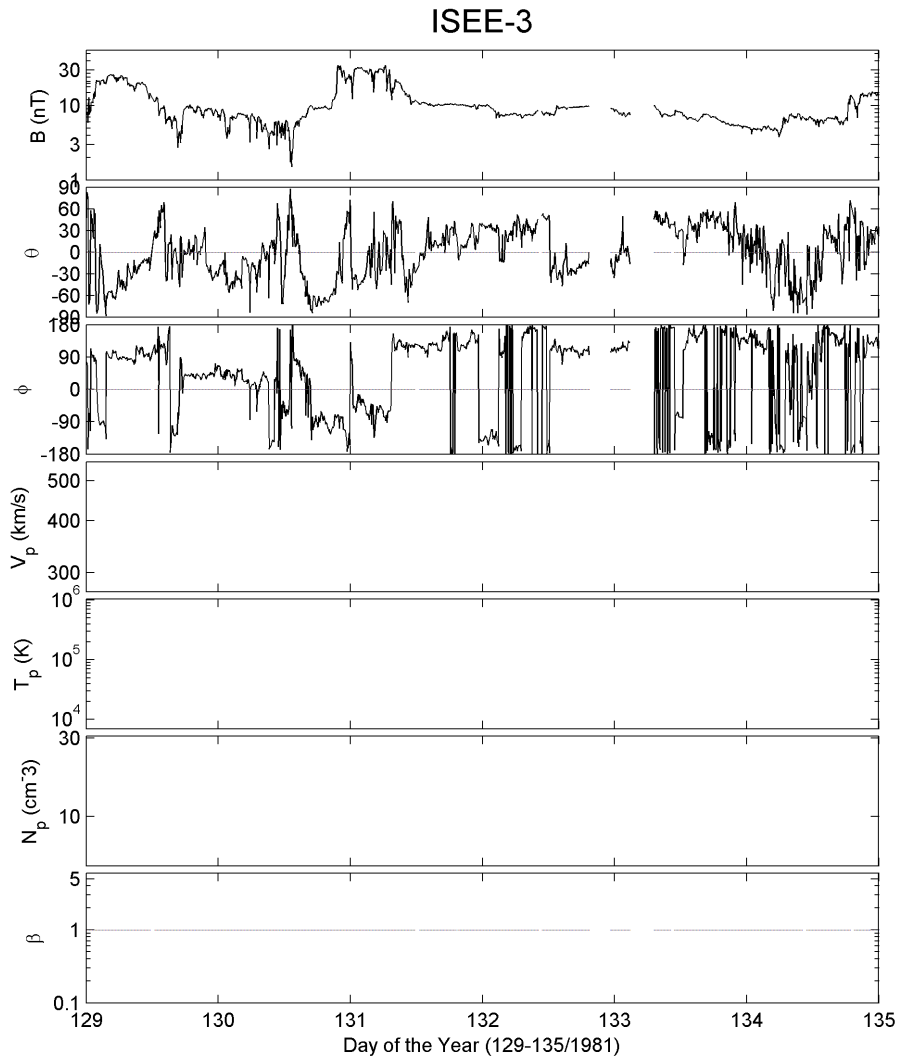


FIGURE 4.32 - ISEE-3 monitoring of the solar wind from DOY 129 to 135/1981. The plots are given in the same sequence as in Figure 4.10. No shock associated to the one at H1 was registered by the spacecraft during the corresponding period.



## 4.4 The Statistical Analysis

When the shock events were selected, we wanted to make sure we were seeing the same shock rather than to increase the number of cases studied without certainty. For this reason, the rate of “safe” events does not correspond to the total number of shocks registered during the Helios mission. The histograms shown in Figures 4.33 and 4.34 are a result of two different classes: shocks observed by a pair of probes (upper panels), and shocks observed by a single probe (lower panels) only, although another probe had sufficient data coverage to detect a shock had there been one.

Since our results depend on the orbits of the probes that might have crossed the shocks in only one part, we might expect that there are larger angles than the ones we found. This guides us to estimate the margin of error, discussed in details in [Appendix B](#).

### 4.4.1 Results

For each case, the angular separation between a pair of spacecraft represented the minimum separation we could expect a shock to extend into the IP medium. As we separated the observations according to the three different constellations, three different estimates were obtained for the whole period of observation. From the group H1 and H2, smaller angles separated the two probes for most of the time of operation, so our estimate was limited to the angles they formed during their orbits. At the beginning, we obtained a sample of angle distributions represented by the histograms in [Figure 4.33](#) as a result of the “safe” single (H1 or H2) and multi-spacecraft (H1 and H2) observations from Helios dataset only. Remember that “safe” events are those when two (or more) spacecraft had sufficient and unique data coverage to detect an event if there were one.

[Figure 4.33](#) shows in the upper panel the result of the observations from H1 and H2 simultaneously. On the other hand, the lower panel shows the result from the single-spacecraft observations from H1 or H2. This means that if only one of the probes did detect a shock, we have an entry in the histogram in the lower panel as a function of the longitudinal separation between the two Helios. In percentage, these events are represented by [Figure 4.34](#) that shows two trends in the multi-spacecraft observation.

As it was previously mentioned, H1 and H2 operated simultaneously for about 4

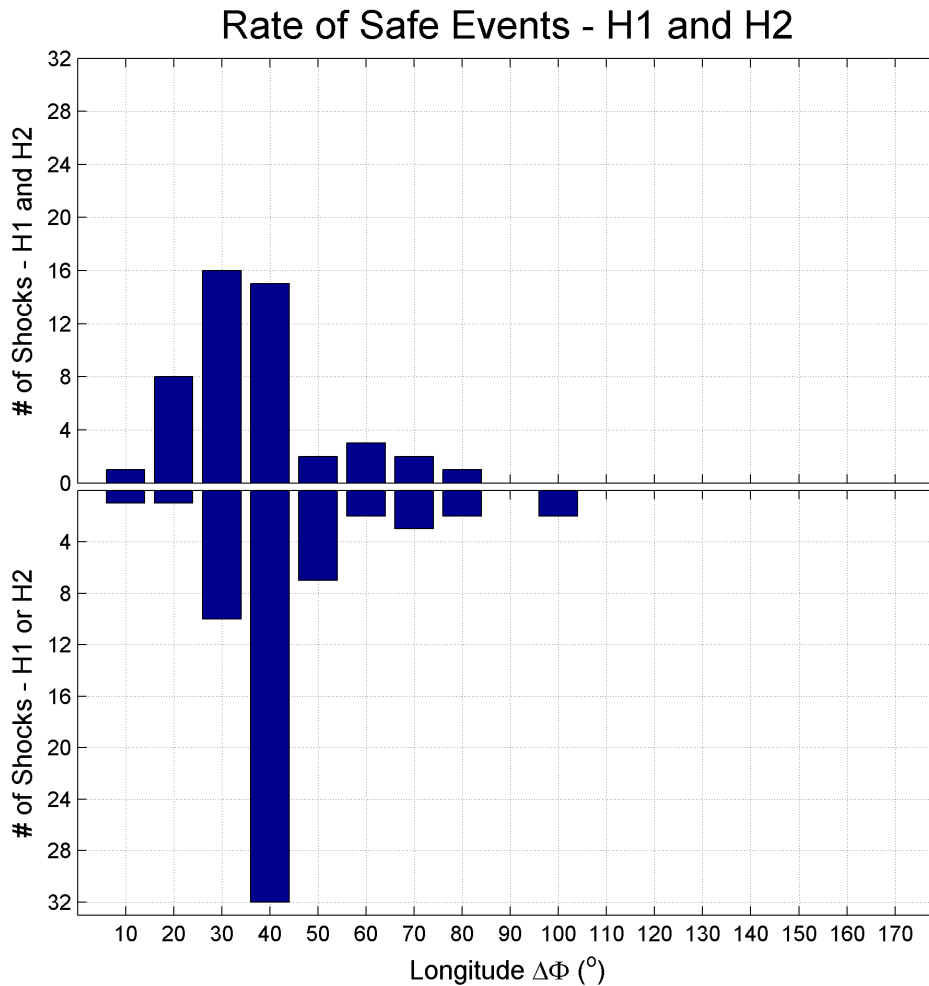


FIGURE 4.33 - Rate of “safe” events observed by H1 (dark blue) and H2 (dark red) probes as a function of the angular separation between them. In the upper panel, the multi-spacecraft observations represent the distribution of the shocks inside each angle, while the lower panel shows that most events are distributed in this class of shock (seen by a single-spacecraft in space).

years. During this period, the events observed by the two Helios probes were considerable. However, we felt the necessity to improve and extend our study. This was specially due to the dependence on the separation of the two Helios along their orbit. As one sees in [Figure 4.8](#), we were limited in longitudinal separation between them to a maximum  $130^\circ$ . This fact motivated us to include another observation point. With the inclusion of IMP-8 (the first spacecraft operating during Helios mission), and ISEE-3 (that started operating in 1979) we improved considerably our analy-

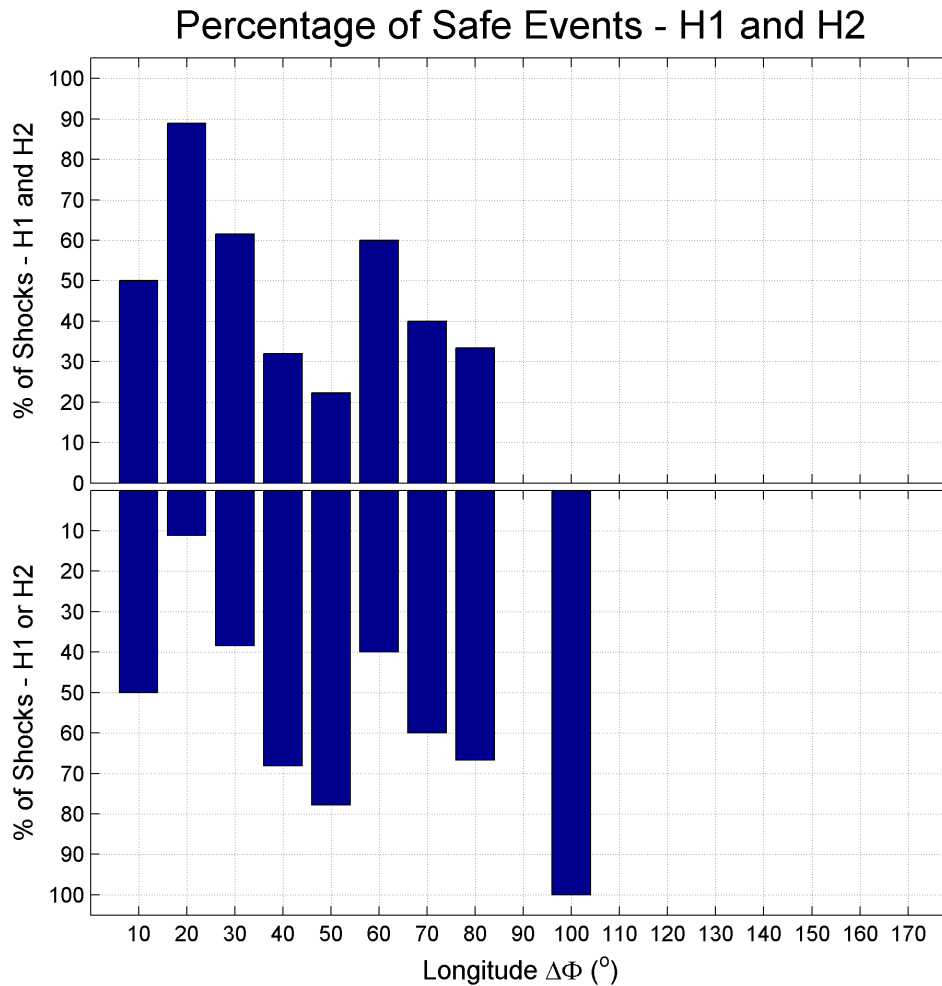


FIGURE 4.34 - Percentage of “safe” registered events by H1 (dark blue) and H2 (dark red). Again, the multi-spacecraft observations are located in the upper panel, while the single-spacecraft ones are represented by the upside down histogram (lower panel).

sis. As a result, when considering IMP-8/ISEE-3 and H1/H2 as isolated points in space, several more cases surged to improve the statistical accurateness of our sample. Even though data from ISEE-3 were more complete compared to IMP-8, the latter operated for a longer period.

From H1 and H2 observations (Table A.1) we primarily checked which shocks were observed in both spacecraft, then looked for related observations at Earth - first with IMP-8 and then with ISEE-3. When near-Earth observations were included, larger

separation angles started to appear, and new shock's extensions were revealed. The full longitudinal range of the inner heliosphere was now covered, and a new scenario for the shocks extension emerged. [Figure 4.35](#) shows the rate of safe shocks for each longitudinal separation considered, from 10 to 170°, and each column centered in a given  $\Phi$  represents the sum of all events in the interval  $I$  ( $\Phi \leq I < (\Phi + 10^\circ)$ ). This means, e.g., that the number of cases centered in 20° is a result of the number of cases in our sample where the angles were bigger than or equal to 20° and smaller than 30°, and consecutively for the other angles in the x-axis. Note that for the number of cases centered in 10°, we considered those angular separation lower than 20°.

As one can see in [Figure 4.35](#), there are bars that are in the right side up and others that are upside down for both the plots. The former corresponds to those safe events where one of the constellations (two different points in the space) had seen the same shock. Thus from the different constellations separated by colors - H1 and H2 (dark blue); H1 and IMP-8 (green); and H2 and IMP-8 (dark red) -, we have the total number of cases in each angular separation considered from the set of shocks under study. And the later ones represent those shock waves observed by only one of the three points of reference.

When considering the distribution of the shock waves according to the solar cycle variation, one can see in [Figure 4.36](#) that the number of observations is bigger at the ascending and maximum phases of the solar cycle, while, in the minimum and descending phases, the number of shocks inside the distribution is smaller. According to the distribution per year, shown in [Figure 4.36](#), bigger separations were observed closer to the maximum phase, in the ascending and descending phases as well. One case with an angular separation of 150° was detected near minimum activity.

In percentage, the distribution of our sample shows a clear trend that is illustrated by [Figure 4.37](#). As we go to larger separations, the percentage of shocks observed by two probes decreases, following a linear decrease. Even though we have some special cases with large separations, like those events at 120°, 130°, and 150°, their presence in the histogram does not influence much the trend observed for the smaller angles, where the probability of observing the same shock is higher. According to the percentage we found in [Figure 4.37](#), at  $\Delta\Phi = 90^\circ$  one has 50% of chance of seeing a shock or not in the two different points of observation.

## Rate of Safe Shocks

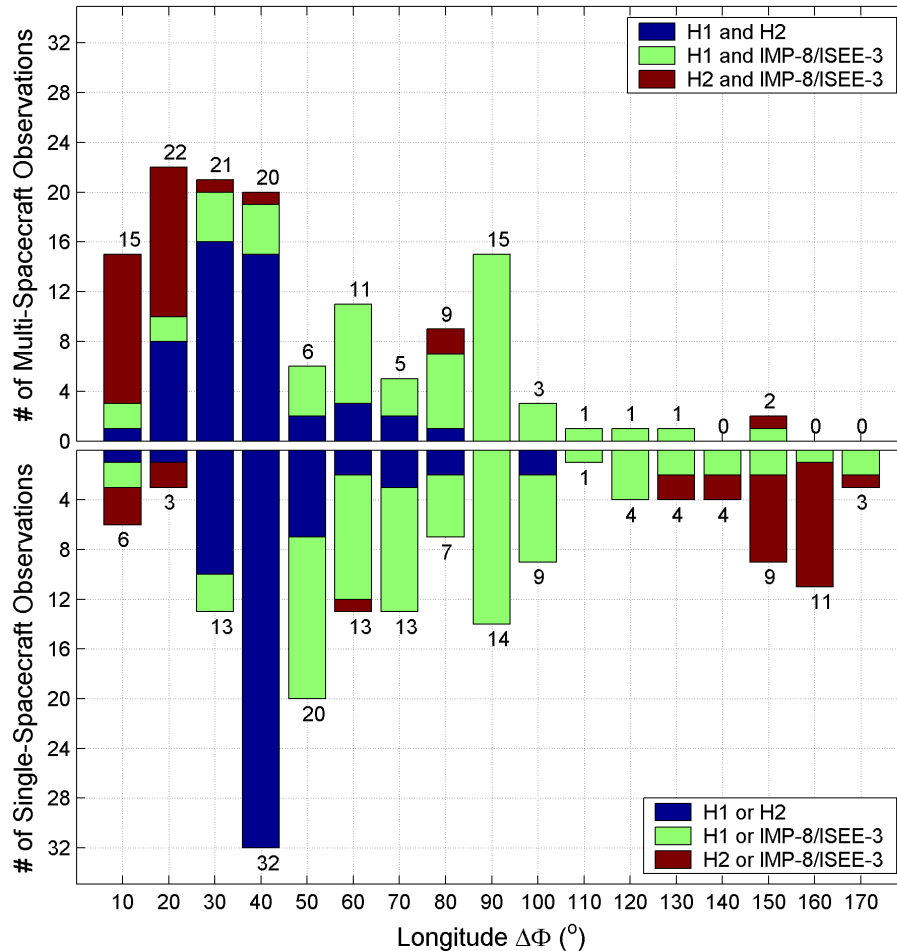


FIGURE 4.35 - Rate of shock waves observed from 1974 to 1985 (Table A.1) by at least two spacecraft (upper panel), or only one of the spacecraft (lower panel) according to the longitudinal separation ( $\Delta\Phi$ ) between the probes. The constellations are divided in three groups according to each two probes: Helios 1 and 2 (dark blue), Helios 1 and IMP-8/ISEE-3 (green), and Helios 2 and IMP-8/ISEE-3 (dark red). A total of 308 entries for the single and multi-spacecraft observations was collected. Note that increasing the angular distance between two different observational points diminishes the number of events observed by each of the constellations during the period of observation. At the top (upper panel) and at the bottom (lower panel) of each bar, one finds the total number of events in each bar according to each type of observation, multi or single-spacecraft.

SOURCE: Adapted from Lucas et al. (2009).

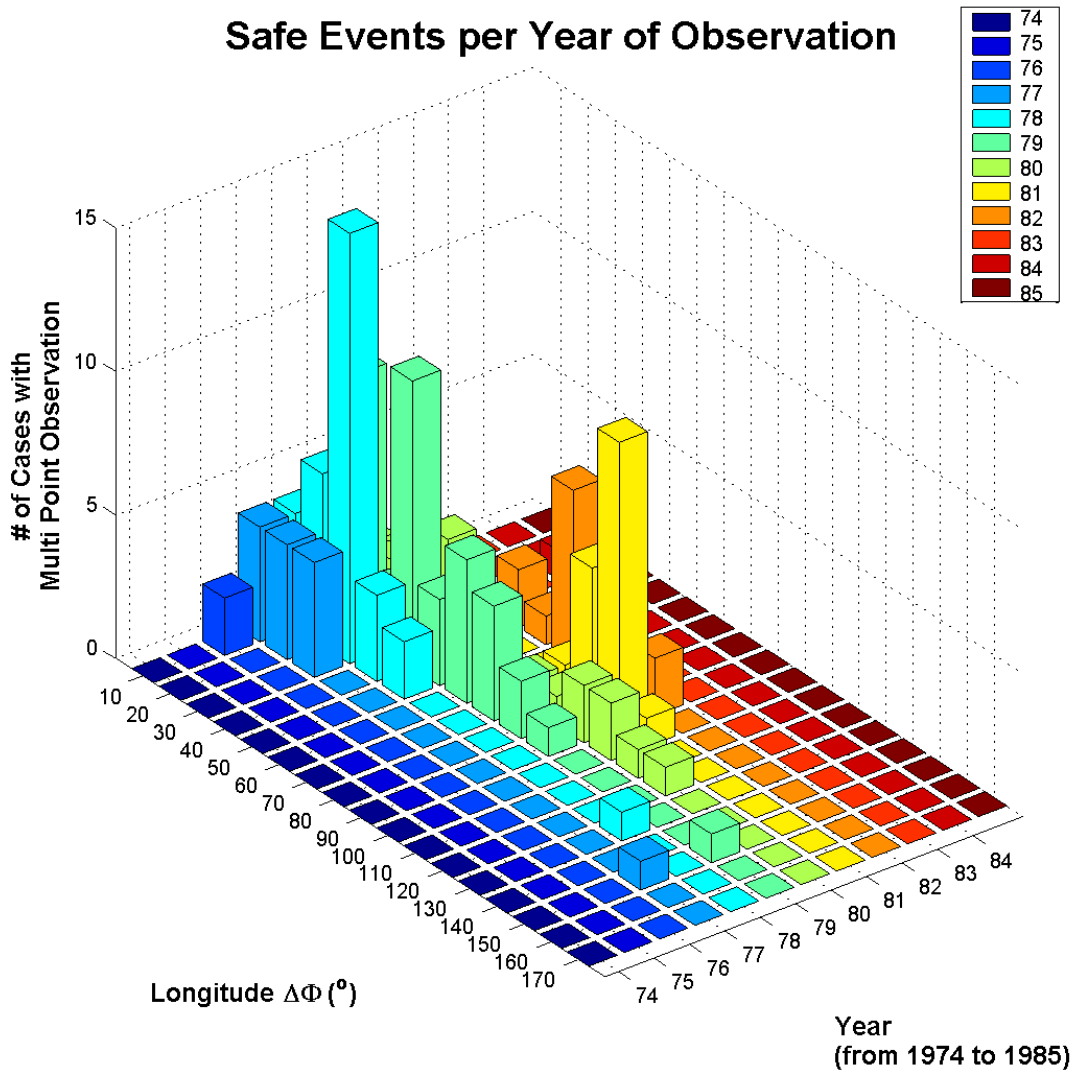


FIGURE 4.36 - Number of safe shocks distributed according to the angular extension and year of observation. At the ascending phase and maximum of the solar cycle, the number of shocks is bigger compared to the years of minimum or descending phase.

The critical interval for the percentage of shocks (Figure 4.37) was determined by using the test of proportions analysis, as described in details in Appendix B. Figure 4.38 shows the error bars that represent a 95% confidence intervals for each angular separation. The estimated value is more accurate as we have a larger number of cases from the sample, like it is shown in Figure 4.38. A critical value at  $\Delta\Phi = 110^\circ$  is found as we have just two cases in this category.

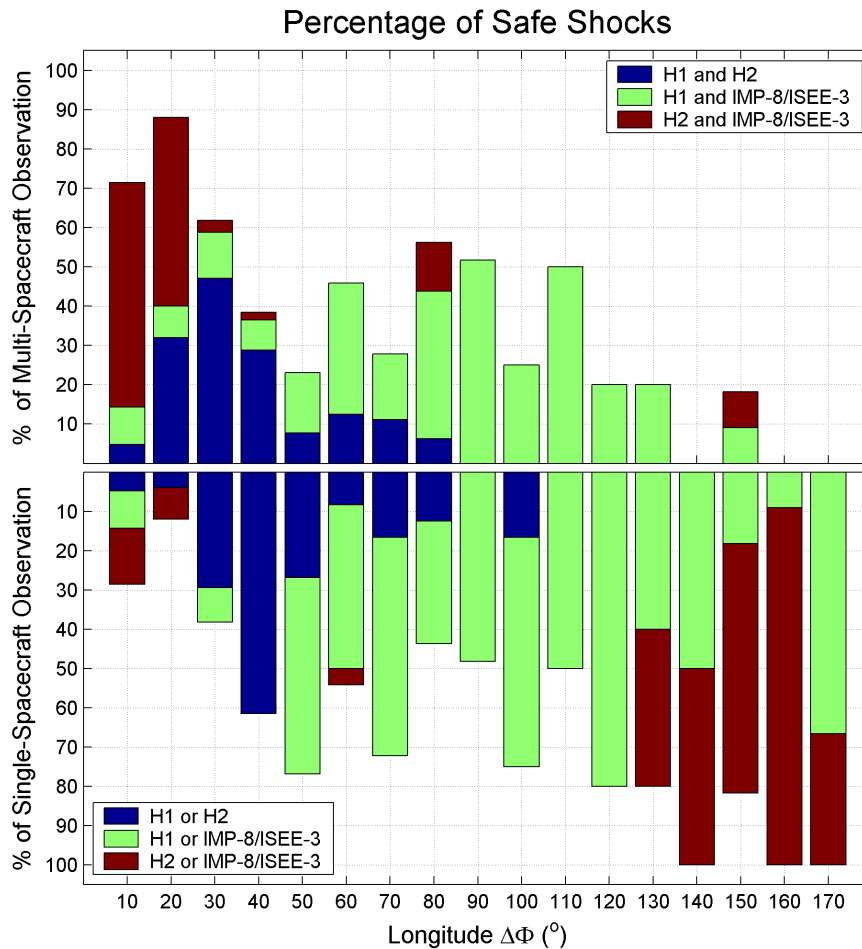


FIGURE 4.37 - The percentage of shock waves observed into a longitudinal angle of separation between different probes shows that there is a bigger tendency for observing shocks in smaller angles ( $\Phi$ ). Helios 1 and 2 were not separated in more than  $120^\circ$  of longitude between them. In  $\Delta\Phi = 90^\circ$ , the same percentage is found for observing or not the shocks in two different points. This means that there is a cutoff value at this angle, so one can expect with the same likelihood a shock expanding in longitude until  $90^\circ$  or not expanding until this angle.

SOURCE: Adapted from [Lucas et al. \(2009\)](#).

## 4.5 Conclusions

We have studied shock angular extension in the inner heliosphere using observations from H1, H2, and IMP-8/ISEE-3 spacecraft. There is a clear trend showing that there are less shocks detected in multi-spacecraft as we increase the angular separation

## Percentage of Safe Events with 95% of Confidence

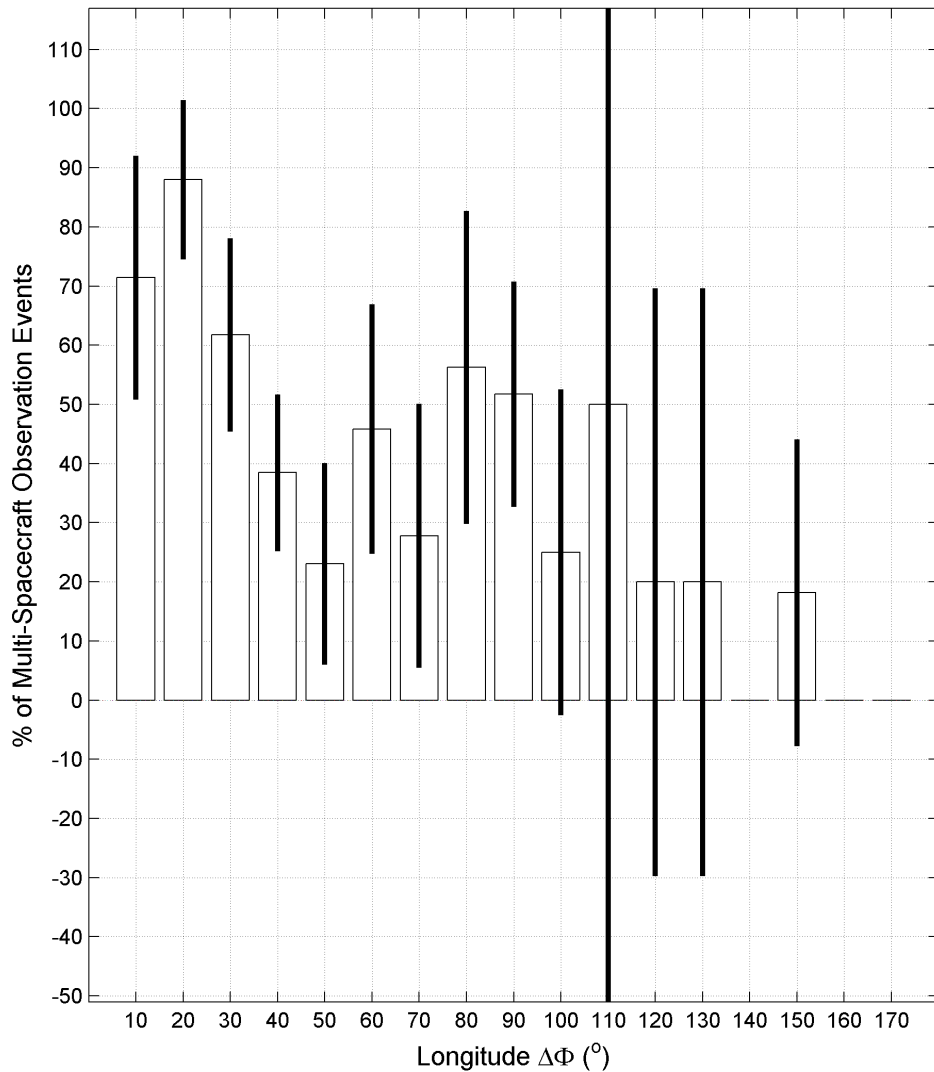


FIGURE 4.38 - This is the same plot as shown before in the percentage of shocks (upper panel of [Figure 4.37](#)). The error margin for the percentage of shocks observed by multi-spacecraft into each longitudinal separation as seen by Helios-1,2 and IMP-8/ISEE-3. As  $\Delta\Phi$  increases, the uncertainty also does. Observe that in  $\Delta\Phi = 110^\circ$  the biggest error for our estimate is found. That is because only two events, as seen in [Figure 4.35](#), were registered for that angle: one was detected by a pair of probes, and the other by a single probe.

between them, according to the statistical results based on the observations in the inner heliosphere.

For longitudinal separation of the order of  $90^\circ$  we found that a shock has 50% of



chance to be observed by both probes and the same likelihood for not being observed by two spacecraft at the same time, when the angle between them is around  $90^\circ$ . In practice, this means that when a CME is observed at the solar limb, for example, there is 50% of probability of seeing the shock driven by the ICME at Earth.

When considering the error on the estimate, one finds that, as we extend the separation of probes to bigger angles, due to the lack of observations, one increases the error in the likelihood to observe a shock.

Further investigation is needed to evaluate those cases with large ( $> 110^\circ$ ) separation once we are handling with structures traveling in a medium filled with many types of structures interacting among themselves with different topologies of magnetic field.

Can a shock be deflected by the presence of the Heliospheric Current Sheet (HCS) as it extends into the IP medium? Could the HCS be so strongly formed as to avoid the passage of a huge and massive structure like an ICME? Simulations have been carried out in order to understand how the HCS plays a role on the propagation of structures in the IP medium. This could help to understand those cases like the present one where shocks do not extend into small angles as some of the observations have shown us. In the work of [Xie et al. \(2006\)](#), a simulation with 180 IP shocks showed that the shock travel time to 1  $AU$  may be affected by the presence of the HCS.

Another point that is fundamental comes from the definition of shock waves. They are only formed if the driving structure moves faster than the magnetosonic speed ( $V_{MS}$ ) relative to the ambient solar wind, where  $V_{MS}$  is a combination of the local sound ( $C_S$ ) and Alfvénic ( $V_A$ ) speeds:  $V_{MS} = \sqrt{C_S^2 + V_A^2}$  of the propagating structure. It might happen that the Alfvén speed was extremely large in the medium so that the shock could not be formed there. Thus, a shock front might not be continuous, depending on local solar wind conditions.

Most of the results presented in this chapter were published in [Lucas et al. \(2009\)](#).



## 5 EXTENSION OF MAGNETIC CLOUDS IN THE INNER HELIOSPHERE BY MULTI-SPACECRAFT OBSERVATIONS

### 5.1 Introduction to the Chapter

A large number of magnetic clouds was observed during the operation time of the Helios mission. Among the set of shocks driven by ICMEs, identified during this time, some of them had a magnetic cloud observed by at least one of the probes, Helios 1 and/or Helios 2. Others were observed by more than one probe/spacecraft contributing for a detailed study of the extension of these MCs in the inner heliosphere. In the present work, we compare the interplanetary features of some magnetic clouds that drove shock waves in the inner heliosphere. By using the Minimum Variance Analysis one gets the informations of the cloud's axis, so that the direction of the magnetic cloud in two different points can be inferred. For those magnetic clouds observed by only one of the probes, the cloud's axis could be an explanation for the fact that there was no observation at the two probes. Highly inclined MCs are less likely to be observed by two probes that are close to the ecliptic plane.

### 5.2 Observation of Magnetic Clouds

Among the group of shock waves identified by Helios (see Chapter 4, Figure 4.35), some of them were driven by MCs. In the subgroup of MCs, the classification is based on the number of spacecraft that detected the shock driven by the MC: multi or single-spacecraft.

Figure 5.1 shows the groups of shock waves according to the constellation that has provided the measurements for the correspondent periods. In the upper and lower panels, the three different constellations are separated by color: dark blue for H1 and H2 monitoring; green, for H1 and IMP-8/ISEE-3; and dark red, for H2 and IMP-8/ISEE-3 observations.

Interplanetary shocks identified by more than one probe, where magnetic clouds were identified as the driver of at least one of them, are represented in the upper histogram in Figure 5.1. This does not mean that both probes observed the magnetic cloud in all the cases, but the MC was observed by at least one of the probes as the driver of a shock. These numbers are given in percentages, as shown in Figure 5.2, also as a function of  $\Delta\Phi$ . A 100% of the distribution in each  $\Delta\Phi$  is the sum of the right side up and upside down number of observations. So each complet column,

from the lower and upper panels of a given  $\Delta\Phi$ , is an independent sample of the observations, when probes were separated by  $\Delta\Phi$ .

A subset of the group of shock waves identified as being driven by MCs is formed, corresponding to those MCs observed by at least two of the probes. On the other hand, those observed by only one probe/spacecraft were classified in the category of single-spacecraft MCs. In this sense, one has the idea of the extension of the MC related shock they propagated when traveling in the IP medium. For those cases when two or more spacecraft observed the same magnetic cloud, we have an estimate of the observed extension of the MCs in longitude. These cases are represented in [Figure 5.3](#), and the number of MCs inside each angular separation between the probes ( $\Delta\Phi$ ) can be seen in the histogram.

As shown in [Figure 5.3](#), a MC can extend in longitudinal angles as large as  $90^\circ$ , according to the multi-spacecraft observations. Since we used observations from the three different available observation points in space, we get the monitoring of the inner heliosphere during one solar cycle for observing MCs traveling and driving shocks. According to [Figures 5.3](#) and [5.1](#), composed by a set of 97 entries for the single and multi-spacecraft observations, MCs are smaller in extension compared to shock waves driven by them (when comparing to [Figure 4.37](#)). This was already suggested by [Borrini et al. \(1982\)](#) and later confirmed based on the number of shocks, about 0.3 per day, crossing an observer in the IP medium during solar maximum ([WEBB; HOWARD, 1994](#)). In this sense, we may conclude that an “in situ” observer is hit by only one out of ten ICME/shocks released at the Sun. This might be equal to or less than the chance for the set of MCs - since they are a subset of the big group of ICMEs.

As suggested by [Schwenn \(2006\)](#), the average shock shell covers about  $100^\circ$ , considering the one tenth of the full solid cone angle ( $= 4\pi$ ). As one may deduce, this average angle for shock extent exceeds significantly the one of the average angular size of the CMEs of about  $45^\circ$  ([HOWARD et al., 1985](#); [ST. CYR et al., 2000](#)). The conclusion is that shock fronts extend much further out in space than their drivers, the ejecta clouds. This explains why an “in situ” observer finds large numbers of shocks followed by sheath plasma only, with no associated ejecta cloud ([SCHWENN, 2006](#)). This might also explain why in many of the multi-spacecraft observations of shock waves only one spacecraft registered the signatures of MCs.

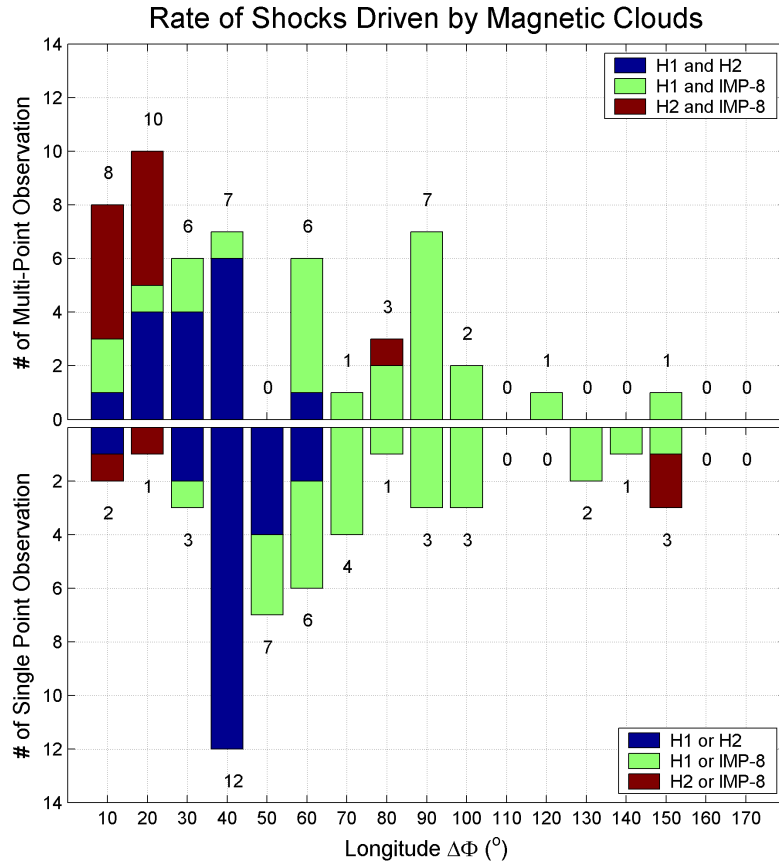


FIGURE 5.1 - Number of shock waves detected at two spacecraft, where MCs were identified at minimum one spacecraft (upper panel) and shocks detected by only one spacecraft and MC as well (lower panel). The three different constellations are separated by colors: H1 and H2 (dark blue), H1 and IMP-8/ISEE-3 (green), and H2 and IMP-8/ISEE-3 (dark red).

The sizes of MCs observed near Earth's orbit cannot be considered to be typical of those that might be observed closer to the Sun. Furthermore, the spacecraft's trajectory through a MC influences the observed duration time and thus its apparent size.

We concentrate our choice of MCs in the Helios data on solar wind events associated with the basic properties of a MC, i.e., a smooth coherent directional change of the magnetic field vector on time scales of several hours to days. These changes can be identified in the magnetic field components  $B_x$ ,  $B_y$ ,  $B_z$  which are the Cartesian components of the IMF in solar ecliptic coordinates (GSE), and in the latitudinal and longitudinal excursions of the magnetic field vector, i.e., by variations in the angles

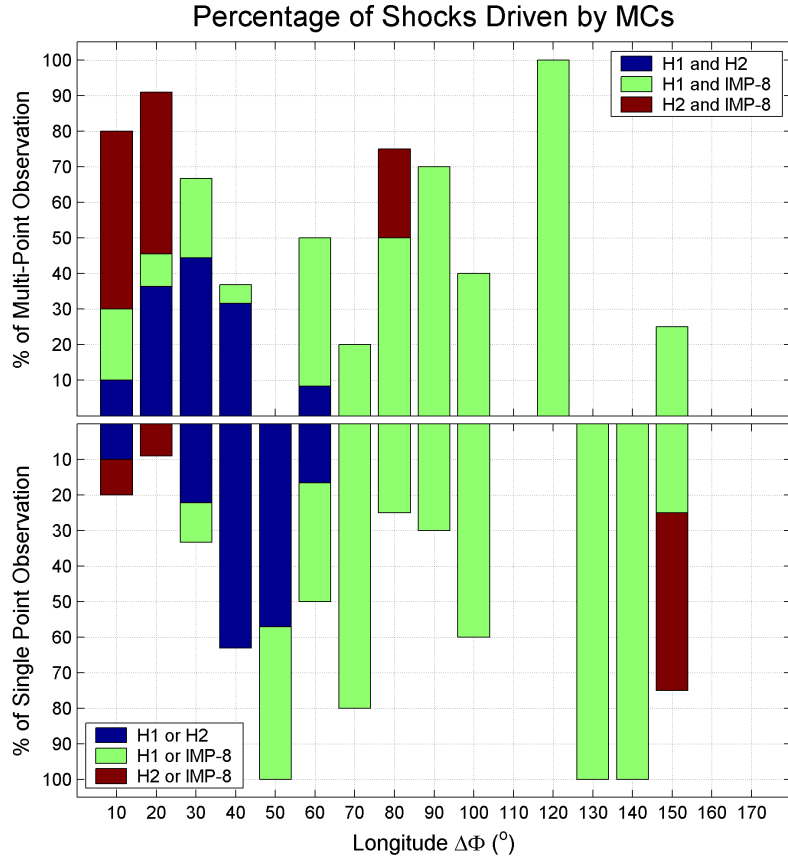


FIGURE 5.2 - Percentage of shock waves driven by MCs in multi-spacecraft (upper panel) and single-spacecraft (lower panel) observations. The legend corresponds to the same presented in Figure 5.1.

$\theta$  and  $\phi$ .  $B_x$  points from the spacecraft toward the Sun,  $B_y$  points in the ecliptic plane normal to  $B_x$  toward the East, and  $B_z$  points normal to the ecliptic, toward the ecliptic north pole. Accordingly,  $\theta$  and  $\phi$  are the magnetic field's inclination ( $\theta = 90^\circ \equiv \text{N}$ ;  $\theta = -90^\circ \equiv \text{S}$ ) and azimuthal ( $\phi = 0^\circ \equiv \text{sunward direction}$ ,  $\phi = 90^\circ \equiv \text{E}$ ;  $\phi = -90^\circ \equiv \text{W}$ ) angles (BOTHMER; SCHWENN, 1998).

Based on these criteria we investigate the plots of plasma and magnetic field data of Helios spacecraft taking into account all events in which variations in the magnetic field direction occurred in  $\theta$  and  $\phi$  and in the cartesian components over time intervals of several hours. We included events with irregular or weak field variations and variations at sector boundaries. All events were then investigated with the minimum variance analysis (MVA) (SONNERUP; CAHILL JR., 1967) to identify smooth rotations of the magnetic field vector on time scales of the order of several

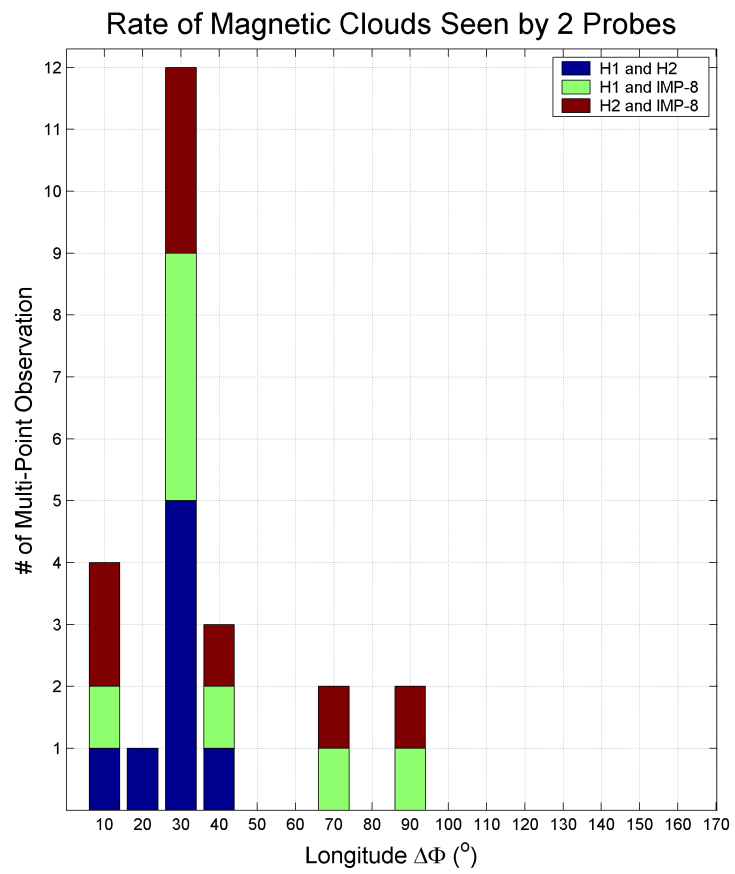


FIGURE 5.3 - Rate of Magnetic Clouds seen by at least two spacecraft according to the separation  $\Delta\Phi$  between the probes/spacecraft. The legend corresponds to the same presented in Figure 5.1.

hours. The MVA-method, described on details in Appendix C, can be accurately applied for directional changes of the magnetic field vector exceeding  $30^\circ$  (BURLAGA; BEHANNON, 1982). Thus, MCs were identified by a smooth rotation of the field direction in the plane of maximum variance ( $B_1^* \times B_2^*$ , where  $B_1^*$  is the component of maximum variance, and  $B_2^*$  is the intermediate variance component), if the plasma temperature was lower and the magnetic field strength higher than in the surrounding solar wind. Finally, the error criterion of the minimum variance method was satisfied ( $\lambda_2/\lambda_3 > 2$ , where  $\lambda_2$  and  $\lambda_3$  correspond to the eigenvalues of the directions of intermediate ( $B_2^*$ ) and minimum variance ( $B_3^*$ ) - see Appendix C).

There is an uncertainty when defining the boundaries of MCs with dependence on the choice of the more important parameters to define these types of structure. In our case, we considered the boundaries based on the lower values of plasma beta ( $\beta < 0.1$ ) and the sudden increase in the magnetic field strength also followed by a rotation in the magnetic field vector. Sometimes, inside the structure one can identify the decrease in the protons temperature, but this is not always clearly visible in all cases. That is probably due to the place the probe crosses the structure. With these ideas, one considers the front part of the MC based on the abrupt decrease of the plasma beta and consecutive increase in the magnetic field strength, also marked by a rotation on the magnetic field. Another very important parameter that identifies the cloud's front boundary is the density discontinuity. The rear part is chosen based on the plasma beta again, this time characterized by an abrupt increase in its values as we are moving out from the high magnetic pressure region. Furthermore, the rotation, strength and smoothness of the magnetic field at the rear part of the MC start behaving like in the normal solar wind.

### 5.3 Magnetic Clouds seen by Multi-Points

Some MCs were observed by multi-spacecraft (Figure 5.3) and this enabled the study of their extension into space. It is widely assumed that these structures are smaller than the shocks they drive in the medium. In this sense, one can compare the longitudinal extension of shock waves with the MC extent in longitude.

In the sequence of this section, some of the MCs observed by at least two spacecraft are described on details. Their main characteristics compared with the ones at the other probe are pointed out. Furthermore, the rotation on the magnetic field, identified through MVA technique, illustrates the smooth and long-duration turning of



the magnetic field vector  $\vec{B}$ .

### 5.3.1 MC observed on DOY 29/1977 by H1 and H2

The same MC seems to have been observed by H1, H2 and IMP-8 simultaneously. [Figure 5.4](#) shows the visible signatures for a very clear magnetic cloud as the instruments onboard H1 detected. The inclination angle of the magnetic field turns from  $90^\circ$  to  $0^\circ$ , with  $\phi = 90^\circ$ , inside the magnetic cloud, characterized by a decrease in the protons density and temperature, as well as in the plasma beta. The strong rotation identified by  $\theta$  corresponds to a strong rotation in  $B_z$  component, from North to South. The angle  $\phi$  ranges from  $90^\circ$  to  $0^\circ$ , that corresponds to positive  $B_y$  component. According to the classification of MCs of [Bothmer and Schwenn \(1998\)](#), shown in [Figure 2.14](#), this MC is classified as NES, parallel to the ecliptic plane.

The magnetic field magnitude peaks were around  $30 nT$  after the sheath region that lasted for less than half a day, as one observes in [Figure 5.4](#). This MC seems to have interacted strongly with the ambient solar wind due to the strong intensity of the magnetic field observed at the beginning of the cloud, which certainly deformed the magnetic field lines carried by it.

Around three days ahead the MC, a HSS was observed by the measurements from H1. According to the representation of the probes location in the inner heliosphere, at the top of [Figures 5.4, 5.5, and 5.6](#), the HSS first passed through H1 ([Figure 5.4](#)) and around three days later by H2, as [Figure 5.5](#) shows. In H2 profiles it is clear how the HSS changes the speed of the medium, increasing its bulk value and avoiding the shock formation due to the propagation of the MC in the inner heliosphere. The HSS seems to squeeze the MC somehow, so that it is only observed almost one day after the weak shock wave is formed. Still the signatures of the magnetic cloud are not clearly visible like they are in H1 measurements.

In [Figure 5.6](#) one cannot identify clearly the rotation on the magnetic field components. In  $B_y$  the rotation seems to be only in the negative side. This is probably due to the MC orientation, parallel to the ecliptic plane. Nevertheless, let us assume that this MC is a SWN cloud, considering the small rotation in  $B_z$  component.

From IMP-8 observation, shown in [Figure 5.7](#), the similarities between the measurements from the two probes/spacecraft (H2 and IMP-8) separated by almost  $10^\circ$  are observed. The HSS is also seen by the increase in proton speed and temperature,

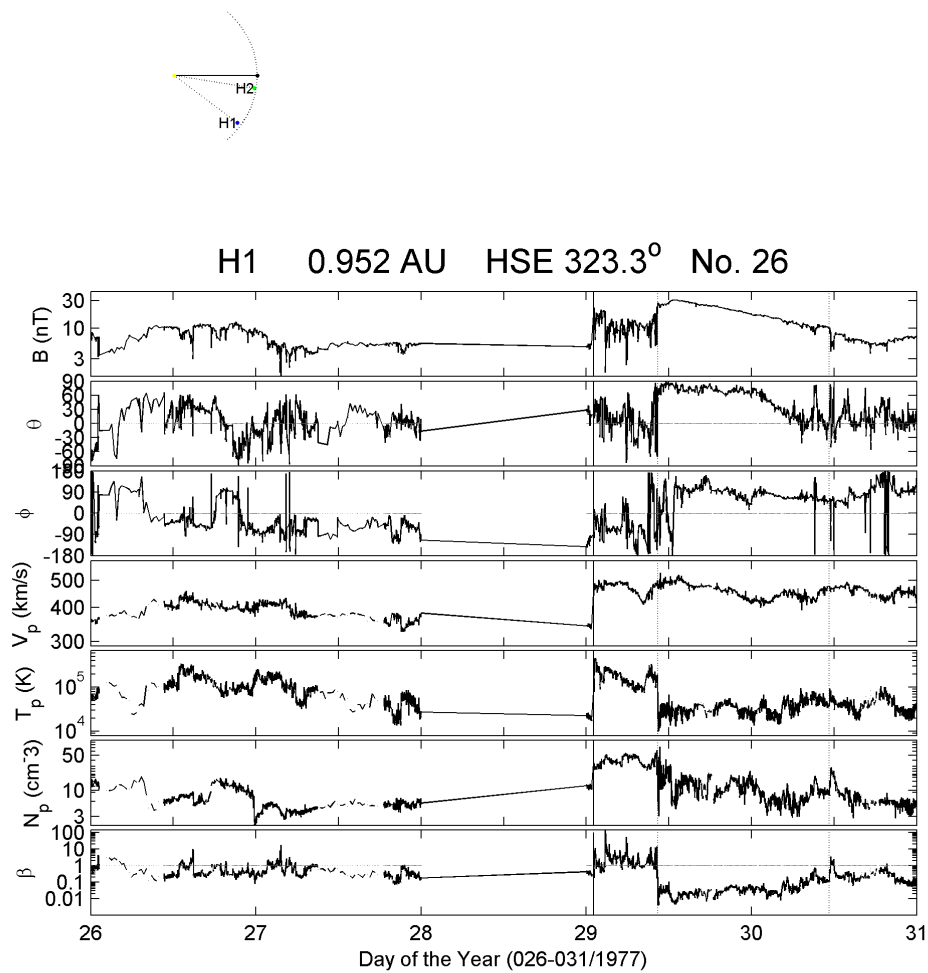
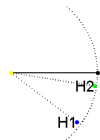


FIGURE 5.4 - H1 observation of a MC from DOY 29/1977, at 10:22 UT, to DOY 30, at 11:16 UT. The plots give, from top to bottom, the profiles of the magnetic field strength, and inclination and azimuthal angles, the protons speed, temperature and density, and the plasma beta, respectively. The vertical continuous line identifies the shock wave, driven by the MC whose boundaries are represented by the dotted lines. Note that at the first half of DOY 026 a HSS is identified by the plasma and magnetic field parameters.



H2 0.978 AU HSE 351.1° No. 277

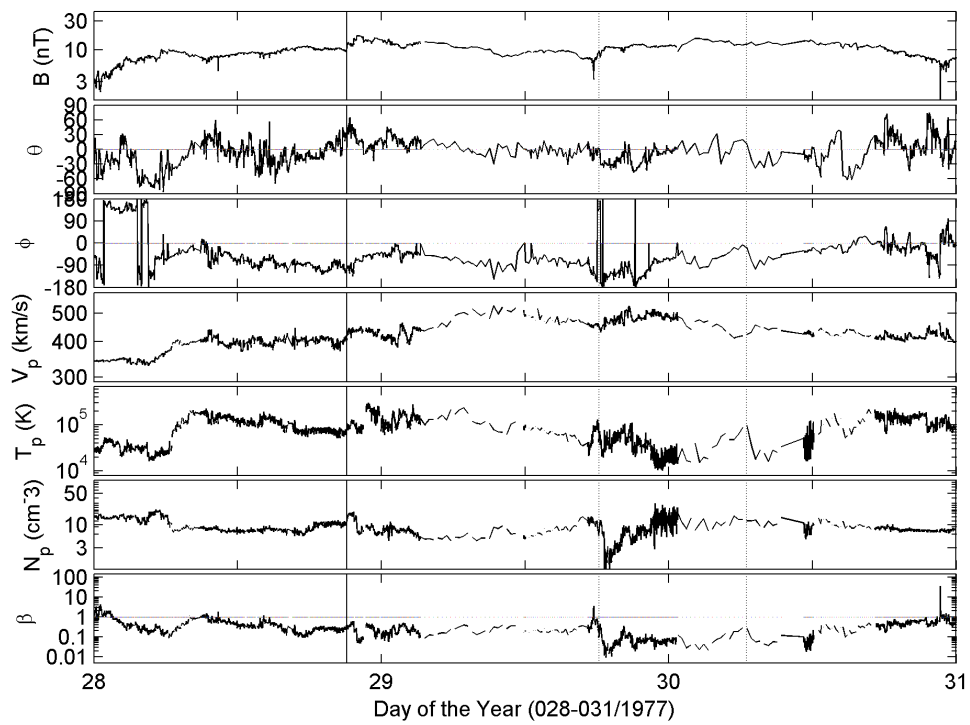


FIGURE 5.5 - H2 observation of a MC from DOY 029/1977, at 18:11 UT, to DOY 030/1977, at 06:31 UT. Meaning similar to Figure 5.4.

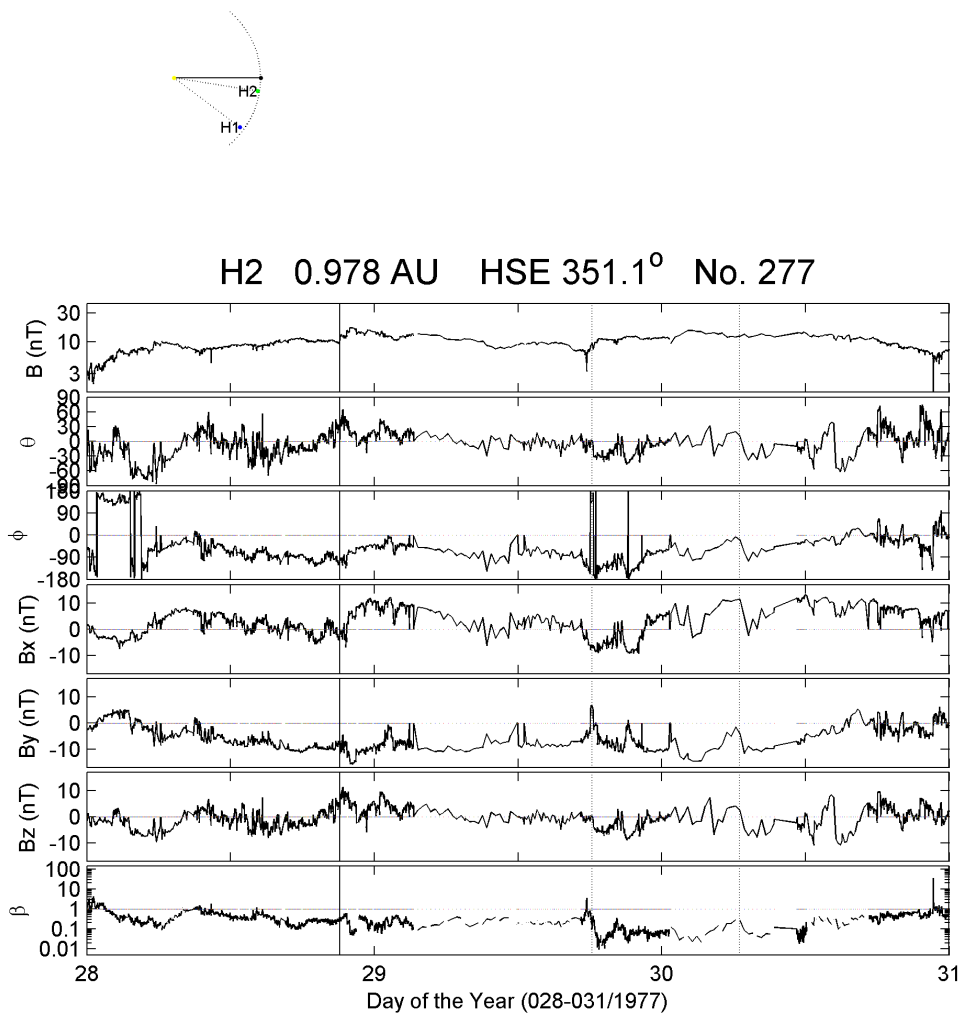


FIGURE 5.6 - H2 magnetic field data for the MC observed on DOY 29-30/1977. The plots give, from top to bottom, the magnetic field strength, inclination and azimuthal angles, and components  $B_x$ ,  $B_y$  and  $B_z$ , followed by the plasma beta, respectively. The vertical continuous line identifies the shock wave, driven by the MC whose boundaries are represented by the dotted lines.

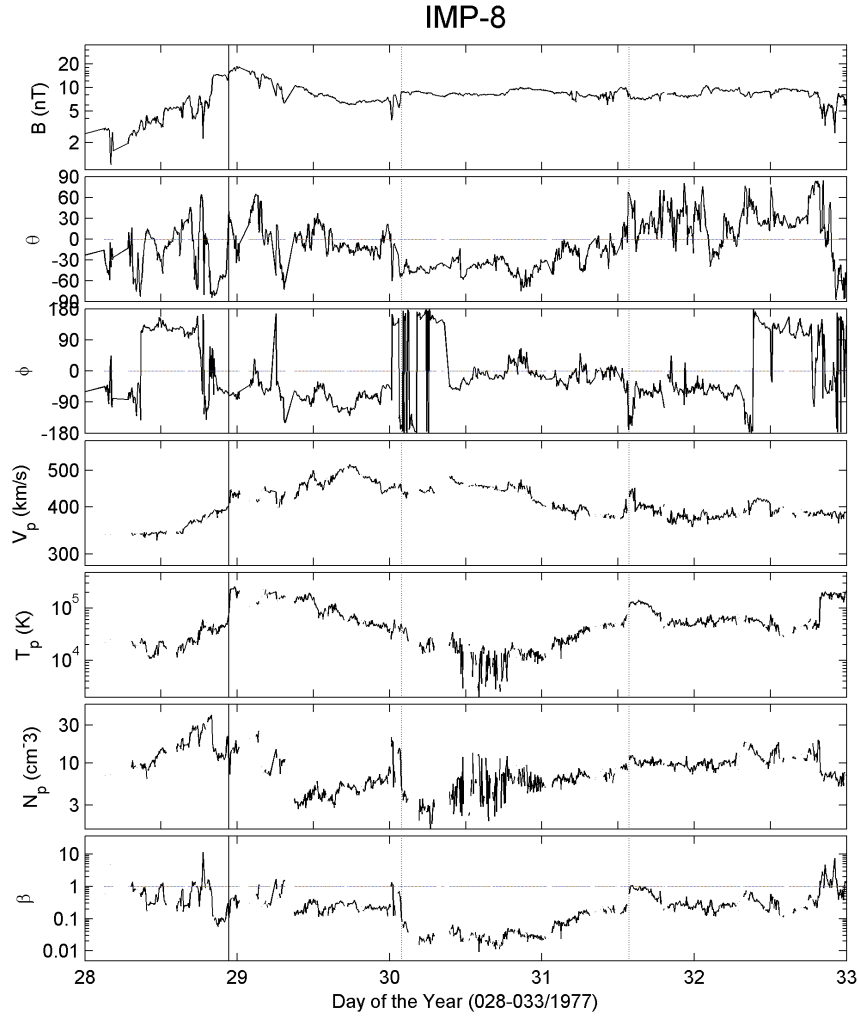


FIGURE 5.7 - IMP-8 observation of a MC from DOY 30/1977, at 01:00 UT, to DOY 31, at 13:00 UT. Meaning similar to [Figure 5.4](#).

and the consequent decrease in proton density. Its arrival time at IMP-8 also corresponds to the separation between H2 and IMP-8, once H2 was supposed to observe before IMP-8, considering that the HSS passed first by H1, due to the influence of the solar rotation.

About one day later, a possible MC is observed in IMP-8 plasma and magnetic field data, corresponding to the observations at H2. Note that the sheath region, the region between the shock wave and the MC lasted about one day in each spacecraft. Even though some discrepancies on the profiles of the measured parameters are found when comparing H2 and IMP-8 measurements, this might be a result of the interaction with the HSS.

Based on the MVA applied to the intervals corresponding to the boundaries of the MC, we determine the plane of maximum variance for H1 magnetic field data during the intervals corresponding to the magnetic cloud, illustrated in Figure 5.8. This plane revealed a quite complex rotation. Probably due to the distortion and compression the magnetic field suffered as it interacted with the ambient slower moving solar wind. The cloud's axis direction is found through the angles  $\theta_2$  and  $\phi_2$  for the intermediate variance direction (for details see Appendix C). These angles are represented in Figure 5.8. In this specific event, the cloud's axis was lying close to the ecliptic ( $\theta_2 = -4.2^\circ$ ) and it was almost parallel to the Sun-H1 line ( $\phi_2 = -62.5^\circ$ ). For a NES MC, as this one was classified, the orientation of the magnetic field, as the criterion defined by Bothmer and Schwenn (1998), is only correct if we consider the ambiguity of  $180^\circ$  (WALKER et al., 2002; ECHER et al., 2006). The arrow indicates the orientation of the magnetic field in Figure 5.8.

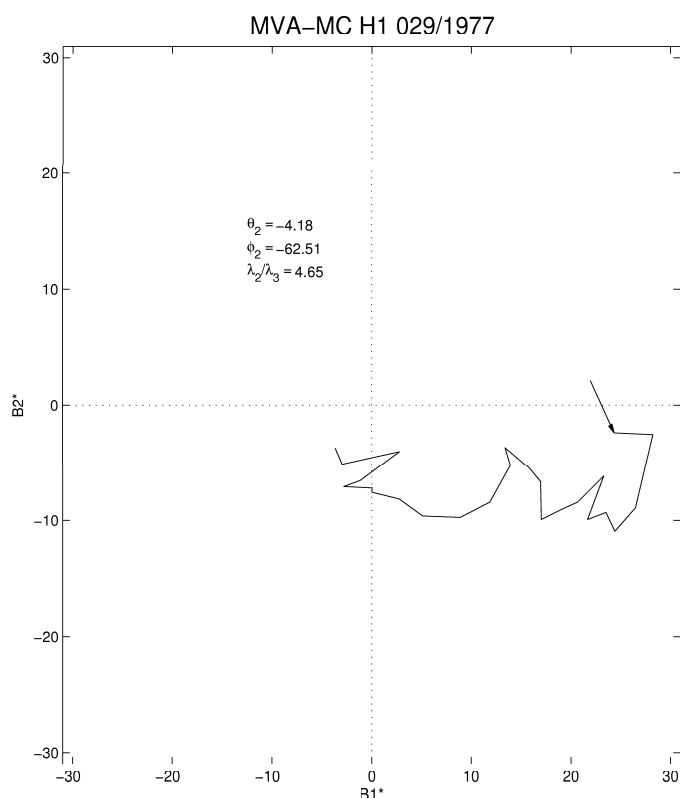


FIGURE 5.8 - Plane of Maximum Variance for the MC on DOY 029-030/1977 as observed by H1. The angles for the direction of the cloud's axis are represented by  $\theta_2$  and  $\phi_2$  in the figure. In addition, the error criteria ( $\lambda_2/\lambda_3 > 2$ ) is satisfied. The arrow indicates the initial points and gives the direction of the rotation of the magnetic field.

At H2, the MVA identifies a rotation on the magnetic field that is very small compared to the rotation seen in H1 data. This is probably a result of the compression of the MC against the HSS at H2. Because H2 is at a distinct longitude, it observes the HSS few days later. We estimate that the HSS and the MC arrived at H2 at approximately the same time.

In [Figure 5.9](#), the angles obtained for the cloud's axis are  $\theta_2 = -9.8^\circ$  and  $\phi_2 = 76.6^\circ$ , that are very similar to the ones measured by using H1 magnetic field data (see [Figure 5.8](#)) considering the ambiguity of  $180^\circ$ . This is probably due to the position the probe crossed the MC into space, or because the cloud suffered some rotation and deviation from its path due to the presence of the HSS. However, according to our assumption, the classification of the MC at H2 is different from the one at H1. We assumed the MC at H2 as a SWN MC-type. The orientation of the magnetic cloud, obtained through MVA analysis, does not correspond to the criterion of [Bothmer and Schwenn \(1998\)](#). Note that when comparing both orientations they have the same direction at H1 and H2, i.e., the MC rotates to the same direction at the two probes.

[Figure 5.10](#) illustrates the maximum variance plane obtained through the local MVA analysis in IMP-8 magnetic field data. Comparing the angles obtained by the intermediate variance with the ones obtained at H2 ([Figure 5.9](#)), we identified different directions for the cloud's axis, even though H2 is  $8^\circ$  eastward from the Earth.

According to the classification of magnetic storms by [Gonzalez et al. \(1994\)](#), a moderate magnetic storm ( $-100 < Dst < -50 \text{ nT}$ ) was observed at the terrestrial magnetosphere caused by the passage of the magnetic cloud. The solar wind energy injected into the magnetosphere was finally dissipated in the ring current, registering a peak Dst index of  $-95 \text{ nT}$ .

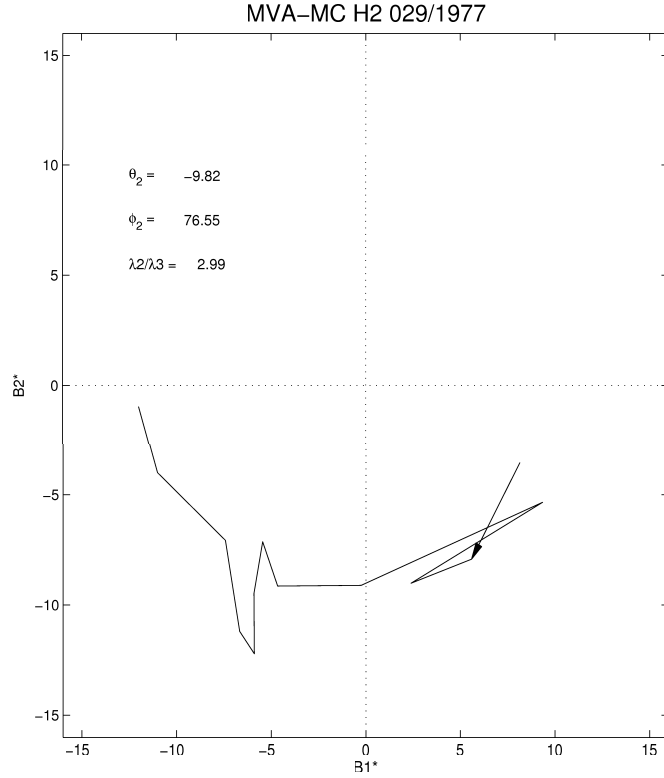


FIGURE 5.9 - Plane of Maximum Variance for the MC observed by H2 on DOY 029-030/1977. Meaning similar to Figure 5.8.

### 5.3.2 MC observed on DOY 76/1977 by H1 and H2

From the observations done by H1, a shock wave was driven by a MC whose boundaries are defined by the dotted vertical lines as observed in Figure 5.11. The MC is identified by the rotation on the inclination angle  $\theta$  from  $90^\circ$  to  $0^\circ$ , resulting from the rotation in the  $B_z$  component. In the azimuthal direction,  $\phi$  was around  $90^\circ$ , until it crossed a sector boundary at the end of the MC. Based on these angles, we classified the structure as a NES MC-type. A density discontinuity is observed in the sheath region, just after the shock detection, followed by a sudden decrease in the density magnitude inside the cloud. Plasma beta goes down to values lower than 0.1 inside the cloud, characteristic of this class of structures.

From Figure 5.12 one can identify that the only component that rotated strongly during the MC passage was  $B_z$ . Considering that the MC is a NES-type, the orientation of the magnetic field does correspond to the criterion established by Bothmer



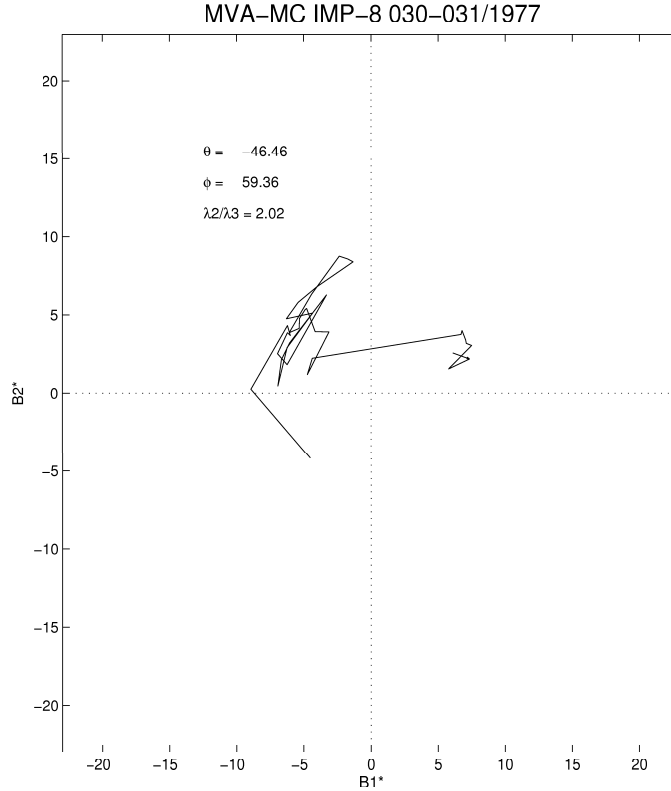
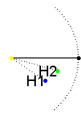


FIGURE 5.10 - Plane of maximum variance for the MC observed on DOYs 030-031/1977. The meaning is similar to [Figure 5.8](#).

and Schwenn (1998). Based on the MVA, the cloud's axis obtained for the MC observed at H1 gives the angles  $\theta_2 = -32.53$  and  $\phi_2 = 99.07$ , as shown in [Figure 5.13](#).

At H2, further away from the Sun in relation to H1 position, the MC was observed some hours later by the instruments onboard the probe. [Figure 5.14](#) shows the boundaries defined for the magnetic cloud. Interestingly, the components of the magnetic field rotate as shown in [Figure 5.15](#), and the inclination angle is different from the one observed in H1. This is a highly inclined MC because  $B_z$  component did not change its signal. The rotation is observed in  $B_x$  and  $B_y$  components. Based on the direction of the components, we classify this cloud as a ESW MC-type, according to [Mulligan et al. \(1998\)](#) definition. What is intriguing is that the probes are separated by less than  $20^\circ$ , and, even though very close, the MC looks different at each spacecraft.

Through MVA we obtained the orientation for the cloud's axis observing the di-



H1 0.61 AU HSE 326.3° No. 27

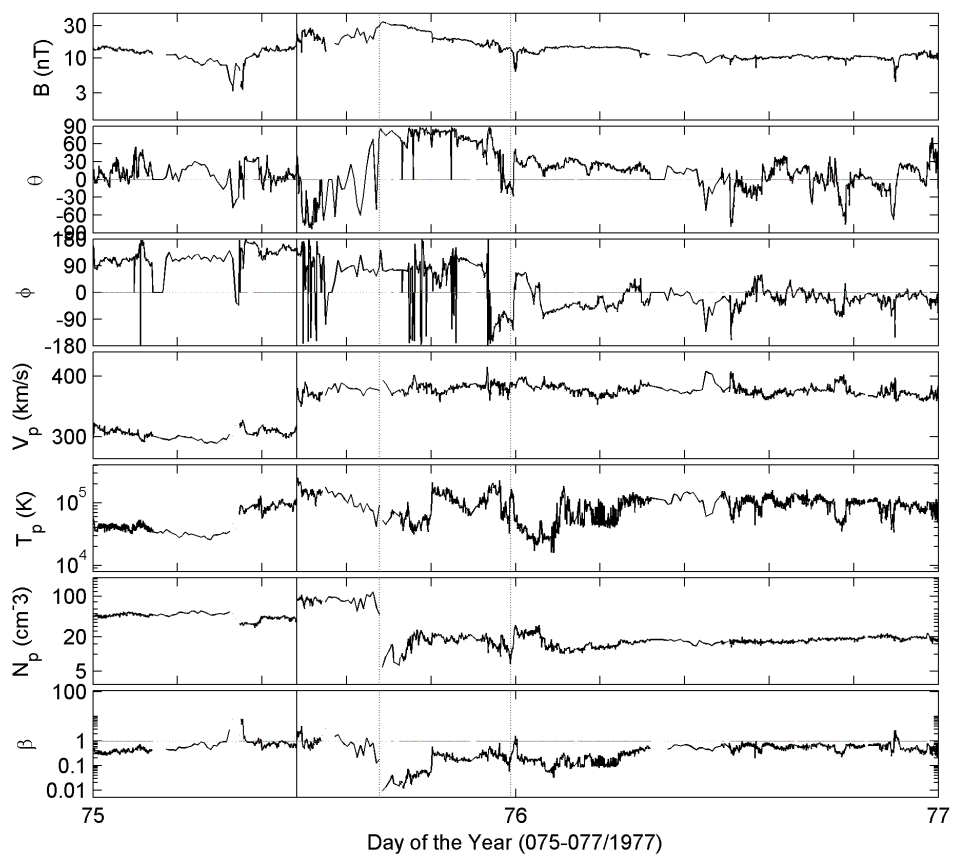


FIGURE 5.11 - H1 observation of a MC on DOY 75/1977, from 16:15 UT to 23:43 UT. Meaning similar to Figure 5.4.

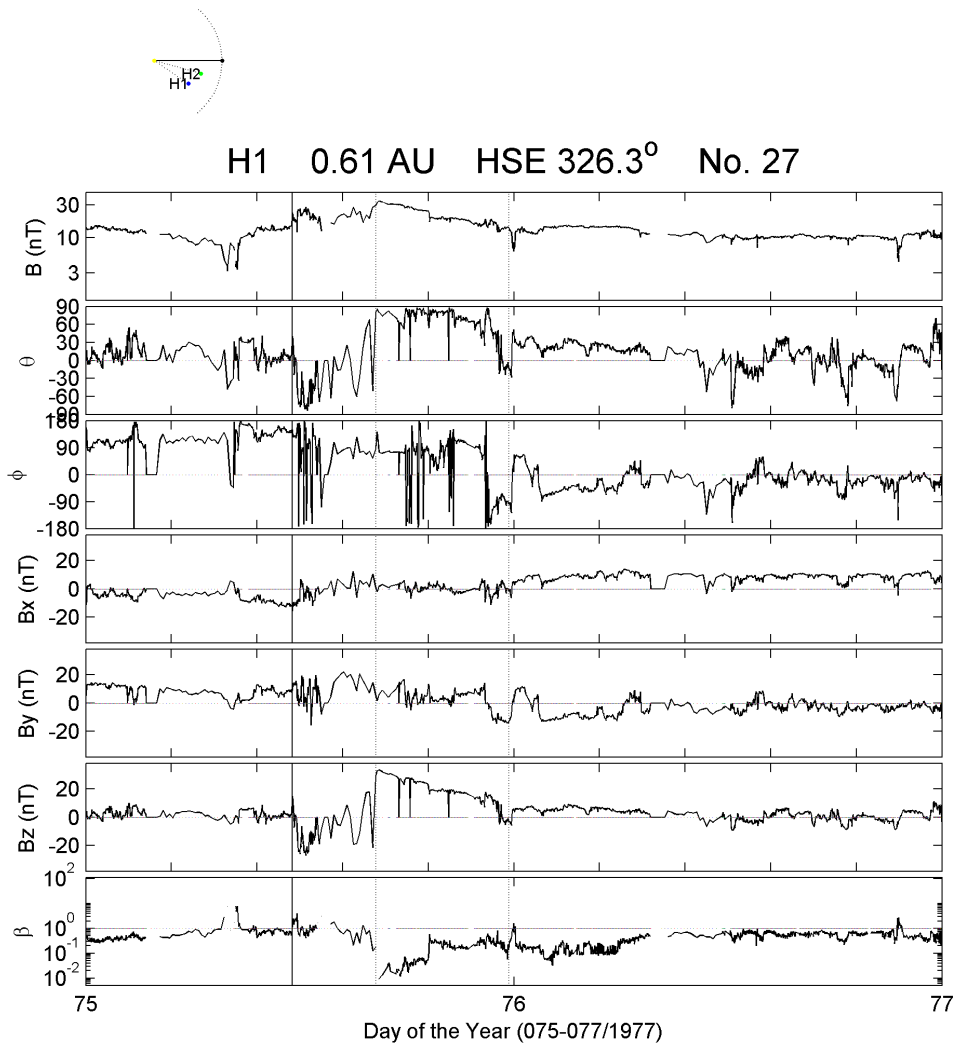


FIGURE 5.12 - H1 magnetic field data for the period from DOY 75 to 77/1977. Meaning similar to [Figure 5.6](#).

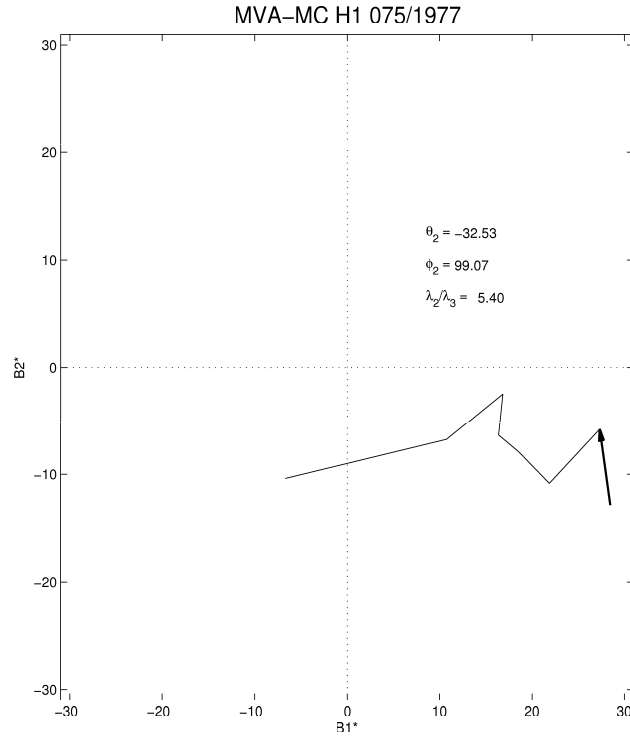


FIGURE 5.13 - Plane of maximum variance for the MC observed by H1 on DOY 75/1977. Cloud's axis is directed according to the angles  $\theta_2$  and  $\phi_2$ . The criterion for the MVA technique is satisfied because  $\lambda_2/\lambda_3 = 5.4$ . The arrow indicates the initial points and gives the direction of the rotation of the magnetic field.

rection of intermediate variance that gives the angles  $\theta_2$  and  $\phi_2$ , represented in Figure 5.16, although probes are separated by only  $18^\circ$ . The values obtained at each probe are very different. The plane of maximum variance, illustrated in Figure 5.13, shows the magnetic field represented by  $B_1^*$  and the intermediate one by  $B_2^*$ .

IMP-8 was not monitoring the solar wind during the period the shock crossed the Earth. No magnetic storm was registered for the period as the data provided by the World Data Center for Geomagnetism from Kyoto (WDC-Kyoto). Interestingly,  $B_z$  was always negative inside the magnetic cloud, as we observed previously in Figure 5.15, however, the MC probably did not reach Earth.

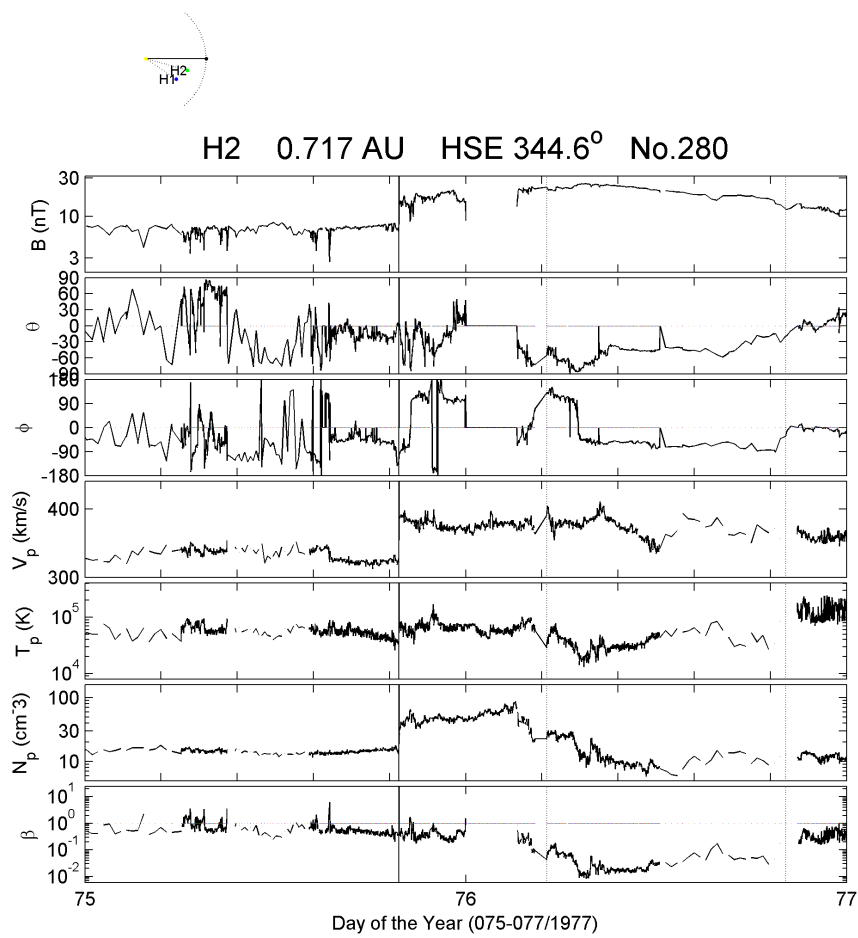


FIGURE 5.14 - H2 observation of the same MC observed by H1 on DOY 76/1977, from 05:06 UT to 20:09 UT. Meaning similar to [Figure 5.4](#).

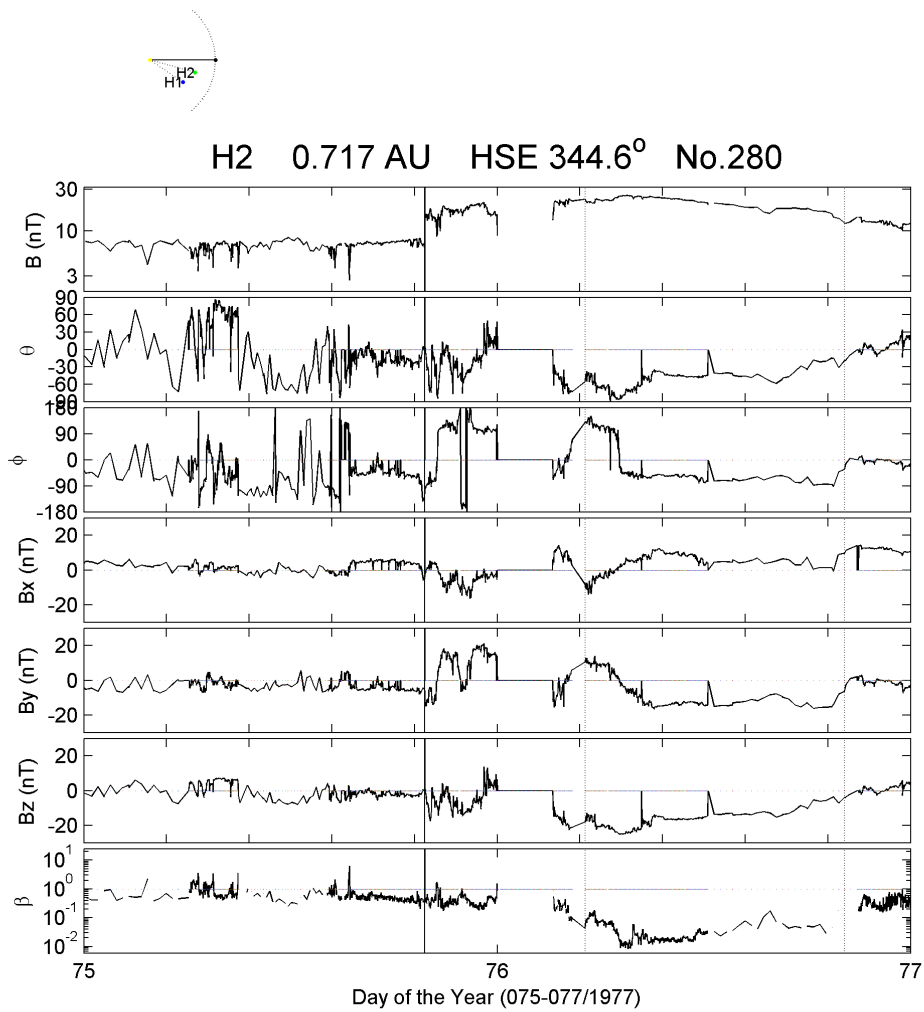


FIGURE 5.15 - Magnetic field data by H2 for the period from DOY 75 to 77/1977. Meaning similar to [Figure 5.6](#).

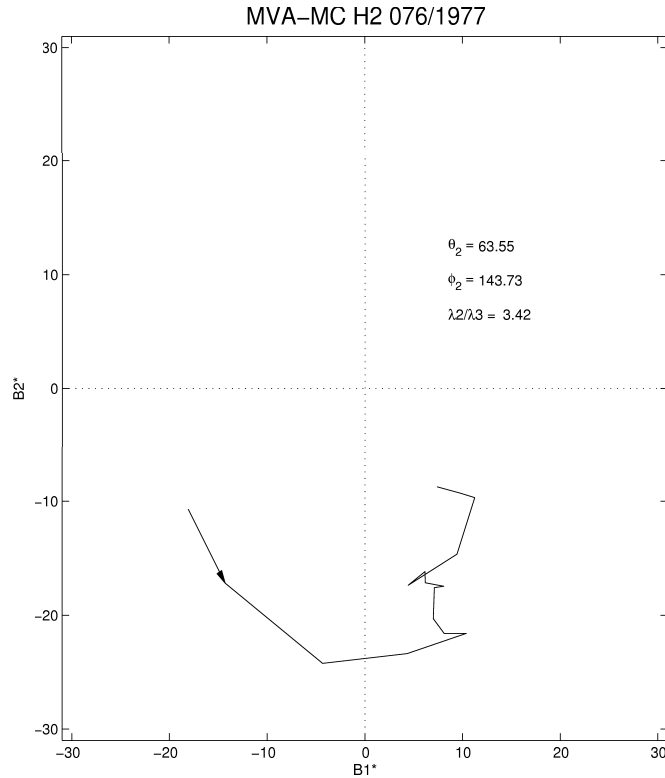


FIGURE 5.16 - Plane of maximum variance for the MC observed by H2 on DOY 76/1977. The meaning is similar to Figure 5.8.

### 5.3.3 MC observed on DOY 327/1977 by H2 and IMP-8

This magnetic cloud is an example of an event seen by two probes where one of the observation point is IMP-8, the point near Earth. The angular separation between the two probes was about  $7^\circ$ , and they saw similar features in the IP medium.

Figure 5.17 shows the magnetic field and plasma properties of the medium when the magnetic cloud was crossed by H2. Even though the plasma beta is low inside the structure, the proton density does not decrease abruptly inside the cloud nor the proton temperature. On the other hand, the rotation on the magnetic field, as described by the inclination and azimuthal angles is illustrated on the respective profiles of  $\theta$  and  $\phi$  in Figure 5.18. The rotation is observed on the components of the magnetic field, mainly in  $B_z$ , following the same rotation as the one described by  $\theta$ . Inside the magnetic cloud, the azimuthal angle  $\phi$  varies from  $-90^\circ$  to  $+90^\circ$ . We classify this cloud as a SEN MC-type, according to Bothmer and Schwenn (1998) classification.

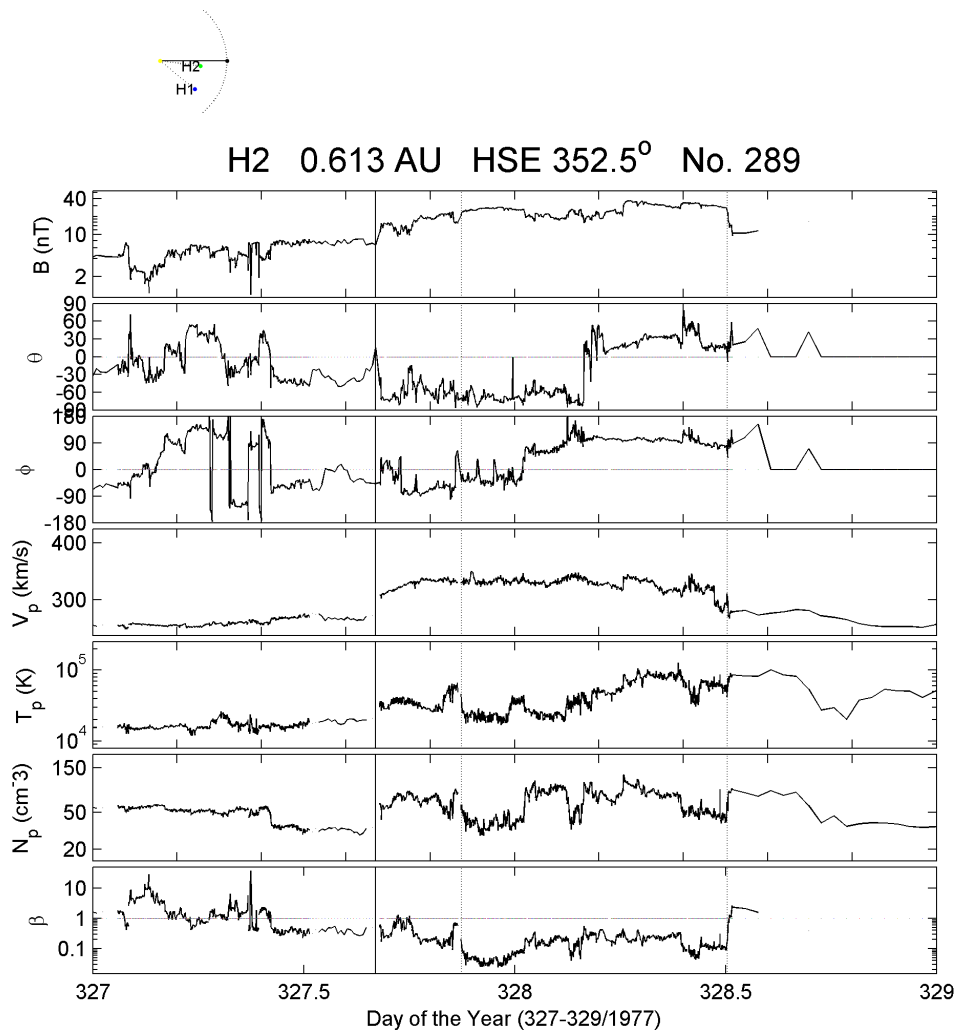


FIGURE 5.17 - H2 observation of a MC from DOY 327/1977, at 21:01 UT, to DOY 328/1977, at 03:52 UT. Meaning similar to [Figure 5.4](#).



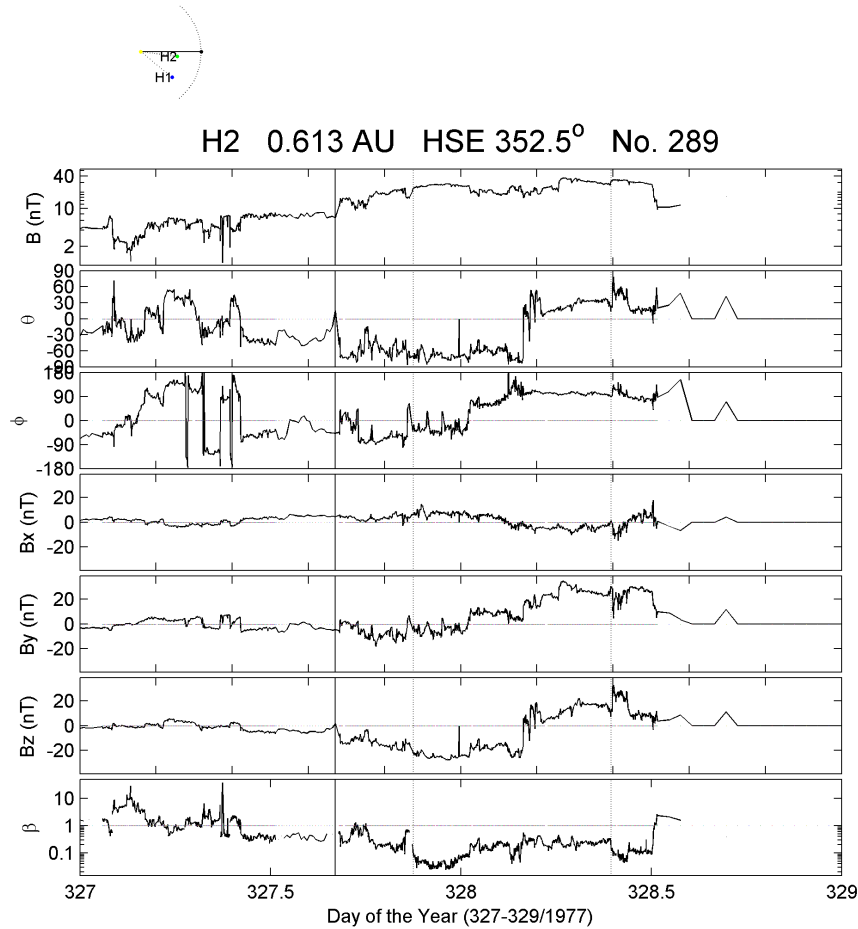


FIGURE 5.18 - H2 observation for the period between 327-329/1977. Meaning similar to Figure 5.6.

Applying the MVA technique one obtains the plane of maximum variance, illustrated in Figure 5.19. The plot of  $B_1^*$ , the maximum variance for  $\vec{B}$ , against  $B_2^*$ , the intermediate variance for  $\vec{B}$ , results in Figure 5.19. The rotation in  $\vec{B}$  is represented by the curve where the arrow shows the direction of the rotations and the initial points. The orientation of the magnetic field turning corresponds to the one defined by the criterion of Bothmer and Schwenn (1998), according to the classification of this cloud: a SEN cloud.

Data gaps are present in the period, as shown in Figure 5.20, however, the signatures of the cloud are visible, as observed by the decrease in the plasma beta at the end of DOY 329/1977. In addition to the decrease on the plasma beta, the proton density measured goes down as the structure crosses the instruments onboard IMP-8, characteristic of MCs. Even though gaps appear at the beginning of the front part

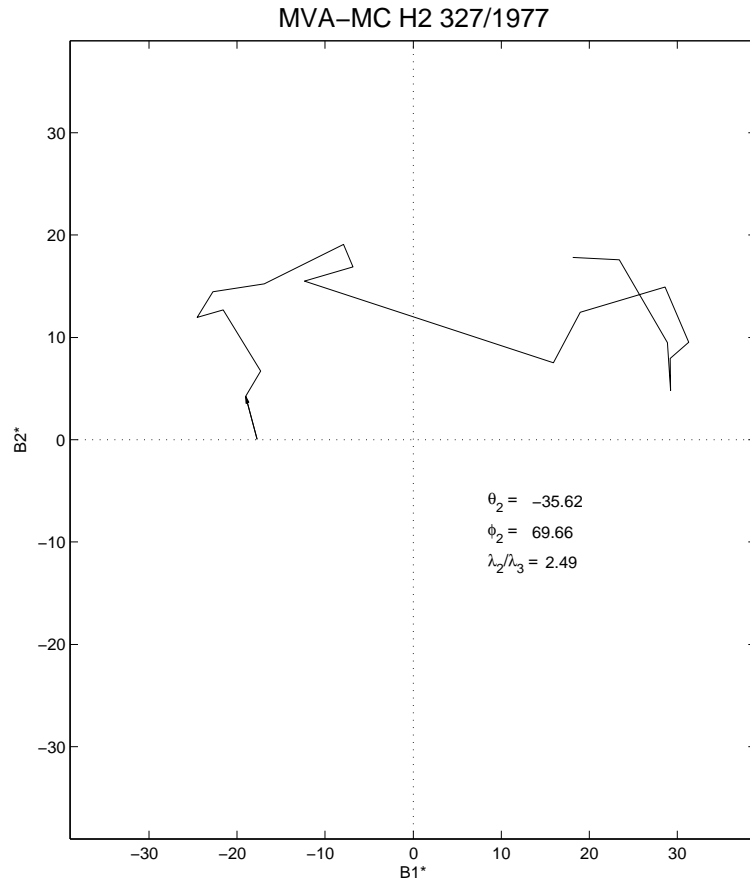


FIGURE 5.19 - Maximum variance plane for the MC observed on DOY 327/1977. Meaning similar to Figure 5.8.

of the cloud, the rotation on the magnetic field azimuthal and inclination angles is noticed, following the same pattern as at H2. Both angles turn from south to north inside the MC.

According to the rotation of the magnetic field components as observed in Figure 5.21, the MC observed at IMP-8 is classified as a SEN type. Despite the presence of data gaps during the period, we can identify the variations on the magnetic field, and we assume this cloud to be a SEN MC-type.

Figure 5.22 represents the plane of maximum variance of the magnetic field during the period defined as the cloud based on the observations from IMP-8. Despite the fact that the period of the MC rotation in the plane of maximum variance is small, we can identify the smoothness in the turning of  $\vec{B}$ . Furthermore, the orientation, given by the arrow, corresponds to the orientation for SEN MC-type (BOTHMER;

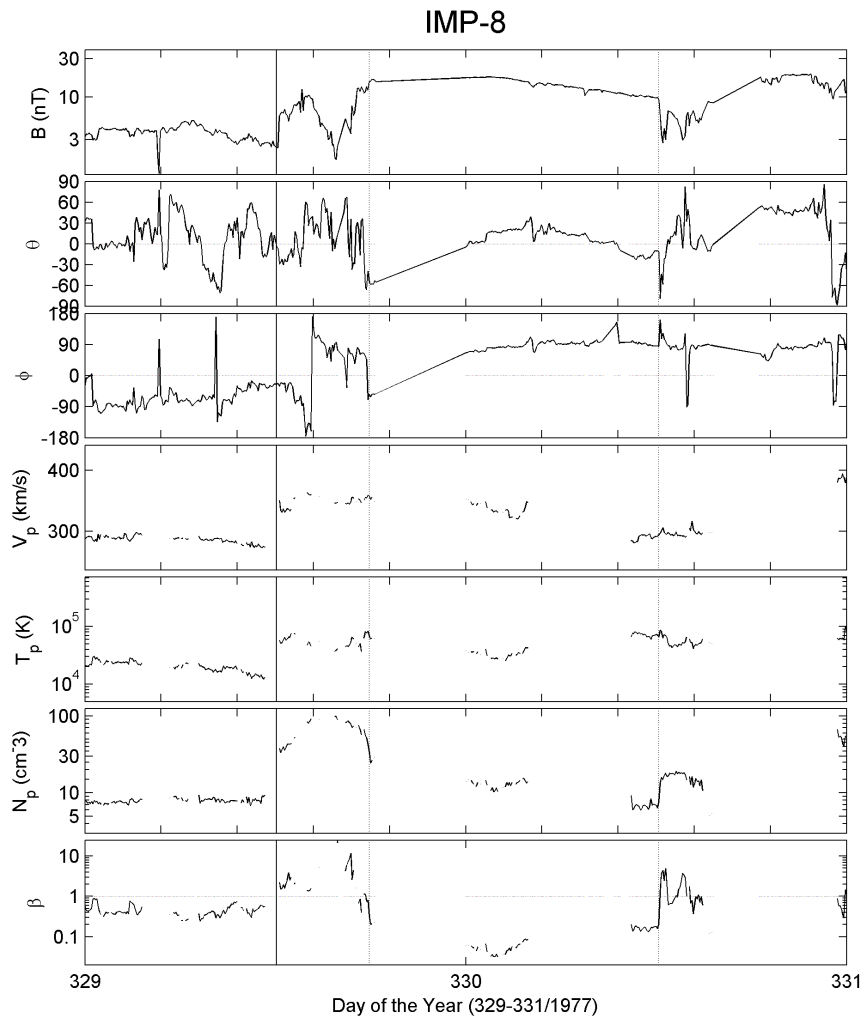


FIGURE 5.20 - IMP-8 observation of a MC on DOY 329/1977, at 17:55 UT, to DOY 330/1977, at 12:10 UT. Meaning similar to [Figure 5.4](#).

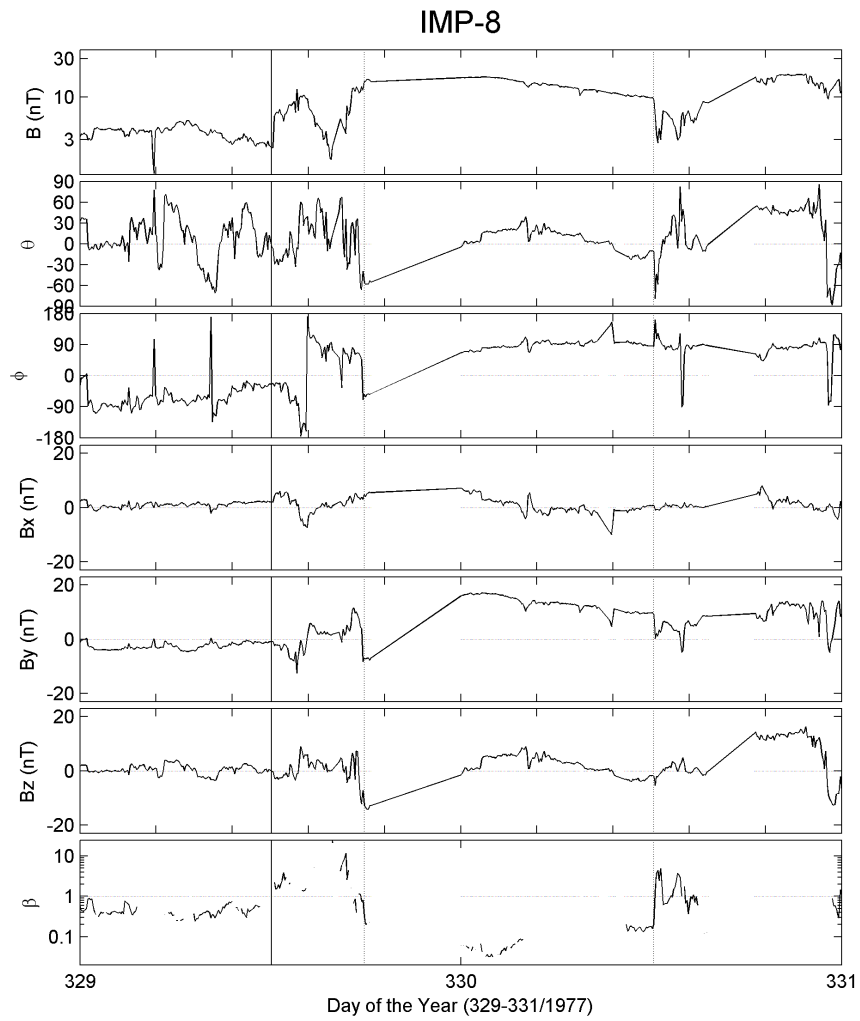


FIGURE 5.21 - IMP-8 magnetic field data for the period from 329 to 331/1977. Meaning similar to [Figure 5.6](#).

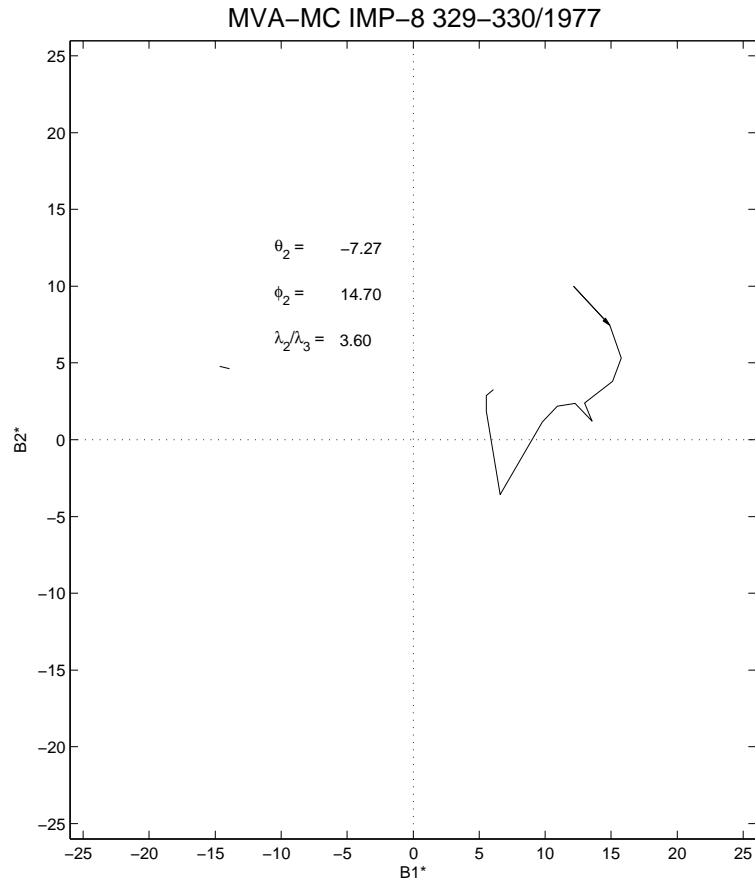


FIGURE 5.22 - Maximum Variance plane for the MC observed on DOY 329/1977. Meaning similar to Figure 5.8.

SCHWENN, 1998). According to the angles obtained through minimum variance, the MC is lying almost parallel to the ecliptic plane ( $\theta_2 = -7.27^\circ$ ). The error criterion ( $\lambda_2/\lambda_3 > 2$ ) for the accuracy of the MVA technique is satisfied.

By comparing Figure 5.19 and Figure 5.22, we find different MC's axis direction, given by  $\theta_2$  and  $\phi_2$ . However, the magnetic field inside the MC as measurements from each probe has similar direction of rotation, as illustrated by the arrow in the plots. Note that probes H2 and IMP-8 are only  $7^\circ$  away from each other.

A moderate magnetic storm with peak  $Dst = -87 \text{ nT}$  was registered at the terrestrial magnetosphere on DOY 330/1977. This was a result of the southward turning of the magnetic field  $B_z$  component measured at IMP-8.

### 5.3.4 MC observed on DOY 335/1977 by H1 and H2

According to H1 observations, there are two possibilities for the MC observed on DOY 335-336/1977. [Figure 5.23](#) shows a MC that can have two possible rear boundaries, one at the beginning of DOY 336/1977, and the other one at the second half of DOY 336/1977. The criterion used to define these boundaries is the smoothness of the magnetic field, mainly in the first choice of MC boundary. From the beginning of DOY 336 until the end of the boundary choice for the MC rear part,  $\vec{B}$  is not so smooth compared to the first option, but it is still smooth. We have chosen the latter interval as the one defining the MC boundaries, since we took into account the low beta ( $\beta < 0.1$ ) inside the structure. In addition to this feature, the rotation on the magnetic field, even though stronger in the former interval for the MC, it is still visible in the latter through  $B_x$  and  $B_z$ .

Inside the MC, the rotation in  $\theta$  follows exactly the same pattern observed in  $B_z$ , as shown in [Figure 5.24](#). Since  $B_y$  is basically all the time positive inside the cloud, one can suggest that the MC was oriented perpendicularly to the Sun-Earth line. We classify this cloud as a SEN type, based on the rotation on  $B_y$  and  $B_z$  components. Through MVA, as shown in [Figure 5.25](#), the intermediate variance gives the cloud's axis inclined as  $\theta_2 = -14^\circ$  (almost parallel to the ecliptic plane) and  $\phi_2 = -60^\circ$ . These are the same angles as the ones obtained by [Bothmer and Schwenn \(1998\)](#), however,  $\theta_2$  is in the opposite direction, while  $180^\circ$  were added to  $\phi_2$ . In particular, as  $\theta_2$  is very close to the ecliptic plane, we confirmed that the MC is oriented perpendicularly to the Sun-Earth line in the ecliptic plane. Note that the direction pointed by the arrow does correspond to the one for SEN MCs.

As shown in [Figure 5.26](#), data gaps filled part of the period from DOY 334-337/1977. The magnetic cloud is assumed to be similar to the one observed by H1. The continuous vertical line identifies the shock time, while the two dotted vertical lines identify the front and rear parts of the cloud. Even though the data gaps follow the assumed time for the end of the cloud, we consider that the cloud finishes after that based on the similarities with H1 observations. The front part starts when the density discontinuity finishes and the proton density decreases abruptly. Plasma beta also goes down but then recovers again for some hours until it decreases inside the MC. The rotation on the magnetic field, mainly in  $\theta$ , is observed inside the cloud and describes the same rotation as the one observed in  $B_z$ , as shown in [Figure 5.27](#).

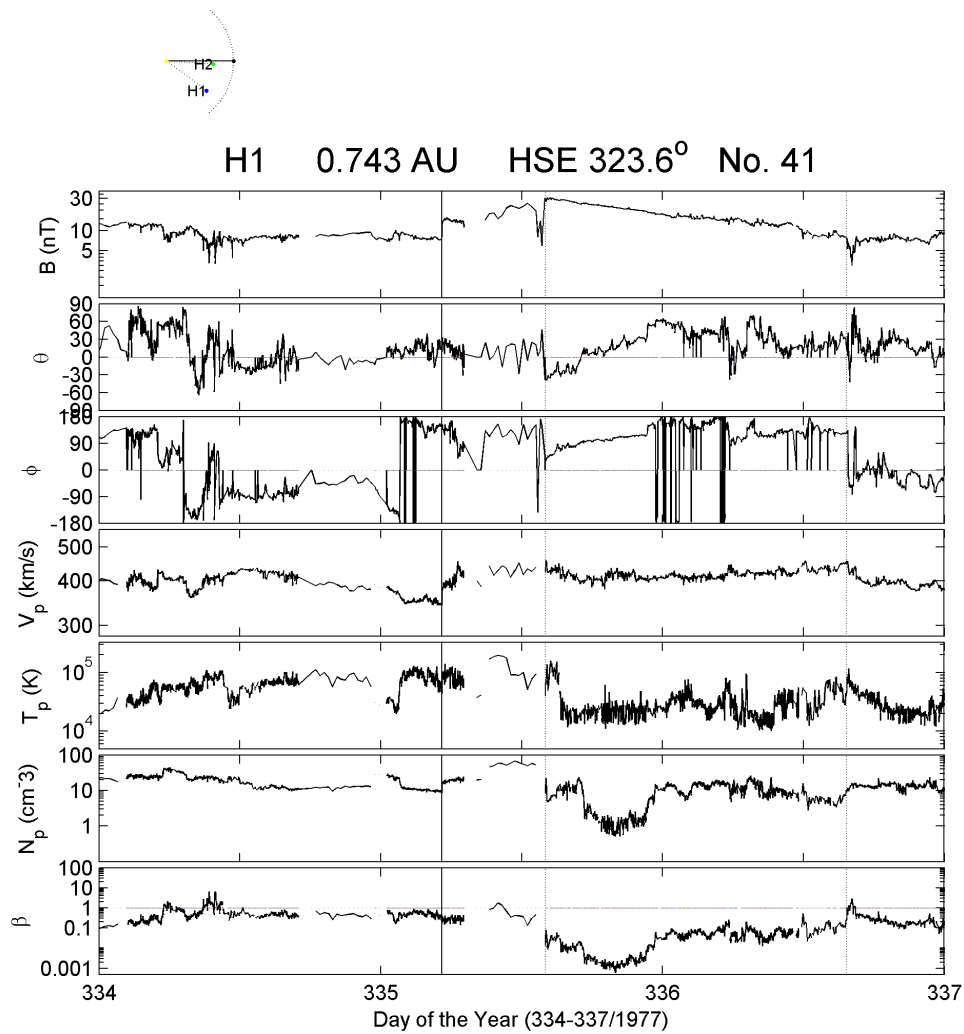


FIGURE 5.23 - H1 observation of a MC on DOY 335/1977, from 14:01 UT to 15:39 UT. Meaning similar to [Figure 5.4](#).

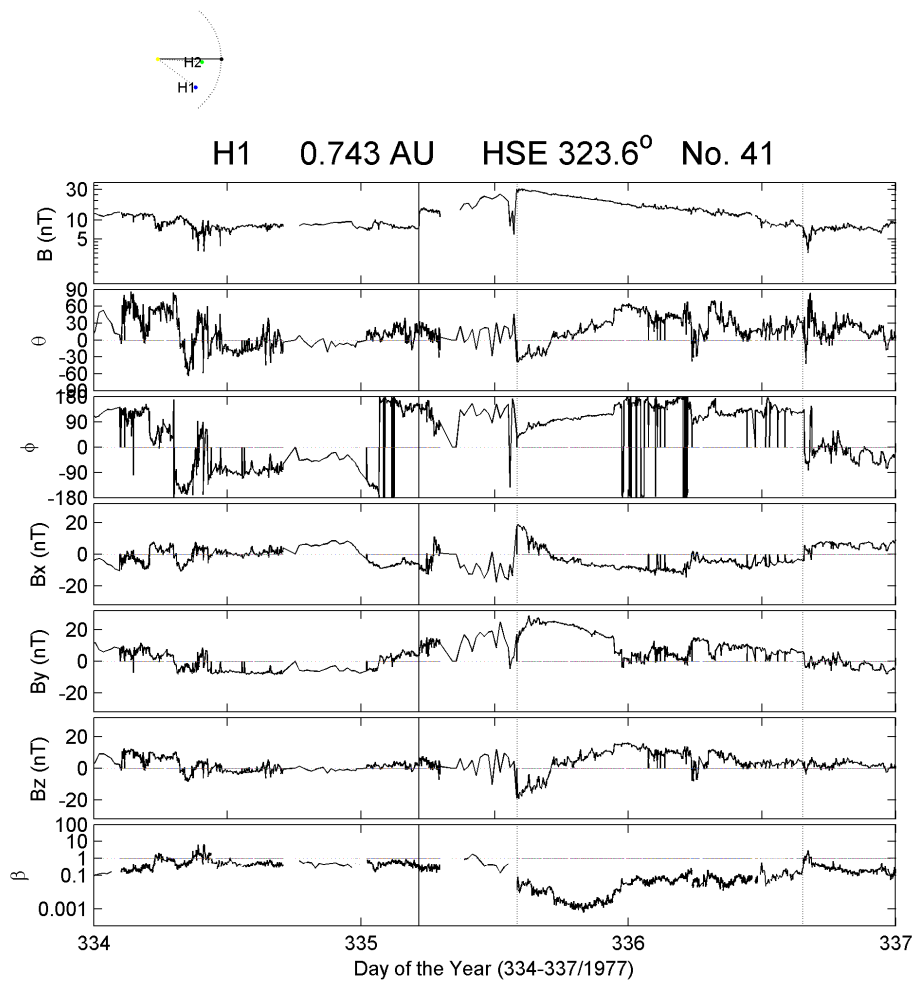


FIGURE 5.24 - H1 magnetic field data for the period from DOY 334 to 337/1977. Meaning similar to [Figure 5.6](#).



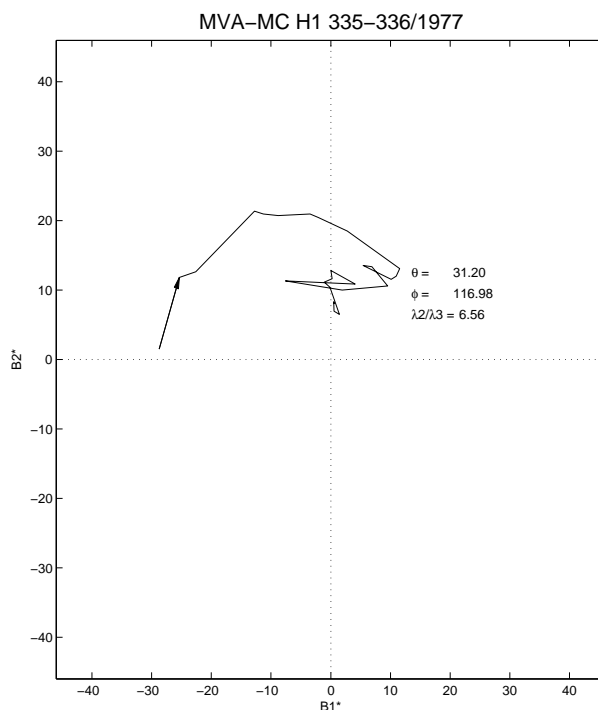


FIGURE 5.25 - Maximum Variance plane for H1 observation of a MC on DOY 335/1977. Through intermediate variance, the angles  $\theta_2$  and  $\phi_2$  that represent the direction of the cloud's axis are obtained. The arrow indicates the initial points and gives the direction of the rotation of the magnetic field.

Comparing plasma and magnetic field data from the two probes, H1 and H2, one can notice the similarities between the MC at two different positions. Mainly  $B_z$ , measured at each probe, follows the same pattern inside the cloud, but the intensities are different. This can be a result of the compression suffered by the MC, as it encountered the slower solar wind moving ahead of it. At H1, the proton speed was on average equal to  $450 \text{ km/s}$  inside the MC. On the other hand, H2 measured a higher proton speed, on average equal to  $520 \text{ km/s}$ . With the compression, the magnetic field increased to  $28 \text{ nT}$  on average. After the big gap that completes the DOY 335/1977, the magnetic field is decreased, implying in the bigger values in the plasma beta profile. The rear end of the cloud is not visibly defined in consequence of the data gaps found in the period.

The similarities we mentioned previously are observed in the plasma beta, mainly on DOY 336/1977, as well as the fluctuations observed in  $\vec{B}$ . This leads one to consider the MC rear boundary as the one characterized by an abrupt increase in the plasma beta, the same parameter taken into account in the MC at H1. However, at this time,

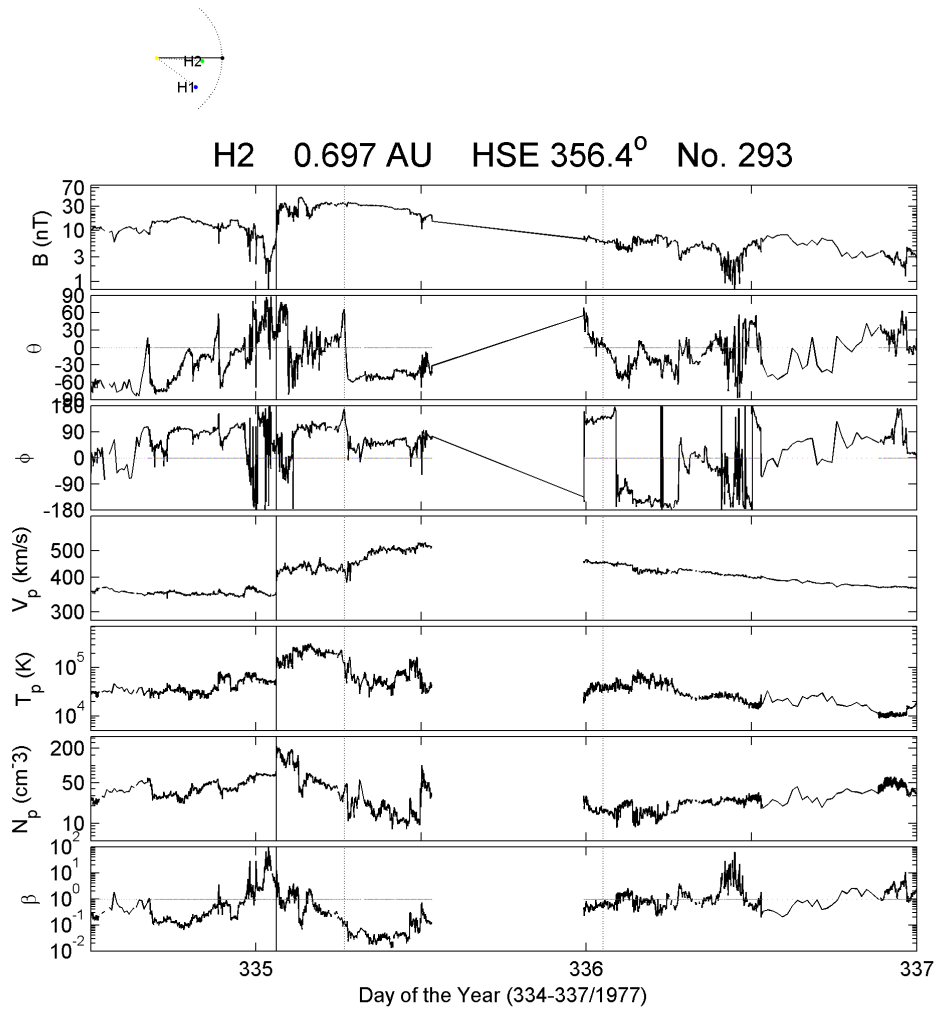


FIGURE 5.26 - H2 magnetic field data for the period from DOY 334-337/1977. Meaning similar to [Figure 5.4](#).

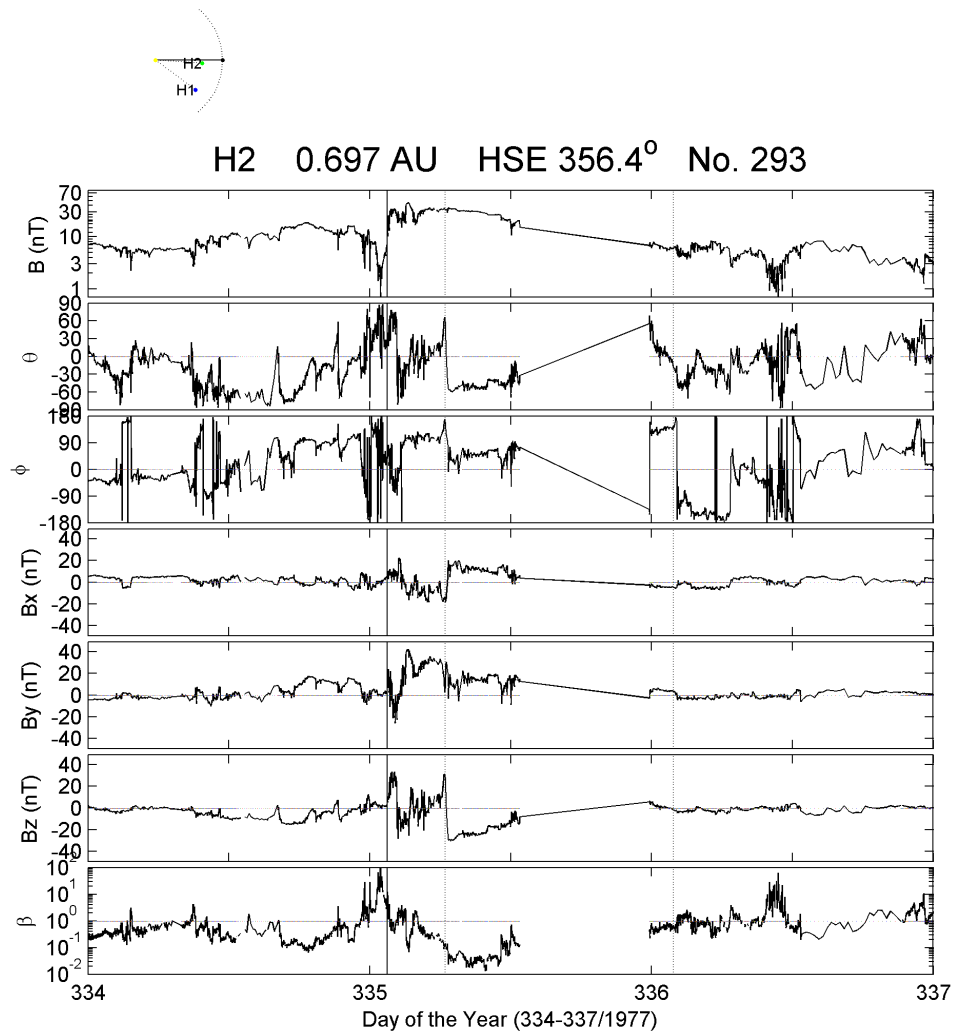


FIGURE 5.27 - H2 observation of a MC on DOY 335/1977, from 06:26 UT to 12:00 UT. Meaning similar to [Figure 5.6](#).

the beta was already bigger than 0, according to H2 measurements. This guides us to consider the period before that, when plasma beta was about 0.1. One can clearly see the rotation on the  $B_z$  component.  $B_y$  rotates mainly westwardly at H1 because its values are basically positive inside the structure. At H2 it is not possible to have an idea about the direction of  $B_y$  in the whole structure since gaps fill part of the period.

From the plane of maximum variance, as observations provided by H2, the rotation on the magnetic field inside the MC is not visible. This is due to the fact that, as we are taking hourly averaged magnetic field data from the probe, a short period of data without gaps was registered by H2, as shown in [Figure 5.26](#).

A magnetic storm was registered later on, according to WDC-Kyoto. The peak  $Dst$  measured during the magnetic storm was  $-124$  nT, registered on DOY 336/1977.

### 5.3.5 MC observed on DOY 003/1978 by H1 and H2

This event corresponds to the famous MC that allowed the identification of the flux tube configuration for MCs. This magnetic cloud was described on details when its discovery was provided due to the observations from 4 different points in space. At that time Voyagers 1 and 2 were already operating in the outer heliosphere, and H1 and H2 both observed the magnetic cloud that was also crossed by IMP-8, near Earth.

As previously discussed by [Burlaga et al. \(1981\)](#), H1 observations presented many data gaps, which did not allow the identification of the rear boundary of the MC. We suggest a different front boundary for the MC, since plasma beta goes down before the period determined in the work of [Burlaga et al. \(1981\)](#). [Figure 5.28](#) illustrates the choice of the MC boundaries determined on basis of the decrease of the plasma beta, followed by the low proton density values found inside the structure. But mainly, the rotation in  $\theta$  starts at that time already. Low proton temperature is also characteristic of this structure, as shown in [Figure 5.28](#). Proton speed is high inside the MC, what characterizes a very fast MC traveling close to 1  $AU$ .

From [Figure 5.29](#), one identifies the rotation on the magnetic field described by the  $B_x$  and  $B_z$  components.  $B_x$  also rotates strongly inside the MC, reaching values of the order of  $-20$   $nT$ . This MC is classified as a highly inclined one due to the rotation in  $B_x$  as a WNE MC-type.

Through MVA one obtains the plane of maximum variance for the magnetic field vector  $\vec{B}$  in the intervals determined in [Figure 5.28](#), the front and rear parts of the MC, according to our criteria of MCs. The smooth rotation on  $\vec{B}$  is observed in [Figure 5.30](#), confirming the presence of the highly inclined ( $\theta = 63^\circ$ ) MC in the considered interval.

Closer to Earth, at 0.938  $AU$ , the twin probe H2 observes the same MC, based on the similarities we found mainly in the magnetic field data. According to [Figure 5.31](#), a MC extended from 004/1978, at 07:36 UT, to 005/1978, at 15:04 UT. The rotation observed in  $\theta$  is similar to the one in H1. From  $\phi$  one cannot say that they are similar. Nevertheless, H2 detects the smooth rotation inside the MC (see [Figure 5.31](#)). Plasma density and temperature are smaller at the same time as low plasma beta values are registered, agreeing with the characteristics of MCs at 1  $AU$

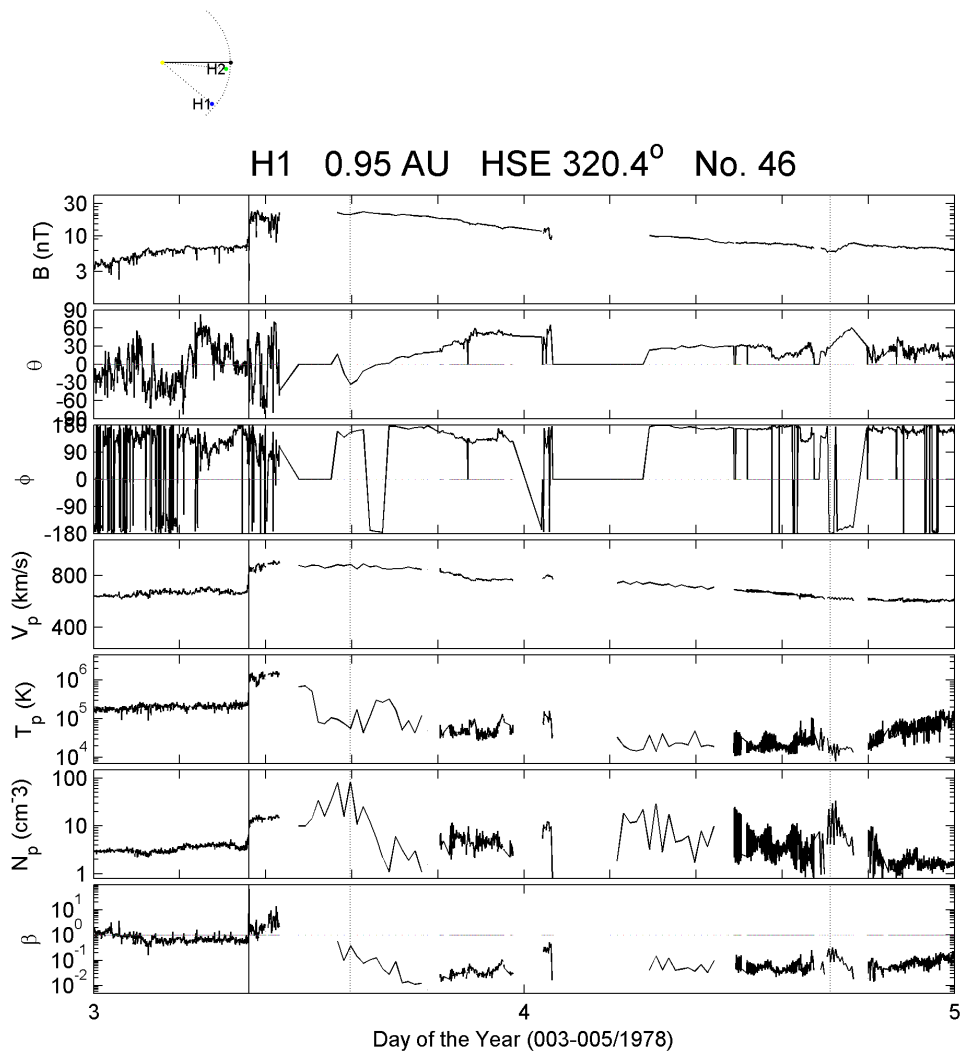


FIGURE 5.28 - H1 observation of a MC from DOY 003/1978, at 14:19 UT, to 004/1978, at 17:05 UT. Meaning similar to [Figure 5.4](#).

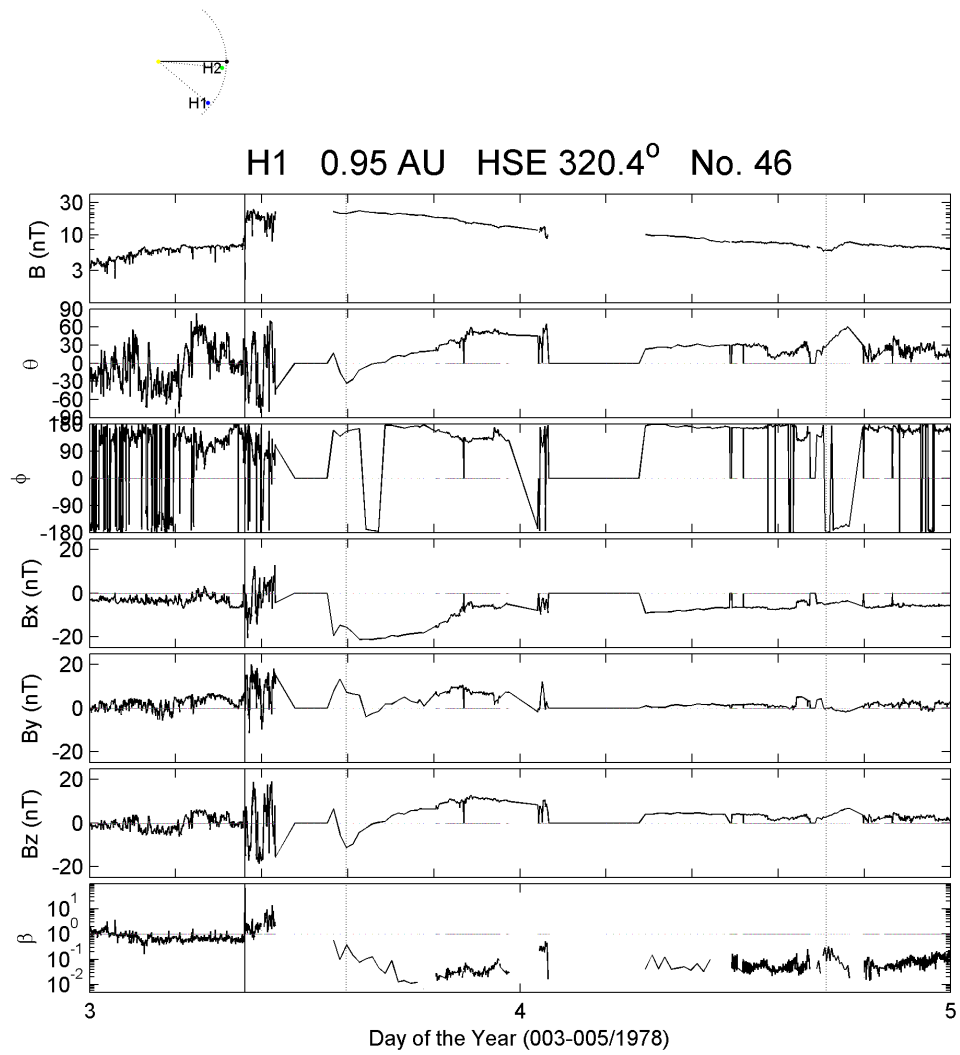


FIGURE 5.29 - H1 observation for the period between 003-005/1978. Meaning similar to [Figure 5.6](#).

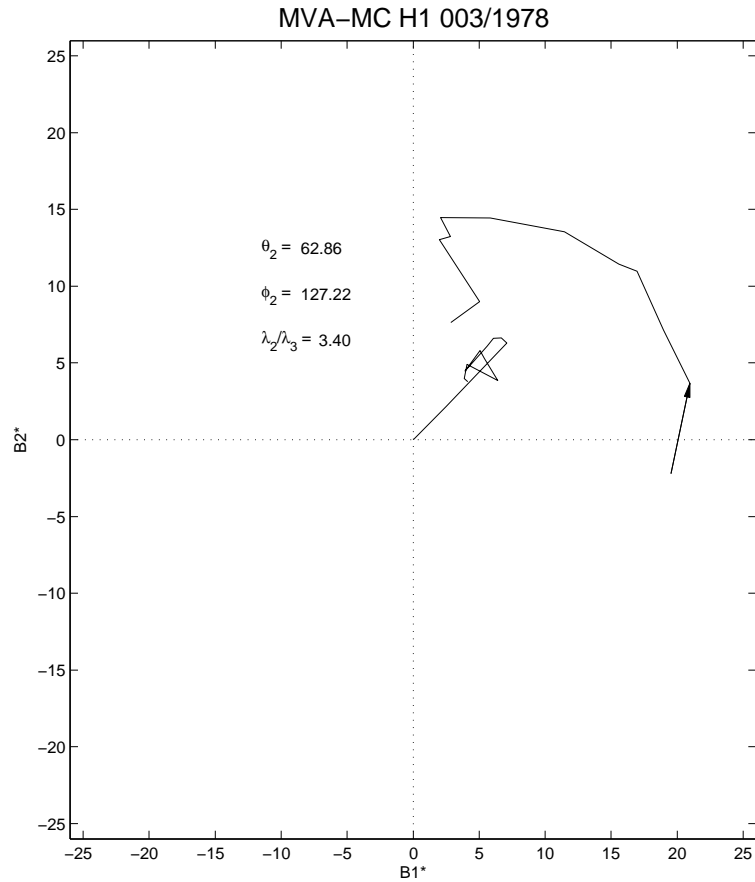


FIGURE 5.30 - Plane of maximum variance analysis for the MC observed on DOYs 003-004/1978. Meaning similar to Figure 5.25.

(BURLAGA, 1991).

By the rotation on  $B_z$ , as observed in Figure 5.32, it is possible to identify the correspondence on the rotation direction with the one at H1. Even though gaps fill part of the interval where the MC was detected by H1,  $B_x$  turns from negative to positive according to H2. In H1,  $B_x$  starts rotating from negative, and we assumed it as rotating to positive values afterward, following the same pattern as in H2. The MC is classified in SWN type, according to the variation on the magnetic field components.

By applying the local MVA technique in H2 magnetic field data results in a MC whose axis is inclined in  $\theta_2 = -20^\circ$  in relation to the ecliptic plane and  $-73^\circ$  rotation in the azimuthal angle,  $\phi$ . The error criteria ( $\lambda_2/\lambda_3 > 2$ ) was satisfied as one certifies in Figure 5.33. Considering the ambiguity of  $180^\circ$  in the azimuthal



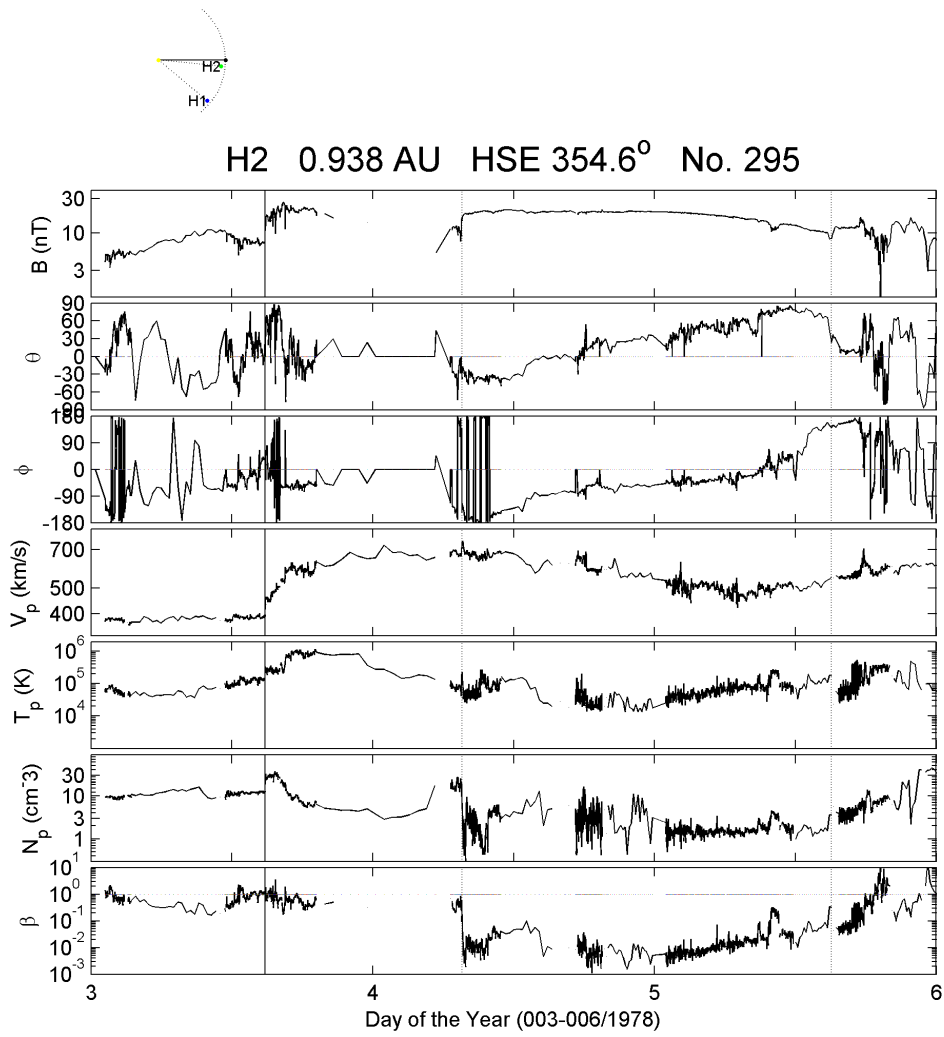


FIGURE 5.31 - H2 observation of a MC from DOY 004, at 07:36 UT, to DOY 005/1978, at 15:04 UT. Meaning similar to Figure 5.4.

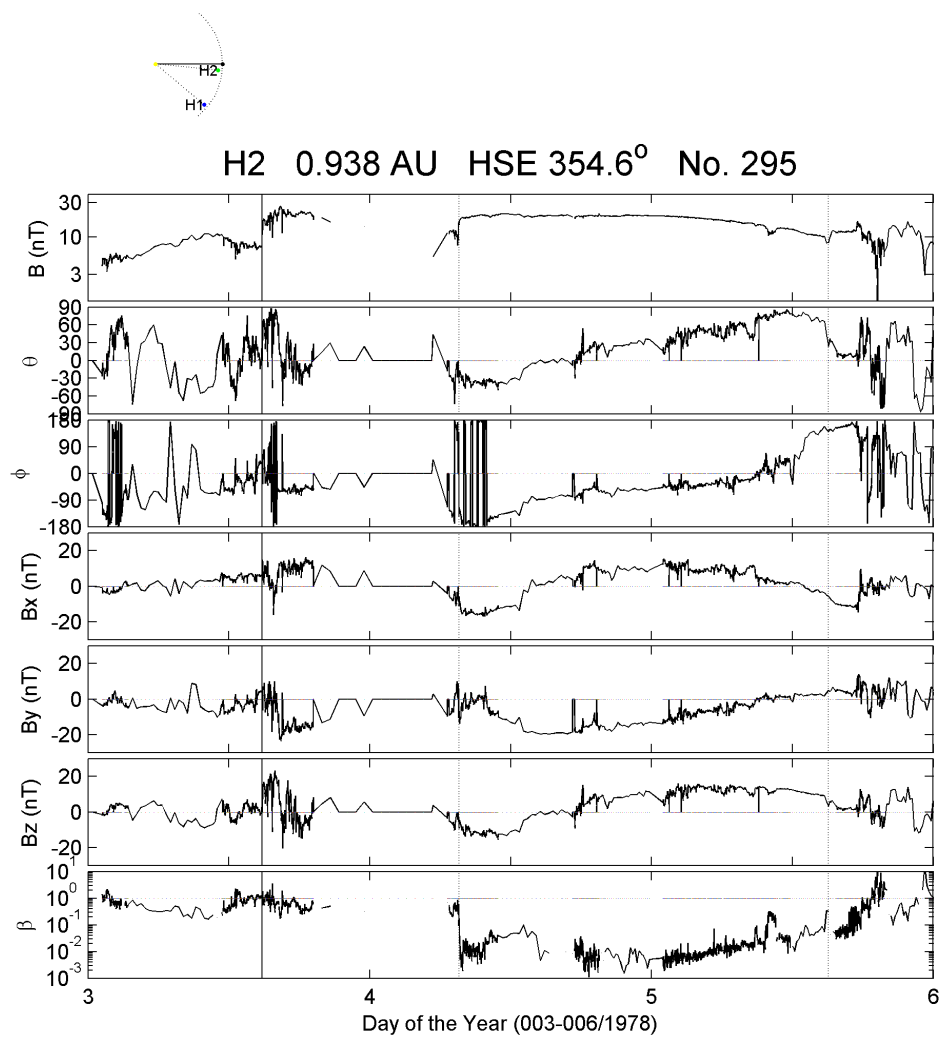


FIGURE 5.32 - H2 magnetic field data for the period from 003-006/1978. The plots give, from top to bottom, the profiles of the magnetic field strength, inclination and azimuthal angles, the components  $B_x$ ,  $B_y$  and  $B_z$ , and the plasma beta, respectively. The vertical continuous line identifies the shock wave, driven by the MC whose boundaries are represented by the dotted lines.

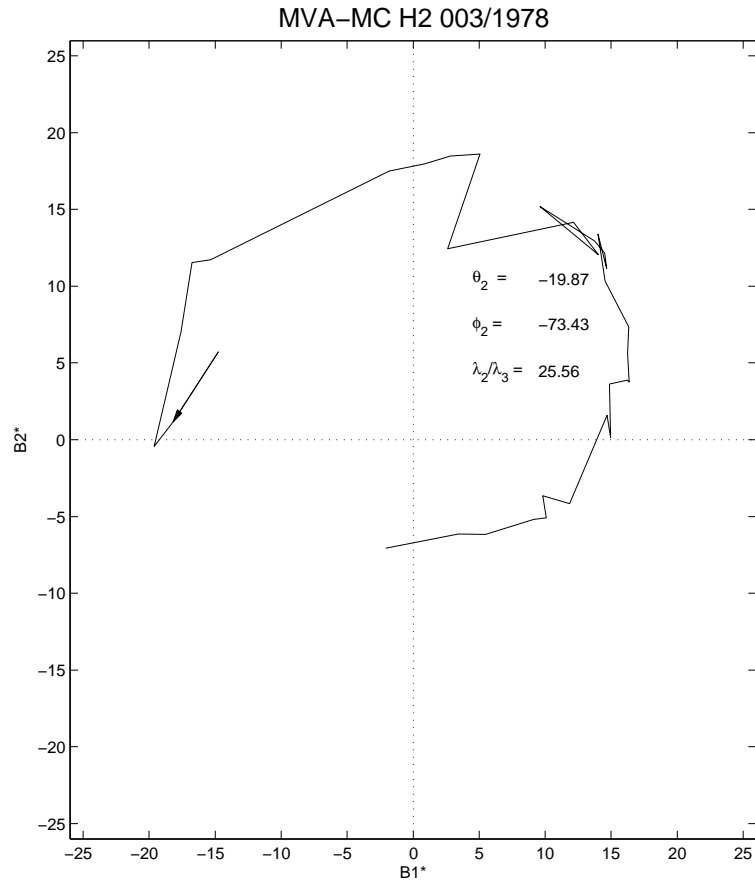


FIGURE 5.33 - Plane of maximum variance for the MC observed by H2 on DOYs 003-004/1978. Meaning similar to Figure 5.25.

direction, the orientation of the MC does correspond to the one defined on Bothmer and Schwenn (1998) for SWN MCs.

The proximity of the location of H2 and IMP-8 in the inner heliosphere, as represented in the top of Figures 5.28 - all the observations from H1 and H2 provide the same representation on top of each plot - enables us to verify that the magnetic field and plasma properties were conserved in this small angular extension in the IP space.

From Figure 5.34, we can identify that the magnetic field increased at the shock by the same order as in H2. Furthermore, the sheath region behind the shock driven by the MC lasted about the same period in H2 and IMP-8. In relation to the angles described by the magnetic field vector,  $\vec{B}$ , despite the data gaps present in IMP-8 measurements,  $\theta$  and  $\phi$  apparently describe the same directions in both spacecraft.

Plasma parameters behave similarly if one compares Figures 5.31 and 5.34. In both probes the proton speed was the typical speed of the slow solar wind, however, at the shock and, later on, its values increased to values around  $700 \text{ km/s}$ . For the proton temperature and density, magnitudes of about the same order are respectively registered at each probe.

Interestingly at the end of the MC, according to the boundaries we defined, a shock wave is observed inside the MC. The abrupt jump on the values of the magnetic field strength, proton speed and temperature, mainly, identify the shock wave. Some studies of shock waves identified inside magnetic clouds have been already carried out (COLLIER et al., 2007).

Notwithstanding data gaps present in the period, the rotation on the components  $B_x$ ,  $B_y$ , and  $B_z$  follows the same patterns as observed previously at H2 plots (Figure 5.35). Applying the MVA method on these components, the smooth rotation of the magnetic field inside the MC, considering the boundaries defined by the dotted lines in Figure 5.35, is represented in Figure 5.36. The values found are different from the ones obtained applying the MVA technique at H2 magnetic field data. This might be due to the ambiguity of the technique (WALKER et al., 2002; ECHER et al., 2006).

A magnetic storm, classified as intense due to its peak value ( $Dst_p = -121 \text{ nT}$ ), was registered at the terrestrial magnetosphere on DOY 005/1978, as shown in Figure 5.37. It was a result of the southward turning of the magnetic field as provided by the observations from IMP-8.

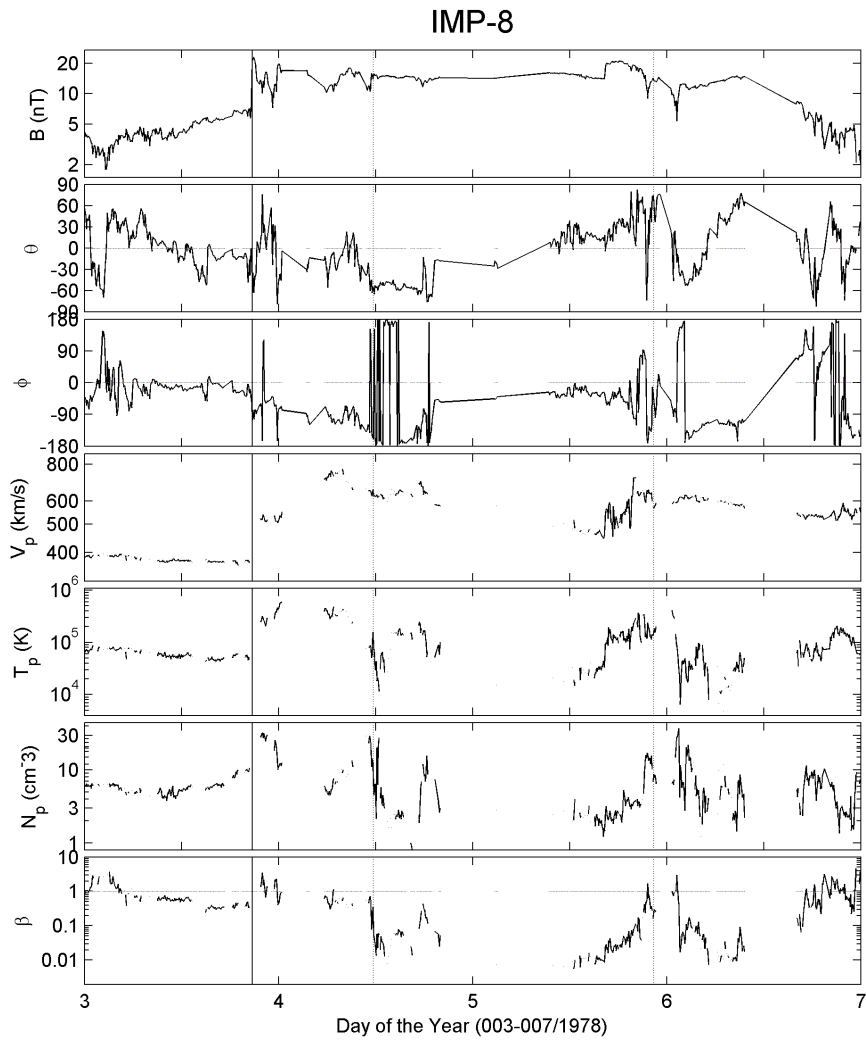


FIGURE 5.34 - IMP-8 observation of a MC on DOY 004/1978, at 11:00 UT, to DOY 005/1978, at 20:00 UT. Meaning similar to [Figure 5.4](#).

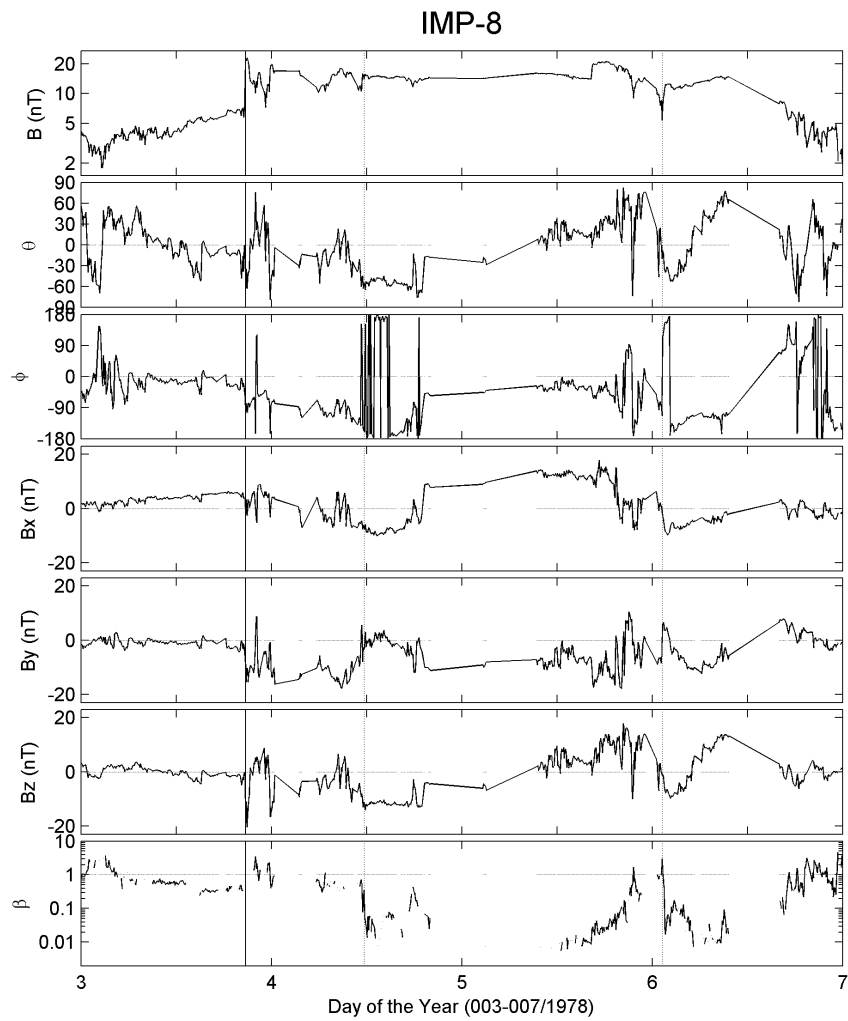


FIGURE 5.35 - IMP-8 magnetic field data for the period from 003 to 007/1977. The plots give, from top to bottom, the profiles of the magnetic field strength, inclination and azimuthal angles, the  $B_x$ ,  $B_y$  and  $B_z$  components, and the plasma beta, respectively. The vertical continuous line identifies the shock wave, driven by the MC whose boundaries are represented by the dotted lines.

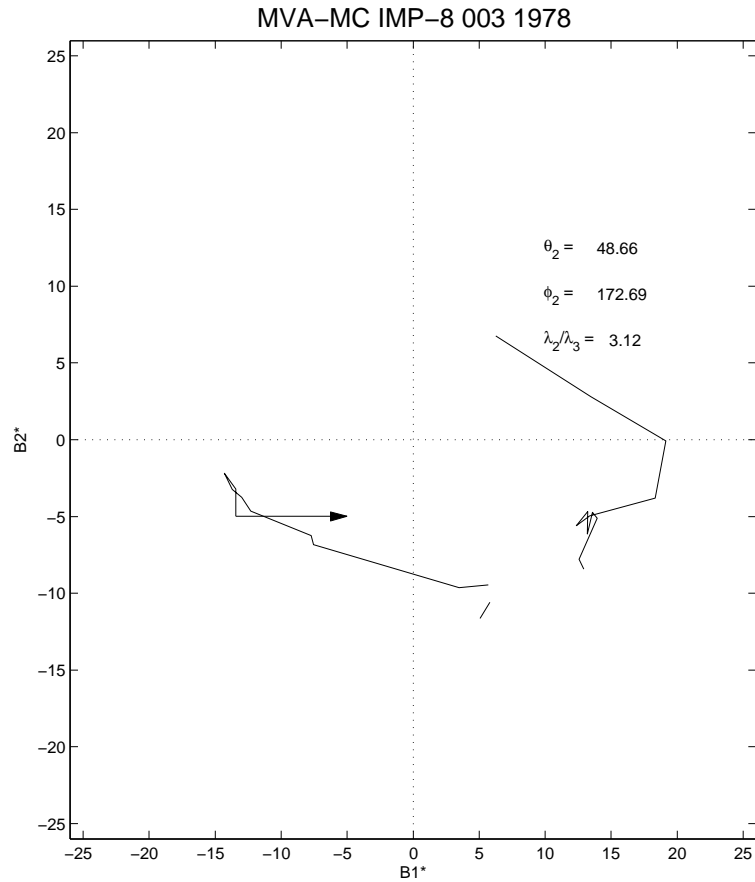


FIGURE 5.36 - Plane of maximum variance for the MC observed by IMP-8. Meaning similar to [Figure 5.25](#).

### 5.3.6 MC observed on DOY 046/1978 by H1 and H2

After a very turbulent sheath region behind the shock wave driven in the IP medium on DOY 46/1978, a MC was observed at H1 and H2. From [Figure 5.38](#), it is possible to identify the MC at H1 by the rotation in  $\phi$  from about  $180^\circ$  to  $-90^\circ$ , as well as by the smoothness of the magnetic field inside the cloud. In the proton density profile, a decrease is observed inside the structure, and plasma beta goes down due to the dominance of the magnetic pressure.

From [Figure 5.39](#), it is possible to see the variation on the magnetic field components, characterizing the rotation observed in the magnetic field azimuthal angle. The rotation is basically concentrated in the x-y plane, since  $B_x$  and  $B_y$  change their signal as they rotate. Through the  $B_z$  component, one notices that it remains close to 0 nT but mostly with small positive values. This characterizes a highly inclined

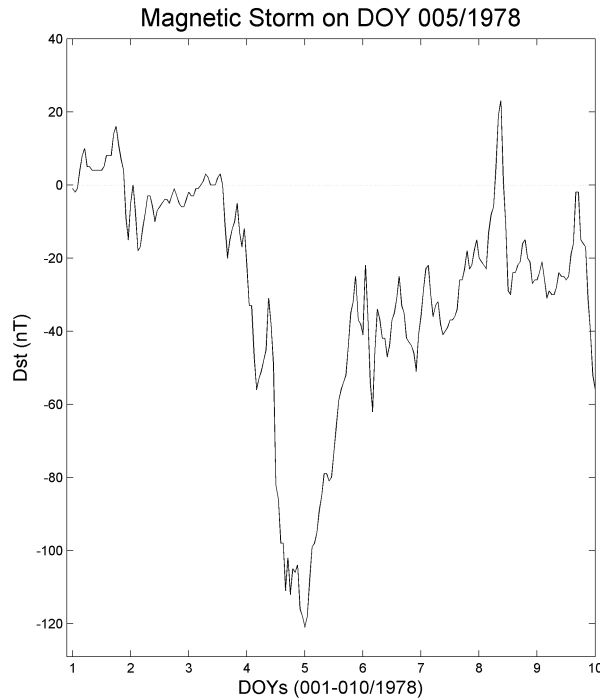


FIGURE 5.37 - Intense geomagnetic storm ( $Dst_p = -121 \text{ nT}$ ) registered on DOY 005/1978, at 00:00 UT.

MC as suggested by [Bothmer and Schwenn \(1998\)](#) and [Mulligan et al. \(1998\)](#). At the middle of the cloud,  $B_z$  goes to small negative values, however, it goes back to zero and then to positive values, as one observes in [Figure 5.39](#). Based on the magnetic field components rotation, we classify this cloud as a ENW MC-type ([MULLIGAN et al., 1998](#)).

The maximum variance plane identifies the cloud through the rotation in the maximum and intermediate variances. The cloud's axis is defined according to the angles  $\theta_2 = -73.8^\circ$  and  $\phi_2 = 83^\circ$ , corresponding to a highly inclined MC, as previously discussed. The estimated error,  $\lambda_2/\lambda_3 = 4.2$ , is inside the acceptable range ( $\lambda_2/\lambda_3 > 2$ ).

Closer to the Earth's orbit, H2 observed the same MC, identified by the rotation on the magnetic field, and on the inclination and azimuthal angle, as shown in [Figure 5.41](#). The smoothness on the magnetic field is also observed inside the considered interval for the MC. According to the interval chosen, the MC lasted for more than two days with visible signatures in all parameters. Inside the cloud, the proton den-



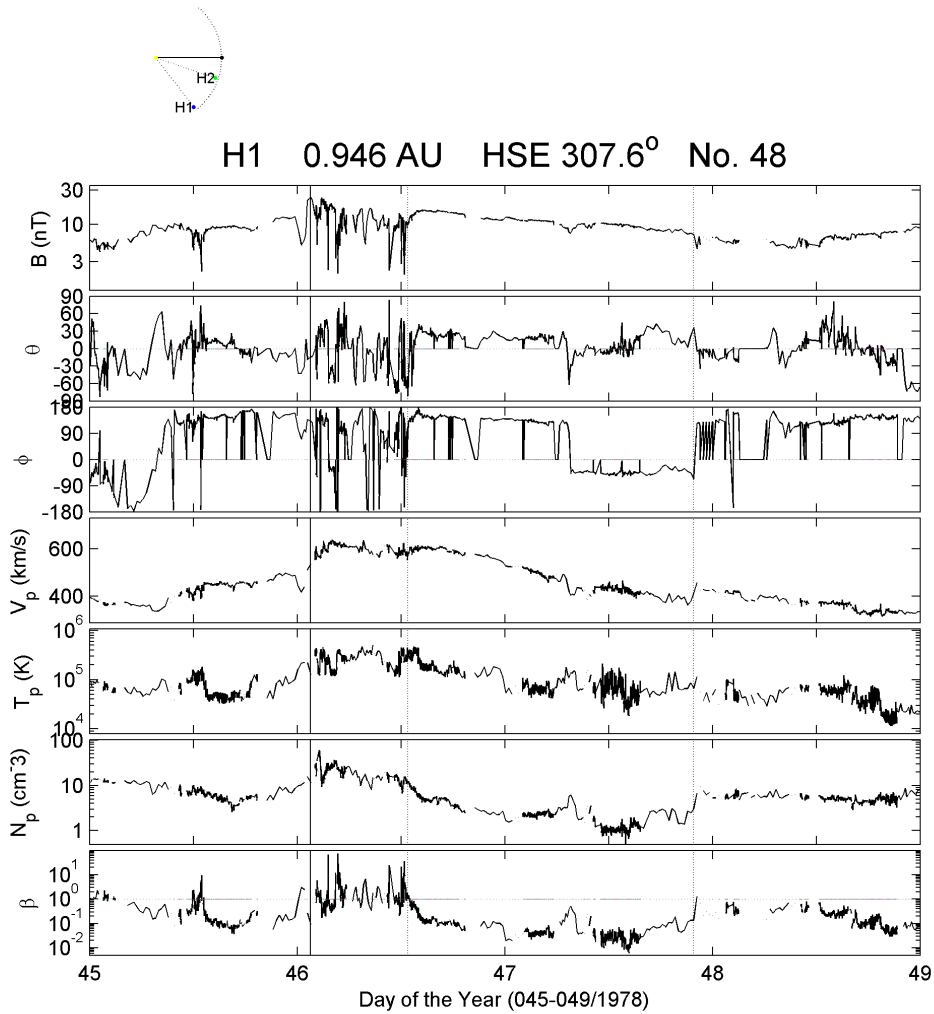


FIGURE 5.38 - H1 observation of a MC from DOY 046, at 12:46 UT, to DOY 047/1978, at 21:50 UT. Meaning similar to [Figure 5.4](#).

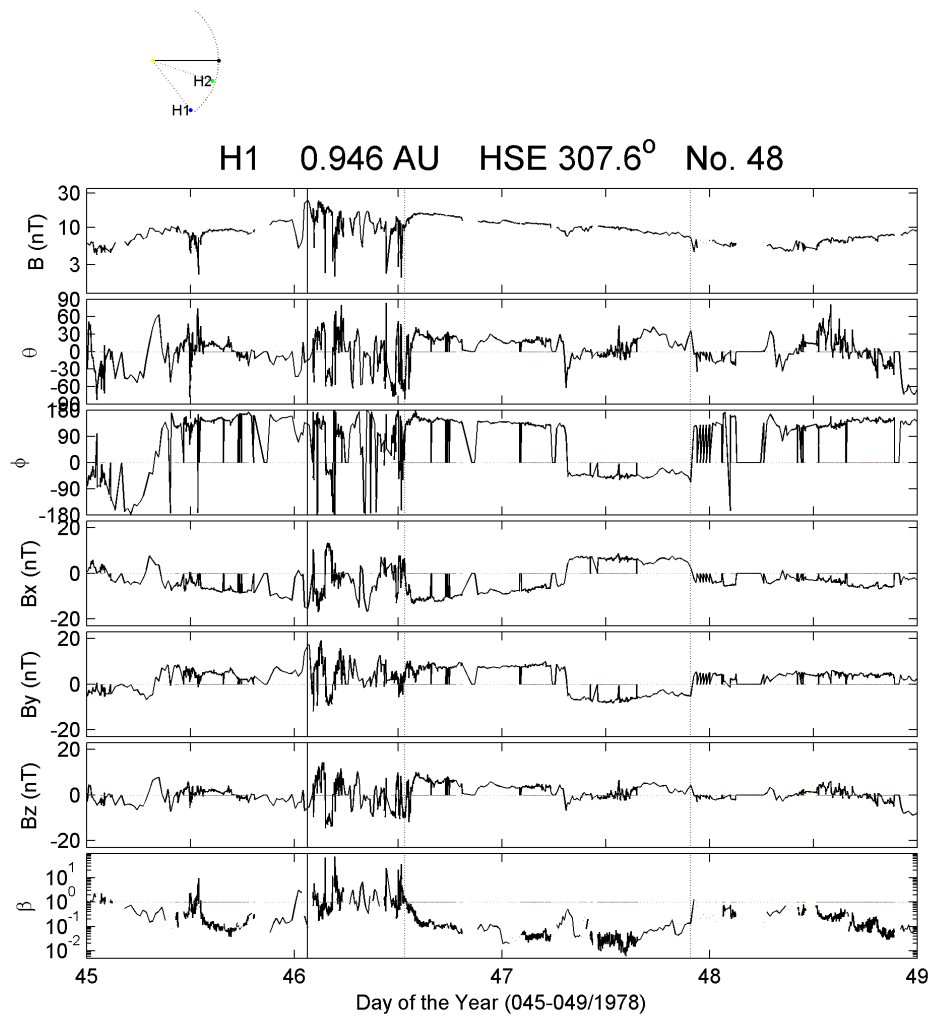


FIGURE 5.39 - H1 observation of a MC from DOY 046/1978, at 12:46 UT, to 047/1978, at 21:50 UT. The plots give, from top to bottom, the profiles of the magnetic field strength, inclination and azimuthal angles, the components  $B_x$ ,  $B_y$  and  $B_z$ , and the plasma beta, respectively. The vertical continuous line identifies the shock wave, driven by the MC whose boundaries are represented by the dotted lines.

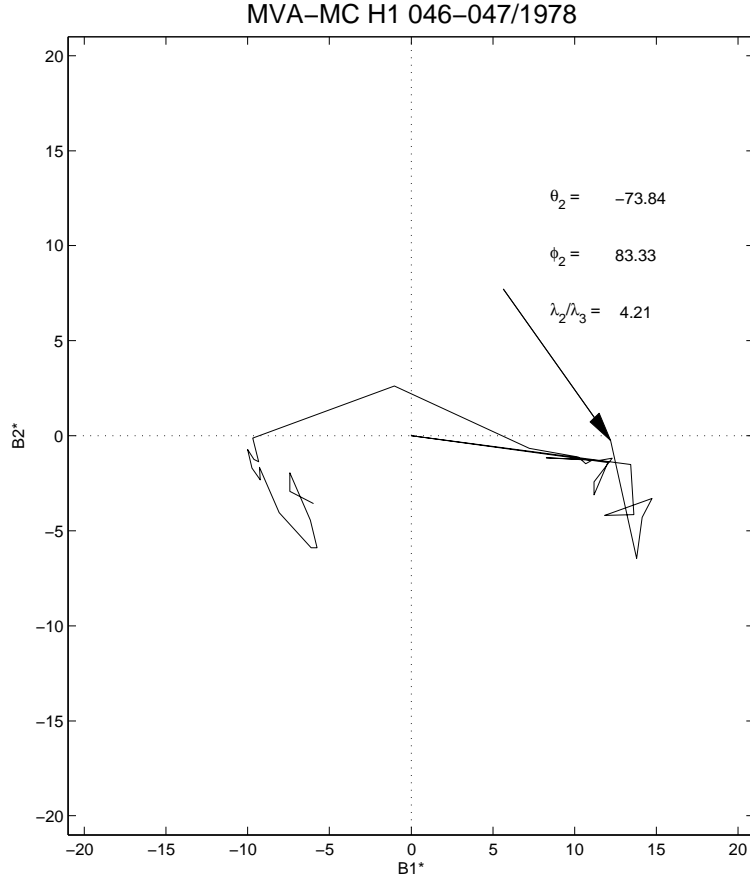


FIGURE 5.40 - Plane of maximum variance analysis for the cloud on DOY 046-047/1978. Meaning similar to [Figure 5.25](#).

sity dropped, decreasing the intensity of the plasma pressure, thus the magnetic field prevails in relation to the plasma, characterizing the low beta values found in the period.

From [Figure 5.42](#), one identifies that the rotation on the magnetic field inside the cloud is concentrated in  $B_y$  and  $B_z$ , which characterizes a MC parallel to the ecliptic plane ([BOTHMER; SCHWENN, 1998](#)). As  $B_z$  goes from North to South, while  $B_y$  turns from East to West, however, it is mostly in the positive side (East), we classify the cloud as a NES MC-type. According to the criterion used by [Bothmer and Schwenn \(1998\)](#) for the orientation of the magnetic field inside MC parallel to the ecliptic plane, the orientation shown in [Figure 5.43](#) is in accordance with the NES MC-type.

The similarities between H1 and H2 in relation to the direction of the rotation of  $\vec{B}$  are basically seen in the  $B_y$  component whose direction corresponds to the one seen

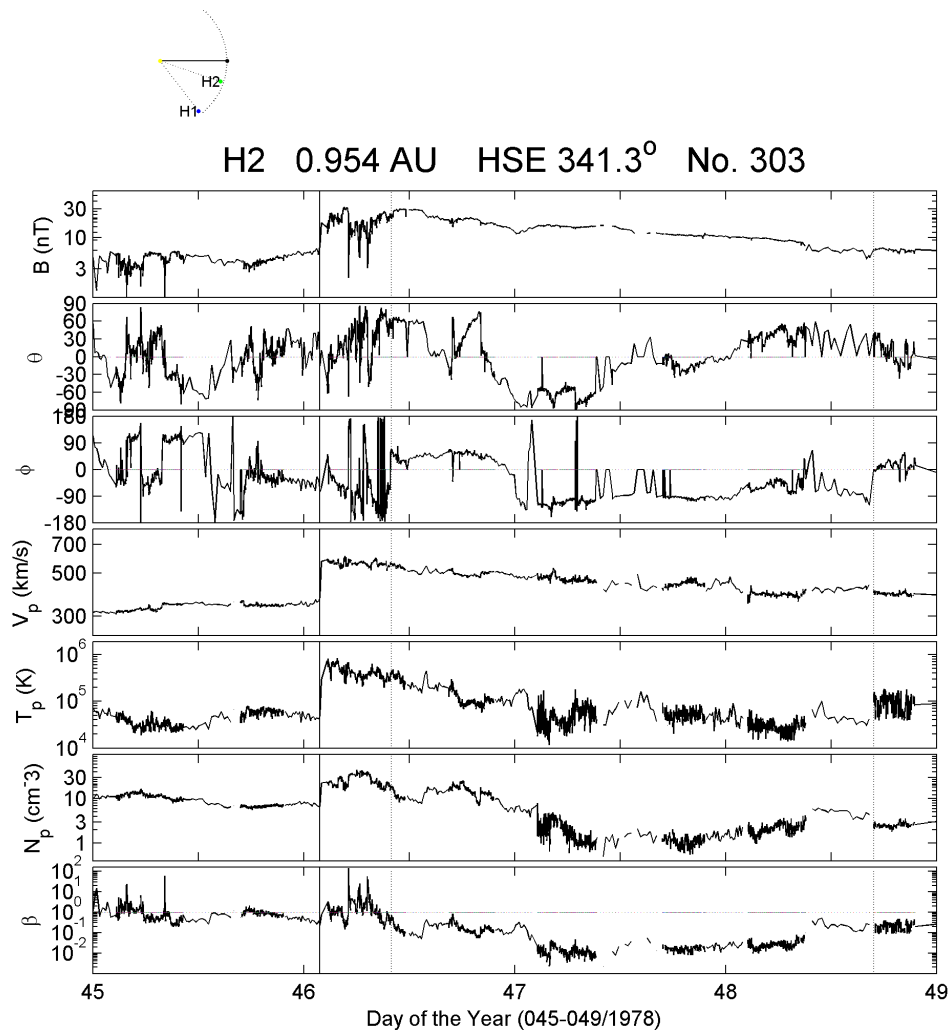


FIGURE 5.41 - H2 observation of a MC from DOY 046, at 09:58 UT, to DOY 048/1978, at 16:51 UT. Meaning similar to [Figure 5.4](#).

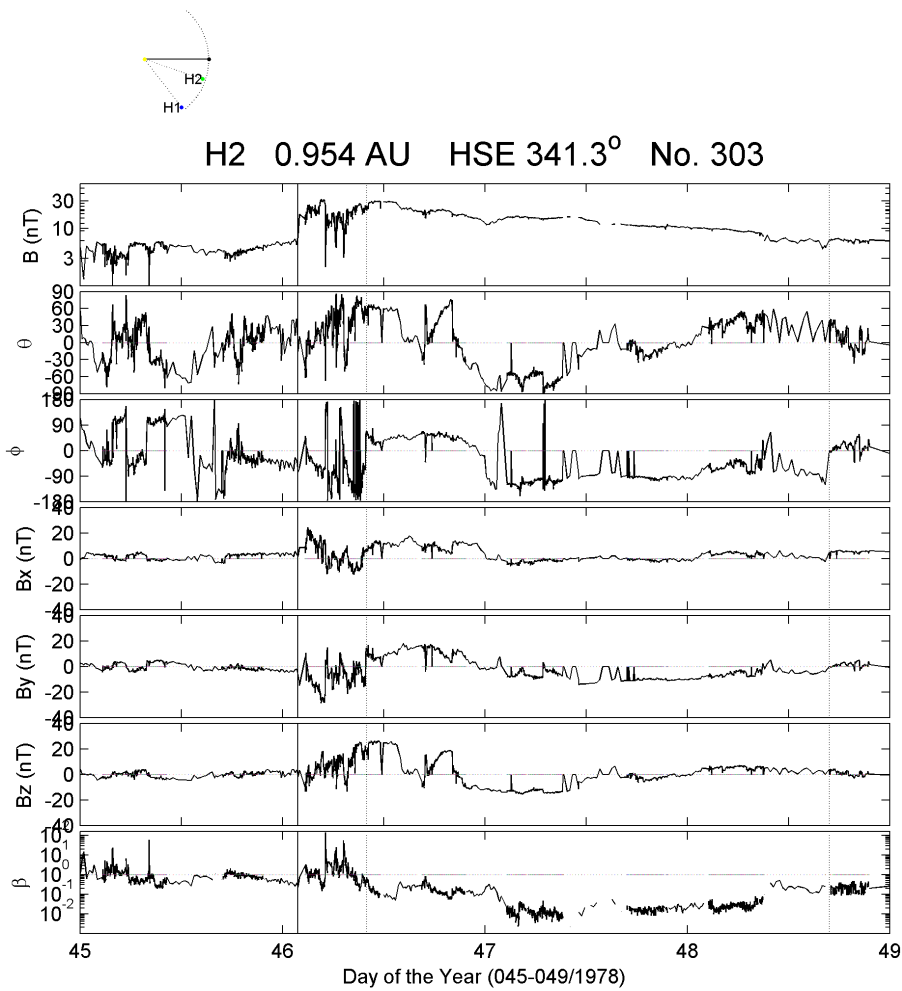


FIGURE 5.42 - H2 magnetic field data for the period from 045 to 049/1977. The plots give, from top to bottom, the profiles of the magnetic field strength, inclination and azimuthal angles, the components  $B_x$ ,  $B_y$  and  $B_z$ , and the plasma beta, respectively. The vertical continuous line identifies the shock wave, driven by the MC whose boundaries are represented by the dotted lines.

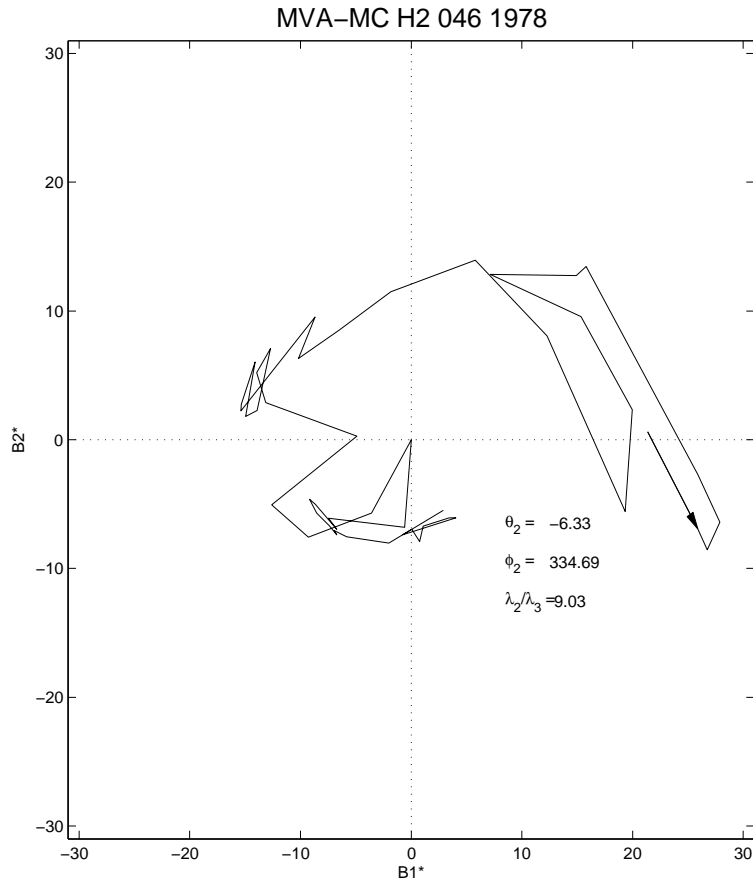


FIGURE 5.43 - Plane of maximum variance for the MC observed on DOYs 046-048/1978. Meaning similar to Figure 5.25.

in H1, as well as the rotation described by  $\phi$ . In  $B_x$ , the signal is contrary to the one observed at H1, and in  $B_z$  component observed by H2 one may notice the rotation, seen in H1  $B_z$  profile.

In spite of the fact that IMP-8 was inside the magnetosphere and that there was no monitoring of the region in front of the magnetosphere, an intense magnetic storm ( $Dst_p = -108 \text{ nT}$ ) disturbed the terrestrial magnetosphere on DOY 47/1978 registered at 12:00 UT, as shown in Figure 5.44. The presence of a southward  $B_z$  component ( $B_S$ ) in front of the magnetosphere led to magnetic reconnection and caused the injection of energy into the magnetosphere. Due to the coincidence on the time occurrence of the magnetic storm and the MC arrival time at H2, at  $0.954 \text{ AU}$ , we may expect that the MC, or the shock driven by it, reached the terrestrial magnetosphere leading to the geomagnetic disturbance.

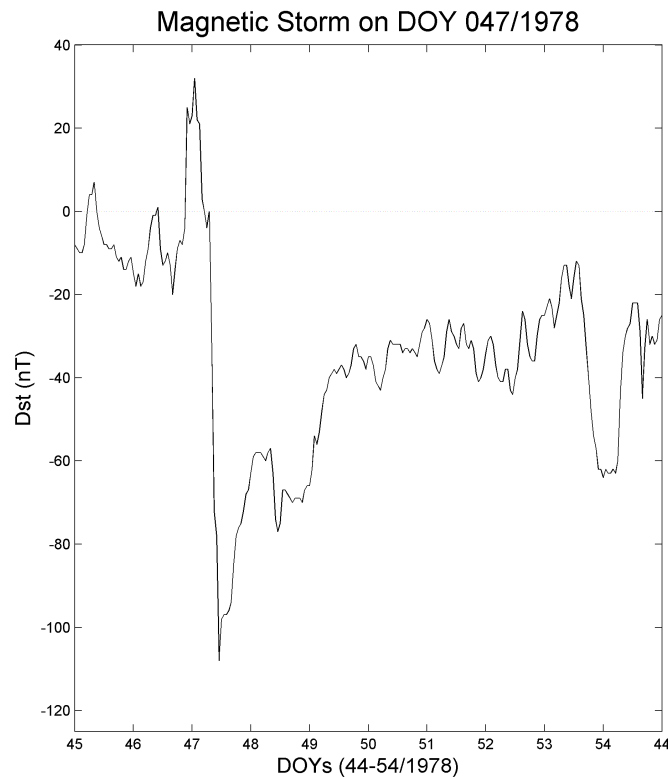


FIGURE 5.44 - Intense magnetic storm ( $Dst_p = -108 \text{ nT}$ ) registered on DOY 047/1978 at the terrestrial magnetosphere.

#### 5.4 Shock Wave observed by Multi-spacecraft where the Magnetic Cloud was observed by a single-spacecraft

During the entire time operation of the Helios mission, MCs were observed as the drivers of shock waves in the IP medium, more specifically in the inner heliosphere. MCs are a subclass of the ICMEs that in general form shock waves at the distance of  $1 \text{ AU}$ . Following some of the shocks identified by the spacecraft, MC signatures were observed by only one of them, although at least two spacecraft were operational. Nevertheless, the shock wave has been identified by two probes at least. In these situations one can think about the shape and the direction of propagation of the “ejecta” and find out that shock waves are bigger than the structures that drive them into the IP medium.

#### 5.4.1 MC observed on DOY 106/1978 only by H2

Traveling close to the Sun, at only 0.41  $AU$  of radial distance, H1 was about  $21^\circ$  separated from the Sun-Earth line, as one observes at the top of [Figure 5.45](#). According to the observations, H1 detected a shock wave at the second half of DOY 106/1978 ( $SN = 56$ ). Despite the data gaps present during this period, the shock is mainly visible by the jump on the plasma density profile, as shown in [Figure 5.45](#). Before the shock is registered by the plasma instrument, we assume that a HSS precedes this shock. The HSS is identified through the drop on the plasma density, followed by the increase on the protons speed and temperature.

Almost aligned with the Sun-Earth line, H2 has some indications of a MC that was probably the driver of the shock wave detected by H1 and H2. The speed of the propagating shock wave was not so big compared to the normal solar wind speed, what resulted in the weak shock observed in [Figure 5.46](#) by H2 ( $SN = 312$ ). However, the sheath region was not small (12  $hr$ ), followed by a clear MC on the solar wind and magnetic field profiles.

The MC is identified at H2 by the low plasma beta ( $< 0.1$ ), proton temperature and density. In addition to these parameters, the rotation in the magnetic field is described by  $\theta$ , as represented in [Figure 5.46](#). The magnetic field strength is also enhanced and very smooth inside the structure whose boundaries are illustrated by the dotted lines in [Figure 5.46](#). Through [Figure 5.47](#), one can observe the turning of the magnetic field in all its components. Based on them, one can classify the MC as a SEN type, based on the rotation of the  $B_y$  and  $B_z$  components. Applying the MVA technique in the interval of the MC, it results in a smooth rotation on the magnetic field whose orientation corresponds to the criterion defined by [Bothmer and Schwenn \(1998\)](#), as shown in [Figure 5.48](#).

According to [Figure 5.48](#), the rotation on the magnetic field is identified by the large turning on the maximum variance plane. The MC is inclined in  $\theta_2 = 33^\circ$  in relation to the ecliptic plane according to the intermediate variance. The error criterion for the MVA accuracy is satisfied since the ratio  $\lambda_2/\lambda_3$  is bigger than 2.

Note that the same HSS is observed in H2 profiles at the second half of DOY 107/1978, as identified by the solar wind parameters in [Figures 5.46](#) and [5.47](#). The fluctuations on the magnetic field angles, as well as in its components are in corre-



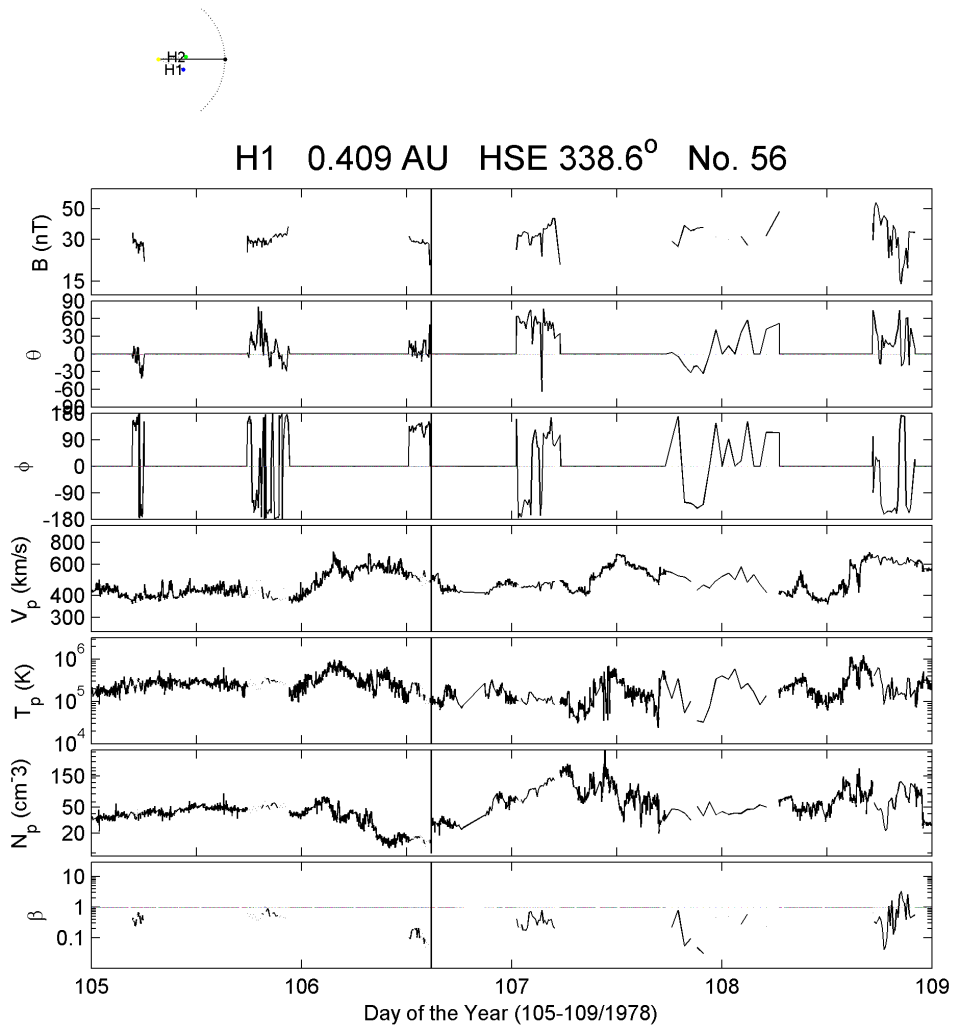
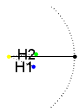


FIGURE 5.45 - H1 plasma and magnetic field data for the period from DOY 105 to 109/1978. The plots are given in the same sequence as in Figure 5.41. The vertical continuous line identifies the shock wave. There is no visible signatures for a MC.



H2 0.421 AU HSE 5.4° No. 312

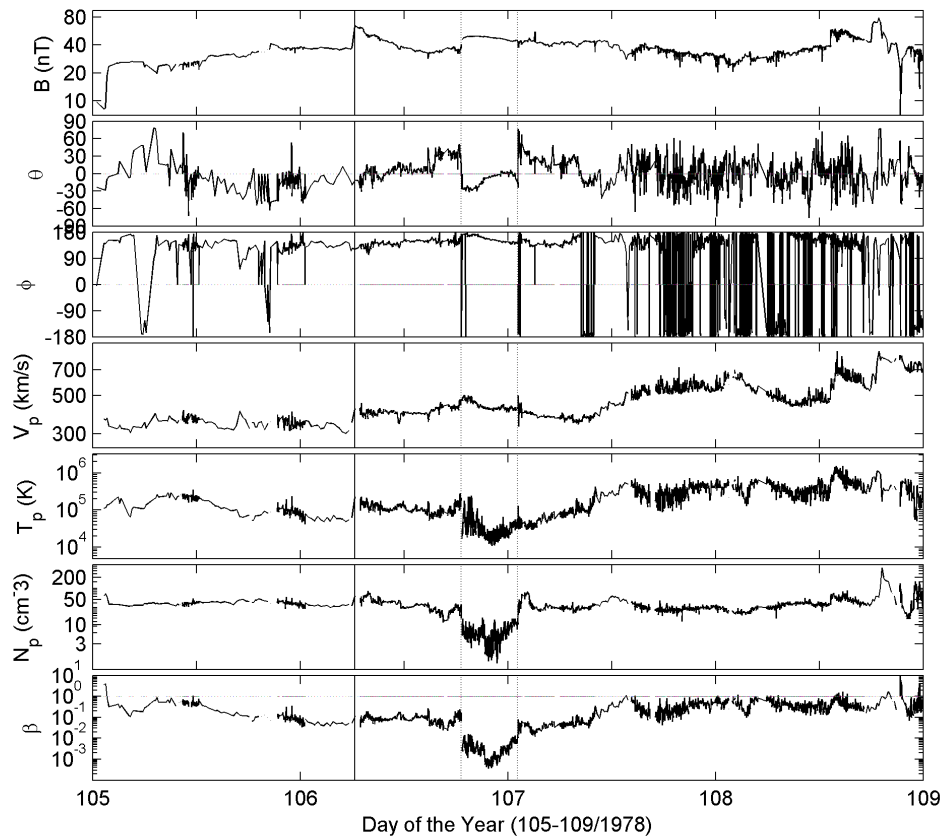


FIGURE 5.46 - H2 observation of a MC from DOY 106/1978, at 18:37 UT, to DOY 107/1978, at 01:08 UT. Meaning similar to [Figure 5.4](#).

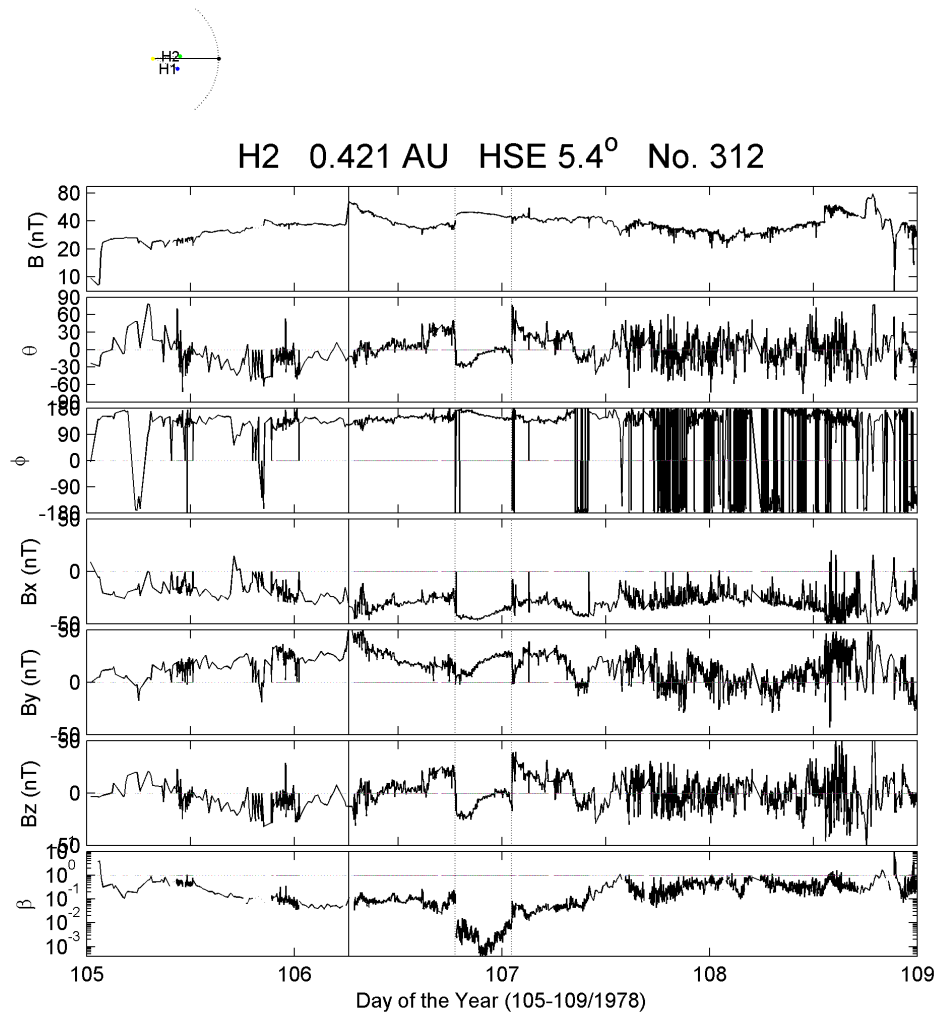


FIGURE 5.47 - H2 magnetic field data for the period from 105-109/1978. Meaning similar to [Figure 5.6](#).

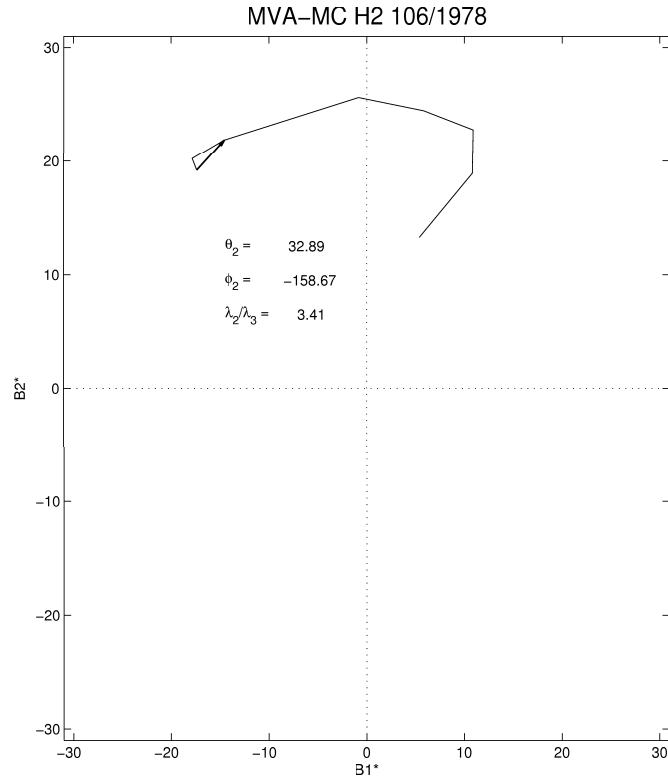


FIGURE 5.48 - Plane of Maximum variance for the MC observed on DOY 106-107/1978 by H2. Meaning similar to [Figure 5.8](#).

spondence with the decrease on the proton density and the subsequent increase on plasma speed and temperature.

Assuming that the HSS has an angular speed of  $14.4^\circ$  per day, and the separation of the two probes is about  $27^\circ$ , the observation of the HSS 1.5 day after H1 is very consistent. This HSS reached H1 before the MC did. Our best guess is that H1 observes the HSS first and H2 detects it afterward. The MC, on the other hand, is not visible on the signatures of H1 probably because it was swept away due to the presence of the HSS.

### 5.4.2 MC observed on DOY 058-059/1979 only by H1

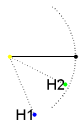
This event is another example of a shock wave seen by two probes where the MC was detected by only one of the probes. At the period of the event, H1 and H2 were separated by  $40^\circ$ . Both Helios were close to Earth's orbit, as we observed on top of [Figure 5.49](#).

At the beginning of DOY 058/1979, a shock wave was identified by H1 and, about 12 *hr* later, a MC traveled crossing the probe at almost 1 *AU*. This MC was the driver of the strong shock wave that reached H1, increasing all the solar wind parameters and the magnetic strength. Through the low beta values, in correspondence with the low plasma temperature and density, the MC was identified. The rotation of the magnetic field is not so strong, as it is shown in [Figure 5.49](#), probably because the probe is crossing a region far from the center of the cloud. Notwithstanding, one can see the rotation of the field, even if it is weak. According to the direction of the rotation of the components, we classify this MC as a WNE MC-type.

The magnetic field did not have a smooth rotation characteristic of the MC. Nevertheless, the limits of the cloud were assumed to be similar to the ones considered in [Bothmer and Schwenn \(1998\)](#). The cloud's axis obtained in their work is similar to the one estimated by us, despite the ambiguity of  $180^\circ$  on the MVA technique. The angles  $\theta_2$  and  $\phi_2$ , are, respectively,  $78^\circ$  and  $-149^\circ$ . The former is the negative of  $\theta$  with an error of approximately  $11^\circ$  of the one estimated in the work of [Bothmer and Schwenn \(1998\)](#). On the other hand, the latter is rotated by  $-180^\circ$  when compared to the estimate in [Bothmer and Schwenn \(1998\)](#).

There is a shock at H2 at the end of DOY 058/1979, identified by the solar wind and magnetic field parameters, as shown in [Figure 5.51](#). This shock probably corresponds to the same shock observed previously at H1, considering the separation between the two probes.

According to the cloud's axis angles, this MC was highly inclined in relation to the ecliptic plane, which was the reason for not being observed by H2 ([Figure 5.50](#)). Furthermore, when MCs are highly inclined, one has less chance to cross the structure, differently from the MCs that are close to the ecliptic plane. The MCs whose axes are parallel to the ecliptic plane are more likely to be detected for more than one probe.



H1 0.957 AU HSE 293.2° No. 104

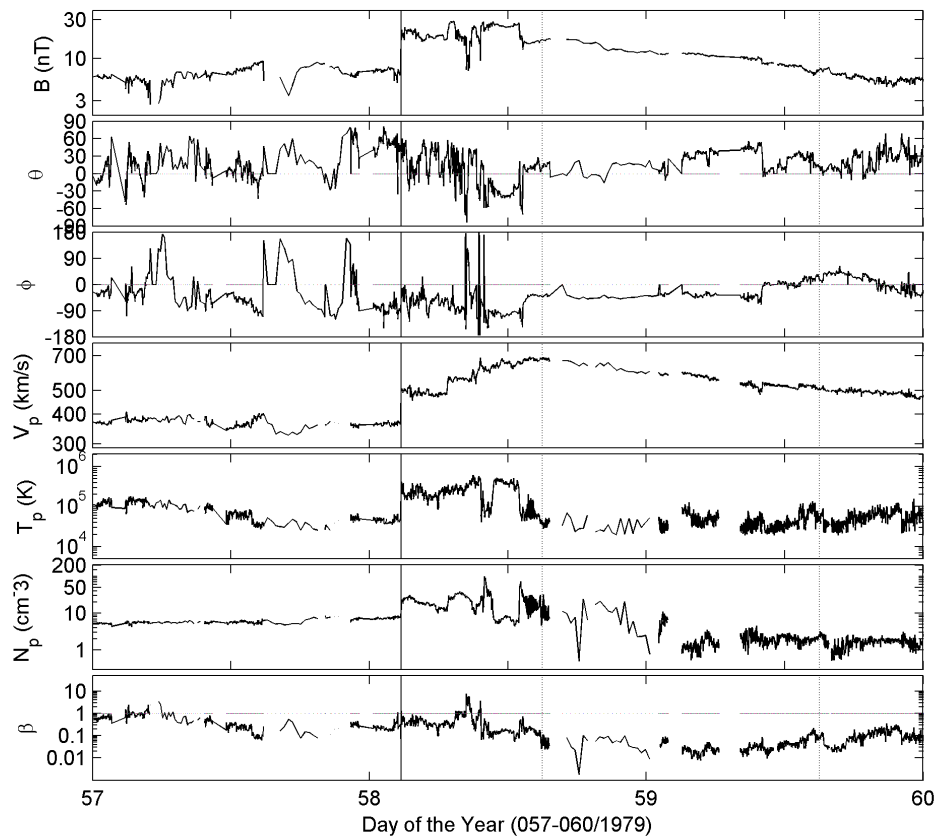


FIGURE 5.49 - H1 observation of a MC on DOY 058/1979, at 15:00 UT, to 059/1979, at 15:00 UT. Meaning similar to [Figure 5.4](#).

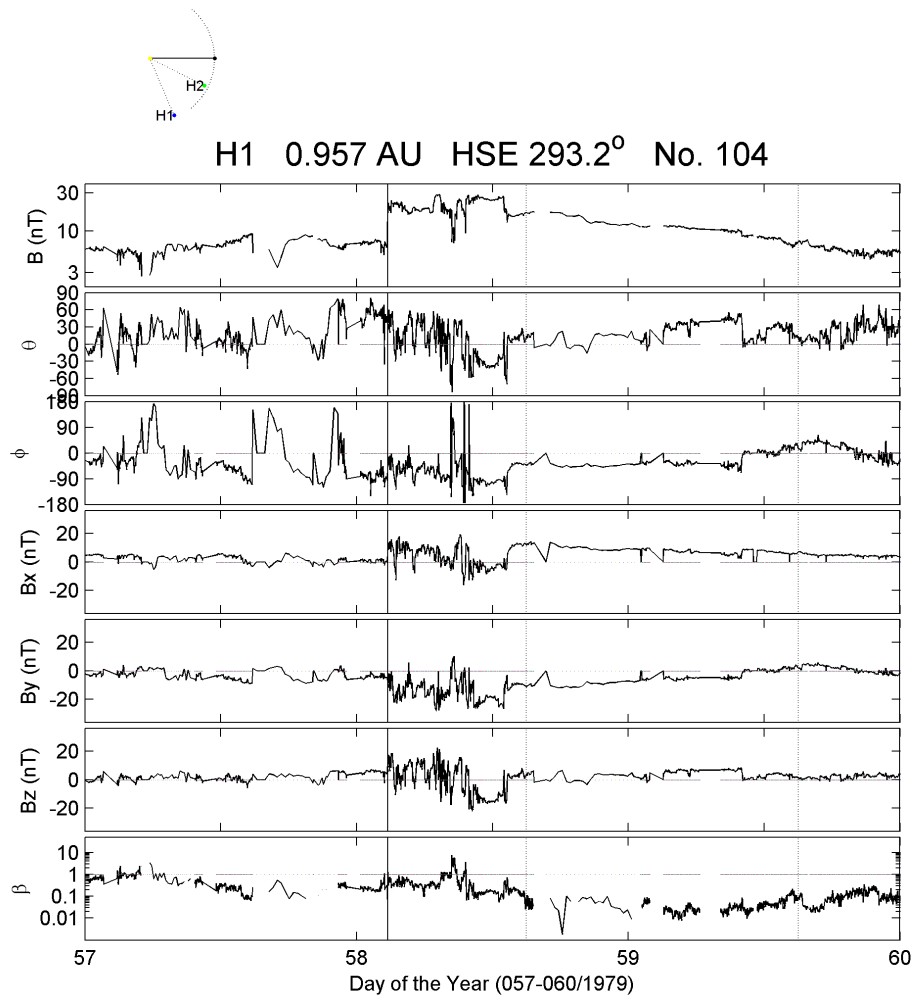


FIGURE 5.50 - H1 magnetic field data for the period from 057-060/1979. Meaning similar to [Figure 5.6](#).

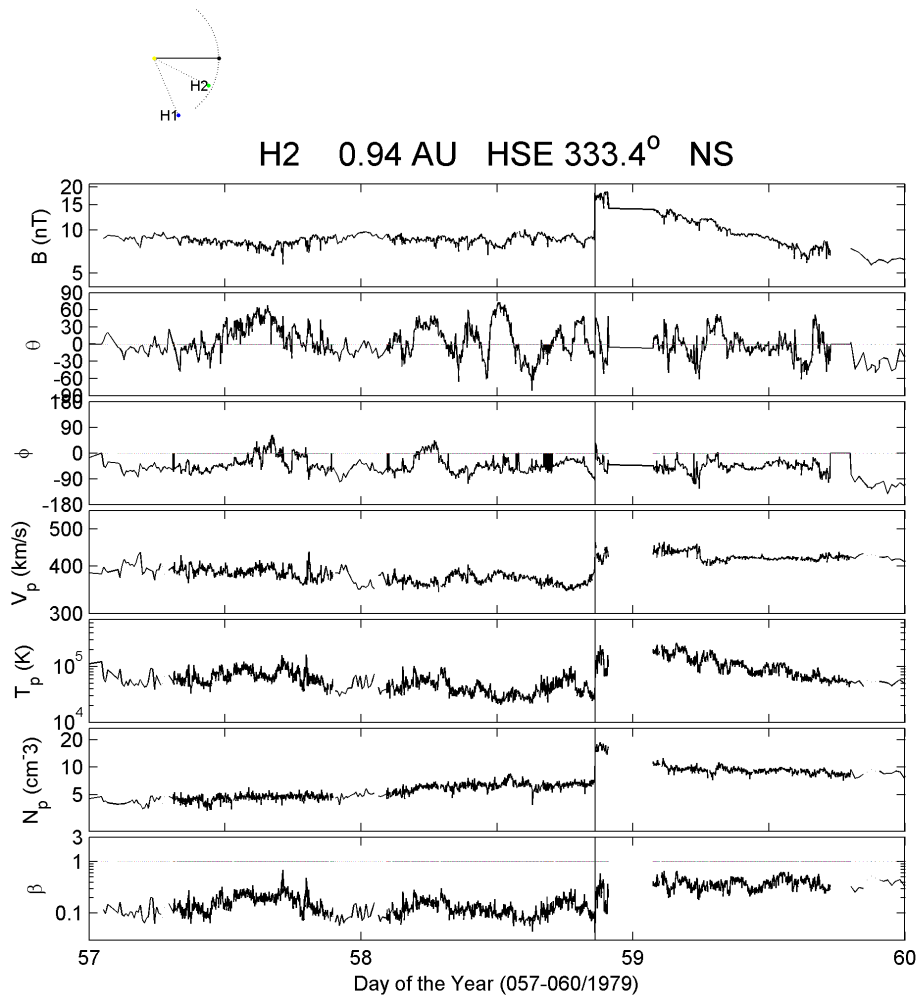


FIGURE 5.51 - H2 monitoring of the period from DOY 057 to 060/1979. The plots give, from top to bottom, the profiles of the magnetic field strength, and inclination and azimuthal angles, the protons speed, temperature, and density, and the plasma beta, respectively.



### 5.4.3 MC observed on DOY 175/1979 by H1

Traveling at radial distances of the order of 0.74 and 0.82  $AU$ , H1 and H2, respectively, provided the coverage of the solar environment in the far side of the Sun. Not only structures traveling toward Earth, but also a fully understanding of the solar activity in different parts of the inner heliosphere, were the tasks of the Helios mission.

As observed by H1 (Figure 5.52), a shock wave is detected by the solar wind and magnetic field instruments onboard the probe. The shock is weak and identified by the jumps on the IMF strength, proton speed, temperature and density because gaps are present at the time the shock was supposed to be detected. To confirm the presence of the shock, a MC is observed some hours later. Recognized by the smooth rotation on the magnetic field and the increase on its values inside the structure, the MC lasts for a few hours, as represented by the dotted lines in Figure 5.52. Besides, the plasma beta is very low inside the structure, as well as the proton density and temperature.

At the rear part of the MC, delimited by the dotted line in Figure 5.52, a HSS is observed by the increase on the proton speed and temperature and the consequent drop on proton density. The angle  $\phi$  still rotates, as one observes in Figure 5.53, following the same pattern as  $B_y$ . This is probably due to the interaction between the two structures, where the innermost rotation of the MC is still registered by the instruments onboard H1. The HSS arrival probably caused the short duration of the MC, as one observes in Figure 5.52.

The IMF components, represented in Figure 5.53, show the smooth rotation described by each of the components. The strongest rotation is observed in  $B_y$  that is always positive inside the structure, what means that probably this cloud has its axial magnetic field pointing to East (E). Since  $B_z$  turns from negative to positive values, one may suggest that this cloud is probably on the ecliptic plane. In this sense, we classify the MC in the group of the SEN MCs, based on the direction of rotation of the component.

The plane of maximum variance, illustrated in Figure 5.54, confirms the previous suggestion for the orientation of the MC. Since  $\theta_2 = -17^\circ$  and  $\phi_2 = -115^\circ$  correspond to the angles of the cloud's axis orientation, one identifies the MC propagating

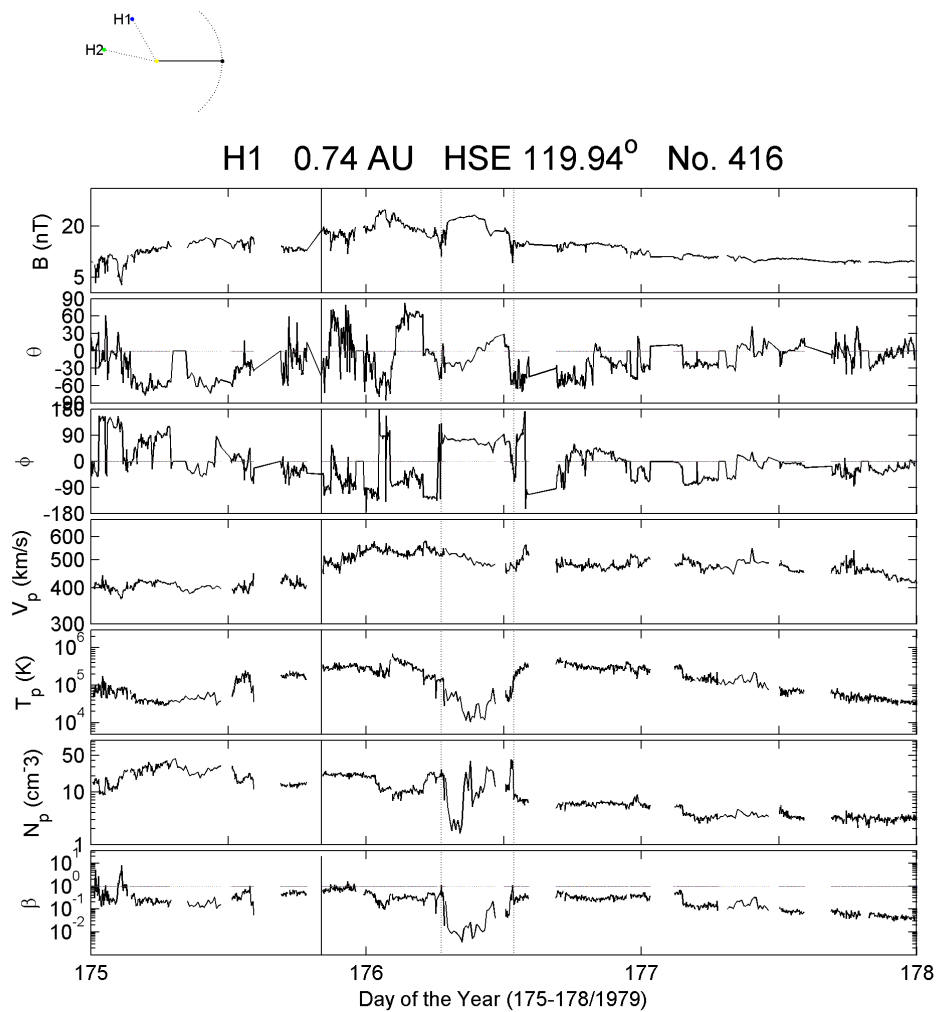


FIGURE 5.52 - H1 observation of a MC on DOY 176/1979, from 06:32 to 12:54 UT. Meaning similar to Figure 5.5.

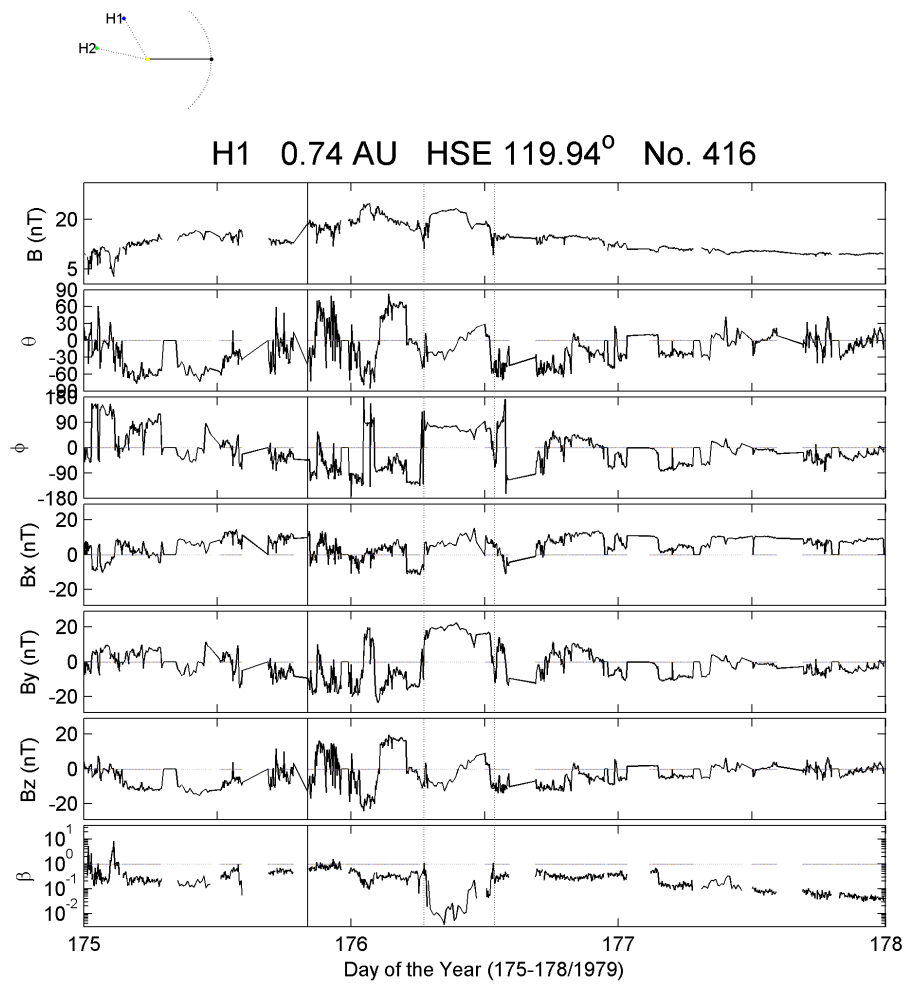


FIGURE 5.53 - H1 magnetic field data for the period from DOY 175-178/1979. Meaning similar to [Figure 5.6](#).

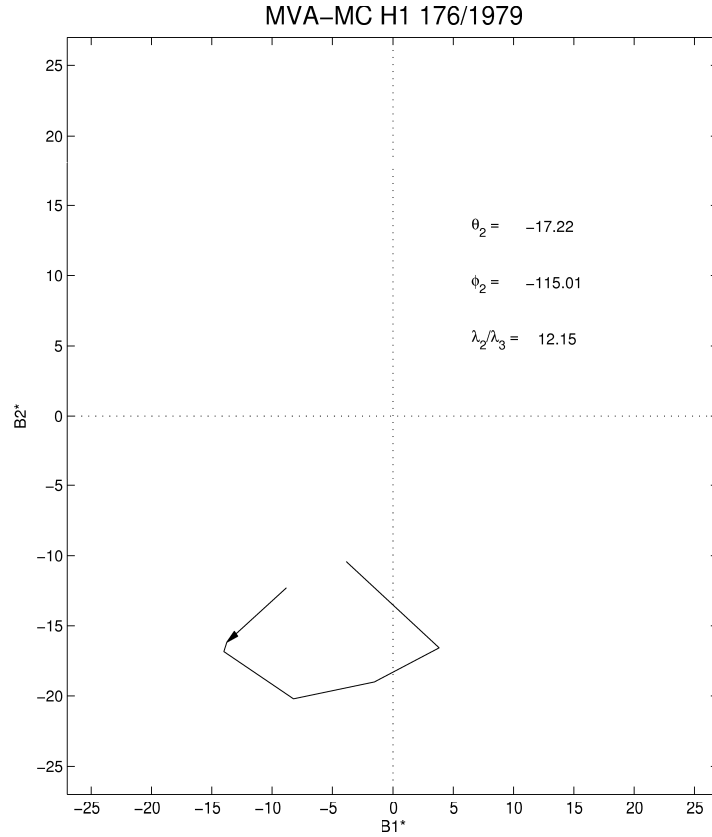


FIGURE 5.54 - Plane of Maximum Variance for the MC observed on DOY 176/1979 by H1. Meaning similar to [Figure 5.8](#).

away from the far side of the Sun, parallel to the ecliptic plane. Considering the ambiguity of  $180^\circ$ , we identify that the orientation of the magnetic field, given by the local MVA analysis, corresponds to the one defined by the MCs' classification criterion as presented by [Bothmer and Schwenn \(1998\)](#).

About  $48^\circ$  away from H1, still at the far side of the Sun, H2 observes a shock wave. However, there is no visible signatures for a MC, as shown in [Figure 5.55](#). A HSS that cannot be the same observed at H1 arrives before the shock wave. It increases the speed of the medium, but does not prevent the shock formation as observed by H2. The second HSS, first observed at H1, was not completely registered by the instruments onboard H2. Data gaps filled part of the period when the HSS was expected to pass through the probe (about 3 days, considering the rate of  $14.4^\circ$  per day). Nevertheless, the beginning of the structure is identified, despite the low

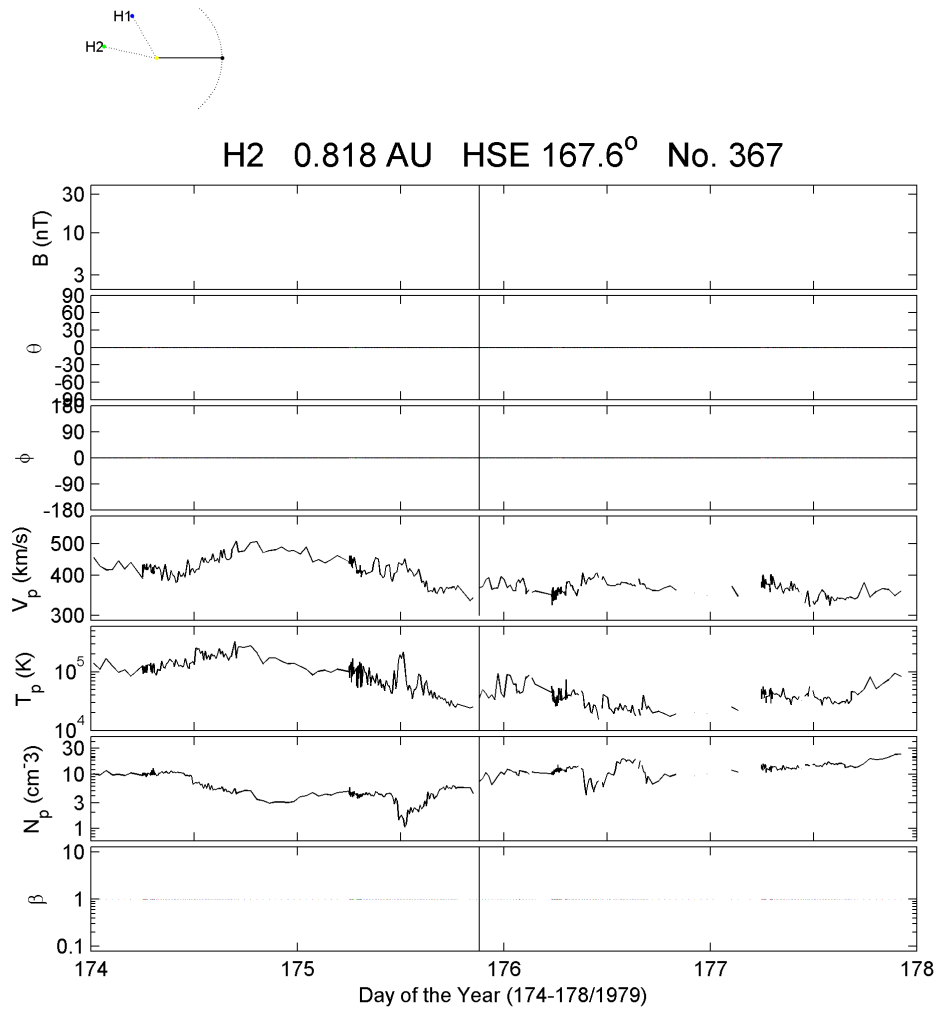


FIGURE 5.55 - H2 observation of a shock wave on DOY 175/1979. The plots are given in the same sequence as in Figure 5.41. The same MC was not observed by the solar wind instruments. From the magnetic field instruments we do not have any data provided by them, so differentiating the structures in the IP medium becomes more difficult. Nevertheless, a HSS precedes the shock arrival on DOY 175/1979.

resolution of the solar wind data. At the second part of DOY 177/1979, the increase on the plasma temperature and speed and the consequent drop on the proton density is assumed to characterize the arrival of the HSS at H2.

## 5.5 Magnetic Clouds and Shock Observed by a Single-Spacecraft

### 5.5.1 MC observed on DOY 78/1977 only by H1

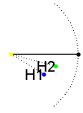
This is a very interesting case of a shock wave and MC observed by H1 only, although there was a small angle separating the two probes ( $\Delta\Phi = 16^\circ$ ), as shown on top of [Figure 5.56](#).

According to [Figure 5.56](#), a MC was identified at H1 as the driver of a shock wave ( $SN = 28$ ), already addressed in [Chapter 4](#). The MC extended itself from DOY 078/1977, at 21:20 UT, to 079/1977, at 08:21 UT. The MC is identified by the smoothness of the magnetic field, the low plasma beta, in accordance with the low density. Even though plasma beta is low already before the time we identified the front part of the MC, we consider the determinant parameter as the density discontinuity inside the MC.

From [Figure 5.56](#), one identifies the rotation on the components of the IMF inside the MC. On the magnetic field angles,  $\theta$  and  $\phi$ , one can identify the rotation inside the structure. The angle  $\theta$  rotates from about  $+30^\circ$  to  $-30^\circ$ , while  $\phi$  goes from about  $+90^\circ$  to  $-90^\circ$ , resulting on the rotations on the components observed in [Figure 5.57](#). Note that  $B_x$  rotates strongly, but it is always positive, while  $B_y$  component goes from positive to negative values inside the MC. Considering that  $B_z$  component is basically negative in the whole structure, we classify this cloud as belonging to the highly inclined group of MCs. Based on the direction of the components, we classify it as a ESW MC-type.

Identified the boundaries of the MC, we can apply a local MVA analysis in order to identify the rotation on the magnetic field through the maximum variance plane, and the cloud's axis, given by the estimate of the angles for the intermediate variance. [Figure 5.58](#) is the result of the MVA technique applied to the MC observed at H1 profiles on DOYs 078-079/1977. According to the intermediate variance, the cloud's axis is directed according to  $\theta = 46^\circ$  and  $\phi = -176^\circ$ , which shows that this MC is indeed inclined (about  $46^\circ$  in relation to the ecliptic plane). This is in accordance with our previous assumption, based on the magnetic field components.

At only  $16^\circ$  away from H1, H2 did not register any signatures regarding a shock wave during the period from DOY 076-081/1977, as the plots of [Figure 5.59](#) show. However, at the beginning of DOY 80/1977, a HSS is identified by the increase on



H1 0.575 AU HSE 329° No. 28

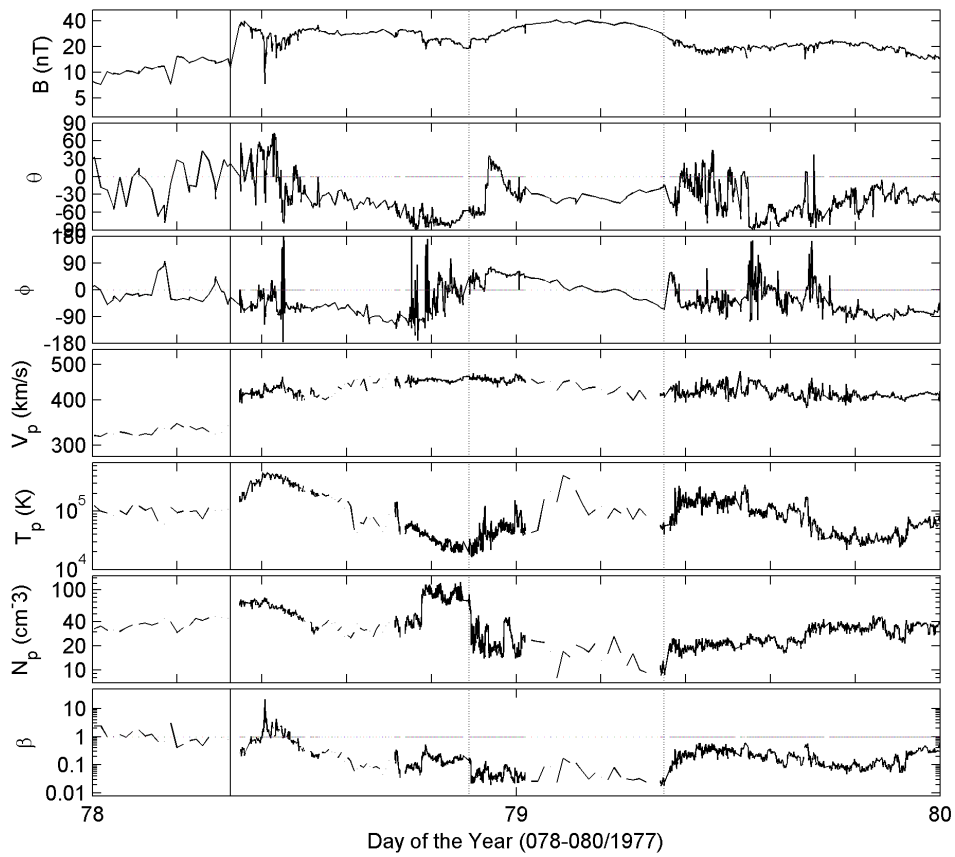


FIGURE 5.56 - H1 observation of a MC from DOY 78/1977, at 21:20 UT, to DOY 079/1978, at 08:21 UT. Meaning similar to [Figure 5.4](#).

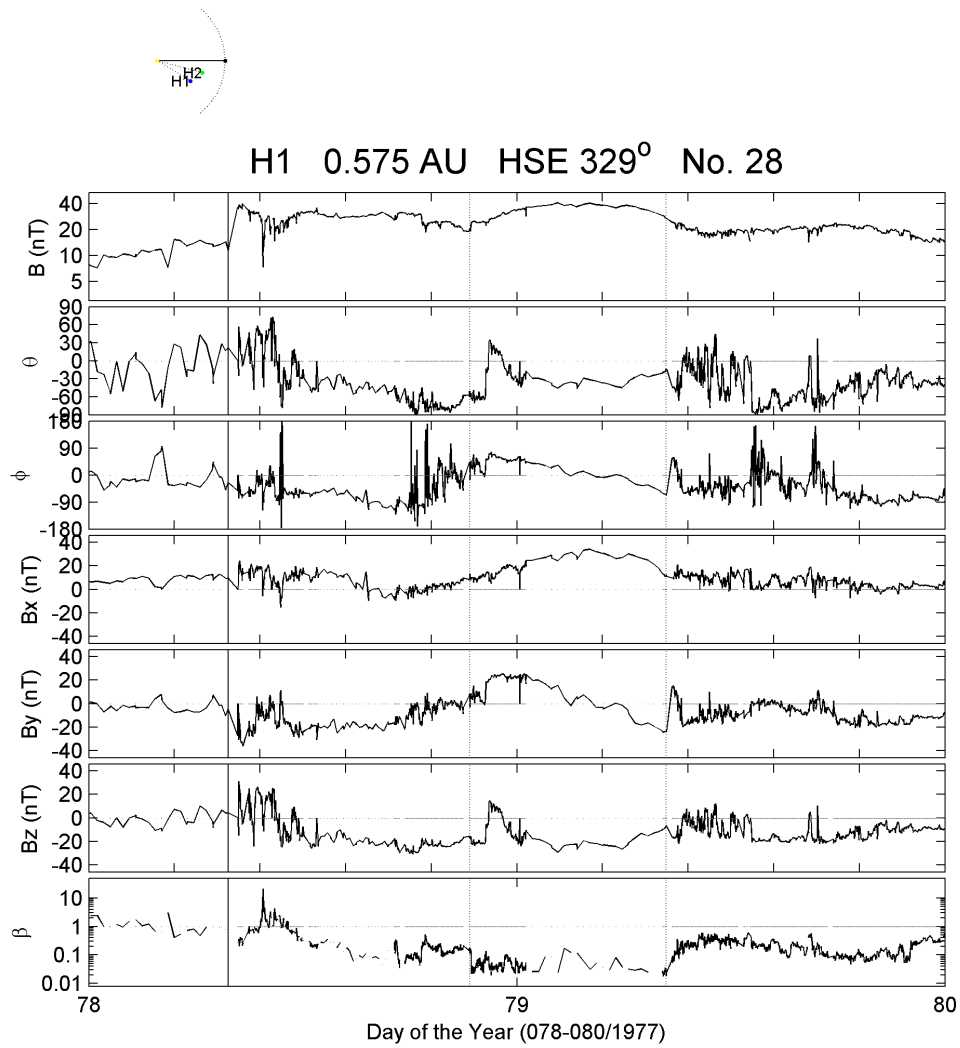


FIGURE 5.57 - H1 magnetic field data for the period from 078-081/1977. Meaning similar to [Figure 5.6](#).



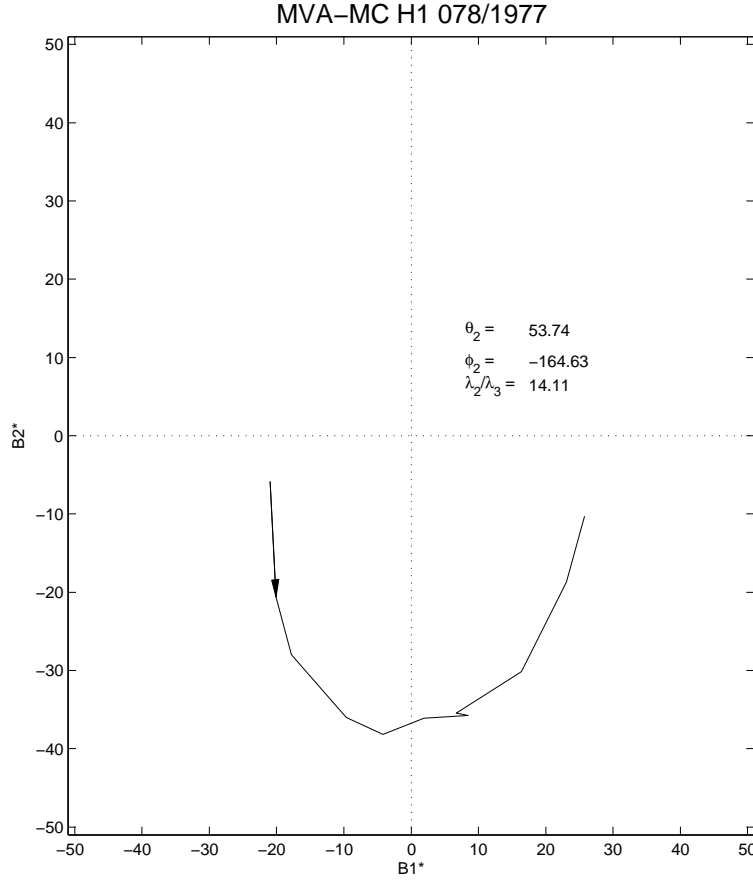


FIGURE 5.58 - Plane of maximum variance for the MC observed from DOY 78/1977, at 21:20 UT, to 79/1977, at 08:21 UT. Meaning similar to Figure 5.8.

the proton velocity and temperature and the correspondent decrease on the proton density (see profiles of Figure 5.59). Furthermore, the fluctuations on the IMF, as represented by  $\theta$  and  $\phi$ , are characteristic of this type of IP structure.

Due to the solar rotation direction, this HSS should pass first by H1 and then by H2. Since the rotation of the Sun around its axis takes about 25 days, considering one entire rotation ( $360^\circ$ ), we estimate that the HSS should have passed through H1 around 1 day ( $360^\circ/25 = 14.4^\circ$ ) before, corresponding to the beginning of DOY 079/1977. From Figure 5.56, one may associate it to the end of the MC on H1, where the fluctuations on the IMF are shown by  $\theta$  and  $\phi$ . We assume that the HSS interaction with the MC behind it is the reason why the MC is small, as H1 detected. Another fact that explains the small size of the cloud is that very close to the sun MCs are not well expanded compared to 1 AU.

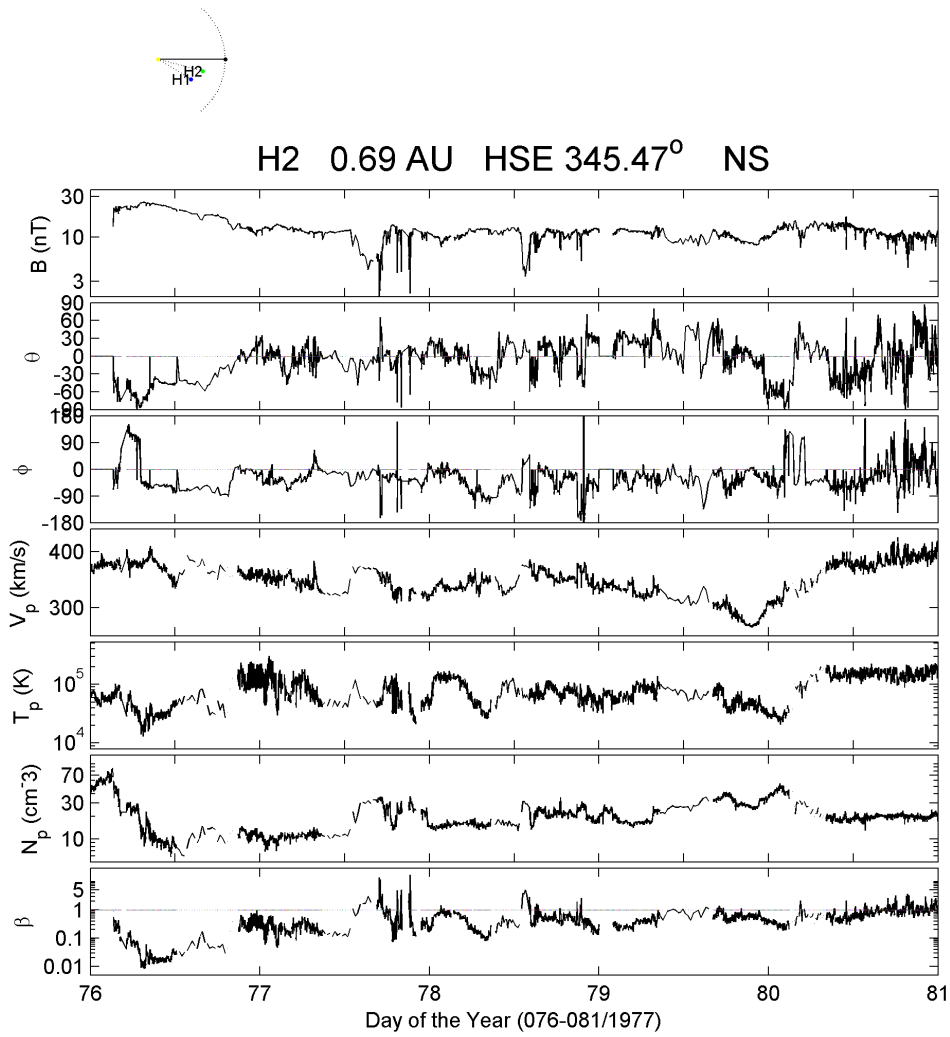


FIGURE 5.59 - H2 magnetic field and plasma data for the period from DOY 076 to 081/1977. The plots are given in the same sequence as in Figure 5.41. There is no shock neither MC identified through the parameter profiles. However, at the beginning of DOY 80/1977 a HSS is identified.

Due to the presence of the HSS passing first by H1 and then traveling in direction to H2, one can suppose that the HSS swept away the MC, preventing it of reaching H2. This could explain why the MC was not observed by H2 as the observations showed us. Indeed, we discard the possibility of the probes remaining at different sides of the HCS, since for both probes (H1 and H2)  $B_x$  is on average always positive. In other words, the probes were located at the same side of the HCS.

Another possibility could be that the MC was highly inclined, diminishing strongly the likelihood that another probe would observe the MC, as well as the result from [Figure 5.58](#) tell us ( $\theta_2 = 54^\circ$ ). Even though the probability of observing this MC decreases considering the axis direction given by  $\theta_2$ , we would expect the shock wave to be observed by H2.

## 5.6 Discussion

Minimum Variance Analysis (MVA) was used in order to identify the MC axis orientation based on the magnetic field variation inside MCs. The orientation of the MC axis is, at first order, aligned with the intermediate variance direction. Furthermore, the technique guarantees that the alignment is the closest when the spacecraft trajectory passes through the axis of the structure. Thus, it has a strong dependence on the region the spacecraft is crossing the structure.

Local MVA analysis have been widely used to identify the direction of the rotation inside the MCs, as well as to identify the minimum variance of the magnetic field, expected to be close to zero at the component perpendicular to the plane of maximum variance ([SONNERUP; SCHEIBLE, 1998](#)).

At the first time a MC was observed by “in situ” measurements, [Burlaga et al. \(1981\)](#) identified it as a highly organized structure in the solar wind through the constellation formed by four space probes. The MVA technique was used to identify the rotation of the magnetic field at different points in the inner and outer heliosphere. As the results from [Burlaga et al. \(1981\)](#), our results from the maximum variance showed a rotation in form of an arc in most cases, characterizing the smooth rotation of the MC.

[Eastwood et al. \(2002\)](#) studied the HCS and a flux rope with observations from ACE and CLUSTER. One of their results is that the flux rope orientation can change in space. This corresponds to what we have observed for some of the cases we investi-

gated in this chapter, specially for the multi-spacecraft observed MCs. According to the results we obtained for the multi or single-spacecraft observations of the MCs, at different spatial distances the same structure can present distinct orientations of the MC axis, as well as the direction of the rotation of the magnetic field inside the cloud changes from one probe to another. For instance, the MC observed at H1 from DOY 003/1978 to DOY 004/1978 and at H2 from DOY 004/1978 to DOY 005/1978 presented different direction for the cloud's magnetic field rotation. Despite the ambiguity of  $180^\circ$  that we might have to consider for the azimuthal direction  $\phi_2$ , they are in the same hemisphere of rotation, however, they rotate to different directions. Note that a different result was obtained by [Burlaga et al. \(1981\)](#) because these authors did not consider H1 observations in their analysis.

A recent work of [Ruan et al. \(2009\)](#) showed that a flux rope is a well organized structure whose axis is invariant in space and time. Note that they evaluated a single case, whereas we are considering a group of MCs. In one of our cases we found the same organization in the magnetic field, provided by the application of the MVA technique on the magnetic field inside the MC, as measurements from different points. The MC observed on DOY 29/1977, assumed to be observed by H1 and H2 simultaneously, is one example. We identify the same direction for the rotation of the magnetic field inside the structure as the maximum variance plane showed. This means that for this case, inside an angular distance of  $28^\circ$  the MC behaved as a well organized structure, in spite of the interaction with the HSS as observed by H2.

## 5.7 Conclusions

In summary, we have studied MCs extent in the inner heliosphere based on the previous observations of shock waves presented in Chapter 4. These MCs were identified as the drivers of some of the shock waves registered in [Table A.1](#).

Some of these MCs were studied through multi-point observations, once we have identified them at least through two space probes. They were not so many, but contributed to improve the understanding of the MC extent in the inner heliosphere as well as the complexity in associating these structures. We found that the angular extent of a MC can be as big as  $90^\circ$ .

Other MCs, but not many of them, were observed by only one probe/spacecraft,

however, the shock wave they drove was detected by at least two probes, including the one that observed the MC. For these clouds, we applied the MVA technique in order to determine their axis orientation. Based on these axes, one could assume that the shock, but not the structures, were observed by two spacecrafts with dependence on the axis inclination of the MC in relation to the ecliptic plane. We suggest that highly-inclined MCs are less likely to be observed by two space probes even if they are very close to each other, as it was shown in some of the cases we have studied in detail.

Note that to a certain inclination to the ecliptic plane the other probe might not observe the same magnetic cloud. The two Helios were always in the ecliptic, as is Earth. But they often were at different heliographic latitude, since the Sun's equatorial plane is inclined by  $7.25^\circ$ . When the MC is aligned to the ecliptic plane the probes are likely to observe the same structure, whereas when an inclination is present the chance decreases considerably.

For magnetic clouds observed by at least two probes, in which observations are in high quality (few data gaps), we applied the MVA analysis in order to compare the MC axis orientation as observed by each of the probes. As a general result, we confirmed that MCs are highly organized structures. However, we found that some of the MCs, even though identified by different points that are not further in longitude separated, present very different MC features. In addition to this, the direction of their axis was distinct when the MVA analysis was applied, considering the intermediate variance angles,  $\theta_2$  and  $\phi_2$ . Sometimes the probes were very close, but their observations were completely different from one another. This goes in contrary to what has been already established that MCs are highly organized structures. This is not only deduced by the application of the MVA technique that has a big dependence on the boundaries choice. But when observing the magnetic field and plasma parameter profiles of these events, one observes different rotation in the components, as well as in the boundaries.

It is extremely challenging to identify unambiguously the characteristics of MCs in the IP medium, considering that they are not isolated structures. They may interact with other structures with different topologies of magnetic field that might change their former configurations. Furthermore, it is also challenging to correctly associate MCs observed by distinct probes.

Nevertheless, our study succeeded in doing this, and found some important new results. For example, if probes are close and the structure is traveling with a determined inclination in relation to the ecliptic plane, the chance an observer sitting at the other probe, which is close to the ecliptic plane, has to see the expanded MC decreases considerably.

It is also important to point out that the Helios dataset is still unique, even after STEREO mission because the latter was launched at the minimum solar activity, when only a few CMEs are expected to occur.

## 6 SUMMARY AND CONCLUSIONS

The possibility to observe structures, such as shock waves and magnetic clouds, by multi-spacecraft as provided by Helios mission in conjunction with near-Earth monitoring, played an important role in the new findings in Interplanetary Physics. Several discoveries were due to the success of the mission, the encouragement given to the large group of researchers engaged in the mission, as well as in the investigation of the data measured by the scientific payload onboard the mission.

The advantage of multi-spacecraft observations over single-spacecraft ones is that they enable us to differentiate space and time variations of interplanetary structures. Furthermore, they give us the possibility to associate the same structure at different distances in the IP medium. Equally important is the study of the magnetic properties and evolution based on multi-point observations. We can now observe the same structure at different points in space, and at one of these points the structure is observed to interact with other magnetic structures that might change its shape due to compression, deceleration/acceleration.

It should be pointed out, however, how difficult is to associate structures at different points in IP space. This consumed a lot of effort during our data analysis. Based on the analysis of observational data, we related the observations from one probe/spacecraft to the ones at another space probe. The variety of interacting structures in the inner heliosphere, the region containing the orbits of all the missions considered in this study, provided us valuable understanding of the complexity of these phenomena. Different IP structures might interact and change and/or exchange their features in the medium through which they propagate.

Nonetheless, as it was discussed in Chapter 4, very important results were obtained when comparing shock waves in different locations of the inner heliosphere. Among these results, the longitudinal separation of the order of  $90^\circ$  was found to be a cutoff value for our distribution of longitudinal extension ( $\Delta\Phi$ ). According to our results, a shock has 50% chance to be observed by both probes, when the angle between them is about  $90^\circ$ . In practice, this means that when a CME is observed at the solar limb, for example, there is a 50% probability of seeing the shock driven by the ICME at Earth. This finding has, of course, very important applications for space weather forecasting.

It should also be pointed out that for small angular separations between the observation points, there were many events where only one of the spacecraft did observe it, even though both were operating properly without data gaps or technical problems. For these events, we investigated their characteristics, looking for parameters as the speed of the medium, determining parameter for the shock formation, as discussed in Chapters 4 and 5. In some of the cases, the upstream speed was considerably higher than the speed of the propagating structure. This may have caused the annihilation of the shock wave when it crossed regions where the conditions for shock formation are not fulfilled.

For large angles, the estimate is not accurate since we are limited to the number of events inside these large angular separations. As pointed out in Chapter 4, despite the fact that the observation points remained for several days inside these large angular distances, there were not many “safe” cases whose longitudinal extensions corresponded to the large separation between the spacecraft. The error on our estimate is big, mainly at the longitudinal separation of  $\Delta\Phi = 110^\circ$ , where a single “safe” case is identified as being observed by at least two probes. The sample size is very small what diminishes the accuracy of the estimate.

Not only shock waves extended over large angles, but MCs also provided important results related to their spatial extent, as described in Chapter 5. These results increased the azimuthal extent of only  $30^\circ$  for MCs as observed by [Burlaga et al. \(1981\)](#) to at least  $90^\circ$  of longitudinal extent. Magnetic clouds were identified as the driver of the shock waves studied in Chapter 4. As expected, based on our statistics, shock waves extend to larger distances compared to MCs.

More interestingly even is the possibility of detecting different shapes for the same MC based on the observations at multi-points, as the ones provided by the Helios probes and IMP-8/ISEE-3 spacecraft. Among the events that we identified by at least two probes/spacecraft, we found remarkable differences that we supposed to be caused by the interaction of the MC with other IP structures, mainly HSSs. In some cases, the HSS passed first by the probe that was more eastward in relation to the other(s) because of its corotation with the Sun. In all the studied cases with signatures of HSS, we could identify the HSS in one probe first and, inside the predicted time, the HSS arrived at the other(s) space probe(s).

For some cases, there was a coincidence on the time the MC was crossing one of the



space probes and the HSS passed through the same probe. In other cases, our best guess was that the pressure exerted by the HSS apparently deviated the MC from its path, so that the MC was not crossed by the probe/spacecraft, whereas the HSS was identified by the probe that did not detect the cloud.

When the local MVA analysis was applied in the MCs, we found that for some cases the direction of the rotation, described by the maximum variance plane, was the same at different points of observation. In general, for the probes separated by small distances, the direction of rotation of the components followed the same configuration at each of the spacecraft, confirming that MCs behave as well-organized structures. However, for other cases this did not happen. We observed that for some MCs the rotation in the magnetic field components, as measured by the multi-spacecraft, showed different directions in the main magnetic field components inside the same structure. In addition to the different values obtained for some of the cloud's axis directions, given by  $\theta_2$  and  $\phi_2$ , they also presented different directions of rotation. Interestingly, some of these cases corresponded to the MCs seen at spacecraft separated by small longitudinal angles.

We think that this work is an important continuation of what has been done so far for the study and prediction in space physics/weather. Much more is still needed in order to improve our understanding of the space where we live. Nonetheless, we have to keep in mind that since we are limited to the available observations of the IP space, there are limitations to our studies.

As future work, we suggest to continue this study, improving the association among the different points of observation by using the particle detector onboard the Helios probes. Based on this dataset, it is possible to associate the same magnetic field line seen at different points, and so the correspondence on the solar source of the ICME at two different points.

As we have observation from MCs seen at different points, specially clouds seen by the probe aligned with the Sun-Earth line, one could study the evolution of these clouds by comparing it with the observation near Earth, provided by IMP-8/ISEE-3. The evolution of the magnetic structure of such interplanetary manifestation of the ICMEs could be analyzed by using the magnetic helicity.

Another possibility for further MC studies is the application of the Grad-Shafranov

reconstruction technique (HAU; SONNERUP, 1999). This technique is a versatile tool to reconstruct space plasma structures possessing an invariant direction.

By using the ICMEs/MCs identified during Helios mission, we can look for those cases where magnetic reconnection was observed specially in the sheath region ahead of the ICMEs or in the front part of these structures. Reconnection in ICMEs and in the IP medium have been already studied by using observations from multi-spacecraft.

## REFERENCES

- ABRAHAM-SHRAUNER, B. Determination of magnetohydrodynamic shock normals. **J. Geophys. Res.**, v. 77, p. 736–739, 1972. [77](#)
- ABRAHAM-SHRAUNER, B.; YUN, S. H. Interplanetary shocks seen by ames plasma probe on pioneer 6 and 7. **J. Geophys. Res.**, v. 81, p. 2097–2102, May 1976. Provided by the Smithsonian/NASA Astrophysics Data System. [77](#)
- ACUÑA, M. H.; BURLAGA, L. F.; LEPPING, R. P.; NESS, N. F. Initial Results from the VOYAGER-1 and VOYAGER-2 Magnetic Field Experiments. In: MAX-PLANCK INSTITUTE, 4., 1981, Burghausen, FRG. **Proceedings...** Katlenburg-Lindau: MPAE, 1981. p. 143–+. ISBN MPAE-100-81-31. [S.l.]: SAO/NASA ADS,. [80](#)
- ALFVÉN, H. Electric currents in cosmic plasmas. **Rev. Geophys. Space Phys.**, v. 15, p. 271–284, 1977. [123](#)
- AXFORD, W. I. The Interaction between the Solar Wind and the Earth's Magnetosphere. **J. Geophys. Res.**, v. 67, p. 3791–+, Sep 1962. [72](#)
- BALOGH, A.; BOTHMER, V.; CROOKER, N. U.; FORSYTH, R. J.; GLOECKLER, G.; HEWISH, A.; HILCHENBACH, M.; KALLENBACH, R.; KLECKER, B.; LINKER, J. A.; LUCEK, E.; MANN, G.; MARSCH, E.; POSNER, A.; RICHARDSON, I. G.; SCHMIDT, J. M.; SCHOLER, M.; WANG, Y.-M.; WIMMER-SCHWEINGRUBER, R. F.; AELLIG, M. R.; BOCHSLER, P.; HEFTI, S.; MIKIĆ, Z. The Solar Origin of Corotating Interaction Regions and Their Formation in the Inner Heliosphere. **Space Science Reviews**, v. 89, p. 141–178, Jul. 1999. [63](#)
- BALOGH, A.; GONZALEZ-ESPARZA, J. A.; FORSYTH, R. J.; BURTON, M. E.; GOLDSTEIN, B. E.; SMITH, E. J. Interplanetary shock waves: Ulysses observations in and out of the ecliptic plane. **Space Science Reviews**, v. 72, p. 171–180, 1995. [71](#), [72](#)
- BAME, S. J.; ASBRIDGE, J. R.; FELDMAN, W. C.; GOSLING, J. T. Evidence for a structure-free state at high solar wind speeds. **J. Geophys. Res.**, v. 82, p. 1487–1492, 1977. [52](#)

- BENOÏHR, H. C.; GOÏLLNITZ, H.; KUTZER, A.; SCHEIL, G. Problems for a flyby mission of the Sun. **Acta Astronautica**, v. 4, p. 237–255, Mar. 1977. [86](#)
- BIRD, M. K.; EDENHOFER, P. Remote sensing observations of the solar corona. In: \_\_\_\_\_. **Physics of the inner heliosphere**. Berlin, Germany; New York, U.S.A.: Springer, 1990. (Physics and Chemistry in Space, I), p. 13–97. [92](#)
- BORRINI, G.; GOSLING, J.; BAME, S.; FELDMAN, W. An analysis of shock wave disturbances observed at 1 au from 1971 through 1978. **J. Geophys. Res.**, v. 87, p. 4365–4373, 1982. [150](#)
- BOTHMER, V.; SCHWENN, R. The structure and origin of magnetic clouds in the solar wind. **Ann. Geophys.**, v. 16, p. 1–24, 1998. [68](#), [69](#), [152](#), [155](#), [160](#), [161](#), [163](#), [169](#), [171](#), [175](#), [176](#), [189](#), [194](#), [197](#), [202](#), [207](#), [214](#), [295](#), [296](#)
- BURKEPILE, J. T.; HUNDHAUSEN, A. J.; STANGER, A. L.; ST. CYR, O. C.; SEIDEN, J. A. Role of projection effects on solar coronal mass ejection properties: 1. a study of cmes associated with limb activity. **J. Geophys. Res.**, v. 109, p. 3103, 2004. [58](#)
- BURLAGA, L. Terminology for ejecta in the solar wind. **Eos Trans. AGU**, v. 82, p. 433, 2001. [95](#)
- BURLAGA, L. F. Hydromagnetic waves and discontinuities in the solar wind. **Space Sci. Rev.**, v. 12, p. 600, 1971. [74](#)
- \_\_\_\_\_. Magnetic clouds. In: SCHWENN, R.; MARSCH, E. (Ed.). **Physics of the inner heliosphere, Vol. II: Particles, waves and turbulence**. Berlin, Germany; New York, U.S.A.: Springer, 1991, (Physics and Chemistry in Space, v. 20). p. 1–22. [66](#), [70](#), [186](#)
- \_\_\_\_\_. **Interplanetary magnetohydrodynamics**. New York, U.S.A.: Oxford University Press, 1995. [66](#), [67](#), [74](#), [76](#), [77](#), [80](#), [81](#)
- BURLAGA, L. F.; BEHANNON, K. W. Magnetic clouds: Voyager observations between 2 and 4 au. **Sol. Phys.**, v. 81, p. 181, 1982. [154](#), [294](#)
- BURLAGA, L. F.; KLEIN, L.; SHEELEY JR., N. R.; MICHELS, D. J.; HOWARD, R. A.; KOOMEN, M. J.; SCHWENN, R.; ROSENBAUER, H. A magnetic cloud and a coronal mass ejection. **Geophysical Research Letters**, v. 9, p. 1317–1320, dez. 1982. [56](#)

BURLAGA, L. F.; LEPPING, R.; WEBER, R.; ARMSTRONG, T.; GOODRICH, C.; SULLIVAN, J.; GURNETT, D.; KELLOGG, P.; KEPPLER, E.; MARIANI, F.; NEUBAUER, F.; ROSENBAUER, H.; SCHWENN, R. Interplanetary particles and fields, november 22 to december 6, 1977: Helios, voyager, and imp observations between 0.6 au and 1.6 au. **J. Geophys. Res.**, v. 85, p. 2227–2242, 1980. [96](#)

BURLAGA, L. F.; LEPPING, R. P.; JONES, J. A. Global configuration of a magnetic cloud. In: RUSSELL, C. T.; PRIEST, E. R.; LEE, L. C. (Ed.). **Physics of Magnetic Flux Ropes**. Washington DC: American Geophysical Union, 1990, (Geophysical Monograph Series, v. 58). p. 373–377. [67](#)

BURLAGA, L. F.; SITTLER, E.; MARIANI, F.; SCHWENN, R. Magnetic loop behind an interplanetary shock: Voyager, helios, and imp 8 observations. **J. Geophys. Res.**, v. 86, p. 6673–6684, 1981. [62](#), [66](#), [93](#), [96](#), [183](#), [221](#), [222](#), [226](#), [295](#), [296](#)

CANE, H. V.; KAHLER, S. W.; SHEELEY JR., N. R. Interplanetary shocks preceded by solar filament eruptions. **J. Geophys. Res.**, v. 91, p. 13321–13329, Dec. 1986. [63](#), [65](#)

CHAPMAN, S.; FERRARO, V. C. A. The electrical state of solar streams of corpuscles. **Monthly Notices of the Royal Astronomical Society**, v. 89, p. 470–+, Mar. 1929. [66](#)

COCCONI, G.; GOLD, T.; GREISEN, K.; HAYAKAWA, S.; MORRISON, P. The cosmic ray flare effect. **Suppl. Nuovo cimento**, v. 8, p. 161, 1958. [66](#)

COLBURN, D. S.; SONETT, C. P. Discontinuities in the Solar Wind. **Space Science Reviews**, v. 5, p. 439–+, 1966. [76](#), [77](#)

COLLIER, M. R.; LEPPING, R. P.; BERDICHEVSKY, D. B. A statistical study of interplanetary shocks and pressure pulses internal to magnetic clouds. **Journal of Geophysical Research (Space Physics)**, v. 112, n. A11, p. 6102–+, Jun. 2007. [190](#)

CREMADES, H.; BOTHMER, V. On the three-dimensional configuration of coronal mass ejections. **Astron. Astrophys.**, v. 422, p. 307–322, 2004. [58](#), [59](#)

CREMADES, H.; BOTHMER, V.; TRIPATHI, D. Properties of structured coronal mass ejections in solar cycle 23. **Advances in Space Research**, v. 38, p. 461–465, 2006. [59](#)

- DASSO, S.; MANDRINI, C. H.; DÉMOULIN, P.; LUONI, M. L.; GULISANO, A. M. Large scale MHD properties of interplanetary magnetic clouds. **Advances in Space Research**, v. 35, p. 711–724, 2005. [70](#)
- DRYER, M.; SMITH, Z. K.; STEINOLFSON, R. S.; MIHALOV, J. D.; WOLFE, J. H.; CHAO, J. K. Interplanetary disturbances caused by the August 1972 solar flares as observed by Pioneer 9. **J. Geophys. Res.**, v. 81, p. 4651–4663, 1976. [96](#)
- DUNGEY, J. W. Interplanetary Magnetic Field and the Auroral Zones. **Physical Review Letters**, v. 6, p. 47–48, jan 1961. [65](#), [66](#)
- EASTWOOD, J. P.; BALOGH, A.; DUNLOP, M. W.; SMITH, C. W. Cluster observations of the heliospheric current sheet and an associated magnetic flux rope and comparisons with ACE. **Journal of Geophysical Research (Space Physics)**, v. 107, p. 1365–+, Nov. 2002. [221](#)
- ECHER, E.; ALVES, M. V.; GONZALEZ, W. D. Ondas de choque não-colisionais no espaço interplanetário. **Revista Brasileira de Ensino de Física**, v. 28, n. 1, p. 51–66, 2006. [72](#), [160](#), [190](#), [295](#)
- ECHER, E.; SANTOS, J. C. d.; BALMACEDA, L. A.; SCHUCH, N. J.; GONZÁLEZ-ALARCON, W. D.; ALVES, M. V.; GONZALEZ, A. L. C. d.; LAGO, A. D.; VIEIRA, L. E. A. Geomagnetic effects of interplanetary shock waves during solar minimum (1995–1996) and solar maximum (2000). In: **Proceedings**. [s.n.], 2003. p. 641–644;. (ESA SP-535). Available on: <http://urlib.net/sid.inpe.br/marciana/2004/01.13.12.26>>. [79](#)
- EDDY, J. A. A Nineteenth-century Coronal Transient. **Astronomy and Astrophysics**, v. 34, p. 235–+, Aug. 1974. [21](#), [55](#)
- FARRUGIA, C. J.; OSHEROVICH, V. A.; BURLAGA, L. F. Magnetic flux rope versus the spheromak as models for interplanetary magnetic clouds. **J. Geophys. Res.**, v. 100, p. 12293–+, Jul. 1995. [71](#)
- FELDMAN, U.; SCHÜHLE, U.; WIDING, K. G.; LAMING, J. M. Coronal Composition above the Solar Equator and the North Pole as Determined from Spectra Acquired by the SUMER Instrument on SOHO. **The Astrophysical Journal**, v. 505, p. 999–1006, Oct. 1998. [51](#)
- FELDMAN, W.; ASBRIDGE, J.; BAME, S.; GOSLING, J. High-speed solar wind flow parameters at 1 au. **J. Geophys. Res.**, v. 81, p. 5054–5060, 1976. [52](#)

- GOLDSTEIN, H. On the field configuration in magnetic clouds. **NASA Conference Publication**, v. 228, p. 731–733, nov 1983. [67](#), [295](#), [296](#)
- GONZALEZ, W.; TSURUTANI, B.; GONZALEZ, A. L. Clúa de. Interplanetary origin of geomagnetic storms. **Space Sci. Rev.**, v. 88, p. 529–562, 1999. [52](#), [65](#)
- GONZALEZ, W. D.; JOSELYN, J. A.; KAMIDE, Y.; KROEHL, H. W.; ROSTOKER, G.; TSURUTANI, B. T.; VASYLIUNAS, V. M. What is a geomagnetic storm? **J. Geophys. Res.**, v. 99, p. 5771–5792, Apr. 1994. [161](#)
- GONZALEZ, W. D.; TSURUTANI, B. T.; LEPPING, R. P.; SCHWENN, R. Interplanetary phenomena associated with very intense geomagnetic storms. **Journal of Atmospheric and Terrestrial Physics**, v. 64, p. 173–181, jan 2002. [62](#), [65](#)
- GONZALEZ, W. D.; TSURUTANI, B. T.; MCINTOSH, P. S.; GONZALEZ, A. L. Clúa de. Coronal hole-active region-current sheet (CHARCS) association with intense interplanetary and geomagnetic activity. **Geophys. Res. Lett.**, v. 23, p. 2577–2580, 1996. [56](#)
- GOPALSWAMY, N. Consequences of Coronal Mass Ejections in the Heliosphere. **Sun and Geosphere**, v. 1, n. 2, p. 020000–12, Dec. 2006. [60](#)
- GOPALSWAMY, N.; LARA, A.; YASHIRO, S.; NUNES, S.; HOWARD, R. A. Coronal mass ejection activity during solar cycle 23. In: WILSON, A. (Ed.). **Proceedings...** Noordwijk: ESA Publications Division, 2003. p. 403–414. ESA SP-535. [60](#)
- GOSLING, J. T. Coronal mass ejections and magnetic flux ropes in interplanetary space. In: RUSSELL, C.; PRIEST, E.; LEE, L. (Ed.). **Physics of magnetic flux ropes**. Washington, U.S.A.: American Geophysical Union, 1990. (Geophysical Monograph Series, v. 58), p. 343–364. [62](#), [65](#), [71](#)
- \_\_\_\_\_. The solar flare myth. **J. Geophys. Res.**, v. 98, p. 18937–18950, 1993. [55](#)
- \_\_\_\_\_. Coronal mass ejections: An overview. In: CROOKER, N.; JOSELYN, J. A.; FEYNMAN, J. (Ed.). **Coronal Mass Ejections**. Washington D. C., U.S.A.: AGU, 1999. p. 9–16. [54](#)

GOSLING, J. T.; HILDNER, E.; MACQUEEN, R. M.; MUNRO, R. H.;  
POLAND, A. I.; ROSS, C. L. Mass ejections from the sun - a view from skylab. **J. Geophys. Res.**, v. 79, p. 4581–4587, 1974. [91](#)

\_\_\_\_\_. Direct observations of a flare related coronal and solar wind disturbance. **Solar Physics**, v. 40, p. 439–448, Feb. 1975. [56](#)

GOSLING, J. T.; HUNDHAUSEN, A. J.; BAME, S. J. Solar wind stream evolution at large heliocentric distances - experimental demonstration and the test of a model. **J. Geophys. Res.**, v. 81, p. 2111–2122, 1976. [63](#)

GOSLING, J. T.; MCCOMAS, D. J.; PHILLIPS, J. L.; BAME, S. J. Geomagnetic activity associated with earth passage of interplanetary shock disturbances and coronal mass ejections. **J. Geophys. Res.**, v. 96, p. 7831–7839, 1991. [60](#), [65](#)

GOSLING, J. T.; PIZZO, V. J. Formation and evolution of corotating interaction regions and their three dimensional structure. **Space Sci. Rev.**, v. 89, p. 21–52, 1999. [63](#)

GURNETT, D. A.; ANDERSON, R. R. Plasma waves in the solar wind: Ten years of HELIOS observations. **Geochimica et Cosmochimica Acta Supplement**, p. 100–105, 1984. [90](#)

HAU, L.-N.; SONNERUP, B. U. Ö. Two-dimensional coherent structures in the magnetopause: Recovery of static equilibria from single-spacecraft data. **J. Geophys. Res.**, v. 104, p. 6899–6918, Apr 1999. [74](#), [228](#)

HILDNER, E.; GOSLING, J. T.; MACQUEEN, R. M.; MUNRO, R. H.;  
POLAND, A. I.; ROSS, C. L. Movie of Comet Kohoutek (1973f) as Observed Near Minimum Elongation by the Hao Coronagraph Aboard SKYLAB. In: Donn, B. (Ed.). **IAU Colloq. 25: The Study of Comets**. [S.l.: s.n.], 1976. p. 124–+. [56](#)

HOWARD, R.; MICHELS, D.; JR, N.; KOOMEN, M. The observation of a coronal transient directed at earth. **Astrophys. J. Lett.**, v. 263, p. L101–L104, 1982. [59](#)

HOWARD, R. A.; SHEELEY JR., N. R.; MICHELS, D. J.; KOOMEN, M. J. Coronal mass ejections - 1979–1981. **J. Geophys. Res.**, v. 90, p. 8173–8191, 1985. [53](#), [150](#)



HUNDHAUSEN, A. The origin and propagation of coronal mass ejections (r). In: PIZZO, V.; HOLZER, T.; SIME, D. (Ed.). **Solar wind six**. Boulder, U.S.A.: Natl. Cent. for Atmos. Res., 1987. (NCAR Technical Notes), p. 181. [71](#)

HUNDHAUSEN, A. J. **Coronal Expansion and Solar Wind**. Berlin, Germany; New York, U.S.A.: Springer, 1972. (Physics and chemistry in space, v. 5). [51](#)

\_\_\_\_\_. An introduction. In: CROOKER, N.; JOSELYN, J. A.; FEYNMAN, J. (Ed.). **Coronal Mass Ejections**. Washington D. C., U.S.A.: AGU, 1999. p. 1–7. [54](#)

HUNDHAUSEN, A. J.; GOSLING, J. T. Solar wind structure at large heliocentric distances - an interpretation of Pioneer 10 observations. **Journal of Geophysical Research**, v. 81, p. 1436–1440, mar. 1976. [97](#)

HUNDHAUSEN, A. J.; SAWYER, C. B.; HOUSE, L.; ILLING, R. M. E.; WAGNER, W. J. Coronal mass ejections observed during the solar maximum mission - latitude distribution and rate of occurrence. **J. Geophys. Res.**, v. 89, p. 2639–2646, 1984. [56](#)

HUTTUNEN, K. E. J.; KOSKINEN, H. E. J. Importance of post-shock streams and sheath region as drivers of intense magnetospheric storms and high-latitude activity. **Ann. Geophys.**, v. 22, p. 1729–1738, 2004. [65](#)

ILLING, R. M. E.; HUNDHAUSEN, A. J. Disruption of a coronal streamer by an eruptive prominence and coronal mass ejection. **J. Geophys. Res.**, v. 91, p. 10951–10960, oct 1986. [53](#)

JEFFREY, A.; TANIUTI, T. **Non-linear wave propagation**. [S.l.]: Mathematics in Science and Engineering, New York: Academic Press, 1964, 1964. [80](#)

KAHLER, S. The morphological and statistical properties of solar X-ray events with long decay times. **Astrophysical Journal**, v. 214, p. 891–897, Jun. 1977. [58](#)

KAHLER, S. W. Solar flares and coronal mass ejections. **Annu. Rev. Astron. Astrophys.**, v. 30, p. 113–141, 1992. [56](#)

KANTROWITZ, A. R.; PETSCHKE, H. E. Mhd characteristics and shock waves. In: KUNKEL, W. B. (Ed.). **Plasma physics in theory and application**. New York, U.S.A.: McGraw-Hill Book Co., 1966. p. 148–206. [74](#)

KELLOGG, P. J. Flow of Plasma around the Earth. **J. Geophys. Res.**, v. 67, p. 3805–+, Sep 1962. [72](#)

KENNEL, C. F.; BLANDFORD, R. D.; COPPI, P. MHD intermediate shock discontinuities. I - Rankine-Hugoniot conditions. **Journal of Plasma Physics**, v. 42, p. 299–319, Oct 1989. [74](#)

KHALISI, E.; SCHWENN, R. Statistical analysis of interplanetary shock waves observed during a complete solar activity cycle. In: **Solar wind eight**. [S.l.: s.n.], 1995. p. 99–+. [97](#), [99](#), [103](#), [245](#), [255](#)

KIVELSON, M. G. Physics of space plasmas. In: KIVELSON, M. G.; RUSSELL, C. T.; COWLEY, S. W. H. (Ed.). **Physics of space plasmas**. Cambridge, United Kingdom: Cambridge University Press, 1995. p. 27–57. [73](#)

KLEIN, L. W.; BURLAGA, L. F. Interplanetary magnetic clouds at 1 au. **Journal of Geophysical Research**, v. 87, p. 613–624, 1982. [66](#), [295](#), [296](#)

KRIEGER, A. S.; TIMOTHY, A. F.; ROELOF, E. C. A coronal hole and its identification as the source of a high velocity solar wind stream. **Solar Physics**, v. 29, p. 505–525, 1973. [51](#), [91](#)

KUNOW, H.; WIBBERENZ, G. The fast individualists in the solar system: Cosmic rays. **Geochimica et Cosmochimica Acta Supplement**, p. 124–148, 1984. [91](#)

KUNOW, H.; WIBBERENZ, G.; GREEN, G.; MÜLLER-MELLIN, R. Energetic particles in the inner solar system. In: SCHWENN, R.; MARSCH, E. (Ed.). **Physics of the inner heliosphere**. Berlin, Germany; New York, U.S.A.: Springer, 1991, (Particles, Waves and Turbulence, II). p. 243. [91](#)

KUTZER, A. Die helios missionen. In: PORSCHE, H. (Ed.). **10 jahre HELIOS**. Munich, Germany: Karl Wenschow Franzis Druck GmbH, 1984. p. 39–48. [85](#), [92](#)

LANDAU, L. D.; LIFSHITZ, E. M. **Electrodynamics of Continuous Media**. Chichester, England: Addison-Wesley, 1960. 224 p. [74](#)

LEPPING, R. P.; BEHANNON, K. W. Magnetic field directional discontinuities: 1. minimum variance errors. **J. Geophys. Res.**, v. 85, p. 4695–4703, 1980. [294](#)

LEPPING, R. P.; BURLAGA, L. F.; JONES, J. A. Magnetic field structure of interplanetary magnetic clouds at 1 AU. **J. Geophys. Res.**, v. 95, p. 11957–11965, Aug. 1990. [71](#)

- LINDEMANN, F. A. Note on the theory of magnetic storms. **Philos. Mag.**, v. 38, p. 669, 1919. [66](#)
- LINDSAY, G.; RUSSELL, C.; LUHMANN, J. Predictability of dst index based upon solar wind conditions monitored inside 1 au. **J. Geophys. Res.**, v. 104, p. 10335–10344, 1999. [60](#)
- LOW, B. C. Equilibrium and dynamics of coronal magnetic fields. **Annual Review of Astronomy and Astrophysics**, v. 28, p. 491–524, 1990. [60](#)
- LUCAS, A. de; SCHWENN, R.; MARSCH, E.; LAGO, A. D.; GONZALEZ, A. L. C. de; ECHER, E.; GONZALEZ, W. D.; SILVA, M. R. da. Multi-spacecraft observations to study the shock extension in the inner heliosphere. In: GOPALSWAMY, N.; WEBB, D. F. (Ed.). **Proceedings...** Cambridge: Cambridge University Press, 2009. (Universal Heliophysical Processes), p. 481–487. IAU Symposium. [143](#), [145](#), [147](#)
- LUNDQUIST, S. Magnetohydrostatic fields. **Ark. Fys.**, v. 2, p. 361–365, 1950. [68](#)
- LYOT, B. **Comp. Rend. Acad. Sci.**, v. 193, p. 1169, 1931. [48](#)
- MARIANI, F.; NEUBAUER, F. M. The interplanetary magnetic field. In: \_\_\_\_\_. **Physics of the inner heliosphere**. Berlin, Germany; New York, U.S.A.: Springer, 1990. (Large-scale phenomena, I), p. 183–206. [89](#), [93](#)
- MARSCH, E. Kinetic physics of the solar wind plasma. In: SCHWENN, R.; MARSCH, E. (Ed.). **Physics of the inner heliosphere**. Berlin, Germany; New York, U.S.A.: Springer, 1991, (Particles, Waves and Turbulence, II). p. 45–133. [92](#), [93](#)
- MARSCH, E.; AXFORD, W. I.; MCKENZIE, J. F. Solar wind. In: DWIVEDI, B. (Ed.). **Dynamic Sun**. Cambridge, U.K.: Cambridge University Press, 2003. p. 374–402. [54](#)
- MARSCH, E.; SCHWENN, R. Introduction. In: SCHWENN, R.; MARSCH, E. (Ed.). **Physics of the inner heliosphere**. Berlin, Germany; New York, U.S.A.: Springer, 1990, (Large-scale phenomena, I). p. 1–12. [85](#), [86](#), [87](#), [91](#), [97](#)
- MARUBASHI, K. Structure of the interplanetary magnetic clouds and their solar origins. **Adv. Space Res.**, v. 6, p. 335–338, 1986. [71](#)

\_\_\_\_\_. The initiation of coronal mass ejections by magnetic shear. In: CROOKER, N.; JOSELYN, J.; FEYNMAN, J. (Ed.). **Coronal Mass Ejections**. Washington, D.C.: American Geophysical Union, 1997, (Geophysical Monograph, v. 99). p. 147–156. [71](#)

MEADOWS, A. **Early solar physics**. Oxford, U.K.: Pergamon Press, 1970. (Selected Readings in Physics). [54](#)

MENDENHALL, W.; BEAVER, R. J.; BEAVER, B. M. **Introduction to probability and statistics**. 12. ed. Duxbury, U.S.A.: Thomson BROOKS/COLE, 2006. [286](#)

MORRISON, P. Solar-connected variations of the cosmic rays. **Physical Review**, v. 95, p. 646, 1954. [66](#)

\_\_\_\_\_. Solar Origin of Cosmic-Ray Time Variations. **Physical Review**, v. 101, p. 1397–1404, fev. 1956. [66](#)

MULLIGAN, T.; RUSSELL, C.; LUHMANN, J. Solar cycle evolution of the structure of magnetic clouds in the inner heliosphere. **Geophys. Res. Lett.**, v. 25, p. 2959–2962, 1998. [67](#), [68](#), [70](#), [163](#), [194](#)

Neubauer, F. M.; Musmann, G. Fast magnetic fluctuations in the solar wind - HELIOS I. **J. Geophys. Res.**, v. 82, p. 3201–3212, ago. 1977. [80](#)

NOCI, G. Energy Budget in Coronal Holes. **Solar Physics**, v. 28, p. 403–+, 1973. [51](#)

PARKER, E. N. Dynamics of the interplanetary gas and magnetic fields. **Astrophys. J.**, v. 128, p. 664–676, 1958. [50](#), [51](#), [52](#), [63](#)

\_\_\_\_\_. **Interplanetary dynamical processes**. [S.l.]: New York, Interscience Publishers, 1963., 1963. [63](#)

PARKS, G. K. **Physics of space plasmas - an introduction**. [S.l.: s.n.], 1991. [51](#), [72](#), [73](#), [74](#)

PIDDINGTON, J. H. Interplanetary Magnetic Field and Its Control of Cosmic-Ray Variations. **Physical Review**, v. 112, p. 589–596, Oct 1958. [66](#)

PLUNKETT, S. P.; WU, S. T. Coronal mass ejections (CMEs) and their geoeffectiveness. **IEEE Transactions on Plasma Science**, v. 28, p. 1807–1817, dez. 2000. [54](#)

PNEUMAN, G. W. Some General Properties of Helmeted Coronal Structures. **Solar Physics**, v. 3, p. 578–+, 1968. [53](#)

PORSCHKE, H. General aspects of the mission Helios 1 and 2. Introduction to a special issue on initial scientific results of the Helios Mission. **Journal of Geophysics Zeitschrift Geophysik**, v. 42, p. 551–559, 1977. [87](#)

\_\_\_\_\_. **Ten years of HELIOS**. Oberpfaffenhoven: NASA STI/Recon Technical Report N, 1984. 27794-+ p. [83](#), [84](#), [87](#), [96](#), [98](#)

PRIEST, E. R. (Ed.). **Solar magnetohydrodynamics**. Dordrecht, Holland: D. Reidel Publishing Company, 2000. [49](#), [73](#)

PUDOVKIN, M. I.; ZAITSEVA, S. A.; BENEVOLENSKA, E. E. The structure and parameters of flare streams. **J. Geophys. Res.**, v. 84, p. 6649–6652, nov. 1979. [66](#)

REDFORD, D. (Ed.). **The ancient gods speak: A guide to egyptian religion**. Dordrecht, Holland: Oxford University Press, 2002. [47](#)

RICHTER, A. K.; HSIEH, K. C.; ROSENBAUER, H.; NEUBAUER, F. M. Parallel fast-forward shock within 1 AU: Helios-1 and 2 observations. **NASA STI/Recon Technical Report N**, v. 85, p. 35847–+, 1984. [80](#)

ROSENBAUER, H.; SCHWENN, R.; MARSCH, E.; MEYER, B.; MIGGENRIEDER, H.; MONTGOMERY, M. D.; MÜHLHÄUSER, K. H.; PILIPP, W.; VOGES, W.; ZINK, S. M. A survey on initial results of the helios plasma experiment. **J. Geophys.**, v. 42, n. 6, p. 561–580, 1977. [52](#)

RUAN, P.; KORTH, A.; MARSCH, E.; INHESTER, B.; SOLANKI, S.; WIEGELMANN, T.; ZONG, Q.-G.; BUCIK, R.; FORNACON, K.-H. Multiple-spacecraft study of an extended magnetic structure in the solar wind. **Journal of Geophysical Research (Space Physics)**, v. 114, p. 2108–+, fev. 2009. [222](#)

RUSSELL, C. In defense of the term icme. **Eos Trans. AGU**, v. 82, p. 433–435, 2001. [95](#)

RUSSELL, C. T.; WANG, Y. L.; RAEDER, J.; TOKAR, R. L.; SMITH, C. W.; OGILVIE, K. W.; LAZARUS, A. J.; LEPPING, R. P.; SZABO, A.; KAWANO, H.; MUKAI, T.; SAVIN, S.; YERMOLAEV, Y. I.; ZHOU, X.-Y.; TSURUTANI, B. T. The interplanetary shock of September 24, 1998: Arrival at Earth. **J. Geophys. Res.**, v. 105, p. 25143–25154, nov 2000. [77](#)

SCEARCE, C.; CANTARANO, S.; NESS, N.; MARIANI, F.; TERENCE, R.; BURLAGA, L. The Rome-GSFC magnetic field experiment for Helios A and B (E3). **Raumfahrtforschung**, v. 19, p. 237–240, 1975. [89](#)

SCHWARTZ, S. J. Shock and Discontinuity Normals, Mach Numbers, and Related Parameters. **Analysis Methods for Multi-Spacecraft Data**, v. 1, p. 249–270, 1998. [77](#)

SCHWENN, R. Relationship of coronal transients to interplanetary shocks 3d aspects. **Space Sci. Rev.**, v. 44, p. 139–168, 1986. [63](#), [65](#)

\_\_\_\_\_. Large-scale structure of the interplanetary medium. In: SCHWENN, R.; MARSCH, E. (Ed.). **Physics of the inner heliosphere**. Berlin, Germany; New York, U.S.A.: Springer, 1990, (Large-Scale Phenomena, I). p. 99. [52](#), [63](#), [64](#), [93](#), [97](#), [109](#)

\_\_\_\_\_. An essay on terminology, myths and known facts: solar transient - flare - cme - driver gas - piston - bde - magnetic cloud - shock wave - geomagnetic storm. **Astrophys. Space Sci.**, v. 243, p. 187, 1996. [55](#), [56](#), [95](#)

\_\_\_\_\_. Space weather: The solar perspective. **Living Reviews in Solar Physics**, v. 3, n. 2, p. 5–76, Jul. 2006. [43](#), [52](#), [54](#), [55](#), [65](#), [150](#)

SCHWENN, R.; MONTGOMERY, M. D.; ROSENBAUER, H.; MIGGENRIEDER, H.; MUEHLHAEUSER, K. H.; BAME, S. J.; FELDMAN, W. C.; HANSEN, R. T. Direct observation of the latitudinal extent of a high-speed stream in the solar wind. **J. Geophys. Res.**, v. 83, p. 1011–1017, 1978. [52](#)

SCHWENN, R.; ROSENBAUER, H. Ten years solar wind experiments on HELIOS 1 and HELIOS 2. **Geochimica et Cosmochimica Acta Supplement**, p. 66–79, 1984. [97](#)

SCHWENN, R.; ROSENBAUER, H.; MIGGENRIEDER, H. Das Plasmaexperiment auf Helios (E1). **Raumfahrtforschung**, v. 19, p. 226–232, 1975. [89](#)

SCHWENN, R.; ROSENBAUER, H.; MÜHLHÄUSER, K.-H. Singly-ionized helium in the driver gas of an interplanetary shock wave. **Geophys. Res. Lett.**, v. 7, p. 201–204, 1980. [109](#)

SHEELEY JR., N.; HOWARD, R. A.; MICHELS, D. J.; KOOMEN, M. J.; SCHWENN, R.; MÜHLHÄUSER, K. H.; ROSENBAUER, H. Coronal mass ejections and interplanetary shocks. **J. Geophys. Res.**, v. 90, p. 163–175, 1985. [63](#), [65](#), [92](#), [96](#), [99](#), [116](#), [120](#), [121](#), [136](#)

SISCOE, G. L.; SUEY, R. W. Significance criteria for variance matrix applications. **J. Geophys. Res.**, v. 77, p. 1321±1322, 1972. [294](#)

SMITH, E. J.; WOLFE, J. H. Observations of interaction regions and corotating shocks between one and five AU - Pioneers 10 and 11. **Geophysical Research Letters**, v. 3, p. 137–140, mar. 1976. [97](#)

SONETT, C.; COLBURN, D.; DAVIS, L.; SMITH, E.; COLEMAN, P. Evidence for a Collision-Free Magnetohydrodynamic Shock in Interplanetary Space. **Physical Review Letters**, v. 13, p. 153–156, Aug. 1964. [72](#)

SONNERUP, B. U. .; CAHILL JR., L. J. Magnetopause Structure and Attitude from Explorer 12 Observations. **J. Geophys. Res.**, v. 72, p. 171–+, jan 1967. [152](#), [293](#)

SONNERUP, B. U. .; SCHEIBLE, M. Minimum and maximum variance analysis. In: PASCHMANN, G.; DALY, P. W. (Ed.). **Analysis methods for multi-Spacecraft data**. Bern, Switzerland: The International Space Science Institute, 1998. v. 1, p. 185–220. [221](#)

SPIEGEL, M. R. (Ed.). **Theory and problems of probability and statistics**. New York, U.S.A.: Schaum Publishing Co., 1961. (Schaum's Outline Series). [285](#)

SPIEGEL, M. R.; SCHILLER, J.; SRINIVASAN, R. A. (Ed.). **Probability and statistics**. 2. ed. New York, U.S.A.: McGraw-Hill Professional, 2000. (Schaum's Outline Series). [285](#)

SPREITER, J. R.; SUMMERS, A. L.; ALKSNE, A. Y. Hidromagnetic flow around the magnetosphere. **Planet. Space Sci.**, v. 14, p. 223, 1966. [76](#), [293](#)

SRIVASTAVA, N.; VENKATAKRISHNAN, P. Relationship between cme speed and geomagnetic storm intensity. **Geophys. Res. Lett.**, v. 29, p. 1, 2002. [65](#)

ST. CYR, O. C.; PLUNKETT, S. P.; MICHELS, D. J.; PASWATERS, S. E.; KOOMEN, M. J.; SIMNETT, G. M.; THOMPSON, B. J.; GURMAN, J. B.; SCHWENN, R.; WEBB, D. F.; HILDNER, E.; LAMY, P. L. Properties of coronal mass ejections: Soho lasco observations from january 1996 to june 1998. **J. Geophys. Res.**, v. 105, n. A8, p. 18169–18186, 2000. [53](#), [150](#)

STEINOLFSON, R. S.; HUNDHAUSEN, A. J. Density and white light brightness in looplike coronal mass ejections - Temporal evolution. **J. Geophys. Res.**, v. 93, p. 14269–14276, dec 1988. [53](#), [71](#)

STURROCK, P.; SMITH, S. Magnetic field structure associated with coronal streamers. **Astronomical Journal**, v. 73, p. 78–+, 1968. [53](#)

TANIUTI, T. A Note on the Evolutionary Condition on Hydromagnetic Shocks. **Progress of Theoretical Physics**, v. 28, p. 756–757, out. 1962. [74](#)

TOUSEY, R. The Solar Corona. In: Rycroft, M. J.; Runcorn, S. K. (Ed.). **Space research**. [S.l.: s.n.], 1973. p. 713–+. [56](#)

TOUSEY, R.; BARTOE, J. D. F.; BOHLIN, J. D.; Brueckner, G. E.; Purcell, J. D.; Scherrer, V. E.; Sheeley JR., N. R.; Schumacher, R. J.; Vanhoosier, M. E. A Preliminary Study of the Extreme Ultraviolet Spectroheliograms from Skylab. **Solar Physics**, v. 33, p. 265–280, dez. 1973. [56](#)

TSURUTANI, B.; GONZALEZ, W. D.; TANG, F.; LEE, Y. T. Great magnetic storms. **Geophysical Research Letters**, v. 19, p. 73–76, 1992. [65](#)

TSURUTANI, B.; SMITH, E.; GONZALEZ, W.; TANG, F.; AKASOFU, S. Origin of interplanetary southward magnetic fields responsible for major magnetic storms near solar maximum (1978–1979). **J. Geophys. Res.**, v. 93, p. 8519–8531, 1988. [65](#)

WALKER, S. N.; BALIKHIN, M. A.; DUNLOP, M. Mirror structures in the magnetosheath: 3D structures on plane waves. **Advances in Space Research**, v. 30, p. 2745–2750, 2002. [160](#), [190](#)

WANG, Y.; ZHANG, J. A Statistical Study of Solar Active Regions That Produce Extremely Fast Coronal Mass Ejections. **The Astrophysical Journal**, v. 680, p. 1516–1522, jun. 2008. [54](#)



WEBB, D.; HOWARD, R. The solar cycle variation of coronal mass ejections and the solar wind mass flux. **J. Geophys. Res.**, v. 99, p. 4201–4220, 1994. [150](#)

WOO, R.; HABBAL, S. R. The Origin of the Solar Wind. **American Scientist**, v. 90, p. 532–+, dec 2002. [52](#)

WU, C. C. Formation, structure, and stability of MHD intermediate shocks. **J. Geophys. Res.**, v. 95, p. 8149–8175, jun. 1990. [74](#)

XIE, Y.; WEI, F.; XIANG, C.; FENG, X. The Effect of the Heliospheric Current Sheet on Interplanetary Shocks. **Solar Physics**, v. 238, p. 377–390, Nov. 2006. [147](#)

YASHIRO, S.; GOPALSWAMY, N.; MICHALEK, G.; CYR, O. S.; PLUNKETT, S.; RICH, N.; HOWARD, R. A catalog of white light coronal mass ejections observed by the soho spacecraft. **J. Geophys. Res.**, v. 109, p. 7105, 2004. [61](#)

YASHIRO, S.; MICHALEK, G.; AKIYAMA, S.; GOPALSWAMY, N.; HOWARD, R. A. Spatial Relationship between Solar Flares and Coronal Mass Ejections. **Astrophysical Journal**, v. 673, p. 1174–1180, Feb. 2008. [116](#)

YURCHYSHYN, V.; WANG, H.; ABRAMENKO, V. Correlation between speeds of coronal mass ejections and the intensity of geomagnetic storms. **Space Weather**, v. 2, 2004. [65](#)

ZHANG, J.; DERE, K. P.; HOWARD, R. A.; VOURLIDAS, A. A study of the kinematic evolution of coronal mass ejections. **Astrophys. J.**, v. 604, p. 420–432, 2004. [56](#)



## A APPENDIX A - LIST OF SHOCKS AS SEEN BY HELIOS MISSION

The 395 shock waves identified by the Helios probes during their time of operation are listed in [Table A.1](#). In this table, several parameters that identify the shocks are given, namely, the time of observation, radial, longitudinal, and latitudinal position of the probes at the time of observation, the upstream and downstream values for the solar wind and magnetic field parameters, the ratio between the upstream and downstream values of the proton density and magnetic field, the shock speed calculated and the interplanetary signatures for MCs.

In the first column, one can see the reference number (“SN”) for each shock, followed by the Helios probe (“SC”) that identified the shock in the year (YY) (third column), day of the year (DOY) (fourth column), at the hour (HH) (fifth column), at the minutes (MM) (sixth column), when they crossed the structures in the inner heliosphere. In the sequence, the date and time (Date/time) in the format “dd:mm:yy hh:mm” are presented, followed by the radial distance (RAD, in AU) (ninth column), the Helios-sun-earth angle (HSE, in degrees), the Carrington longitude (CLONG) (eleventh column) and latitude (CLAT) (twelfth column) (both given in degrees). The protons speed and density, and the IMF strength in the regions upstream and downstream, represented by  $v_1$  and  $v_2$ ,  $n_1$  and  $n_2$ , and  $B_1$  and  $B_2$ , respectively, are followed by the ratios  $R_N (=n_2/n_1)$  and  $R_B (=B_2/B_1)$  and the shock speed ( $V_S$ ) that compose the following columns, complemented by the solar wind and magnetic field signatures for MCs. The last five columns describe, for each event, the observed features in the density (“N”), pressure (“P”), temperature (“T”), magnetic field strength (“B”), and Helium composition (“H”) that report the presence of MCs as the drivers of the listed shock waves.

The reference number, “SN”, is a result of the preliminary classification of [Khalisi and Schwenn \(1995\)](#) that has suffered changes in the subsequent studies after the list was created. Revisions that came with the new studies by using this table have taken place. However, these changes have not modified the original sequence of the shock waves discoveries since the beginning of the classification. That explains why SN jumps from higher numbers to lower ones and its maximum is 419, while the total number of shocks that composes this list is 395. Another detail of SN is that it starts by the observations from H1, since first data were available from this probe. Probably, like we proceeded during the present study, changes on the technique and parameters considered for the shock identification have suffered modifications along

the time.

Missing values for the upstream parameters ( $v_1$ ,  $n_1$ , and  $B_1$ ) are defined by  $-1$ , and by  $1$  for the downstream ones ( $v_2$ ,  $n_2$ , and  $B_2$ ). In the case of  $R_N$ ,  $R_B$ , and  $V_S$ , the absence of data in these variables is represented by  $0$  for the listed shocks. When the signatures of MC are present in the solar wind data for each of its measured parameters, representations using upper-case letters like “N”, “P”, “T”, “H” mean that there is strong evidence of the presence of these MC signatures in the data. However, when low evidence is present, the representation is given by lower-case letters “n”, “p”, “t”, “h”. In the absence of data, the signal “/” represents the presence of gaps during the interval correspondent to the MC boundaries, while, when there is no signatures of MCs, the signal is “-”.

TABLE A.1 – Shock Waves Driven by ICMEs observed by Helios 1 and 2.

SN	SC	YY	DOY	HH	MM	Date/time	RAD	HSE	CLONG	CLAT	$v_1$	$v_2$	$v_{t1}$	$v_{t2}$	$B_1$	$B_2$	$R_N$	$R_B$	$V_S$	N	P	T	B	H
1	H1	74	359	10	15	25.12.74 10:15	0.966	355.3	8.0	-1.70	462.5	482.1	3.59	4.50	4.6	5.5	1.253	1.196	559.42	n	p	t	b	H
2	H1	74	362	3	3	28.12.74 3:03	0.959	354.5	331.7	-1.93	512.0	524.0	4.00	6.30	4.0	6.3	1.575	1.575	544.87	-	-	-	-	-
4	H1	75	6	20	43	6.1.75 20:43	0.924	352.0	201.1	-2.78	558.0	632.0	5.90	13.40	5.0	14.2	2.271	2.582	690.21	N	P	T	B	-
5	H1	75	8	0	21	8.1.75 0:21	0.918	351.7	185.5	-2.88	502.0	561.0	4.00	6.90	8.0	13.6	1.725	1.700	642.38	-	-	-	-	-
6	H1	75	77	13	46	18.3.75 13:46	0.317	182.7	100.5	2.82	305.0	346.0	158.00	271.00	28.7	59.6	1.715	2.077	403.33	n	p	t	b	h
7	H1	75	91	13	11	1.4.75 13:11	0.487	155.8	329.0	7.25	328.7	350.0	87.20	125.00	5.8	11.2	1.433	1.931	399.14	-	-	-	B	h
9	H1	75	210	23	0	29.7.75 23:00	0.844	163.7	197.5	-4.20	450.0	504.5	5.80	13.00	4.5	11.0	2.444	2.444	548.40	-	-	-	-	-
14	H1	75	322	11	30	18.11.75 11:30	0.873	354.3	356.0	2.95	352.0	390.0	16.00	25.00	10.0	19.2	1.562	1.920	457.56	n	p	t	-	-
15	H1	75	325	14	5	21.11.75 14:05	0.891	353.9	315.0	2.65	383.0	433.0	7.60	16.20	6.0	13.0	2.167	2.167	477.19	n	p	t	B	H
17	H1	75	342	4	4	8.12.75 4:04	0.960	350.1	92.7	1.12	398.0	443.0	8.20	14.40	6.8	12.8	1.756	1.882	502.52	n	-	t	-	-
271	H2	76	90	4	32	30.3.76 4:32	0.476	8.5	62.3	-6.22	303.2	326.0	34.20	61.00	18.5	29.1	1.784	1.573	355.10	N	P	T	B	-
272	H2	76	90	17	44	30.3.76 17:44	0.469	9.5	55.9	-6.11	411.0	503.0	6.80	8.10	43.5	55.8	1.191	1.283	984.23	N	p	t	b	H
273	H2	76	92	13	28	1.4.76 13:28	0.443	13.5	36.3	-5.69	402.0	525.0	24.00	50.00	21.0	46.8	2.083	2.229	638.54	N	P	T	b	/
18	H1	76	216	19	35	3.8.76 19:35	0.902	150.3	329.1	-3.32	440.0	530.0	8.00	12.00	-1.0	1.0	1.500	0.000	710.00	/	/	/	/	/
19	H1	76	228	4	43	15.8.76 4:43	0.830	149.4	177.7	-4.45	531.0	537.0	7.05	7.90	-1.0	1.0	1.121	0.000	772.65	/	/	/	/	/
20	H1	76	234	2	15	21.8.76 2:15	0.784	149.8	100.4	-5.04	344.0	353.0	16.00	24.40	-1.0	1.0	1.525	0.000	370.14	n	p	t	/	/
21	H1	76	272	23	2	28.9.76 23:02	0.345	207.0	4.0	-4.71	296.0	329.0	88.00	148.00	25.7	46.4	1.682	1.805	377.40	N	P	T	B	H
22	H1	76	328	10	27	23.11.76 10:27	0.808	339.6	125.1	3.93	330.0	360.0	7.00	10.00	6.3	8.1	1.429	1.286	430.00	-	-	/	b	/
275	H2	76	351	5	41	16.12.76 5:41	0.877	3.0	209.2	-1.70	327.0	352.0	16.00	32.20	6.0	10.0	2.013	1.667	376.69	/	/	/	b	/
25	H1	77	25	14	54	25.1.77 14:54	0.962	324.2	358.0	-1.72	323.0	344.0	16.30	31.40	2.2	3.9	1.926	1.773	366.67	N	P	t	b	H
277	H2	77	28	21	3	28.1.77 21:03	0.978	351.1	342.3	-5.02	411.0	429.0	11.00	14.30	9.5	12.3	1.300	1.295	489.00	-	-	-	-	-
26	H1	77	29	1	3	29.1.77 1:03	0.952	323.3	312.0	-2.01	338.1	454.5	11.50	31.40	5.3	18.9	2.730	3.566	521.77	N	P	T	B	H
278	H2	77	47	1	51	16.2.77 1:51	0.925	345.8	97.3	-6.04	335.0	369.0	7.60	10.10	-1.0	1.0	1.329	0.000	472.36	-	-	-	/	-
279	H2	77	50	17	36	19.2.77 17:36	0.907	345.0	48.2	-6.23	332.0	342.0	13.30	18.80	3.5	4.6	1.414	1.314	366.18	-	-	-	-	-
416	H1	77	50	21	40	19.2.77 21:40	0.840	319.3	20.4	-4.11	317.8	326.3	15.92	20.70	4.3	5.5	1.300	1.283	354.71	-	-	-	-	-
27	H1	77	75	11	33	16.3.77 11:33	0.610	326.3	63.5	-6.57	312.0	367.3	39.07	87.80	16.5	19.9	2.247	1.206	411.64	N	P	T	B	H
28	H1	77	75	19	47	16.3.77 19:47	0.717	344.6	77.1	-7.21	322.0	386.0	13.80	31.40	6.9	13.9	2.275	2.014	436.18	N	P	T	B	H
282	H2	77	83	4	15	24.3.77 4:15	0.638	347.9	343.6	-7.23	363.0	407.0	44.60	66.00	14.5	34.9	1.480	2.407	502.87	n	p	t	b	h
283	H2	77	107	14	35	17.4.77 14:35	0.322	43.5	76.6	-0.59	285.0	328.0	146.00	273.00	21.6	41.3	1.870	1.912	377.43	n	p	t	b	h
284	H2	77	110	20	21	20.4.77 20:21	0.297	62.9	53.2	2.05	379.0	414.0	82.00	120.30	48.2	75.6	1.467	1.568	488.93	n	p	t	b	H
29	H1	77	159	7	55	8.6.77 7:55	0.857	150.1	219.3	3.47	349.8	393.5	17.58	38.37	7.1	9.0	2.183	1.268	430.45	N	P	T	B	H
30	H1	77	160	16	1	9.6.77 16:01	0.865	150.0	201.7	3.34	374.7	410.6	25.87	35.52	13.3	26.1	1.373	1.962	506.84	-	-	-	-	-
31	H1	77	172	6	0	21.6.77 6:00	0.927	148.7	47.0	2.15	335.4	355.8	18.60	23.14	5.8	12.0	1.244	2.069	439.38	-	-	-	-	-
33	H1	77	195	16	10	14.7.77 16:10	0.984	143.5	91.4	-4.26	420.0	450.0	3.77	7.50	4.1	7.5	1.989	1.829	480.32	-	-	-	-	-
34	H1	77	240	6	50	28.8.77 6:50	0.846	134.9	212.7	-4.47	259.0	380.0	20.80	68.60	2.2	9.3	3.298	4.227	432.65	N	P	T	B	h
35	H1	77	242	7	15	30.8.77 7:15	0.832	134.9	186.0	-4.47	388.0	432.6	6.35	23.50	11.2	14.3	3.701	1.277	449.11	-	-	-	-	-
36	H1	77	263	19	07	20.9.77 19:07	0.631	141.1	268.0	-6.60	387.1	429.6	22.00	39.00	10.5	21.1	1.773	2.010	484.60	/	/	/	/	/
37	H1	77	263	20	37	20.9.77 20:37	0.630	141.2	267.0	-6.60	440.0	520.0	35.11	71.32	16.3	25.6	2.031	1.571	597.57	n	-	t	b	/
38	H1	77	268	2	40	25.9.77 2:40	0.580	144.9	215.0	-6.95	602.0	1101.0	11.71	85.00	15.1	58.2	7.259	3.854	1180.73	N	P	T	B	H
285	H2	77	268	12	51	25.9.77 12:51	0.643	168.3	232.8	-7.19	330.0	500.0	21.60	73.40	18.0	45.0	3.398	2.500	570.89	n	p	t	b	H
286	H2	77	269	12	6	26.9.77 12:06	0.631	168.9	220.6	-7.16	520.0	665.0	5.80	18.00	19.4	31.5	3.103	1.624	733.93	n	p	t	/	h
39	H1	77	311	18	15	7.11.77 18:15	0.474	303.2	5.86	7.22	350.0	413.0	40.00	69.00	26.7	44.0	1.725	1.648	492.76	-	-	-	b	-
288	H2	77	311	18	54	7.11.77 18:54	0.400	326.1	-0.21	6.42	307.0	330.0	69.80	98.60	26.8	35.2	1.413	1.313	396.01	n	p	t	-	/

TABLE A.1 - continues

SN	SC	YY	DOY	HH	MM	Date/time	RAD	HSE	CLONG	CLAT	v <sub>1</sub>	v <sub>2</sub>	n <sub>1</sub>	n <sub>2</sub>	B <sub>1</sub>	B <sub>2</sub>	R <sub>N</sub>	R <sub>B</sub>	V <sub>S</sub>	N	P	T	B	H
289	H2	77	327	16	9	23.11.77 16:09	0.613	352.5	357.3	2.51	276.0	307.0	34.50	61.00	6.7	11.5	1.768	1.716	347.36	n	p	-	-	h
290	H2	77	328	6	11	24.11.77 6:11	0.620	352.9	350.0	2.39	315.0	335.0	84.10	117.70	22.0	32.4	1.400	1.473	385.06	n	p	t	-	-
40	H1	77	328	22	27	24.11.77 22:27	0.681	321.5	309.8	5.55	314.0	331.0	46.00	65.00	7.4	13.6	1.413	1.838	372.16	-	-	-	-	-
292	H2	77	332	12	57	28.11.77 12:57	0.669	355.4	295.3	1.57	339.0	369.0	48.50	75.50	4.7	11.4	1.557	2.426	422.89	-	-	-	-	-
293	H2	77	335	1	29	1.12.77 1:29	0.697	356.4	284.0	1.14	350.0	413.0	73.40	195.60	6.3	14.7	2.665	2.333	450.84	N	P	T	b	-
41	H1	77	335	5	13	1.12.77 5:13	0.743	323.6	229.1	4.83	345.0	383.0	9.60	16.40	7.6	13.2	1.708	1.737	436.65	/	/	/	/	/
42	H1	77	335	8	54	1.12.77 8:54	0.744	323.6	227.4	4.81	386.0	441.0	20.20	46.20	14.5	18.1	2.287	1.248	483.73	N	P	t	B	h
294	H2	77	353	2	12	19.12.77 2:12	0.853	357.8	28.3	-1.27	283.0	298.0	13.70	23.20	4.5	5.8	1.693	1.289	319.63	-	-	-	-	-
43	H1	77	356	20	20	22.12.77 20:20	0.900	323.1	304.5	2.60	354.0	370.0	19.00	27.00	7.7	9.5	1.421	1.234	408.00	-	-	-	-	-
44	H1	78	1	17	11	1.1.78 17:11	0.944	320.8	172.3	1.69	412.5	450.1	3.10	4.40	8.5	12.3	1.419	1.447	539.76	-	-	-	-	-
45	H1	78	2	1	41	2.1.78 1:41	0.948	320.7	167.1	1.65	429.0	496.0	5.50	9.00	8.0	15.2	1.636	1.900	601.29	n	-	t	b	-
46	H1	78	3	8	39	3.1.78 8:39	0.950	320.4	150.2	1.54	693.1	869.4	4.98	10.55	8.4	15.4	2.118	1.833	1027.03	N	P	T	B	H
295	H2	78	3	14	50	3.1.78 14:50	0.938	354.6	180.5	-2.74	394.4	449.0	12.50	27.00	7.8	15.1	2.160	1.936	496.07	N	P	T	B	H
47	H1	78	5	3	23	5.1.78 3:23	0.956	319.9	126.0	1.38	546.7	567.9	1.31	1.71	-1.0	1.0	1.305	0.000	637.33	-	-	-	-	-
296	H2	78	9	20	10	9.1.78 20:10	0.959	253.0	97.0	-3.26	406.0	485.0	4.67	8.86	7.0	11.3	1.897	1.614	573.05	-	p	t	b	-
297	H2	78	19	21	44	19.1.78 21:44	0.979	349.8	321.8	-3.99	274.0	305.5	5.60	7.55	6.7	8.1	1.348	1.209	395.96	/	/	/	/	/
298	H2	78	23	20	38	23.1.78 20:38	0.983	348.5	268.0	-4.26	309.0	333.6	13.80	22.30	9.5	10.6	1.616	1.116	373.54	n	p	t	b	h
299	H2	78	25	6	3	25.1.78 6:03	0.984	348.0	249.5	-4.35	338.0	351.0	15.10	17.60	6.3	8.1	1.166	1.286	429.52	n	p	t	b	-
300	H2	78	29	21	44	29.1.78 21:44	0.983	246.4	186.0	-4.65	484.0	519.0	2.01	2.48	15.5	19.8	1.234	1.277	668.68	n	p	t	b	h
301	H2	78	34	19	28	3.2.78 19:28	0.979	344.8	119.0	-4.97	444.0	472.0	7.90	13.20	6.0	10.0	1.671	1.667	513.74	n	-	-	-	-
302	H2	78	37	7	2	6.2.78 7:02	0.976	344.0	86.6	-5.11	378.0	401.0	7.70	12.60	5.0	6.8	1.636	1.360	437.14	N	P	T	B	H
48	H1	78	46	1	30	15.2.78 1:30	0.946	307.6	294.6	-2.12	527.2	546.3	11.62	29.13	6.0	23.7	2.507	3.950	558.98	n	p	t	b	-
303	H2	78	46	1	53	15.2.78 1:53	0.954	341.3	328.6	-5.62	377.0	572.0	6.70	22.60	6.8	16.8	3.373	2.471	654.17	n	p	-	B	H
304	H2	78	56	4	54	25.2.78 4:54	0.913	338.8	192.5	-6.16	627.0	662.0	5.80	8.30	9.2	10.8	1.431	1.174	743.20	n	p	t	b	-
305	H2	78	60	4	16	1.3.78 4:16	0.892	338.0	139.5	-6.36	527.4	619.0	4.40	8.30	7.3	11.0	1.886	1.507	722.34	n	p	t	b	-
49	H1	78	60	12	15	1.3.78 12:15	0.878	304.7	102.0	-3.44	381.0	490.7	15.60	29.80	7.0	24.7	1.910	3.529	611.22	N	P	T	B	H
50	H1	78	64	16	15	5.3.78 16:15	0.851	304.3	46.6	-3.65	375.0	389.0	26.00	33.00	9.7	13.4	1.269	1.381	441.00	-	-	-	-	-
306	H2	78	66	23	54	7.3.78 23:54	0.850	337.1	49.6	-6.69	402.0	570.0	11.40	21.00	13.0	28.0	1.842	2.154	769.50	N	P	t	b	H
51	H1	78	67	8	44	8.3.78 8:44	0.832	304.2	10.9	-4.11	337.0	401.0	8.92	20.90	7.3	19.2	2.343	2.630	448.65	-	p	-	-	-
307	H2	78	70	13	40	11.3.78 13:40	0.823	336.9	0.8	-6.84	352.9	359.0	8.45	16.90	8.0	10.0	2.000	1.250	365.10	n	p	t	b	H
52	H1	78	91	5	30	1.4.78 5:30	0.604	311.7	63.6	-6.61	587.0	677.0	4.96	9.13	12.9	17.3	1.841	1.341	784.05	-	p	-	/	-
308	H2	78	91	8	34	1.4.78 8:34	0.619	342.6	110.3	-6.62	455.4	462.4	21.80	28.50	15.4	20.7	1.307	1.344	485.18	N	P	t	B	h
53	H1	78	92	12	7	2.4.78 12:07	0.589	312.9	48.0	-6.73	443.0	465.0	8.00	9.00	-1.0	1.0	1.125	0.000	641.00	-	-	-	-	-
309	H2	78	92	23	15	2.4.78 23:15	0.600	344.4	73.0	-7.15	528.0	597.0	9.95	20.00	15.8	19.6	2.010	1.241	665.31	-	-	-	-	-
54	H1	78	93	19	13	3.4.78 19:13	0.573	314.2	31.7	-6.85	389.0	505.2	12.60	36.00	-1.0	1.0	2.857	0.000	567.77	n	p	t	/	-
310	H2	78	93	7	16	9.4.78 7:16	0.518	351.1	356.5	-6.67	380.3	481.9	31.00	66.50	23.3	49.7	2.145	2.133	570.62	N	P	T	b	H
55	H1	78	93	7	18	9.4.78 7:18	0.504	321.7	326.9	-7.20	404.0	439.0	58.00	87.00	19.3	30.8	1.500	1.596	509.00	n	p	t	/	h
311	H2	78	102	14	14	12.4.78 14:14	0.421	5.4	279.0	-5.21	351.0	418.0	34.00	61.00	37.1	65.2	1.794	1.757	627.09	N	P	T	B	H
56	H1	78	106	14	50	16.4.78 14:50	0.409	338.6	319.2	-6.16	422.0	540.4	17.50	41.40	21.2	35.0	2.366	1.651	502.07	-	-	-	-	-
57	H1	78	107	8	55	17.4.78 8:55	0.400	341.0	24.0	-6.78	421.3	494.7	92.20	143.52	-1.0	1.0	1.557	0.000	626.57	-	-	-	-	-
313	H2	78	108	13	19	18.4.78 13:19	0.390	12.4	255.5	-4.33	475.0	579.0	37.40	59.00	39.3	56.1	1.578	1.427	759.07	/	/	/	/	/
58	H1	78	108	13	50	18.4.78 13:50	0.385	345.1	228.2	-6.52	464.9	490.0	75.60	135.00	-1.0	1.0	1.786	0.000	521.95	n	p	t	/	h
314	H2	78	108	18	0	18.4.78 18:00	0.387	13.1	253.5	-4.24	543.5	655.0	35.00	47.00	43.3	67.3	1.343	1.554	980.21	N	P	T	b	H
59	H1	78	109	5	46	19.4.78 5:46	0.378	347.5	221.5	-6.34	472.0	486.0	21.00	45.00	-1.0	1.0	2.143	0.000	498.25	-	-	-	-	-
60	H1	78	109	13	0	19.4.78 13:00	0.374	348.7	218.8	-6.24	422.1	443.2	39.96	51.60	-1.0	1.0	1.291	0.000	515.64	n	p	t	/	h

TABLE A.1 - continues

SN	SC	YY	DOY	HH	MM	Date/time	RAD	HSE	CLONG	CLAT	v <sub>1</sub>	v <sub>2</sub>	n <sub>1</sub>	n <sub>2</sub>	B <sub>1</sub>	B <sub>2</sub>	R <sub>N</sub>	R <sub>B</sub>	V <sub>S</sub>	N	P	T	B	H
316	H2	78	119	2	56	29.4.78 2:56	0.292	67.4	170.7	3.50	410.0	465.0	98.00	137.00	59.4	87.5	1.398	1.473	603.21	N	P	T	b	-
61	H1	78	119	3	49	29.4.78 3:49	0.310	38.7	141.5	-0.03	311.2	421.6	65.70	141.60	44.4	90.5	2.155	2.038	517.16	n	p	t	b	-
62	H1	78	120	11	16	30.4.78 11:16	0.311	46.7	132.8	1.13	352.0	475.0	79.00	115.00	38.3	83.2	1.456	2.172	744.92	n	p	t	b	-
63	H1	78	122	13	30	2.5.78 13:30	0.318	58.8	117.2	2.94	360.0	470.0	150.00	230.00	59.8	82.0	1.533	1.371	676.25	-	-	-	-	-
64	H1	78	127	20	5	7.5.78 20:05	0.361	85.4	73.7	5.96	405.0	561.0	20.00	46.20	34.9	60.2	1.725	1.725	680.08	-	-	-	b	-
317	H2	78	127	22	22	7.5.78 22:22	0.340	121.3	108.3	7.25	413.4	497.0	57.00	95.60	42.6	66.6	1.677	1.563	620.45	-	-	-	-	-
65	H1	78	129	9	36	9.5.78 9:36	0.379	91.6	59.2	6.47	417.0	522.0	29.00	52.00	35.9	58.4	1.793	1.627	654.39	-	-	-	-	-
318	H2	78	129	11	25	9.5.78 11:25	0.358	128.2	94.9	7.14	396.6	424.3	32.00	38.80	35.9	42.6	1.212	1.187	554.65	-	-	-	-	-
66	H1	78	130	15	2	10.5.78 15:02	0.392	95.8	48.0	6.78	390.0	510.0	30.00	75.00	33.1	60.2	2.500	1.819	590.00	N	P	t	b	-
415	H2	78	130	6	28	10.5.78 28:38	0.370	131.4	7.0	6.98	510.8	524.9	31.85	32.10	40.7	39.3	1.008	0.965	2275.10	-	-	-	-	-
67	H1	78	132	2	30	12.5.78 2:30	0.411	100.7	32.8	7.00	330.0	700.0	25.00	90.00	35.6	105.8	3.600	2.972	842.31	-	P	t	B	h
319	H2	78	132	5	15	12.5.78 5:15	0.394	138.4	68.8	6.69	344.0	478.0	22.70	37.00	32.6	51.0	1.630	1.564	690.71	N	P	t	b	/
68	H1	78	132	13	25	12.5.78 13:25	0.417	102.1	27.9	7.06	570.0	778.0	27.00	40.00	50.0	85.0	1.481	1.700	1210.00	n	p	t	B	H
69	H1	78	134	9	24	14.5.78 9:24	0.441	107.1	8.4	7.21	387.0	453.0	5.50	9.60	34.6	40.6	1.745	1.173	541.54	n	p	t	B	h
320	H2	78	134	15	1	14.5.78 15:01	0.428	145.5	43.8	6.13	316.0	364.5	31.00	49.00	34.1	43.5	1.581	1.276	448.03	/	/	/	/	/
321	H2	78	137	22	25	17.5.78 22:25	0.473	153.1	7.8	5.30	341.0	370.0	31.00	50.00	22.9	34.1	1.613	1.489	417.32	/	/	/	b	/
402	H2	78	138	8	0	18.5.78 8:00	0.478	153.8	3.5	5.15	373.7	537.7	7.88	26.99	12.0	30.0	3.425	2.500	605.33	n	p	t	b	-
413	H1	78	153	8	18	2.6.78 8:18	0.673	131.5	142.4	5.81	348.9	383.2	14.38	17.26	20.0	35.0	1.200	1.750	554.46	-	-	-	-	-
70	H1	78	164	3	58	13.6.78 3:58	0.777	135.1	2.7	4.57	397.0	519.0	16.00	40.00	18.3	38.6	2.500	2.109	600.33	-	-	-	-	-
71	H1	78	177	11	41	26.6.78 11:41	0.875	135.6	186.5	3.12	302.0	313.0	8.00	9.00	5.7	6.8	1.125	1.193	401.00	-	-	-	-	-
72	H1	78	189	10	20	8.7.78 10:20	0.935	134.0	26.0	1.90	365.0	460.0	11.00	20.00	7.4	23.7	1.818	3.203	576.11	n	p	t	b	h
323	H2	78	191	19	58	10.7.78 19:58	0.946	171.2	32.9	-2.98	345.0	360.0	7.20	11.20	-1.0	1.0	1.556	0.000	387.00	/	/	/	/	/
73	H1	78	201	8	16	20.7.78 8:16	0.971	131.5	227.2	0.77	420.0	477.0	5.00	8.50	-1.0	1.0	1.700	0.000	558.43	n	p	t	/	-
74	H1	78	202	19	36	21.7.78 19:36	0.974	131.1	210.7	0.65	420.0	499.0	5.90	10.00	-1.0	1.0	1.695	0.000	612.68	n	p	t	/	-
325	H2	78	207	12	2	26.7.78 12:02	0.981	167.3	181.0	-4.25	414.0	471.0	5.20	12.10	-1.0	1.0	2.327	0.000	513.96	-	-	-	-	-
326	H2	78	219	11	49	7.8.78 11:49	0.981	164.0	19.2	-5.07	328.0	388.0	5.80	13.50	-1.0	1.0	2.328	0.000	433.19	-	-	-	-	-
327	H2	78	240	13	48	28.8.78 13:48	0.921	159.0	95.5	-6.28	317.0	422.0	11.00	38.00	8.0	14.3	3.455	1.788	464.78	N	P	T	b	-
328	H2	78	268	1	26	25.9.78 1:26	0.721	158.8	92.4	-7.24	311.0	562.0	22.00	102.00	10.0	30.0	4.636	3.000	631.02	n	p	t	b	-
75	H1	78	268	2	30	25.9.78 2:30	0.745	121.4	54.5	-5.52	409.0	556.4	15.00	50.00	12.3	22.2	3.333	1.805	619.57	n	p	t	b	h
419	H2	78	279	3	50	06.10.78 3:50	0.600	164.8	311.6	-7.09	-1.0	-1.0	-1.00	-1.00	38.7	41.4	-1.000	1.071	-1.00	N	P	t	B	?
77	H1	78	286	13	42	13.10.78 13:42	0.541	133.7	182.4	-7.14	370.0	435.0	26.00	59.00	23.3	41.4	2.269	1.777	486.21	/	/	/	/	/
78	H1	78	286	20	41	13.10.78 20:41	0.537	134.1	179.1	-7.16	374.0	420.0	29.00	50.00	27.0	41.7	1.724	1.544	483.52	-	-	-	-	-
79	H1	78	287	13	50	14.10.78 13:50	0.528	135.1	171.0	-7.19	384.0	400.0	12.90	13.80	8.6	12.3	1.070	1.430	629.33	n	p	t	B	-
80	H1	78	290	9	0	17.10.78 9:00	0.493	139.5	139.0	-7.25	357.0	446.0	31.00	55.00	20.1	43.5	1.774	2.164	560.96	n	p	t	b	H
81	H1	78	291	16	12	18.10.78 16:12	0.475	142.1	123.9	-7.23	400.0	473.0	30.00	100.00	25.8	57.9	3.333	2.244	504.29	N	P	t	B	H
414	H2	78	294	1	45	21.10.78 1:45	0.395	191.6	141.7	-4.11	367.7	439.9	30.77	49.28	30.0	50.0	1.602	1.667	559.92	/	/	/	/	/
329	H2	78	297	7	47	24.10.78 7:47	0.353	204.0	111.2	-2.35	270.0	340.0	42.00	67.00	40.8	52.5	1.595	1.287	457.60	n	p	t	b	/
330	H2	78	305	16	47	1.11.78 16:47	0.291	252.3	49.4	4.42	238.0	313.0	114.00	296.00	38.0	62.3	2.596	1.639	359.98	n	p	t	B	-
331	H2	78	312	7	26	8.11.78 7:26	0.324	293.9	3.8	7.23	266.0	506.0	90.00	212.00	26.9	33.4	2.356	1.242	683.05	n	p	t	B	h
82	H1	78	333	3	17	29.11.78 3:17	0.552	297.6	93.1	6.81	460.0	785.0	12.50	35.00	21.1	47.8	2.800	2.265	965.56	N	P	t	b	H
83	H1	78	334	13	24	30.11.78 13:24	0.569	299.2	75.9	6.67	460.0	540.0	7.00	13.50	15.1	23.6	1.929	1.563	626.15	n	p	t	b	H
84	H1	78	335	17	37	1.12.78 17:37	0.583	300.4	62.0	6.55	401.5	413.0	7.30	10.70	12.4	16.3	1.466	1.315	439.58	-	p	t	b	h
85	H1	78	339	17	37	5.12.78 17:47	0.631	303.7	12.5	6.11	272.0	388.0	30.00	91.00	9.5	19.1	3.033	2.011	445.05	N	P	T	B	H
86	H1	78	343	14	58	9.12.78 14:58	0.674	306.0	323.6	5.66	329.0	359.0	39.00	62.00	21.0	24.7	1.590	1.176	409.87	-	-	-	b	-
87	H1	78	344	2	42	10.12.78 2:42	0.679	306.2	317.1	5.60	355.0	373.0	37.00	60.00	12.2	16.2	1.622	1.328	401.96	N	P	t	b	H
332	H2	78	347	2	47	13.12.78 2:47	0.750	351.1	322.9	0.35	381.1	423.2	14.75	16.14	14.9	19.8	1.094	1.329	869.94	n	p	t	B	h

TABLE A.1 - continues

SN	SC	Y Y	DOY	HH	MM	Date/time	RAD	HSE	CLONG	CLAT	v <sub>1</sub>	v <sub>2</sub>	n <sub>1</sub>	n <sub>2</sub>	B <sub>1</sub>	B <sub>2</sub>	R <sub>N</sub>	R <sub>B</sub>	V <sub>S</sub>	N	P	T	B	H
333	H2	78	347	12	45	13.12.78 12:45	0.754	351.2	317.0	0.28	479.6	529.3	23.20	49.00	15.9	17.8	2.112	1.119	573.99	n	p	t	b	h
335	H2	78	355	10	2	21.12.78 10:02	0.821	351.6	21.7	-0.75	438.2	464.3	8.60	16.00	10.1	15.0	1.860	1.485	494.63	N	p	T	b	h
89	H1	78	356	9	2	22.12.78 9:02	0.794	309.0	159.1	4.24	393.0	412.0	13.00	15.00	13.6	17.5	1.154	1.287	535.50	N	-	T	b	h
90	H1	78	356	20	20	22.12.78 20:20	0.798	309.0	152.6	4.19	441.0	545.0	12.40	27.60	14.4	19.9	2.226	1.382	629.84	N	p	t	-	h
336	H2	78	358	8	1	24.12.78 8:01	0.843	351.4	175.2	-1.08	372.7	411.5	5.60	8.80	6.7	9.4	1.571	1.403	479.40	N	p	T	B	h
417	H2	78	359	2	2	25.12.78 02:02	0.850	351.3	165.2	-1.07	410.7	394.7	10.93	11.58	-1.0	1.0	1.060	-1.000	125.65	-	-	-	-	-
91	H1	78	359	17	30	25.12.78 17:30	0.820	309.1	115.0	3.88	609.0	670.0	3.80	10.00	9.1	17.3	2.632	1.901	707.39	-	-	-	-	-
337	H1	78	362	23	1	28.12.78 23:01	0.844	308.9	72.1	3.55	614.0	867.0	2.30	6.80	3.5	10.1	2.957	2.886	996.31	N	p	t	B	H
93	H2	78	363	6	5	29.12.78 6:05	0.875	350.8	109.7	-1.61	597.2	692.3	4.30	7.60	6.5	10.0	1.767	1.538	816.22	N	p	t	b	-
93	H1	79	1	8	6	1.1.79 8:06	0.866	308.6	27.0	3.21	420.0	560.0	6.00	15.00	-1.0	1.0	2.500	0.000	653.33	n	p	t	-	-
94	H1	79	2	5	37	2.1.79 5:37	0.872	308.5	15.6	3.13	466.0	563.0	10.70	23.60	-1.0	1.0	2.206	0.000	643.46	N	p	T	/	H
338	H2	79	2	12	54	2.1.79 12:54	0.900	350.0	52.8	-2.03	479.0	530.0	4.40	6.30	7.4	11.1	1.432	1.500	648.11	-	-	/	/	-
339	H2	79	7	5	6	7.1.79 5:06	0.923	348.9	350.2	-2.46	408.0	415.0	4.60	7.00	8.2	10.9	1.522	1.329	428.42	/	/	/	/	/
340	H2	79	7	10	33	7.1.79 10:33	0.925	348.9	347.1	2.48	430.0	501.0	9.30	20.10	12.0	18.4	2.161	1.533	562.14	N	p	t	B	H
340	H2	79	7	10	33	7.1.79 10:33	0.925	348.9	347.1	2.48	430.0	501.0	9.30	20.10	12.0	18.4	2.161	1.533	562.14	N	p	t	B	H
344	H2	79	34	13	40	3.2.79 13:40	0.984	340.6	341.7	-4.50	459.0	499.0	11.90	36.30	-1.0	1.0	3.050	0.000	518.51	N	p	t	/	h
102	H1	79	39	19	23	8.2.79 19:23	0.985	298.7	230.5	-0.22	353.0	418.0	7.00	11.00	-1.0	1.0	1.571	0.000	531.75	-	-	-	-	-
345	H2	79	41	18	33	10.2.79 18:33	0.979	338.2	244.6	-4.96	344.0	478.0	6.90	21.40	-1.0	1.0	3.101	0.000	541.77	N	p	T	/	H
103	H1	79	42	2	10	11.2.79 2:10	0.984	298.0	200.4	-0.40	370.0	397.0	10.00	19.00	-1.0	1.0	1.900	0.000	427.00	-	-	-	-	-
412	H1	79	48	10	35	17.2.79 10:35	0.978	296.0	114.8	-0.95	540.0	816.0	0.92	1.06	-1.0	1.0	1.152	0.000	2629.71	n	p	t	/	h
346	H2	79	48	19	37	17.2.79 19:37	0.966	336.0	149.4	-5.38	523.0	625.0	4.50	12.00	3.9	11.3	2.667	2.897	686.20	n	p	t	b	h
347	H2	79	51	22	10	20.2.79 22:10	0.957	335.1	107.6	-5.56	427.0	489.0	2.60	4.60	7.0	12.0	1.769	1.714	569.60	n	p	t	b	/
104	H1	79	58	2	44	27.2.79 2:44	0.957	293.2	344.7	-1.78	372.0	505.0	8.00	20.00	8.2	19.2	2.500	2.341	593.67	N	p	T	B	h
348	H2	79	58	20	40	27.2.79 20:40	0.932	333.2	14.3	-5.94	388.0	448.0	7.20	15.40	6.2	13.7	2.139	2.210	500.68	-	-	-	-	-
105	H1	79	62	2	2	3.3.79 2:02	0.944	292.2	291.1	-2.14	374.0	612.0	6.20	9.00	10.9	22.1	1.452	2.028	1139.00	N	p	T	B	H
349	H2	79	62	9	34	3.3.79 9:34	0.916	332.4	326.9	-6.13	452.0	515.0	6.60	12.40	6.0	12.4	1.879	2.067	586.69	N	p	T	/	/
350	H2	79	66	17	20	7.3.79 17:20	0.894	331.6	269.1	-6.35	345.0	364.0	14.20	17.50	8.8	9.6	1.232	1.091	445.76	N	p	T	b	h
106	H1	79	70	3	40	11.3.79 3:40	0.909	290.5	183.1	-2.88	314.0	420.0	14.00	32.40	11.7	23.9	2.314	2.043	500.65	-	-	-	-	-
351	H2	79	71	0	20	12.3.79 0:20	0.868	330.9	212.0	-6.55	280.0	354.0	12.40	34.20	6.6	15.4	2.758	2.333	396.09	N	p	t	b	-
107	H1	79	75	9	30	16.3.79 9:30	0.881	289.7	113.7	-3.37	352.0	394.0	5.30	9.30	-1.0	1.0	1.755	0.000	449.65	n	p	-	/	h
108	H1	79	76	21	56	17.3.79 21:56	0.871	289.5	93.0	-3.53	412.0	448.0	4.60	6.70	-1.0	1.0	1.457	0.000	526.86	-	-	-	-	-
352	H2	79	79	4	36	20.3.79 4:36	0.809	330.5	103.4	-6.91	355.0	465.0	9.20	23.00	10.0	22.7	2.500	2.270	538.33	N	p	T	b	-
353	H2	79	80	17	15	21.3.79 17:15	0.798	330.5	83.3	-6.96	473.0	515.0	6.80	7.30	12.2	14.4	1.074	1.180	1086.20	-	-	-	-	-
109	H1	79	83	21	4	24.3.79 21:04	0.823	289.1	0.2	-4.22	380.0	520.0	8.20	22.20	-1.0	1.0	2.707	0.000	602.00	N	p	T	B	h
354	H2	79	86	8	53	27.3.79 8:53	0.746	331.2	9.8	-7.14	390.0	900.0	16.00	40.00	12.9	17.8	2.500	1.380	1240.00	N	p	t	b	h
110	H1	79	87	10	4	28.3.79 10:04	0.796	289.3	314.0	-4.60	370.0	440.0	8.90	15.80	-1.0	1.0	1.775	0.000	530.29	-	-	-	-	-
111	H1	79	89	1	45	30.3.79 1:45	0.782	289.5	292.3	-4.76	395.0	413.0	17.00	22.00	-1.0	1.0	1.294	0.000	474.20	n	p	t	/	h
355	H2	79	92	20	7	2.4.79 20:07	0.680	333.2	286.5	-7.25	353.0	473.0	12.50	43.00	10.3	16.1	3.440	1.563	522.18	N	p	-	B	H



TABLE A.1 - continues

SN	SC	YY	DOY	HH	MM	Date/time	RAD	HSE	CLONG	CLAT	v <sub>1</sub>	v <sub>2</sub>	n <sub>1</sub>	n <sub>2</sub>	B <sub>1</sub>	B <sub>2</sub>	R <sub>N</sub>	R <sub>B</sub>	V <sub>S</sub>	N	P	T	B	H
112	H1	79	93	19	45	3.4.79 19:45	0.740	290.3	230.5	-5.26	351.0	417.0	30.50	69.80	-1.0	1.0	2.289	0.000	468.22	n	p	t	/	h
356	H2	79	94	13	30	4.4.79 13:30	0.656	334.0	264.5	-7.25	373.0	545.0	13.00	27.00	21.4	28.3	1.923	1.322	731.33	-	P	T	B	/
357	H2	79	95	15	28	5.4.79 15:28	0.648	334.6	250.5	-7.24	446.0	600.0	12.00	25.00	18.2	39.9	2.250	2.192	723.20	N	P	t	B	h
113	H1	79	105	4	5	15.4.79 4:05	0.621	295.8	86.0	-6.47	325.0	437.0	31.20	80.00	-1.0	1.0	2.564	0.000	508.61	N	P	T	B	H
114	H1	79	112	13	32	22.4.79 13:32	0.530	303.7	356.0	-7.10	430.0	470.0	43.00	59.00	22.0	38.9	1.372	1.768	577.50	N	P	t	-	-
358	H2	79	113	15	16	23.4.79 15:16	0.412	0.8	39.3	-4.98	493.0	778.0	39.00	83.00	33.0	42.7	2.128	1.294	1030.61	N	P	t	b	h
115	H1	79	114	1	18	24.4.79 1:18	0.511	306.0	338.7	-7.18	571.6	597.0	25.40	35.30	20.2	24.1	1.390	1.193	662.17	-	-	-	-	-
116	H1	79	118	4	27	28.4.79 4:27	0.457	313.9	292.0	-7.25	434.4	473.4	25.30	32.40	22.7	27.5	1.281	1.211	612.37	n	p	t	b	h
117	H1	79	122	21	40	2.5.79 21:40	0.397	326.9	243.0	-6.73	269.0	279.0	133.60	173.60	27.0	35.9	1.299	1.330	312.40	-	-	-	B	-
359	H2	79	123	13	53	3.5.79 13:53	0.301	45.9	312.8	1.47	295.0	369.0	97.00	210.00	53.1	86.0	1.620	1.620	432.52	N	P	t	B	-
361	H2	79	129	3	30	9.5.79 3:30	0.295	83.2	276.6	5.88	405.0	550.0	88.00	180.00	65.2	110.5	2.045	1.695	688.70	n	P	T	b	h
360	H2	79	129	8	30	9.5.79 8:30	0.296	84.6	275.3	5.99	502.0	580.0	70.00	84.00	117.8	144.0	1.200	1.222	970.00	n	p	t	b	/
118	H1	79	141	11	5	21.5.79 11:05	0.344	63.2	93.6	5.26	292.0	319.0	63.00	75.80	53.9	64.2	1.203	1.191	451.89	-	-	-	-	-
362	H2	79	142	15	58	22.5.79 15:58	0.445	142.7	157.4	5.81	380.0	420.0	38.00	55.00	25.0	35.0	1.447	1.400	509.41	-	-	-	-	/
363	H2	79	148	7	57	28.5.79 7:57	0.524	153.1	92.4	4.36	310.0	348.0	28.30	57.00	-1.0	1.0	2.014	0.000	385.47	/	/	/	/	/
364	H2	79	148	10	28	28.5.79 10:28	0.525	153.0	91.4	4.34	355.0	426.0	96.00	254.00	-1.0	1.0	2.646	0.000	469.14	n	p	t	-	-
119	H1	79	148	18	41	28.5.79 18:41	0.428	90.1	24.0	7.15	374.0	512.0	81.00	234.90	27.2	55.4	2.900	2.037	584.63	n	P	T	B	h
365	H2	79	150	4	42	30.5.79 4:42	0.548	155.6	70.3	3.91	405.0	460.0	23.00	33.00	-1.0	1.0	1.435	0.000	586.50	N	P	T	B	h
366	H2	79	162	6	15	11.6.79 6:15	0.692	164.8	280.2	1.44	310.0	414.0	12.00	25.00	10.0	17.0	2.083	1.700	510.00	-	-	-	-	/
401	H2	79	162	19	5	11.6.79 19:05	0.698	165.0	272.8	1.34	399.0	440.0	32.00	50.00	15.0	22.0	1.562	1.467	512.89	-	-	-	-	-
120	H1	79	162	20	55	11.6.79 20:55	0.607	113.1	220.5	6.44	263.0	284.0	63.00	113.00	14.5	24.2	1.794	1.669	310.46	-	-	-	-	-
416	H1	79	175	20	6	24.6.79 20:06	0.740	119.9	55.4	4.94	-1.0	453.5	-1.00	13.77	-1.0	13.8	-1.000	-1.000	-1.00	N	P	T	B	?
367	H2	79	175	21	9	24.6.79 21:09	0.818	167.6	103.1	-0.60	339.0	366.0	5.00	7.90	8.0	10.0	1.580	1.500	412.55	-	/	/	/	/
410	H2	79	178	16	14	27.6.79 16:14	0.838	167.6	67.0	-0.90	389.0	417.0	13.66	21.23	10.0	15.0	1.554	1.500	467.53	/	/	/	/	/
403	H1	79	186	11	30	5.7.79 11:30	0.832	121.3	276.0	3.74	395.4	544.2	6.42	8.43	8.0	13.5	1.313	1.688	1019.47	n	p	t	/	h
121	H1	79	192	10	0	11.7.79 10:00	0.872	-1.0	190.0	3.10	-1.0	1.0	-1.00	1.00	-1.0	1.0	0.000	0.000	0.00	/	/	/	/	/
122	H1	79	202	18	22	21.7.79 18:22	0.927	120.0	59.2	2.05	328.3	409.5	15.00	40.00	-1.0	1.0	2.667	0.000	458.22	/	/	/	/	/
368	H2	79	203	15	42	22.7.79 15:42	0.962	163.8	90.5	-3.44	328.0	390.0	5.44	11.20	-1.0	1.0	2.059	0.000	448.56	/	p	/	/	-
369	H2	79	205	16	21	24.7.79 16:21	0.967	63.7	163.3	-3.61	340.0	361.0	10.80	14.50	-1.0	1.0	1.343	0.000	422.30	/	p	/	/	-
370	H2	79	239	20	33	27.8.79 20:33	0.951	154.3	323.0	-5.90	448.0	848.0	10.80	17.00	12.0	40.0	1.574	3.333	1544.77	/	/	/	/	/
372	H2	79	252	2	29	9.9.79 2:29	0.896	151.9	158.4	-6.52	430.0	519.0	4.90	12.30	6.0	9.5	2.510	1.583	577.93	/	/	/	/	/
371	H2	79	252	14	15	9.9.79 14:15	0.894	151.8	153.0	-6.55	697.0	996.0	8.50	20.60	8.0	50.0	2.424	6.250	1206.04	N	P	t	B	H
405	H1	79	253	13	45	10.9.79 13:45	0.939	0.0	94.9	-2.67	-1.0	-1.0	-1.00	-1.00	9.0	22.0	0.000	2.444	0.00	/	/	/	/	/
411	H2	79	253	20	35	10.9.79 20:35	0.884	151.6	135.0	-6.60	633.8	1266.0	1.43	-1.00	-1.0	1.0	0.000	0.000	0.00	/	/	/	/	/
406	H1	79	255	18	55	12.9.79 18:55	0.930	0.0	65.4	-2.87	-1.0	-1.0	-1.00	-1.00	13.0	20.0	0.000	1.538	0.00	/	/	/	/	/
373	H2	79	283	23	15	10.10.79 23:15	0.621	156.9	102.5	-7.13	265.0	337.0	23.00	88.00	10.0	16.0	3.826	1.600	362.48	N	P	t	b	h
404	H1	79	286	2	30	13.10.79 2:30	0.719	107.3	24.7	-5.80	330.9	413.5	7.00	13.90	8.0	22.0	1.986	2.750	497.30	-	-	-	-	-
374	H2	79	288	4	31	15.10.79 4:31	0.587	160.5	50.6	-6.87	304.0	334.0	15.50	28.90	16.0	22.0	1.865	1.375	368.70	n	p	t	b	/
375	H2	79	303	10	21	30.10.79 10:21	0.360	194.0	244.0	-2.80	294.0	380.0	109.00	201.00	-1.0	1.0	1.844	0.000	481.89	N	P	t	/	h
376	H2	79	303	23	4	30.10.79 23:04	0.355	196.8	239.0	-2.45	348.0	397.0	39.00	70.00	-1.0	1.0	1.795	0.000	458.65	n	p	t	/	h
377	H2	79	306	3	28	2.11.79 3:28	0.330	207.0	220.5	-0.93	302.0	358.0	287.00	468.00	-1.0	1.0	1.631	0.000	446.80	n	p	t	/	h
123	H1	79	306	23	54	2.11.79 23:54	0.475	127.0	129.6	-7.24	312.0	317.0	30.00	55.00	21.0	29.6	1.833	1.410	359.00	-	-	-	-	-
378	H2	79	307	20	7	3.11.79 20:07	0.313	216.2	207.4	0.45	318.0	374.0	81.50	156.00	45.0	80.0	1.778	1.410	435.26	N	P	t	b	/
379	H2	79	313	7	22	9.11.79 7:22	0.291	251.6	170.9	5.08	323.0	343.0	83.00	114.00	40.0	55.0	1.373	1.375	396.55	-	-	-	-	/
400	H1	79	328	0	45	24.11.79 0:45	0.318	219.5	304.8	3.22	244.7	285.8	136.60	280.00	15.0	40.0	2.050	2.667	324.95	n	p	t	-	-
380	H2	79	332	16	0	28.11.79 16:00	0.502	329.8	354.0	4.52	405.0	472.0	13.40	24.90	-1.0	1.0	1.858	0.000	550.07	-	-	-	-	-

TABLE A.1 - continues

SN	SC	YY	DOY	HH	MM	Date/time	RAD	HSE	CLONG	CLAT	v <sub>1</sub>	v <sub>2</sub>	n <sub>1</sub>	n <sub>2</sub>	B <sub>1</sub>	B <sub>2</sub>	R <sub>N</sub>	R <sub>B</sub>	V <sub>S</sub>	N	P	T	B	H
124	H1	79	347	8	53	13.12.79 8:53	0.538	280.9	111.2	6.93	307.0	391.0	19.00	46.00	13.6	26.4	2.421	1.941	450.11	N	P	t	B	h
381	H2	79	347	12	24	13.12.79 12:24	0.685	342.8	171.7	1.37	350.0	405.0	9.80	14.70	-1.0	1.0	1.500	0.000	515.00	/	/	/	B	/
125	H1	79	349	12	32	15.12.79 12:32	0.585	283.5	85.6	6.73	315.0	363.0	20.00	50.00	10.0	15.2	2.500	1.520	395.00	-	p	-	B	-
126	H1	79	357	13	2	23.12.79 13:02	0.659	289.9	346.7	5.86	349.0	452.0	14.00	31.00	12.1	24.7	2.214	2.041	536.82	-	-	-	/	-
382	H2	79	358	1	36	24.12.79 1:36	0.788	344.0	345.4	-0.21	375.0	405.0	6.42	14.10	16.0	20.0	2.196	1.250	430.08	n	p	t	b	/
127	H1	79	360	9	31	26.12.79 9:31	0.689	291.2	310.4	5.53	412.0	486.0	36.00	70.00	5.0	30.3	1.944	6.060	564.35	n	p	t	b	-
383	H2	79	364	15	52	30.12.79 15:52	0.839	344.8	307.8	-1.00	340.0	404.0	21.00	57.00	5.0	13.0	2.714	2.600	441.33	n	p	t	b	h
128	H1	80	3	12	24	3.1.80 12:24	0.767	293.3	206.0	4.63	338.0	521.0	4.00	9.00	11.3	25.5	2.250	2.257	667.40	N	P	T	B	h
384	H2	80	10	20	48	10.1.80 20:48	0.908	343.0	158.8	-2.15	410.6	495.0	6.80	13.00	9.0	18.0	1.912	2.000	587.57	-	-	-	-	-
129	H1	80	10	23	9	10.1.80 23:09	0.827	293.7	107.8	3.84	338.0	434.0	6.00	15.00	7.9	11.4	2.500	1.443	498.00	-	-	-	-	h
130	H1	80	13	7	29	13.1.80 7:29	0.844	293.6	77.3	3.60	327.0	382.0	9.00	19.00	8.2	17.1	2.111	2.085	431.50	n	p	t	b	H
385	H2	80	30	12	18	30.1.80 12:18	0.975	337.5	255.1	-3.74	542.0	561.0	1.62	2.51	-1.0	1.0	1.549	0.000	595.58	-	-	-	/	-
386	H2	80	33	11	12	2.2.80 11:12	0.979	336.5	214.5	-3.96	352.0	363.0	5.40	7.40	-1.0	1.0	1.370	0.000	392.70	-	-	-	/	-
387	H2	80	34	7	28	3.2.80 7:28	0.980	336.3	204.8	-4.01	356.0	398.0	6.50	10.00	-1.0	1.0	1.538	0.000	476.00	-	-	-	/	-
388	H2	80	36	15	3	5.2.80 15:03	0.983	335.5	172.0	-4.17	333.0	414.0	1.00	1.30	-1.0	1.0	1.300	0.000	684.00	N	P	T	/	-
389	H2	80	37	20	40	6.2.80 20:40	0.983	335.1	155.0	-4.25	493.0	546.0	1.70	3.30	-1.0	1.0	1.941	0.000	602.31	-	-	-	/	-
131	H1	80	38	0	28	7.2.80 0:28	0.982	288.6	106.5	1.31	345.0	415.0	3.30	8.00	4.3	6.9	2.424	1.605	464.15	-	-	-	b	h
132	H1	80	43	22	21	12.2.80 22:21	0.975	286.9	27.3	0.79	298.0	406.0	8.00	20.00	4.4	11.1	2.500	2.523	478.00	N	P	T	b	h
133	H1	80	60	14	55	29.2.80 14:55	0.982	281.8	162.9	-0.63	416.0	450.0	3.10	4.30	6.8	10.2	1.387	1.500	537.83	-	-	-	b	-
134	H1	80	65	1	46	5.3.80 1:46	0.976	280.5	102.3	-1.02	359.0	457.0	4.90	12.00	5.7	11.4	2.449	2.000	524.63	N	P	t	B	h
390	H2	80	65	14	34	5.3.80 14:34	0.932	326.7	141.8	-5.93	391.0	445.0	4.05	7.10	6.5	13.0	1.753	2.000	516.70	N	P	t	b	h
135	H1	80	72	10	47	12.3.80 10:47	0.960	278.4	3.0	-1.67	295.0	333.0	9.10	16.30	6.4	8.8	1.791	1.375	381.03	n	p	t	b	-
136	H1	80	82	14	3	22.3.80 14:03	0.923	276.0	227.0	-2.59	353.0	383.0	14.00	26.00	3.2	8.4	1.857	2.625	418.00	N	P	T	-	-
137	H1	80	89	11	53	29.3.80 11:53	0.887	274.9	134.6	-3.25	359.0	548.0	8.10	24.00	8.3	22.3	2.963	2.687	644.28	N	P	T	B	H
138	H1	80	110	10	59	19.4.80 10:59	0.727	275.9	218.5	-5.41	382.0	398.0	10.70	14.30	9.2	13.1	1.336	1.424	445.56	-	-	-	-	-
139	H1	80	122	6	20	1.5.80 6:20	0.600	282.6	69.9	-6.65	300.0	377.0	51.00	133.00	10.3	34.1	2.608	3.311	424.89	n	-	-	b	-
140	H1	80	122	13	47	1.5.80 13:47	0.596	282.9	65.6	-6.70	368.0	385.0	44.00	55.00	18.0	27.7	1.250	1.539	453.00	N	P	t	b	h
141	H1	80	125	18	27	4.5.80 18:27	0.557	286.3	26.6	-6.96	338.0	383.0	26.00	40.00	26.9	42.1	1.538	1.565	466.57	-	-	-	-	-
142	H1	80	143	20	57	22.5.80 20:57	0.337	335.8	196.8	-4.55	310.0	360.0	62.00	107.00	31.0	43.6	1.726	1.406	428.89	n	p	t	b	h
143	H1	80	148	2	28	27.5.80 2:28	0.312	359.2	164.4	-1.42	218.0	339.0	43.00	76.00	40.0	60.0	1.767	1.500	496.67	N	P	t	b	h
144	H1	80	150	11	6	29.5.80 11:06	0.310	13.6	147.4	0.69	283.0	510.0	74.00	191.00	61.5	136.8	2.581	2.224	653.57	N	P	t	b	h
145	H1	80	155	9	14	3.6.80 9:14	0.332	41.8	110.6	4.50	270.0	291.0	122.00	191.00	35.3	48.7	1.566	1.380	328.13	n	-	-	b	h
146	H1	80	161	18	36	9.6.80 18:36	0.399	68.7	53.0	6.88	301.0	386.0	112.00	134.00	28.8	53.6	1.196	1.861	818.73	-	-	-	b	h
147	H1	80	171	19	30	19.6.80 19:30	0.529	91.3	302.6	7.03	297.0	468.0	27.00	106.00	9.9	16.9	3.926	1.707	526.44	N	P	T	B	H
148	H1	80	174	20	34	22.6.80 20:34	0.567	95.3	266.3	6.67	292.0	375.0	40.00	115.00	11.9	30.6	2.875	2.571	419.27	N	-	-	b	h
149	H1	80	182	17	23	30.6.80 17:23	0.659	102.0	168.6	5.89	279.0	304.0	32.00	106.00	15.6	18.6	1.281	1.192	392.89	n	p	t	-	h
150	H1	80	183	15	20	1.7.80 15:20	0.669	102.5	157.5	5.79	405.0	420.0	12.00	17.00	29.2	30.0	1.417	1.027	456.00	-	p	-	b	h
151	H1	80	189	11	27	7.7.80 11:27	0.728	105.1	82.6	5.10	407.0	551.0	7.00	20.00	7.1	16.4	2.857	2.310	628.54	N	P	T	B	H
152	H1	80	192	22	45	10.7.80 22:45	0.760	106.0	37.6	4.69	358.0	498.0	3.60	10.00	9.7	20.0	2.778	2.062	576.75	-	-	-	-	-
153	H1	80	195	20	15	13.7.80 20:15	0.700	106.1	0.0	4.36	400.0	460.0	10.00	16.00	9.7	12.5	1.600	1.289	560.00	N	P	t	b	-
154	H1	80	203	1	20	21.7.80 1:20	0.841	107.0	265.0	3.60	330.0	360.0	11.50	22.00	4.0	13.0	1.913	3.250	392.86	n	P	t	-	h
155	H1	80	207	3	21	25.7.80 3:21	0.868	106.9	210.0	3.12	382.0	418.0	5.90	8.00	7.6	9.9	1.356	1.303	519.14	-	-	-	-	-
156	H1	80	209	22	35	27.7.80 22:35	0.885	106.7	173.6	2.82	292.0	310.0	11.00	13.50	7.0	10.0	1.227	1.429	389.20	N	-	-	-	-
157	H1	80	214	10	13	1.8.80 10:13	0.909	106.1	113.7	2.36	400.0	450.0	5.50	11.00	6.1	9.7	2.000	1.590	500.00	n	-	-	-	-
158	H1	80	215	4	51	2.8.80 4:51	0.913	106.0	103.2	2.28	358.0	412.0	6.00	12.00	6.8	12.1	2.000	1.779	466.00	-	p	-	-	-
159	H1	80	230	18	57	17.8.80 18:57	0.968	102.9	252.0	0.77	305.0	365.0	11.00	35.00	6.0	9.0	3.182	1.500	392.50	N	P	t	B	H

TABLE A.1 - continues

SN	SC	YY	DOY	HH	MM	Date/time	RAD	HSE	CLONG	CLAT	$v_1$	$v_2$	$n_1$	$n_2$	$B_1$	$B_2$	$R_N$	$R_B$	$V_S$	N	P	T	B	H
160	H1	80	238	15	15	25:8.80 15:15	0.982	100.9	148.0	0.05	372.0	412.0	14.80	26.50	8.8	15.9	1.791	1.807	462.60	n	-	t	b	/
161	H1	80	247	12	6	3:9.80 12:06	0.984	98.5	28.6	-0.76	315.0	471.0	29.00	74.00	13.5	39.1	2.552	2.896	571.53	N	P	t	B	/
162	H1	80	257	8	20	13:9.80 8:20	0.973	95.9	255.0	-1.64	306.0	346.0	11.90	18.50	6.5	9.3	1.555	1.431	418.12	N	/	t	B	/
163	H1	80	266	21	12	22:9.80 21:12	0.948	93.6	127.1	-2.50	512.0	605.0	5.00	10.00	5.9	10.3	2.000	1.746	698.00	n	t	-	-	/
164	H1	80	272	7	44	28:9.80 7:44	0.925	54.7	54.7	-3.00	286.0	294.0	22.90	28.00	2.8	3.3	1.223	1.179	329.92	/	/	/	-	/
166	H1	80	312	3	48	7:11.80 3:48	0.604	98.2	255.0	-6.78	541.0	678.0	12.00	27.00	17.0	20.0	2.250	1.538	787.60	N	P	t	b	H
167	H1	80	318	1	31	13:11.80 1:31	0.530	104.8	183.5	-7.17	431.0	445.0	26.00	48.00	13.0	28.4	1.846	1.671	461.55	-	-	-	-	-
168	H1	80	319	10	33	14:11.80 10:33	0.512	106.8	167.2	-7.22	494.0	550.0	15.00	28.00	18.0	29.0	1.867	1.611	614.62	-	p	-	-	-
169	H1	80	319	21	11	14:11.80 21:11	0.507	107.5	162.4	-7.23	512.0	1193.0	11.00	50.00	17.8	43.2	4.545	2.427	1385.08	N	P	T	b	H
170	H1	80	323	13	48	18:11.80 13:48	0.458	114.6	120.4	-7.19	459.0	499.0	17.00	33.00	24.5	35.3	1.941	1.441	541.50	-	-	-	-	-
171	H1	80	327	16	45	22:11.80 16:45	0.405	125.4	77.5	-6.73	268.0	333.0	48.00	116.00	25.6	35.5	2.417	1.387	378.88	n	p	t	B	H
172	H1	80	330	9	4	25:11.80 9:04	0.374	134.7	51.4	-6.03	404.0	470.0	20.00	33.00	36.3	52.8	1.650	1.455	571.54	n	p	t	B	h
173	H1	80	348	18	52	13:12.80 18:52	0.362	231.0	265.4	6.19	446.0	558.0	26.50	43.00	30.3	47.1	1.623	1.554	737.88	n	p	t	-	/
174	H1	80	365	18	41	30:12.80 18:41	0.577	269.2	80.0	6.66	378.0	440.0	17.00	34.00	15.0	28.5	2.000	1.900	502.00	N	P	T	B	H
175	H1	81	23	8	25	23:1.81 8:25	0.813	278.4	139.1	4.09	354.0	392.0	13.00	26.00	7.2	13.0	2.000	1.806	430.00	N	P	t	b	-
176	H1	81	27	0	8	27:1.81 0:08	0.840	278.3	90.7	3.72	476.0	564.0	7.00	14.00	11.6	25.9	2.000	2.233	652.00	n	p	t	b	h
177	H1	81	27	17	48	27:1.81 17:48	0.845	278.2	81.6	3.64	580.0	630.0	4.10	6.10	14.0	22.0	1.488	1.571	732.50	-	-	-	-	-
178	H1	81	28	15	36	28:1.81 15:36	0.851	278.2	69.0	0.85	535.0	555.0	4.50	7.20	5.2	6.9	1.600	1.327	588.33	-	-	-	-	-
179	H1	81	50	13	37	19:2.81 13:37	0.957	273.9	136.7	1.51	432.0	543.0	8.00	20.00	-1.0	1.0	2.500	0.000	617.00	-	p	/	/	/
180	H1	81	51	16	0	20:2.81 16:00	0.960	273.6	121.2	1.41	541.0	830.0	3.80	12.80	-1.0	1.0	3.368	0.000	952.02	N	P	/	/	/
181	H1	81	53	16	0	22:2.81 16:00	0.966	273.0	94.3	1.23	514.0	599.0	1.50	2.24	-1.0	1.0	1.493	0.000	771.30	-	-	-	-	/
182	H1	81	60	1	16	1:3.81 1:16	0.978	271.2	9.0	0.68	422.0	600.0	5.00	17.00	-1.0	1.0	3.400	0.000	674.17	N	P	T	/	/
183	H1	81	68	21	0	9:3.81 21:00	0.985	268.5	249.0	-0.08	324.0	402.0	19.00	70.00	-1.0	1.0	3.684	0.000	431.06	N	-	t	/	/
184	H1	81	80	6	53	21:3.81 6:53	0.975	265.2	95.8	-1.08	518.0	580.0	5.50	10.00	-1.0	1.0	1.818	0.000	655.78	-	-	-	-	/
185	H1	81	90	10	45	31:3.81 10:45	0.948	262.0	320.0	-1.99	340.0	410.0	22.00	50.00	-1.0	1.0	2.273	0.000	465.00	N	P	t	/	/
186	H1	81	93	5	56	3:4.81 5:56	0.938	261.9	280.9	-2.25	347.0	415.0	11.00	23.00	-1.0	1.0	2.091	0.000	477.33	N	P	t	/	/
187	H1	81	98	2	58	8:4.81 2:58	0.917	260.9	215.8	-2.71	523.0	593.0	3.90	6.40	16.6	19.9	1.641	1.199	702.20	N	P	t	B	/
188	H1	81	103	9	12	13:4.81 9:12	0.890	260.1	145.8	-3.21	319.0	367.0	17.00	29.00	10.1	18.2	1.706	1.802	435.00	/	/	/	/	/
189	H1	81	103	9	59	13:4.81 9:59	0.890	260.1	145.4	-3.21	387.0	580.0	48.00	127.00	23.0	50.1	2.646	2.178	697.27	N	P	T	b	H
190	H1	81	106	7	48	16:4.81 7:48	0.872	259.8	106.4	-3.50	470.0	522.0	5.10	9.10	5.6	9.9	1.784	1.768	588.30	n	p	t	-	h
191	H1	81	106	19	52	16:4.81 19:52	0.869	259.8	100.1	-3.55	474.0	565.0	12.00	26.00	9.2	18.2	2.167	1.978	643.00	N	-	T	b	h
192	H1	81	110	0	42	20:4.81 0:42	0.848	259.6	57.0	-3.87	361.0	545.0	-1.00	1.00	8.0	20.0	0.000	2.500	0.00	N	P	T	B	h
193	H1	81	115	11	4	25:4.81 11:04	0.808	259.6	345.5	-4.44	430.0	520.0	5.00	10.00	9.5	17.1	2.000	1.800	610.00	N	P	t	b	-
194	H1	81	116	8	27	26:4.81 8:27	0.801	259.7	333.8	-4.53	421.0	457.0	3.90	9.40	19.6	25.9	2.410	1.321	482.53	-	-	-	-	-
195	H1	81	117	3	4	27:4.81 3:04	0.795	259.8	323.6	-4.61	434.0	537.0	23.00	90.00	9.1	12.8	3.913	1.407	572.36	N	P	t	B	H
196	H1	81	122	10	48	2:5.81 10:48	0.749	260.6	254.0	-5.18	315.0	381.0	16.00	25.00	14.9	20.5	1.562	1.376	498.33	n	p	t	-	-
197	H1	81	126	17	26	6:5.81 17:26	0.708	261.9	199.8	-5.64	400.0	437.0	5.10	6.40	15.1	20.6	1.255	1.364	582.15	-	-	-	-	-
198	H1	81	130	3	12	10:5.81 3:12	0.673	263.5	155.6	-6.01	405.0	565.0	12.40	33.00	14.1	30.9	2.661	2.191	661.31	n	p	T	B	-
199	H1	81	131	7	9	11:5.81 7:09	0.660	264.1	141.9	-6.13	768.0	1110.0	3.60	9.00	11.3	30.6	2.500	2.708	1338.00	N	P	T	B	-
200	H1	81	133	21	23	13:5.81 21:23	0.631	265.8	108.4	-6.40	678.0	980.0	5.00	9.50	10.9	21.8	1.900	2.000	1315.56	N	P	T	B	-
201	H1	81	135	16	35	15:5.81 16:35	0.610	267.3	85.8	-6.59	460.4	483.0	6.87	7.22	13.8	18.5	1.051	1.341	926.61	n	p	t	-	h
202	H1	81	136	24	0	17:5.81 0:00	0.595	268.5	70.4	-6.70	380.0	800.0	2.30	6.50	11.1	30.3	2.826	2.730	1030.00	N	P	t	b	-
418	H1	81	143	5	54	23:5.81 5:54	0.520	276.2	354.6	-7.16	366.4	387.0	36.64	38.94	27.9	28.0	1.060	1.004	752.35	N	P	t	-	-
203	H1	81	145	20	29	25:5.81 20:29	0.483	280.7	325.0	-7.25	290.0	480.0	40.00	118.00	23.2	66.3	2.950	2.858	577.44	N	P	t	B	H
205	H1	81	163	12	36	12:6.81 12:36	0.310	351.6	161.8	-0.37	306.0	367.0	120.00	213.00	44.9	80.1	1.775	1.784	445.71	N	P	T	-	-
206	H1	81	170	1	5	19:6.81 1:05	0.334	29.0	114.0	4.70	440.0	700.0	40.00	80.00	36.5	60.9	2.000	1.668	960.00	N	P	T	B	H

TABLE A.1 - continues

SN	SC	YY	DOY	HH	MM	Date/time	RAD	HSE	CLONG	CLAT	v <sub>1</sub>	v <sub>2</sub>	n <sub>1</sub>	n <sub>2</sub>	B <sub>1</sub>	B <sub>2</sub>	R <sub>N</sub>	R <sub>B</sub>	V <sub>S</sub>	N	P	T	B	H
207	H1	81	202	23	44	21:7.81 23:44	0.721	90.5	98.2	5.14	357.0	580.0	16.00	37.00	-1.0	1.0	2.312	0.000	749.90	N	P	t	/	-
208	H1	81	205	15	34	24:7.81 15:34	0.746	91.3	63.6	4.83	484.0	532.0	6.00	10.00	-1.0	1.0	1.667	0.000	604.00	-	-	-	/	-
209	H1	81	212	5	10	31:7.81 5:10	0.802	92.4	338.3	4.07	393.0	525.0	5.00	11.00	-1.0	1.0	2.200	0.000	635.00	-	-	-	/	-
210	H1	81	228	2	24	16:8.81 2:24	0.906	91.8	127.4	2.37	471.0	620.0	8.80	23.00	-1.0	1.0	2.614	0.000	712.34	N	P	T	/	-
211	H1	81	230	15	47	18:8.81 15:47	0.919	91.4	93.3	2.12	378.0	452.0	9.00	13.20	-1.0	1.0	1.467	0.000	610.57	-	-	-	/	-
212	H1	81	283	8	37	10:10.81 8:37	0.938	78.3	104.0	-2.70	367.0	398.0	7.20	11.30	-1.0	1.0	1.569	0.000	452.44	-	-	-	/	-
213	H1	81	284	12	47	11:10.81 12:47	0.933	78.1	88.2	-2.81	474.0	491.0	8.50	13.70	-1.0	1.0	1.612	0.000	518.79	-	-	-	/	-
214	H1	81	286	5	7	13:10.81 5:07	0.926	77.7	65.4	-2.96	427.0	438.0	8.30	10.30	-1.0	1.0	1.241	0.000	483.65	-	-	-	/	-
215	H1	81	287	18	58	14:10.81 18:58	0.919	77.4	44.9	-3.10	409.0	436.0	10.30	18.00	-1.0	1.0	1.748	0.000	472.12	-	-	-	/	-
216	H1	81	293	4	21	20:10.81 4:21	0.892	76.5	332.6	-3.60	309.0	337.0	48.00	86.00	-1.0	1.0	1.792	0.000	372.37	-	-	-	/	-
217	H1	81	293	14	29	20:10.81 14:29	0.889	76.4	326.8	-3.64	339.0	493.0	27.00	69.00	-1.0	1.0	2.556	0.000	592.00	-	p	/	/	-
218	H1	81	302	6	12	29:10.81 6:12	0.834	75.7	212.3	-4.45	366.0	433.0	3.80	8.00	-1.0	1.0	2.105	0.000	493.62	-	-	-	/	-
219	H1	81	302	10	53	29:10.81 10:53	0.832	75.7	209.7	-4.47	408.0	439.0	4.40	7.50	-1.0	1.0	1.705	0.000	483.00	n	p	t	/	-
220	H1	81	304	0	48	31:10.81 0:48	0.821	75.7	189.0	-4.62	382.0	449.0	14.00	27.70	-1.0	1.0	1.979	0.000	517.47	-	-	-	/	-
221	H1	81	313	9	51	9:11.81 9:51	0.742	76.7	66.0	-5.54	333.0	354.0	19.00	25.00	-1.0	1.0	1.316	0.000	420.50	-	-	-	/	-
222	H1	81	318	9	45	14:11.81 9:45	0.692	78.2	1.5	-6.03	326.0	381.0	7.40	15.00	-1.0	1.0	2.027	0.000	434.55	n	p	t	/	-
223	H1	81	320	15	19	16:11.81 15:19	0.668	79.2	333.5	-6.25	342.0	459.0	27.00	52.00	-1.0	1.0	1.926	0.000	585.36	n	p	t	/	-
224	H1	81	324	0	54	20:11.81 0:54	0.631	81.2	291.0	-6.56	381.0	677.0	0.59	1.14	-1.0	1.0	1.932	0.000	994.53	N	P	T	/	-
225	H1	81	324	12	35	20:11.81 12:35	0.625	81.6	284.3	-6.61	335.0	529.0	2.36	4.80	-1.0	1.0	2.034	0.000	716.64	N	P	T	/	-
226	H1	81	326	23	28	22:11.81 23:28	0.597	83.6	254.4	-6.82	371.0	487.0	22.00	59.00	-1.0	1.0	2.682	0.000	555.97	N	P	T	/	-
227	H1	81	345	21	16	11:12.81 21:16	0.360	124.3	46.3	-5.58	263.0	346.0	81.00	179.00	-1.0	1.0	2.210	0.000	414.60	n	p	t	/	-
228	H1	81	355	4	8	21:12.81 4:08	0.310	174.3	334.7	1.00	322.0	462.0	279.00	424.00	-1.0	1.0	1.520	0.000	731.38	/	/	/	/	/
229	H1	81	357	2	56	23:12.81 2:56	0.315	186.0	320.0	2.73	587.0	930.0	41.00	111.00	-1.0	1.0	2.707	0.000	1130.90	N	T	/	/	/
230	H1	81	357	7	0	12:1.82 7:00	0.542	250.7	119.2	6.94	309.0	335.0	79.00	134.00	-1.0	1.0	1.696	0.000	372.35	n	p	t	/	-
231	H1	81	357	5	18	27:1.82 5:18	0.711	261.4	293.9	5.37	344.0	413.0	50.00	120.00	-1.0	1.0	2.400	0.000	462.29	n	p	t	/	-
232	H1	81	357	12	59	27:1.82 12:59	0.715	261.5	289.5	5.33	444.0	478.0	13.50	34.00	-1.0	1.0	2.519	0.000	500.39	N	P	T	/	-
233	H1	81	357	6	23	4:2.82 6:23	0.785	262.9	189.0	4.49	428.0	576.0	11.70	71.40	-1.0	1.0	6.103	0.000	605.01	N	P	t	/	h
234	H1	81	357	14	48	6:2.82 14:48	0.805	263.1	158.1	4.24	518.0	525.0	8.00	16.00	-1.0	1.0	2.000	0.000	532.00	-	-	-	/	-
235	H1	81	357	11	31	11:2.82 11:31	0.841	263.0	94.4	3.75	673.0	717.0	4.50	8.10	-1.0	1.0	1.800	0.000	772.00	-	-	-	/	-
236	H1	81	357	11	2	22:2.82 11:02	0.907	261.6	307.9	2.67	445.0	486.0	7.00	11.00	-1.0	1.0	1.571	0.000	557.75	n	p	/	/	/
237	H1	81	357	1	20	26:2.82 1:20	0.925	260.9	259.9	2.34	366.0	383.0	5.70	7.00	-1.0	1.0	1.228	0.000	457.54	n	p	/	/	/
238	H1	81	358	2	4	27:2.82 2:04	0.929	260.7	246.5	2.25	344.0	396.0	29.00	73.00	-1.0	1.0	2.517	0.000	430.27	N	P	/	/	/
239	H1	81	358	10	0	4:6.82 10:00	0.555	257.4	36.8	-6.99	530.0	665.0	47.30	89.00	-1.0	1.0	1.882	0.000	818.13	N	P	T	/	-
240	H1	81	358	16	10	6:6.82 16:10	0.527	260.5	10.6	-7.14	532.0	656.0	33.00	83.00	-1.0	1.0	2.515	0.000	737.84	/	/	/	/	-
241	H1	81	358	19	10	8:6.82 19:10	0.499	263.9	345.3	-7.23	363.0	533.0	82.00	130.00	-1.0	1.0	1.585	0.000	823.42	n	p	t	/	h
242	H1	81	358	10	58	9:6.82 10:58	0.492	265.1	338.4	-7.24	389.0	617.0	84.00	178.00	-1.0	1.0	2.119	0.000	820.74	n	p	t	/	/
243	H1	81	358	16	7	10:6.82 7:05	0.480	266.7	329.0	-7.25	-1.0	1.0	-1.00	1.00	-1.0	1.0	0.000	0.000	0.00	N	P	T	/	h
244	H1	81	358	8	47	12:6.82 8:47	0.453	271.1	305.9	-7.21	454.0	547.0	21.00	37.00	-1.0	1.0	1.762	0.000	669.06	n	p	t	/	/
245	H1	81	358	12	31	12:6.82 12:31	0.451	271.5	304.0	-7.20	426.0	470.0	15.50	25.00	-1.0	1.0	1.613	0.000	541.79	/	/	/	/	/
246	H1	81	358	13	3	12:6.82 13:03	0.451	271.5	304.1	-7.20	617.0	654.0	18.30	22.50	-1.0	1.0	1.230	0.000	815.21	-	-	-	/	/
247	H1	81	358	18	30	12:6.82 18:30	0.449	272.1	301.6	-7.19	620.0	740.0	9.50	25.00	-1.0	1.0	2.632	0.000	813.55	-	-	-	/	/
248	H1	81	358	9	51	18:6.82 9:51	0.378	289.3	244.2	-6.26	465.0	500.0	45.60	51.00	-1.0	1.0	1.118	0.000	795.56	-	-	-	/	/
249	H1	81	358	14	32	18:6.82 14:32	0.450	290.0	304.0	-7.20	457.0	488.0	39.90	45.00	-1.0	1.0	1.128	0.000	730.53	-	-	-	/	/
250	H1	81	358	19	7	10:7.82 13:07	0.401	40.5	62.2	6.95	387.0	451.0	49.00	83.00	-1.0	1.0	1.694	0.000	543.24	-	-	-	/	/
251	H1	81	358	19	2	11:7.82 3:43	0.409	42.4	56.2	7.03	306.0	329.0	52.00	82.00	-1.0	1.0	1.577	0.000	368.87	-	-	-	/	/
252	H1	81	358	19	2	11:7.82 14:32	0.414	43.8	51.6	7.08	476.0	520.0	47.00	53.00	-1.0	1.0	1.128	0.000	864.67	-	-	-	/	/

TABLE A.1 - continues

SN	SC	YY	DOY	HH	MM	Date/time	RAD	HSE	CLONG	CLAT	v <sub>1</sub>	v <sub>2</sub>	n <sub>1</sub>	n <sub>2</sub>	B <sub>1</sub>	B <sub>2</sub>	R <sub>N</sub>	R <sub>B</sub>	V <sub>S</sub>	N	P	T	B	H
253	H1	82	194	3	10	13:7.82 3:10	0.434	48.1	35.7	7.20	570.0	790.0	42.00	116.00	-1.0	1.0	2.762	0.000	914.86	-	P	t	/	-
254	H1	82	196	13	48	15:7.82 13:48	0.466	54.0	9.6	7.25	469.0	539.0	32.00	35.00	-1.0	1.0	1.094	0.000	1285.67	-	-	-	/	/
255	H1	82	201	6	2	20:7.82 6:02	0.526	62.4	315.7	7.01	444.0	546.0	13.90	25.00	-1.0	1.0	1.799	0.000	673.73	-	/	/	/	/
256	H1	82	201	9	28	20:7.82 9:28	0.528	62.6	314.2	7.00	487.0	761.0	19.00	52.00	-1.0	1.0	2.737	0.000	918.76	N	P	T	/	H
407	H1	82	203	1	44	22:7.82 1:44	0.550	64.9	294.1	6.90	-1.0	745.0	-1.00	85.00	-1.0	1.0	0.000	0.000	0.00	N	P	t	/	/
257	H1	82	204	7	59	23:7.82 7:59	0.565	66.9	279.0	6.73	578.0	1067.0	70.00	188.00	-1.0	1.0	2.686	0.000	1357.08	-	n	P	t	/
258	H1	82	217	4	13	5:8.82 4:13	0.710	75.7	118.4	5.24	360.0	420.0	25.00	42.00	-1.0	1.0	1.680	0.000	508.24	N	P	t	/	/
408	H1	82	327	12	3	23:11.82 12:03	0.734	61.7	61.6	-5.60	604.0	744.0	2.23	4.04	-1.0	1.0	1.812	0.000	916.49	n	P	/	/	/
259	H1	82	328	0	54	24:11.82 0:54	0.748	61.3	80.9	-5.44	491.0	740.0	4.60	11.30	-1.0	1.0	2.457	0.000	910.96	n	P	/	/	/
260	H1	82	330	17	53	26:11.82 17:53	0.722	62.0	46.1	-5.71	556.0	1130.0	30.00	44.00	-1.0	1.0	1.467	0.000	2360.00	n	P	t	/	/
261	H1	82	342	13	0	8:12.82 13:00	0.594	68.5	256.9	-6.82	435.0	627.0	8.20	12.00	-1.0	1.0	1.463	0.000	1041.32	N	P	t	/	/
262	H1	82	353	4	0	19:12.82 4:00	0.456	64.1	133.0	-7.20	327.0	360.0	33.00	43.00	-1.0	1.0	1.303	0.000	468.90	-	-	-	/	/
263	H1	82	354	11	8	20:12.82 11:08	0.441	67.0	118.5	-7.13	354.0	812.0	55.00	185.00	-1.0	1.0	3.364	0.000	1005.77	N	P	t	/	/
264	H1	82	360	20	29	26:12.82 20:29	0.364	107.5	55.2	-5.78	445.0	1123.0	42.00	94.00	-1.0	1.0	2.238	0.000	1670.62	N	P	t	/	/
265	H1	82	364	2	50	30:12.82 2:50	0.333	122.7	26.9	-4.10	620.0	1084.0	37.40	87.40	-1.0	1.0	2.337	0.000	1431.07	n	P	t	/	/
409	H1	83	12	12	0	12:1.83 12:00	0.354	196.8	284.7	5.80	-1.0	640.0	-1.00	89.00	-1.0	1.0	0.000	0.000	0.00	N	P	-	/	/
266	H1	83	28	4	16	28:1.83 4:16	0.549	236.1	118.2	6.91	438.0	457.0	18.80	20.80	-1.0	1.0	1.106	0.000	635.60	-	-	-	/	-
267	H1	83	28	8	58	28:1.83 8:58	0.551	236.4	115.9	6.89	462.0	551.0	22.00	43.00	-1.0	1.0	1.955	0.000	644.24	n	P	t	/	/
268	H1	83	192	16	12	11:7.83 16:12	0.313	314.4	184.7	-1.49	650.0	710.0	50.00	67.00	-1.0	1.0	1.340	0.000	886.47	n	P	t	/	/
269	H1	83	218	11	2	6:8.83 11:02	0.551	50.8	298.7	6.82	438.0	486.0	27.00	44.00	-1.0	1.0	1.630	0.000	562.24	-	-	-	/	/
391	H1	83	221	16	45	9:8.83 16:45	0.590	54.5	260.0	6.55	590.0	750.0	8.50	14.00	-1.0	1.0	1.647	0.000	997.27	n	/	/	/	/
392	H1	84	38	13	30	7:2.84 13:30	0.488	213.6	181.0	7.22	430.0	475.0	34.00	66.00	-1.0	1.0	1.941	0.000	522.81	n	P	-	/	/
393	H1	84	182	15	20	30:6.84 15:20	0.607	225.2	89.4	-6.75	305.0	360.0	120.00	167.00	-1.0	1.0	1.392	0.000	500.43	/	/	/	/	/
394	H1	84	236	9	41	23:8.84 9:41	0.586	39.5	273.0	6.50	325.0	375.0	49.00	98.00	-1.0	1.0	2.000	0.000	425.00	-	-	-	/	/
395	H1	85	22	17	10	22:1.85 17:10	0.393	18.0	92.3	-6.61	612.0	753.0	17.20	24.00	-1.0	1.0	1.395	0.000	1109.65	-	p	-	/	/
396	H1	85	23	12	5	23:1.85 12:05	0.384	70.1	85.2	-6.40	491.0	540.0	83.20	149.00	-1.0	1.0	1.791	0.000	601.96	n	P	t	/	/
397	H1	85	24	11	35	24:1.85 11:35	0.371	73.6	75.2	-6.10	612.0	688.0	16.50	27.00	-1.0	1.0	1.636	0.000	807.43	/	/	/	/	/
398	H1	85	245	9	17	2:9.85 9:17	0.518	18.4	342.2	7.00	387.0	405.0	22.40	33.30	-1.0	1.0	1.487	0.000	441.99	-	-	-	/	/
399	H1	86	37	22	5	6:2.86 22:05	0.394	52.0	100.1	-6.66	427.0	580.0	81.00	170.00	-1.0	1.0	2.099	0.000	719.25	/	/	/	/	/

SOURCE: Adapted from Khalisi and Schwenn (1995).

The classification of the events according to the constellation considered is based on the observation or non-observation of shocks by each of the probes/spacecraft that constitute the constellation. For instance, let us consider the first shock in [Table A.2](#). The first column represents the reference number (SN) for the shock; 9 for the considered example. The second column identifies the probe/spacecraft (SC=H1) that observed the shock, meaning that for the considered shock H1 was the probe that identified the shock. During the period, H1 observations - H2 was launched at the beginning of the year 1976 - were complemented by IMP-8, outside the terrestrial magnetosphere at that period. The following columns represent the year (YY=75) of observation (third column), day of the year (DOY=210) (fourth column), hour (HH=23) (fifth column), and minutes (MM=0) (sixth column), when the shock was detected by the probe.

The following four columns correspond to the radial distance (RAD = 0.844 AU), the Helios-sun-earth angle ( $HSE = 163.7^\circ$ ) (in degrees), the Carrington latitude (CLAT =  $-4.20^\circ$ ) (in degrees), and the solar wind parameters and magnetic field signature for MCs (MC sign). The signatures of MCs are pointed out when observed in the Helios probe data for the corresponding period of the shock observation. If a density discontinuity is present, characteristic of MCs, in the density profile, we register this fact by using “N”, the pressure discontinuity by “P”, temperature signature by “T”, magnetic field strength abrupt variation by “B”, and Helium composition by “H”, reporting the presence of MCs as the drivers of the listed shock waves. Like one can see in the last column, when “NO” appears, it means that, for sure, there is no signatures for MC. In the case of low evidence, the signatures are characterized by lower-case letters “n”, “p”, “t”, “h” representing the respective parameters discontinuity in “ $N_p$ ”, “ $P$ ” discontinuity, low temperature “ $T_p$ ” profile, and Helium (He) composition. In the absence of data, the signal “/” represents the presence of gaps in the profiles of the solar wind and/or magnetic field data during the interval correspondent to the MC boundaries while, when there is no signatures of MCs in the solar wind and/or magnetic field parameters, the signal is “-”. The question tag (“?”) that appears in some of the shocks stands for those events where there is no certainty about the presence or not of MCs. Sometimes “?” describes the indeterminacy in the magnetic field or solar wind parameter profiles for the signatures of MCs.

Following the sequence of the columns, the classification (CLASS) (eleventh column)

is a result of the comparison of observations of the probe that detected the shock (on the list) with the other probes/spacecraft operating in the same period. If another probe observed the shock, CLASS is “Y”, that means, “YES”. On the other hand, if the other probe did not observe the same shock, CLASS is “N”, that means “NO”. For the cases where there is no clear understanding of the association between the observations, CLASS is “X”, that means non-excluded. When “D” appears in “CLASS”, it means that the shock was discarded from the sample because of lack of data from the probe(s)/spacecraft that was(were) also available during the period of the shock observation. Finally, the probe/spacecraft (CORR) with what we make the comparison of the shock observation is described - in the example it was IMP-8.

As it is shown in Table [A.2](#), the association between H1 and IMP-8 for the example we took into account is N because the shock was not observed near Earth (IMP-8). In this case, one can say that there was a single point observation of a shock wave, and we consider that the shock expanded less than  $164^\circ$ . Based on our sample, we say that we have an entry for our statistical analysis for the group of single point observation at the position correspondent to the longitudinal separation  $\Delta\Phi = 160^\circ$  that corresponds to an angle between  $160$  and  $170^\circ$ .

TABLE A.2 - Classification of the type of observation done by Helios missions and IMP-8/ISEE-3

SN	SC	YY	DOY	HH	MM	RAD	HSE	CLAT	MC Sign	CLASS	CORR
9	H1	75	210	23	0	0.844	163.7	-4.20	NO	N	IMP8
14	H1	75	322	11	30	0.873	354.3	2.95	npt-	X	IMP8
15	H1	75	325	14	5	0.891	353.9	2.65	nptBH	D	H2
17	H1	75	342	4	4	0.960	350.1	1.12	n-t-	D	H2
271	H2	76	90	4	32	0.476	8.5	-6.22	NPTB-	D	H1
										Y	IMP8
272	H2	76	90	17	44	0.469	9.5	-6.11	NptbH	D	H1
										Y	IMP8
273	H2	76	92	13	28	0.443	13.5	-5.69	NPTb/	N	H1
										X	IMP8
18	H1	76	216	19	35	0.902	150.3	-3.32	?	D	H1
										D	IMP8
19	H1	76	228	4	43	0.830	149.4	-4.45	NO	D	H2
										D	IMP8
20	H1	76	234	2	15	0.784	149.8	-5.04	npt//	D	H2
										X	IMP8
21	H1	76	272	23	2	0.345	207.0	-4.71	NPTBH	D	H2
										D	IMP8
22	H1	76	328	10	27	0.808	339.6	3.93	NO	X	H2
275	H2	76	351	5	41	0.877	3.0	-1.70	?b	X	H1
25	H1	77	25	14	54	0.962	324.2	-1.72	NPTbH	X	H2



TABLE A.2 - continues

SN	SC	YY	DOY	HH	MM	RAD	HSE	CLAT	MC Sign	CLASS	CORR
277	H2	77	28	21	3	0.978	351.1	-5.02	NO	Y	H1
26	H1	77	29	1	3	0.952	323.3	-2.01	NPTBH	Y	IMP8
278	H2	77	47	1	51	0.925	345.8	-6.04	NO?	N	H1
279	H2	77	50	17	36	0.907	345.0	-6.23	NO	Y	H1
416	H1	77	50	21	40	0.840	319.3	-4.11	?	Y	H2
27	H1	77	75	11	33	0.610	326.3	-6.57	NPTBH	Y	H2
280	H2	77	75	19	47	0.717	344.6	-7.21	NPTBH	Y	H1
28	H1	77	78	7	55	0.575	329.0	-0.68	nptbh	N	H2
282	H2	77	83	4	15	0.638	347.9	-7.23	np-bH	X	IMP8
283	H2	77	107	14	35	0.322	43.5	-0.78	nptbh	N	H1
284	H2	77	110	20	21	0.297	62.9	2.05	nptbH	X	H1
29	H1	77	159	7	55	0.857	150.1	3.47	NPTBH	D	H2
30	H1	77	160	16	1	0.865	150.0	3.34	NO	D	H2
31	H1	77	172	6	0	0.927	148.7	2.15	NO	D	H2
33	H1	77	195	16	10	0.984	143.5	-0.07	NO	X	H2
34	H1	77	240	6	50	0.846	134.9	-4.26	NPTbh	D	H2
35	H1	77	242	7	15	0.832	134.9	-4.47	NO	N	IMP8
										X	H2

TABLE A.2 - continues

SN	SC	YY	DOY	HH	MM	RAD	HSE	CLAT	MC Sign	CLASS	CORR
										X	IMP8
36	H1	77	263	19	07	0.631	141.1	-6.60	?	X	H2
37	H1	77	263	20	37	0.630	141.2	-6.60	n-tb/	X	H2
38	H1	77	268	2	40	0.580	144.9	-6.95	NPTBH	Y	H2
										X	IMP8
285	H2	77	268	12	51	0.643	168.3	-7.19	nptbH	Y	H1
										X	IMP8
286	H2	77	269	12	6	0.631	168.9	-7.16	npt/h	X	H1
										X	IMP8
39	H1	77	311	18	15	0.474	303.2	7.22	NO?	Y	H2
288	H2	77	311	18	54	0.400	326.1	6.42	npt-/	Y	H1
289	H2	77	327	16	9	0.613	352.5	2.51	np-h	N	H2
290	H2	77	328	6	11	0.620	352.9	2.39	npt-	Y	H1
										Y	IMP8
40	H1	77	328	22	27	0.681	321.5	5.55	NO	Y	H2
										Y	IMP8
292	H2	77	332	12	57	0.669	355.4	1.57	NO	N	H1
										Y	IMP8
293	H2	77	335	1	29	0.697	356.4	1.14	NPTb-	Y	H1
41	H1	77	335	5	13	0.743	323.6	4.83	?	Y	H2
42	H1	77	335	8	54	0.744	323.6	4.81	NPTBh	X	H2
294	H2	77	353	2	12	0.853	357.8	-1.27	NO	N	H1

TABLE A.2 - continues

SN	SC	YY	DOY	HH	MM	RAD	HSE	CLAT	MC Sign	CLASS	CORR
										X	IMP8
43	H1	77	356	20	20	0.900	323.1	2.60	NO	X	H2
										X	IMP8
44	H1	78	1	17	11	0.944	320.8	1.69	NO	N	H2
45	H1	78	2	1	41	0.948	320.7	1.65	n-tb-	N	H2
46	H1	78	3	8	39	0.950	320.4	1.54	NPTBH	Y	H2
										Y	IMP8
295	H2	78	3	14	50	0.938	354.6	-2.74	NPTBH	Y	H1
										Y	IMP8
47	H1	78	5	3	23	0.956	319.9	1.38	NO	X	H2
										X	IMP8
296	H2	78	9	20	10	0.959	253.0	-3.26	-ptb-	X	H1
297	H2	78	19	21	44	0.979	349.8	-3.99	NO?	X	IMP8
298	H2	78	23	20	38	0.983	348.5	-4.26	nptbh	D	H1
299	H2	78	25	6	3	0.984	348.0	-4.35	NO?	D	H1
300	H2	78	29	21	44	0.983	246.4	-4.65	nptbh	X	H1
301	H2	78	34	19	28	0.979	344.8	-4.97	NO	D	H1
302	H2	78	37	7	2	0.976	344.0	-5.11	NPTBH	D	H1
48	H1	78	46	1	30	0.946	307.6	-2.12	nptb-	Y	H2
303	H2	78	46	1	53	0.954	341.3	-5.62	np-BH	Y	H1
304	H2	78	56	4	54	0.913	338.8	-6.16	nptb-	X	H1

TABLE A.2 - continues

SN	SC	YY	DOY	HH	MM	RAD	HSE	CLAT	MC Sign	CLASS	CORR
										Y	IMP8
305	H2	78	60	4	16	0.892	338.0	-6.36	NO?	Y	H1
49	H1	78	60	12	15	0.878	304.7	-3.44	NPTBH	Y	H2
50	H1	78	64	16	15	0.651	304.3	-3.65	NO	X	H2
306	H2	78	66	23	54	0.850	337.1	-6.69	NPTbH	Y	H1
										Y	IMP8
51	H1	78	67	8	44	0.832	304.2	-4.11	NO?	Y	H2
										Y	IMP8
307	H2	78	70	13	40	0.823	336.9	-6.84	nptbH	Y	H1
52	H1	78	91	5	30	0.604	311.7	-6.61	NO?	Y	H2
										Y	IMP8
308	H2	78	91	8	34	0.619	342.6	-6.62	NPTBh	Y	H1
										Y	IMP8
53	H1	78	92	12	7	0.589	312.9	-6.73	NO?	X	H2
										X	IMP8
309	H2	78	92	23	15	0.600	344.4	-7.15	NO	X	H1
										X	IMP8
54	H1	78	93	19	13	0.573	314.2	-6.85	npt/-	X	H2
										X	IMP8
310	H2	78	99	7	16	0.518	351.1	-6.67	NPTbH	Y	H1
55	H1	78	99	7	18	0.504	321.7	-7.20	npt/h	Y	H2
311	H2	78	102	14	14	0.473	356.8	-6.16	NPTBH	X	H1

TABLE A.2 - continues

SN	SC	YY	DOY	HH	MM	RAD	HSE	CLAT	MC Sign	CLASS	CORR
										Y	IMP8
312	H2	78	106	6	20	0.421	5.4	-5.21	NPTBH	Y	H1
56	H1	78	106	14	50	0.409	338.6	-6.91	NO?	Y	H2
57	H1	78	107	8	55	0.400	341.0	-6.78	NO?	X	H2
313	H2	78	108	13	19	0.390	12.4	-4.33	?	Y	H1
58	H1	78	108	13	50	0.385	345.1	-6.52	npt/h	Y	H2
314	H2	78	108	18	0	0.387	13.1	-4.24	NPTbH	X	H1
59	H1	78	109	5	46	0.378	347.5	-6.34	NO?	X	H2
60	H1	78	109	13	0	0.374	348.7	-6.24	npt/h	X	H2
316	H2	78	119	2	56	0.292	67.4	3.50	NPTb-	Y	H1
61	H1	78	119	3	49	0.310	38.7	-0.03	nptb-	Y	H2
62	H1	78	120	11	16	0.311	46.7	1.13	NO	X	H2
63	H1	78	122	13	30	0.318	58.8	2.94	NO	X	H2
64	H1	78	127	20	5	0.361	85.4	5.96	NO?	Y	H2
317	H2	78	127	22	22	0.340	121.3	7.25	NO	Y	H1
65	H1	78	129	9	36	0.379	91.6	6.47	NO	Y	H2
										X	IMP8
318	H2	78	129	11	25	0.358	128.2	7.14	NO	Y	H1
										X	IMP8
66	H1	78	130	15	2	0.392	95.8	6.78	NPTb-	X	H2
415	H2	78	130	6	28	0.370	131.4	6.98	NO?	X	H1

TABLE A.2 - continues

SN	SC	YY	DOY	HH	MM	RAD	HSE	CLAT	MC Sign	CLASS	CORR
67	H1	78	132	2	30	0.411	100.7	7.00	-PtBh	Y	H2
319	H2	78	132	5	15	0.394	138.4	6.69	NPtb/	X	IMP8
68	H1	78	132	13	25	0.417	102.0	7.06	-ptBH	Y	H1
69	H1	78	134	9	24	0.441	107.1	7.21	nptBh	X	IMP8
320	H2	78	134	15	1	0.428	145.5	6.13	?	N	H2
321	H2	78	137	22	25	0.473	153.1	5.30	?b	Y	H1
402	H2	78	138	8	0	0.478	153.8	5.15	nptb-	X	H1
413	H1	78	153	8	18	0.673	131.5	5.81	NO	Y	H2
70	H1	78	164	3	58	0.777	135.1	4.57	NO	Y	IMP8
71	H1	78	177	11	41	0.875	135.6	3.12	NO	X	H2
72	H1	78	189	10	20	0.935	134.0	1.90	nptbh	D	IMP8
323	H2	78	191	19	58	0.946	171.2	-2.98	?	X	H2
73	H1	78	201	8	16	0.971	131.5	0.77	npt/-	N	IMP8
74	H1	78	202	19	36	0.974	131.1	0.65	npt/-	N	H2

TABLE A.2 - continues

SN	SC	YY	DOY	HH	MM	RAD	HSE	CLAT	MC Sign	CLASS	CORR
										N	IMP8
325	H2	78	207	12	2	0.981	167.3	-4.25	NO?	X	H1
326	H2	78	219	11	49	0.981	164.0	-5.07	NO?	N	H1
327	H2	78	240	13	48	0.921	159.0	-6.28	NPTb-	N	H1
										N	IMP8
328	H2	78	268	1	26	0.721	158.8	-7.24	nptb-	Y	H1
										X	IMP8
75	H1	78	268	2	30	0.745	121.4	-5.52	nptbh	Y	H2
										X	IMP8
419	H2	78	279	3	50	0.600	164.8	-7.09	NO	X	H1
										X	IMP8
77	H1	78	286	13	42	0.541	133.7	-7.14	?	D	H2
78	H1	78	286	20	41	0.537	134.1	-7.16	NO	D	H2
79	H1	78	287	13	50	0.528	135.1	-7.19	nptB-	D	H2
80	H1	78	290	9	0	0.493	139.5	-7.25	nptbH	D	H2
										X	IMP8
81	H1	78	291	16	12	0.475	142.1	-7.23	NPtBH	D	H2
										N	IMP8
414	H2	78	294	1	45	0.395	191.6	-4.11	?	N	H1
										N	IMP8
329	H2	78	297	7	47	0.353	204.0	-2.35	nptb/	X	H1
330	H2	78	305	16	47	0.291	252.3	4.42	nptB-	D	H1

TABLE A.2 - continues

SN	SC	YY	DOY	HH	MM	RAD	HSE	CLAT	MC Sign	CLASS	CORR
										N	IMP8
331	H2	78	312	7	26	0.324	293.9	7.23	nptBh	N	H1
82	H1	78	333	3	17	0.552	297.6	6.81	NPtbH	N	H2
										N	IMP8
83	H1	78	334	13	24	0.569	299.2	6.67	nptbH	X	H2
										X	IMP8
84	H1	78	335	17	37	0.583	300.4	6.55	-pt-h	X	H2
										N	IMP8
85	H1	78	339	17	47	0.631	303.7	6.11	NPTBH	N	H2
										N	ISEE3
86	H1	78	343	14	58	0.674	306.0	5.66	?b	N	H2
										N	ISEE3
87	H1	78	344	2	42	0.679	306.2	5.60	NPtbH	N	H2
										N	ISEE3
332	H2	78	347	2	47	0.750	351.1	0.35	nptBh	N	H1
										X	ISEE3
333	H2	78	347	12	45	0.754	351.2	0.28	nptbh	N	H1
										Y	ISEE3
335	H2	78	355	10	2	0.821	351.6	-0.75	NPTbh	X	H1
										N	IMP8
89	H1	78	356	9	2	0.794	309.0	4.24	NO	N	H2
										N	ISEE3



TABLE A.2 - continues

SN	SC	YY	DOY	HH	MM	RAD	HSE	CLAT	MC Sign	CLASS	CORR
90	H1	78	356	20	20	0.798	309.0	4.19	NPt-h	N	H2 ISEE3
336	H2	78	358	8	1	0.843	351.4	-1.08	NPTBh	N	H1 ISEE3
417	H2	78	359	2	2	0.850	351.3	-1.07	NO	Y	H1 ISEE3
91	H1	78	359	17	30	0.820	309.1	3.88	NO	Y	H2 ISEE3
92	H1	78	362	23	1	0.844	308.9	3.55	NPtBH	Y	H2 ISEE3
337	H2	78	363	6	5	0.875	350.8	-1.61	-ptb-	Y	H1 IMP8
93	H1	79	1	8	6	0.866	308.6	3.21	npt/-	Y	H2 IMP8
94	H1	79	2	5	37	0.872	308.5	3.13	NPT/H	Y	H2 IMP8
338	H2	79	2	12	54	0.900	350.0	-2.03	NO	Y	H1 ISEE3
339	H2	79	7	5	6	0.923	348.9	-2.46	?	X	H1 ISEE3
340	H2	79	7	10	33	0.925	348.9	2.48	NPtBH	Y	H1 ISEE3

TABLE A.2 - continues

SN	SC	YY	DOY	HH	MM	RAD	HSE	CLAT	MC Sign	CLASS	CORR
95	H1	79	7	21	59	0.904	307.6	2.59	Npt/-	Y	H2 ISEE3
341	H2	79	9	3	6	0.932	348.4	-2.62	NptB-	X Y	H1 ISEE3
96	H1	79	12	20	22	0.928	306.5	2.13	NO	X D	H2 ISEE3
97	H1	79	13	8	0	0.930	306.4	2.08	npt/-	N X	H2 ISEE3
342	H2	79	21	8	18	0.971	344.9	-3.60	NPTbh	N X	H1 ISEE3
99	H1	79	25	17	55	0.970	303.0	0.99	NO?	N N	H2 ISEE3
343	H2	79	30	4	10	0.983	342.0	-4.21	NPT/h	Y Y	H1 ISEE3
100	H1	79	30	6	34	0.978	301.7	0.60	npt/-	Y	H2
101	H1	79	32	22	21	0.981	300.8	0.37	NO?	D N	H2 ISEE3
344	H2	79	34	13	40	0.984	340.6	-4.50	Npt/h	N Y	H1 ISEE3
102	H1	79	39	19	23	0.985	298.7	-0.22	NO?	N N	H2 ISEE3
345	H2	79	41	18	33	0.979	338.2	-4.96	NPT/H	Y	H1

TABLE A.2 - continues

SN	SC	YY	DOY	HH	MM	RAD	HSE	CLAT	MC Sign	CLASS	CORR
										Y	ISEE3
103	H1	79	42	2	10	0.984	298.0	-0.40	NO?	Y	H2
										Y	ISEE3
412	H1	79	48	10	35	0.978	296.0	-0.95	npt/h	Y	H2
										Y	ISEE3
346	H2	79	48	19	37	0.966	336.0	-5.38	NPTbh	Y	H1
										Y	ISEE3
347	H2	79	51	22	10	0.957	335.1	-5.56	nptb/	N	H1
										Y	ISEE3
104	H1	79	58	2	44	0.957	293.2	-1.78	NPTBh	N	H2
										N	ISEE3
348	H2	79	58	20	40	0.932	333.2	-5.94	NO	N	H1
										Y	ISEE3
105	H1	79	62	2	2	0.944	292.2	-2.14	NPTBH	Y	H2
										N	ISEE3
349	H2	79	62	9	34	0.916	332.4	-6.13	NPT//	Y	H1
										N	ISEE3
350	H2	79	66	17	20	0.894	331.6	-6.35	NPTbh	N	H1
										N	ISEE3
106	H1	79	70	3	40	0.909	290.5	-2.88	NO	N	H2
										N	ISEE3
351	H2	79	71	0	20	0.868	330.9	-6.55	NPTb-	N	H1

TABLE A.2 - continues

SN	SC	YY	DOY	HH	MM	RAD	HSE	CLAT	MC Sign	CLASS	CORR
										X	ISEE3
107	H1	79	75	9	30	0.881	289.7	-3.37	np-/h	N	H2
										Y	ISEE3
108	H1	79	76	21	56	0.871	289.5	-3.53	NO?	N	H2
										N	ISEE3
352	H2	79	79	4	36	0.809	330.5	-6.91	NPTb-	D	H1
										Y	ISEE3
353	H2	79	80	17	15	0.798	330.5	-6.96	NO	N	H1
										Y	ISEE3
109	H1	79	83	21	4	0.823	289.1	-4.22	NPTBh	N	H2
										N	ISEE3
354	H2	79	86	8	53	0.746	331.2	-7.14	NPTbh	N	H1
										Y	ISEE3
110	H1	79	87	10	4	0.796	289.3	-4.60	NO?	X	H2
										X	ISEE3
111	H1	79	89	1	45	0.782	289.5	-4.76	npt/h	N	H2
										N	ISEE3
355	H2	79	92	20	7	0.680	333.2	-7.25	NP-BH	N	H1
										Y	ISEE3
112	H1	79	93	19	45	0.740	290.3	-5.26	npt/h	Y	H2
										X	ISEE3
356	H2	79	94	13	30	0.656	334.0	-7.25	-PTB/	X	H1

TABLE A.2 - continues

SN	SC	YY	DOY	HH	MM	RAD	HSE	CLAT	MC Sign	CLASS	CORR
										Y	ISEE3
357	H2	79	95	15	28	0.648	334.6	-7.24	NPtbh	X	H1
										X	ISEE3
113	H1	79	105	4	5	0.621	295.8	-6.47	NPTBH	N	H2
										N	ISEE3
114	H1	79	112	13	32	0.530	303.7	-7.10	npt-	X	H2
										N	ISEE3
358	H2	79	113	15	16	0.412	0.8	-4.98	NPtbh	X	H1
										Y	ISEE3
115	H1	79	114	1	18	0.511	306.0	-7.18	NO	X	H2
										N	ISEE3
116	H1	79	118	4	27	0.457	313.9	-7.25	nptbh	X	H2
										X	ISEE3
117	H1	79	122	21	40	0.397	326.9	-6.73	-b-	N	H2
										N	ISEE3
359	H2	79	123	13	53	0.301	45.9	1.47	NPtB-	N	H1
										X	ISEE3
361	H2	79	129	3	30	0.295	83.2	5.88	nPTbh	X	H1
										Y	ISEE3
360	H2	79	129	8	30	0.296	84.6	5.99	nptb/	X	H1
										Y	ISEE3
118	H1	79	141	11	5	0.344	63.2	5.26	NO	Y	H2

TABLE A.2 - continues

SN	SC	YY	DOY	HH	MM	RAD	HSE	CLAT	MC Sign	CLASS	CORR
										N	ISEE3
362	H2	79	142	15	58	0.445	142.7	5.81	NO?	Y	H1
										N	ISEE3
363	H2	79	148	7	57	0.524	153.1	4.36	?	Y	H1
										X	ISEE3
364	H2	79	148	10	28	0.525	153.0	4.34	npt-	Y	H1
										Y	ISEE3
119	H1	79	148	18	41	0.428	90.1	7.15	NPTBh	Y	H2
										Y	ISEE3
365	H2	79	150	4	42	0.548	155.6	3.91	NPTBh	N	H1
										N	ISEE3
366	H2	79	162	6	15	0.692	164.8	1.44	NO?	N	H1
										N	ISEE3
401	H2	79	162	19	5	0.698	165.0	1.34	NO	Y	H1
										N	ISEE3
120	H1	79	162	20	55	0.607	113.1	6.44	-b-	Y	H2
										N	ISEE3
416	H1	79	175	20	6	0.740	119.9	4.94	NPTB/	Y	H2
										N	ISEE3
367	H2	79	175	21	9	0.818	167.6	-0.60	NO	Y	H1
										N	ISEE3
410	H2	79	178	16	14	0.838	167.6	-0.90	?	N	H1

TABLE A.2 - continues

SN	SC	YY	DOY	HH	MM	RAD	HSE	CLAT	MC Sign	CLASS	CORR
										N	ISEE3
403	H1	79	186	11	30	0.832	121.3	3.74	npt/h	D	H2
										X	ISEE3
121	H1	79	192	10	0	0.872	-1.0	3.10	?	D	H2
122	H1	79	202	18	22	0.927	120.0	2.05	?	N	H2
										N	ISEE3
368	H2	79	203	15	42	0.962	163.8	-3.44	?p	X	H1
										X	H1
369	H2	79	205	16	21	0.967	63.7	-3.61	?p	X	H1
										N	ISEE3
370	H2	79	239	20	33	0.951	154.3	-5.90	?	D	H1
										X	ISEE3
372	H2	79	252	2	29	0.896	151.9	-6.52	?b	X	ISEE3
371	H2	79	252	14	15	0.894	151.8	-6.55	NPtBH	X	ISEE3
405	H1	79	253	13	45	0.939	0.0	-2.67	?b	Y	H2
										N	ISEE3
411	H2	79	253	20	35	0.884	151.6	-6.60	?	Y	H1
										N	ISEE3
406	H1	79	255	18	55	0.930	0.0	-2.87	?	D	H2
										N	ISEE3
373	H2	79	283	23	15	0.621	156.9	-7.13	NPtBH	N	H1
										N	ISEE3

TABLE A.2 - continues

SN	SC	YY	DOY	HH	MM	RAD	HSE	CLAT	MC Sign	CLASS	CORR
404	H1	79	286	2	30	0.719	107.3	-5.80	—b-	X N	H2 ISEE3
374	H2	79	288	4	31	0.587	160.5	-6.87	nptb/	X N	H1 ISEE3
375	H2	79	303	10	21	0.360	194.0	-2.80	NPt/h	X N	H1 ISEE3
376	H2	79	303	23	4	0.355	196.8	-2.45	npt/h	Y N	H1 ISEE3
377	H2	79	306	3	28	0.330	207.0	-0.93	npt/h	Y N	H1 ISEE3
123	H1	79	306	23	54	0.475	127.0	-7.24	NO	Y N	H2 ISEE3
378	H2	79	307	20	7	0.313	216.2	0.45	NPtb/	N N	H1 ISEE3
379	H2	79	313	7	22	0.291	314.3	5.08	NO?	N Y	H1 ISEE3
400	H1	79	328	0	45	0.318	219.5	3.22	nptb-	N N	H2 ISEE3
380	H2	79	332	16	0	0.502	329.8	4.52	NO?	N Y	H1 ISEE3
124	H1	79	347	8	53	0.538	61.9	6.93	NPtBh	Y N	H2 ISSE3



TABLE A.2 - continues

SN	SC	YY	DOY	HH	MM	RAD	HSE	CLAT	MC Sign	CLASS	CORR
381	H2	79	347	12	24	0.685	61.9	1.37	?	Y	H1
										N	ISSE3
125	H1	79	349	12	32	0.585	76.5	6.73	-p-B-	X	H2
										N	ISSE3
126	H1	79	357	13	2	0.659	54.1	5.86	NO?	Y	H2
										N	ISEE3
382	H2	79	358	1	36	0.788	54.1	-0.21	nptb/	Y	H1
										N	ISEE3
127	H1	79	360	9	31	0.689	53.8	5.53	nptb-	N	H2
										N	ISEE3
383	H2	79	364	15	52	0.839	52.2	-1.00	Nptbh	N	H1
										X	ISEE3
128	H1	80	3	12	24	0.767	51.1	4.63	NPTBh	N	H2
										N	ISEE3
384	H2	80	10	20	48	0.908	49.3	-2.15	NO	Y	H1
										X	ISEE3
129	H1	80	10	23	9	0.827	49.3	3.84	-t-h	Y	H2
										X	ISEE3
130	H1	80	13	7	29	0.844	48.9	3.60	nptbH	X	H2
										X	ISEE3
385	H2	80	30	12	18	0.975	46.9	-3.74	NO?	N	H1
										N	ISEE3

TABLE A.2 - continues

SN	SC	YY	DOY	HH	MM	RAD	HSE	CLAT	MC Sign	CLASS	CORR
386	H2	80	33	11	12	0.979	46.6	-3.96	NO?	X	H1 ISEE3
387	H2	80	34	7	28	0.980	46.7	-4.01	NO?	X X	H1 ISEE3
388	H2	80	36	15	3	0.983	35.8	-4.17	NPT/-	X Y	H1 ISEE3
389	H2	80	37	20	40	0.983	46.5	-4.25	NO?	Y X	H1 ISEE3
131	H1	80	38	0	28	0.982	46.5	1.31	-bh	Y X	H2 ISEE3
132	H1	80	43	22	21	0.975	46.2	0.79	NPTb-	X Y	H2 ISEE3
133	H1	80	60	14	55	0.982	46.2	-0.63	NO	X N	H2 ISEE3
134	H1	80	65	1	46	0.976	46.2	-1.02	NPtBh	Y X	H2 ISEE3
390	H2	80	65	14	34	0.932	46.2	-5.93	NPtbh	Y X	H1 ISEE3
135	H1	80	72	10	47	0.960	81.6	-1.67	nptb-	Y	ISEE3
136	H1	80	82	14	3	0.923	84.0	-2.59	NpT-	X	ISEE3
137	H1	80	89	11	53	0.887	85.1	-3.25	NPTBH	X	ISEE3
138	H1	80	110	10	59	0.727	84.1	-5.41	NO	D	ISSE3

TABLE A.2 - continues

SN	SC	YY	DOY	HH	MM	RAD	HSE	CLAT	MC Sign	CLASS	CORR
139	H1	80	122	6	20	0.600	77.4	-6.65	n-b-	N	ISEE3
140	H1	80	122	13	47	0.596	77.1	-6.70	NPtbh	N	ISEE3
142	H1	80	143	20	57	0.337	24.2	-4.55	nptbh	Y	ISEE3
143	H1	80	148	2	28	0.312	0.8	-1.42	NPtbh	Y	ISEE3
144	H1	80	150	11	6	0.310	13.6	0.69	NPtbh	Y	ISEE3
145	H1	80	155	9	14	0.332	41.8	4.50	n-tbh	Y	ISEE3
146	H1	80	161	18	36	0.399	68.7	6.88	-tbh	X	ISEE3
147	H1	80	171	19	30	0.529	91.3	7.03	NPTBH	D	ISEE3
148	H1	80	174	20	34	0.567	95.3	6.67	N-tbh	Y	ISEE3
149	H1	80	182	17	23	0.659	102.0	5.89	npt-h	N	ISEE3
150	H1	80	183	15	20	0.669	102.5	5.79	-p-bh	N	ISEE3
151	H1	80	189	11	27	0.728	105.1	5.10	NPTBH	N	ISEE3
152	H1	80	192	22	45	0.760	106.0	4.69	NO	X	ISEE3
153	H1	80	195	20	15	0.700	106.1	4.36	NPtb-	X	ISEE3
154	H1	80	203	1	20	0.841	107.0	3.60	nPt-h	X	ISEE3
155	H1	80	207	3	21	0.868	106.9	3.12	NO	Y	ISEE3
156	H1	80	209	22	35	0.885	106.7	2.82	Npt-	X	ISEE3
157	H1	80	214	10	13	0.909	106.1	2.36	n--	X	ISEE3
158	H1	80	215	4	51	0.913	106.0	2.28	-p--	X	ISEE3
159	H1	80	230	18	57	0.968	102.9	0.77	NptBH	Y	ISEE3
160	H1	80	238	15	15	0.982	100.9	0.05	n-tb/	X	ISEE3

TABLE A.2 - continues

SN	SC	YY	DOY	HH	MM	RAD	HSE	CLAT	MC Sign	CLASS	CORR
161	H1	80	247	12	6	0.984	98.5	-0.76	NPtB/	N	ISEE3
162	H1	80	257	8	20	0.973	95.9	-1.64	?	Y	ISEE3
163	H1	80	266	21	12	0.948	93.6	-2.50	npt-/	X	ISEE3
164	H1	80	272	7	44	0.925	92.5	-3.00	n-t-	N	ISEE3
166	H1	80	312	3	48	0.604	98.2	-6.78	NPtbh	X	ISEE3
167	H1	80	318	1	31	0.530	104.8	-7.17	NO	X	ISEE3
168	H1	80	319	10	33	0.512	106.8	-7.22	-p-	N	ISEE3
169	H1	80	319	21	11	0.507	107.5	-7.23	NPTbH	N	ISEE3
170	H1	80	323	13	48	0.458	114.6	-7.19	NO	Y	ISEE3
171	H1	80	327	16	45	0.405	125.4	-6.73	nptBH	Y	ISEE3
172	H1	80	330	9	4	0.374	134.7	-6.03	nptBh	N	ISEE3
173	H1	80	348	18	52	0.362	129.0	6.19	npt-/	N	ISEE3
174	H1	80	365	18	41	0.577	90.8	6.66	NPTBH	N	ISEE3
175	H1	81	23	8	25	0.813	81.6	4.09	NPtb-	N	ISEE3
176	H1	81	27	0	8	0.840	81.7	3.72	nptbh	N	ISEE3
177	H1	81	27	17	48	0.845	81.8	3.64	NO	N	ISEE3
178	H1	81	28	15	36	0.851	81.8	0.85	NO	Y	ISEE3
179	H1	81	50	13	37	0.957	86.1	1.51	-p///	Y	ISEE3
180	H1	81	51	16	0	0.960	86.4	1.41	NP///	X	ISEE3
181	H1	81	53	16	0	0.966	87.0	1.23	NO?	Y	ISEE3
182	H1	81	60	1	16	0.978	88.8	0.68	NPT//	Y	ISEE3

TABLE A.2 - continues

SN	SC	YY	DOY	HH	MM	RAD	HSE	CLAT	MC Sign	CLASS	CORR
183	H1	81	68	21	0	0.985	91.5	-0.08	N-t//	Y	ISEE3
184	H1	81	80	6	53	0.975	94.8	-1.08	NO?	N	ISEE3
185	H1	81	90	10	45	0.948	98.0	-1.99	NPt//	X	ISEE3
186	H1	81	93	5	56	0.938	98.1	-2.25	NPt//	Y	ISEE3
187	H1	81	98	2	58	0.917	99.1	-2.71	NPtB/	Y	ISEE3
188	H1	81	103	9	12	0.890	99.9	-3.21	?	X	ISEE3
189	H1	81	103	9	59	0.890	99.9	-3.21	NPTbH	X	ISEE3
190	H1	81	106	7	48	0.872	100.2	-3.50	npt-h	X	ISEE3
191	H1	81	106	19	52	0.869	100.2	-3.55	N-Tbh	X	ISEE3
192	H1	81	110	0	42	0.848	100.4	-3.87	NPTBh	N	ISEE3
193	H1	81	115	11	4	0.808	100.4	-4.44	NPtb-	Y	ISEE3
194	H1	81	116	8	27	0.801	100.3	-4.53	NO	X	ISEE3
195	H1	81	117	3	4	0.795	100.2	-4.61	NPtBH	X	ISEE3
196	H1	81	122	10	48	0.749	99.4	-5.18	nPt-	Y	ISEE3
197	H1	81	126	17	26	0.708	98.1	-5.64	NO	N	ISEE3
198	H1	81	130	3	12	0.673	96.5	-6.01	npt-	Y	ISEE3
199	H1	81	131	7	9	0.660	95.9	-6.13	NPTB-	N	ISEE3
200	H1	81	133	21	23	0.631	94.2	-6.40	NPTb/	Y	ISEE3
201	H1	81	135	16	35	0.610	92.7	-6.59	npt-h	Y	ISEE3
202	H1	81	136	24	0	0.595	91.5	-6.70	NPtb-	Y	ISEE3
418	H1	81	143	5	54	0.520	276.2	-7.16	NO	X	ISEE3

TABLE A.2 - continues

SN	SC	YY	DOY	HH	MM	RAD	HSE	CLAT	MC Sign	CLASS	CORR
203	H1	81	145	20	29	0.483	79.3	-7.25	NPtBH	X	ISEE3
205	H1	81	163	12	36	0.310	8.4	-0.37	NPT-	X	ISEE3
206	H1	81	170	1	5	0.334	29.0	4.70	NPTBH	Y	ISEE3
207	H1	81	202	23	44	0.721	90.5	5.14	NPt/-	Y	ISEE3
208	H1	81	205	15	34	0.746	91.3	4.83	NO?	Y	ISEE3
209	H1	81	212	5	10	0.802	92.4	4.07	NO?	X	ISEE3
210	H1	81	228	2	24	0.906	91.8	2.37	NPT//	X	ISEE3
211	H1	81	230	15	47	0.919	91.4	2.12	NO?	N	ISEE3
215	H1	81	287	18	58	0.919	77.4	-3.10	NO?	X	ISEE3
216	H1	81	293	4	21	0.892	76.5	-3.60	NO?	X	ISEE3
217	H1	81	293	14	29	0.889	76.4	-3.64	-p///	X	ISEE3
218	H1	81	302	6	12	0.834	75.7	-4.45	NO?	X	ISEE3
219	H1	81	302	10	53	0.832	75.7	-4.47	npt//	X	ISEE3
220	H1	81	304	0	48	0.821	75.7	-4.62	NO?	X	ISEE3
221	H1	81	313	9	51	0.742	76.7	-5.54	NO?	X	ISEE3
222	H1	81	318	9	45	0.692	78.2	-6.03	npt//	N	ISEE3
223	H1	81	320	15	19	0.668	79.2	-6.25	nPt/-	Y	ISEE3
224	H1	81	324	0	54	0.631	81.2	-6.56	NPT/-	N	ISEE3
225	H1	81	324	12	35	0.625	81.6	-6.61	NPT/-	N	ISEE3
226	H1	81	326	23	28	0.597	83.6	-6.82	NPtBH	Y	ISEE3
227	H1	81	345	21	16	0.360	124.3	-5.58	npt//	N	ISEE3

TABLE A.2 - continues

SN	SC	YY	DOY	HH	MM	RAD	HSE	CLAT	MC Sign	CLASS	CORR
228	H1	81	355	4	8	0.310	174.3	1.00	?	N	ISEE3
229	H1	81	357	2	56	0.315	174.0	2.73	NP///	N	ISEE3
230	H1	82	12	7	0	0.542	109.3	6.94	NO?	X	ISEE3
231	H1	82	27	5	18	0.711	98.6	5.37	npt///	X	ISEE3
232	H1	82	27	12	59	0.715	98.5	5.33	NPT///	X	ISEE3
233	H1	82	35	6	23	0.785	97.1	4.49	NPt/h	X	ISEE3
234	H1	82	37	14	48	0.805	96.9	4.24	NO?	N	ISEE3
235	H1	82	42	11	31	0.841	97.0	3.75	NO?	Y	ISEE3
236	H1	82	53	11	2	0.907	98.4	2.67	np///	X	ISEE3
237	H1	82	57	1	20	0.925	99.1	2.34	np///	N	ISEE3
238	H1	82	58	2	4	0.929	99.3	2.25	NP///	N	ISEE3
239	H1	82	155	10	0	0.555	102.6	-6.99	NPT/-	Y	ISEE3
240	H1	82	157	16	10	0.527	99.5	-7.14	?	N	ISEE3
241	H1	82	159	19	10	0.499	263.9	345.3	npt/h	N	ISEE3
242	H1	82	160	10	58	0.492	265.1	338.4	npt///	N	ISEE3
243	H1	82	161	7	5	0.480	266.7	329.0	NPT/h	X	ISEE3
244	H1	82	163	8	47	0.453	271.1	305.9	npt///	X	ISEE3
245	H1	82	163	12	31	0.451	271.5	304.0	?	X	ISEE3
246	H1	82	163	13	3	0.451	271.5	304.1	?	X	ISEE3
247	H1	82	163	18	30	0.449	272.1	301.6	NO?	X	ISEE3
248	H1	82	169	9	51	0.378	289.3	244.2	NO?	X	ISEE3

TABLE A.2 - continues

SN	SC	YY	DOY	HH	MM	RAD	HSE	CLAT	MC Sign	CLASS	CORR
249	H1	82	169	14	32	0.450	290.0	304.0	NO?	X	ISEE3
250	H1	82	191	13	7	0.401	40.5	62.2	NO?	X	ISEE3
251	H1	82	192	3	43	0.409	42.4	56.2	NO?	Y	ISEE3
252	H1	82	192	14	32	0.414	43.8	51.6	'-pt///	X	ISEE3
253	H1	82	194	3	10	0.434	48.1	35.7	-pt/-	Y	ISEE3
254	H1	82	196	13	48	0.466	54.0	9.6	NO?	Y	ISEE3
255	H1	82	201	6	2	0.526	62.4	315.7	?	Y	ISEE3
256	H1	82	201	9	28	0.528	62.6	314.2	NPT/H	Y	ISEE3
407	H1	82	203	1	44	0.550	64.9	294.1	NPt//	X	ISEE3
257	H1	82	204	7	59	0.565	66.9	279.0	npt//	Y	ISEE3
258	H1	82	217	4	13	0.710	75.7	118.4	NPt//	X	ISEE3
408	H1	82	327	12	3	0.734	61.7	61.6	nP///	X	ISEE3
259	H1	82	328	0	54	0.748	61.3	-5.44	np///	Y	ISEE3
260	H1	82	330	17	53	0.722	62.0	-5.71	npt//	Y	ISEE3
261	H1	82	342	13	0	0.594	68.5	-6.82	NPt//	Y	ISEE3
262	H1	82	353	4	0	0.456	64.1	-7.20	NO?	X	ISEE3
263	H1	82	354	11	8	0.441	67.0	-7.13	NPt//	X	ISEE3
264	H1	82	360	20	29	0.364	107.5	-5.78	NPt//	D	ISEE3
265	H1	82	364	2	50	0.333	122.7	-4.10	npt//	D	ISEE3
409	H1	83	12	12	0	0.354	196.8	5.80	NP-//	D	ISEE3
266	H1	83	28	4	16	0.549	236.1	6.91	NO?	X	ISEE3



TABLE A.2 - continues

SN	SC	YY	DOY	HH	MM	RAD	HSE	CLAT	MC Sign	CLASS	CORR
267	H1	83	28	8	58	0.551	236.4	6.89	npt//	X	ISEE3
268	H1	83	192	16	12	0.313	314.4	-1.49	npt//	D	ISEE3
269	H1	83	218	11	2	0.551	50.8	6.82	NO?	D	ISEE3
391	H1	83	221	16	45	0.590	54.5	6.55	n/////	D	ISEE3
392	H1	84	38	13	30	0.488	213.6	7.22	np-//	X	ISEE3
393	H1	84	182	15	20	0.607	225.2	-6.75	?	X	ISEE3
394	H1	84	236	9	41	0.586	39.5	6.50	NO?	Y	ISEE3
395	H1	85	22	17	10	0.393	18.0	-6.61	-p-//	D	ISEE3
396	H1	85	23	12	5	0.384	70.1	-6.40	npt//	D	ISEE3
397	H1	85	24	11	35	0.371	73.6	-6.10	?	D	ISEE3
398	H1	85	245	9	17	0.518	18.4	7.00	NO?	X	ISEE3



## B APPENDIX B - CONFIDENCE INTERVAL FOR PROPORTIONS

Let us consider  $P$  the proportion of “success” for our  $N$ -sized sample  $S$  that was taken from a population where  $p_S$  is the proportion. The confidence limits for  $p_S$  are given by  $P \pm z_c \sigma_S$ , where  $\sigma_S$  is the sample variance (SPIEGEL, 1961).

If the sampling distribution of  $S$  is nearly normal (this happens when the size is  $N \geq 30$  (SPIEGEL et al., 2000)), we can be confident to find  $p$  in the intervals of  $P - \sigma_S$  and  $P + \sigma_S$ , of  $P - 2\sigma_S$  and  $P + 2\sigma_S$ , or of  $P - 3\sigma_S$  and  $P + 3\sigma_S$ , approximately, in 68.27%, 95.45%, and 99.73% of the times, respectively. For that reason these intervals are so-called confidence intervals of 68.27%, 95.45%, and 99.73% for the evaluation of  $p_S$ . The upper and lower limits in the intervals  $P \pm 1.96\sigma_S$  and  $P \pm 2.58\sigma_S$  are the confidence limits for 95 and 99% for  $p_S$ . The percentage of confidence is frequently denominated confidence levels. The numbers 1.96 and 2.58 etc. of the confidence limits represent the critical values for the intervals of confidence, also called confidence coefficients, and they are represented by  $z_c$ .

In this case, the limits of our confidence interval are given by:

$$P \pm z_c \sqrt{\frac{\hat{p}_S \hat{q}_S}{N}} = P \pm z_c \sqrt{\frac{\hat{p}_S (1 - \hat{p}_S)}{N}}, \quad (\text{B.1})$$

when the population is infinite, or when there is reposition in a finite population.

Depending on the confidence level adopted, a different critical value is found. The factor 1.96 is the  $z_c$  value obtained from the normal table. It corresponds to the  $z_c$  value beyond which 2.5% of the population lie. Since the normal distribution is symmetric, 2.5% of the distribution lies above  $z_c$  and 2.5% below  $-z_c$ . The notation commonly used to denote  $z_c$  values for confidence interval construction or hypothesis testing is  $z_c - \alpha_c/2$  where  $100(1 - \alpha_c)$  is the desired confidence level in per cent. This means that, if we want 95% confidence,  $\alpha_c = 0.05$ ,  $100(1 - \alpha_c) = 95\%$ , and  $z_c(0.025) = 1.96$ . In hypothesis testing the value of  $\alpha_c$  is known as the significance level.

On the other hand, if the sample has a size  $N < 30$ , the Central Limit Theorem will not guarantee that  $P \pm z_c \sigma_S$  is approximately normal. Therefore, all the critical values of  $z$  for the normal distribution are no longer correct. In this case, one cannot

say that  $p_S$  will lie within 1.96 standard errors of  $P$  95% of the time.

In such way, the Student t-distribution, also known as t-distribution, with  $N - 1$  degrees of freedom ( $df$ ) should be used. Once we know  $N$ , we can go through [Table B.1](#) to find the correspondent  $t_{\alpha_c/2}$  value that guarantees a 95% confidence in the estimate of  $p_S$ . For instance, for  $N = 20$ ,  $df = 20 - 1 = 19$ , so for a 95% confidence level, we must look to the column  $t_{\alpha/2} = t_{0.05/2} = 2.093$ . Based on that, the  $(1 - \alpha_c)100\%$  confidence interval for  $p$  will be given by:

$$P \pm t_{\alpha/2} \sqrt{\frac{\hat{p}_S \hat{q}_S}{N}}, \quad (\text{B.2})$$

where  $\sqrt{\frac{\hat{p}_S \hat{q}_S}{N}}$  is the estimated standard error of  $p_S$ , often referred to us as the standard error of the proportion ([MENDENHALL et al., 2006](#)).

### B.1 Estimate of the Error Margin for the “Safe” Events

The shock observations by the considered probes generated different entries in the histograms. For example, when a shock is seen by three different probes, or at three different points in the inner heliosphere, we have an entry for H1 and H2 observation, another for H1 and IMP-8/ISEE-3, and another point when H2 and IMP-8/ISEE-3 are considered. Based on that, we can say that we are superposing angles since we could consider the largest longitudinal angle as the one representing our sample. But we are interested on the minimum angular distance into each we expect a shock to expand. These entries increment the  $\Delta\Phi$  bars represented in [Figure B.1](#). The result in percentage is the histograms with the multi and single points observations like we saw in [Chapter 4](#). [Figure B.2](#) has information about how much in longitude one can expect a shock to expand and says that if we have an event in the limb, we have a 50% of chance of seeing this shock at Earth environment. However, these proportions have some error associated to them that will be taken into account only for the multi-spacecraft observations.

When applying the estimate in our group of shock waves, we have first to consider each distribution separately. In [Figure B.1](#), every single  $\Delta\Phi$  (right side up plus upside down bars) represents a distribution of size  $N$ . Since the Student t-distribution is only applied to  $N < 30$ , since this distribution with  $N > 30$  is nearly normal, we separate the analysis of each sample  $\Delta\Phi$  according to its size ( $N$ ). When  $N < 30$ ,

<i>df</i>	$t_{0.25}$	$t_{0.20}$	$t_{0.15}$	$t_{0.10}$	$t_{0.05}$	$t_{0.025}$	$t_{0.010}$	$t_{0.005}$	$t_{0.001}$	$t_{0.0005}$	$t_{0.00025}$
<b>1</b>	1.000	1.376	1.963	3.078	6.314	12.71	31.82	63.66	127.3	318.3	636.6
<b>2</b>	0.816	1.061	1.386	1.886	2.920	4.303	6.965	9.925	14.09	22.33	31.60
<b>3</b>	0.765	0.978	1.250	1.638	2.353	3.182	4.541	5.841	7.453	10.21	12.92
<b>4</b>	0.741	0.941	1.190	1.533	2.132	2.776	3.747	4.604	5.598	7.173	8.610
<b>5</b>	0.727	0.920	1.156	1.476	2.015	2.571	3.365	4.032	4.773	5.893	6.869
<b>6</b>	0.718	0.906	1.134	1.440	1.943	2.447	3.143	3.707	4.317	5.208	5.959
<b>7</b>	0.711	0.896	1.119	1.415	1.895	2.365	2.998	3.499	4.029	4.785	5.408
<b>8</b>	0.706	0.889	1.108	1.397	1.860	2.306	2.896	3.355	3.833	4.501	5.041
<b>9</b>	0.703	0.883	1.100	1.383	1.833	2.262	2.821	3.250	3.690	4.297	4.781
<b>10</b>	0.700	0.879	1.093	1.372	1.812	2.228	2.764	3.169	3.581	4.144	4.587
<b>11</b>	0.697	0.876	1.088	1.363	1.796	2.201	2.718	3.106	3.497	4.025	4.437
<b>12</b>	0.695	0.873	1.083	1.356	1.782	2.179	2.681	3.055	3.428	3.930	4.318
<b>13</b>	0.694	0.870	1.079	1.350	1.771	2.160	2.650	3.012	3.372	3.852	4.221
<b>14</b>	0.692	0.868	1.076	1.345	1.761	2.145	2.624	2.977	3.326	3.787	4.140
<b>15</b>	0.691	0.866	1.074	1.341	1.753	2.131	2.602	2.947	3.286	3.733	4.073
<b>16</b>	0.690	0.865	1.071	1.337	1.746	2.120	2.583	2.921	3.252	3.686	4.015
<b>17</b>	0.689	0.863	1.069	1.333	1.740	2.110	2.567	2.898	3.222	3.646	3.965
<b>18</b>	0.688	0.862	1.067	1.330	1.734	2.101	2.552	2.878	3.197	3.610	3.922
<b>19</b>	0.688	0.861	1.066	1.328	1.729	2.093	2.539	2.861	3.174	3.579	3.883
<b>20</b>	0.687	0.860	1.064	1.325	1.725	2.086	2.528	2.845	3.153	3.552	3.850
<b>21</b>	0.686	0.859	1.063	1.323	1.721	2.080	2.518	2.831	3.135	3.527	3.819
<b>22</b>	0.686	0.858	1.061	1.321	1.717	2.074	2.508	2.819	3.119	3.505	3.792
<b>23</b>	0.685	0.858	1.060	1.319	1.714	2.069	2.500	2.807	3.104	3.485	3.767
<b>24</b>	0.685	0.857	1.059	1.318	1.711	2.064	2.492	2.797	3.091	3.467	3.745
<b>25</b>	0.684	0.856	1.058	1.316	1.708	2.060	2.485	2.787	3.078	3.450	3.725
<b>26</b>	0.684	0.856	1.058	1.315	1.706	2.056	2.479	2.779	3.067	3.435	3.707
<b>27</b>	0.684	0.855	1.057	1.314	1.703	2.052	2.473	2.771	3.057	3.421	3.690
<b>28</b>	0.683	0.855	1.056	1.313	1.701	2.048	2.467	2.763	3.047	3.408	3.674
<b>29</b>	0.683	0.854	1.055	1.311	1.699	2.045	2.462	2.756	3.038	3.396	3.659
<b>30</b>	0.683	0.854	1.055	1.310	1.697	2.042	2.457	2.750	3.030	3.385	3.646

TABLE B.1 - Student-t Distribution with the correspondent critical  $t_{\alpha_c/2}$  values and the degrees of freedom (*df*).

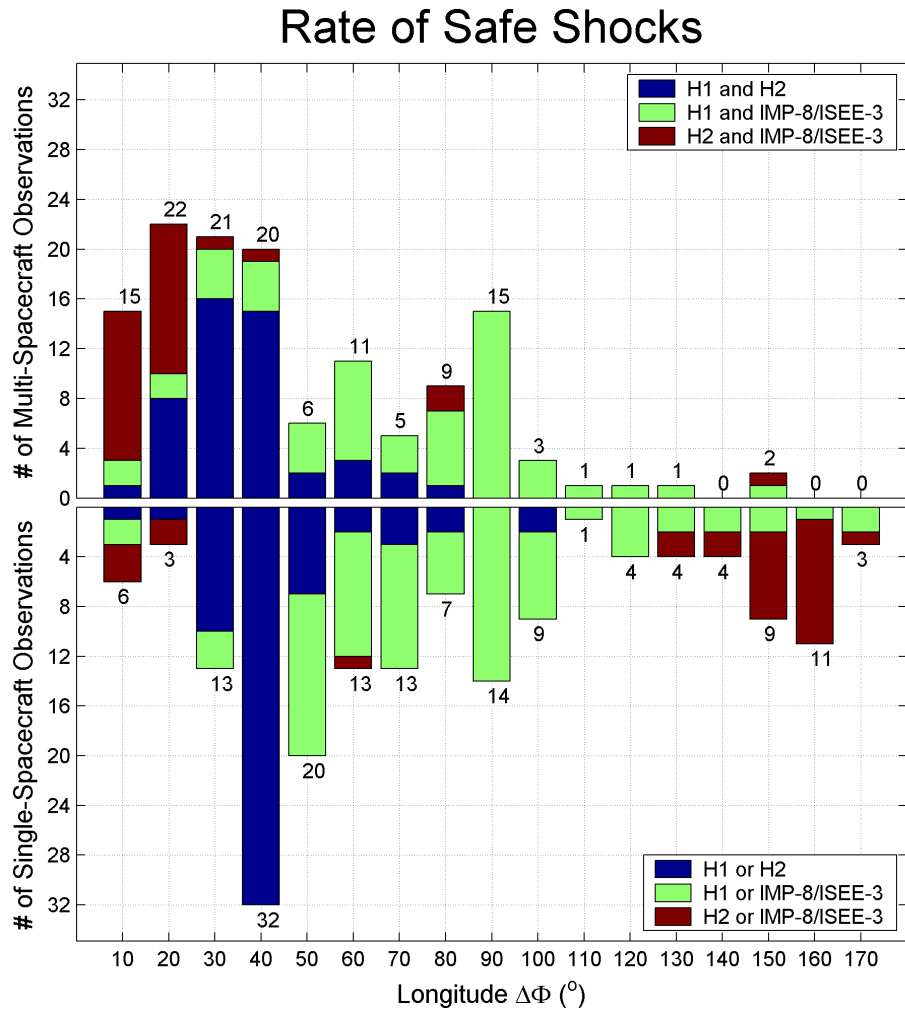


FIGURE B.1 - Rate of shock waves observed from 1974 to 1985 by at least two spacecraft (upper panel), or a single-spacecraft (lower panel) according to the longitudinal separation ( $\Delta\Phi$ ) between the probes. At the top (upper panel) and bottom (lower panel) of each bar, one finds the total number of events in each bar according to each type of observation: multi or single-spacecraft, respectively.

the margin of error increases as we try to obtain confidence in our results based on the observations.

For each bar in the first panel of Figure B.2 we considered the margin of error on the estimate, so we had an interval with 95% of confidence in our results concerning the observations by multi-spacecraft. As each bar represented the probability or percentage of occurrence of shock waves inside each angular distance, we proceeded

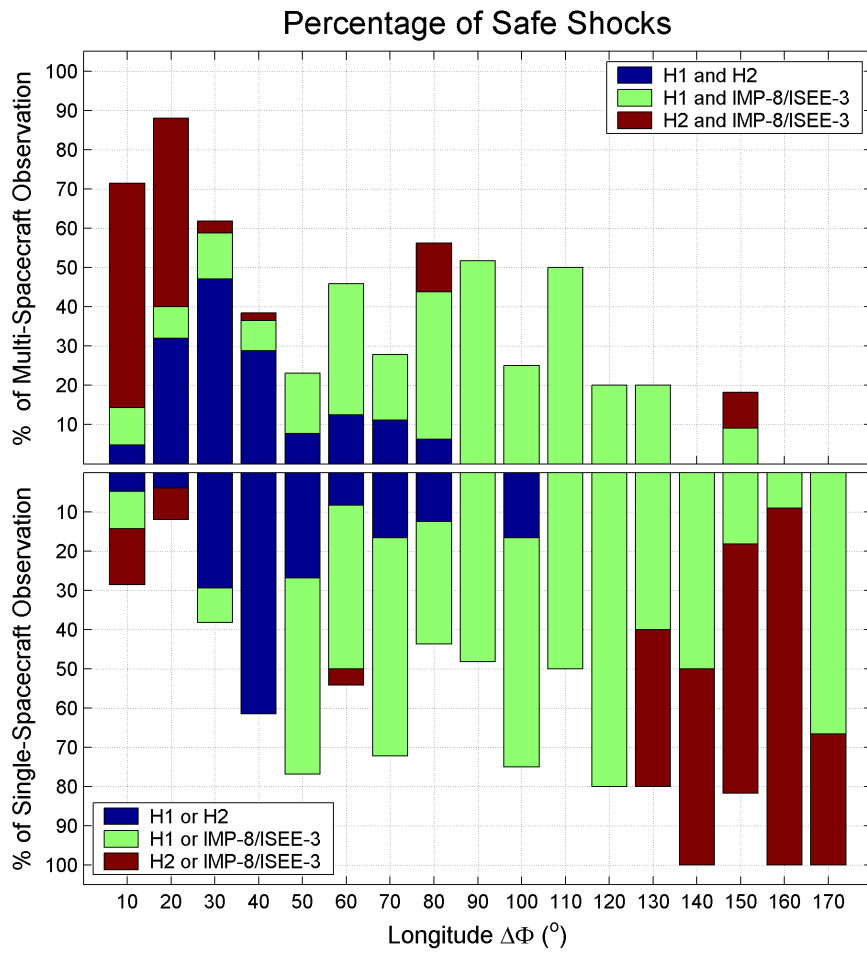


FIGURE B.2 - The percentage of “safe” events as a function of the longitudinal separation among the probes. In the upper panel, one can see the observations from multi-spacecraft (H1, H2, and IMP-8/ISEE-3), and in the lower panel one finds the sample of single-spacecraft observed events.

to the estimate of the confidence interval for proportions. According to [Equation B.1](#) the confidence interval is given by  $P \pm z_c \sqrt{\frac{\hat{p}_S(1-\hat{p}_S)}{N}}$ , where  $z_c = 1.96$ . The other parameters  $\hat{p}_S$  (the success) and  $\hat{q}_S$  (the failure) are dependent on the estimates of the success (multi-spacecraft observation) and the failure (single-spacecraft observation). For example, the first bar ([Figure B.2](#)) represents those events where the probes were located around  $10^\circ$  apart from each other. The values for  $\hat{p}_S$  and  $\hat{q}_S$  are 0.71 and 0.29, respectively, the total number of events in the first angular separation is 21 events ([Figure B.1](#)) of IP shocks following a Student-t distribution. These values are applied in [Equation B.2](#) like it follows:

$$0.71 \pm 2.086 \sqrt{\frac{0.71 \times 0.29}{21}} = 0.71 \pm 2.086 \sqrt{\frac{0.71(1 - 0.71)}{21}} = 0.71 \pm 0.21. \quad (\text{B.3})$$

Another example is the longitudinal separation of  $110^\circ$ , with  $N = 2$ , that has  $\hat{p}_S = \hat{q}_S = 0.5$ . Since the number of events in this sample is very small, the confidence level of 95% gives the interval  $50 \pm 499.4\%$  that is longer than the acceptable limits for our percentage. The margin of error in [Figure B.3](#) for  $\Delta\Phi = 110^\circ$  was not fully represented, however, we know that at this angular separation one can not be 95% confident of the proportion to observe a shock. This means that smaller the number of events in the sample, bigger is the margin of error for our estimate.

For  $\Delta\Phi = 40^\circ$ , one gets a sample with size  $N = 52$ , so then we can consider that the 95% confidence interval based in a Normal Distribution, applied in [Equation B.1](#):

$$0.38 \pm 1.96 \sqrt{\frac{0.38 \times 0.62}{52}} = 0.38 \pm 1.96 \sqrt{\frac{0.38(1 - 0.38)}{52}} = 0.38 \pm 0.13. \quad (\text{B.4})$$

By proceeding in the same manner with all the angular separations, as the bars represented in [Figure B.2](#), we obtain [Figure B.3](#), this time with the 95% confidence level.



### Percentage of Safe Events with 95% of Confidence

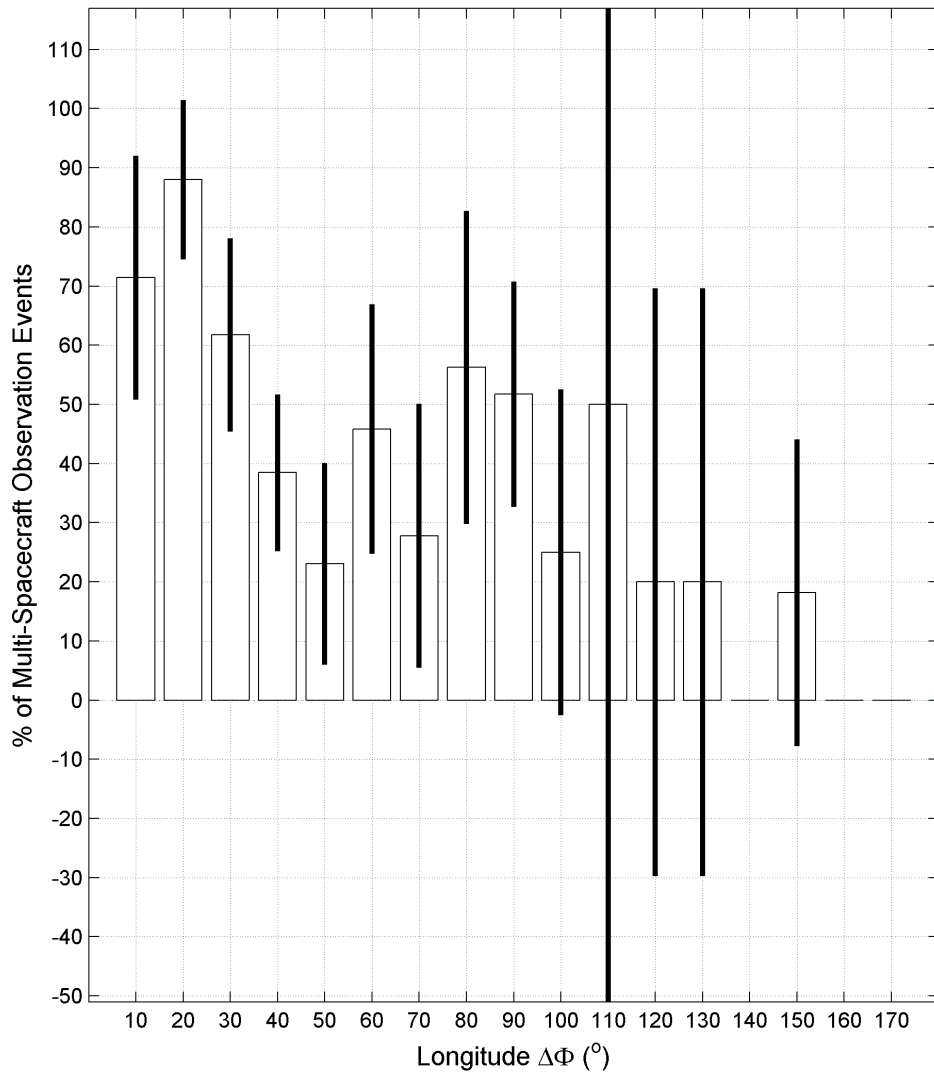


FIGURE B.3 - Percentage of shocks observed by multi-spacecraft and the error margin estimated for the percentage of shock waves observed in each angular separation  $\Delta\Phi$  based on the test for proportions.



## C APPENDIX C - MINIMUM VARIANCE ANALYSIS

The minimum variance analysis (MVA) technique, also known as the principal component, principal axis, or empirical orthogonal functions method, was developed by [Sonnerup and Cahill Jr. \(1967\)](#). It applies to magnetic field vector data measured during a spacecraft traversal of a transition layer, determines the normal vector  $\hat{n}$  for the direction of minimum variance of  $\vec{B}$  based on the conservation of the normal component of magnetic fields ( $[B_n = 0]$  ([Spreiter et al. \(1966\)](#) and references therein). The idea is to reduce a data set containing a large number of variables to a data set with a lower number of variables that represents a large fraction of the variability contained in the original data set. This can be achieved by calculating the mean quadratic deviation of the individual products  $B^i \cdot n$  from the average value  $\langle B^i \rangle \cdot n$ :

$$\sigma^2 = \frac{1}{N} \sum_{i=1}^N (B^i \cdot n - \langle B^i \rangle \cdot n)^2, \quad (\text{C.1})$$

with the normalization condition  $|\hat{n}| = 1$  ([SONNERUP; CAHILL JR., 1967](#)), and  $B^i$  denoting the individual measurements of magnetic fields. If during the passage of a MC, the magnetic field vector  $\vec{B}$  was measured at N successive times t, then the mean value of  $\vec{B}$  in Cartesian components is given by:

$$\langle B \rangle = \frac{1}{N} \sum_{i=1}^N B^i, \quad (\text{C.2})$$

with  $B^i = (B_x^i, B_y^i, B_z^i)$ ,  $i = 1, \dots, N$ .

Optimizing [Equation C.1](#) is equivalent to finding the smallest eigenvalue,  $\lambda$ , of the covariance-matrix  $M_{\alpha,\beta}$ , or the magnetic variance matrix, defined as:

$$M_{\alpha,\beta} = (\langle B_\alpha B_\beta \rangle - \langle B_\alpha \rangle \langle B_\beta \rangle), \quad (\text{C.3})$$

where the subscripts  $\alpha, \beta = 1, 2, 3$  denote cartesian components along the  $x, y, z$  system.

The individual  $B_{\alpha,\beta}$  in Equation C.3 are the Cartesian components of  $B$  for a single measurement. Since  $M_{\alpha,\beta}$  is symmetric, the eigenvalues are all real and the corresponding eigenvectors,  $e_i$  with  $i=1,2,3$ , are orthogonal. The latter correspond to the directions of minimum, intermediate and maximum variance of  $\vec{B}$ , this means to the directions of a new principal axis (the minimum variance) system. The eigenvector  $\hat{e}_3$  corresponds to the smallest eigenvalue,  $\lambda_3$ , and used as the estimator for vector normal to the boundary and  $\lambda_3$  itself represents the variance of the magnetic field component along the estimated normal. The eigenvectors  $\hat{e}_1$  and  $\hat{e}_2$ , corresponding to maximum and intermediate variance, are then tangential to the transition layer and the set  $\hat{e}_1, \hat{e}_2, \hat{e}_3$  arranged as a right-handed orthonormal triad provides suitable basis vectors for the local coordinate system  $(x, y, z)$ . In other words, for any measured set of vectors  $B^i$ , not necessarily obtained from a spacecraft traversal of a transition layer or wave front, the eigenvector set of the variance matrix  $M_{\alpha,\beta}$ , derived from the data, provides a convenient natural coordinate system independent of temporal order of the measured vectors.

The variance directions are well determined if some error criteria (SISCOE; SUEY, 1972; LEPPING; BEHANNON, 1980) are satisfied. The following conditions have to be fulfilled in order to improve the accuracy of the MVA for  $\vec{B}$ :

$$\frac{\lambda_2}{\lambda_3} > 2, \tag{C.4}$$

$$\angle(\vec{B}_1, \vec{B}_N) \geq 30^\circ. \tag{C.5}$$

The error for the MVA estimate of  $\vec{B}$  can be of  $\approx 10^\circ$  (BURLAGA; BEHANNON, 1982). In the Geocentric Solar-Ecliptic (GSE) coordinate system, the calculated variance directions are given by:

$$\phi_k = \arctan \frac{y_k}{x_k}, \tag{C.6}$$

$$\theta_k = \arcsin \frac{z_k}{|\hat{e}_k|}, \tag{C.7}$$

with  $|\hat{e}| = 1$ ;  $\hat{e}_k = (x_k, y_k, z_k)$ ;  $k = 1, 2, 3$ . However, it should be pointed out that

the  $\phi_k$  angles values present a larger difference, reaching around  $180^\circ$ , which means that the angles are calculated around the same axis (ECHER *et al.*, 2006).

Finally, the measured components of  $\vec{B}$  in the minimum variance system are:

$$B_k^{i*} = e_k \cdot B^i, \quad (\text{C.8})$$

with

- $B_1^* = B_x^* =$  component of maximum variance;
- $B_2^* = B_y^* =$  component of intermediate variance;
- $B_3^* = B_z^* =$  component of minimum variance.

The components above can be also found in Magnetic Clouds (MCs), as it is shown in the schematic representation of a flux tube in [Figure C.1](#). The first time the magnetic configuration of a MC was explained through force-free cylindrical magnetic flux tubes was in the work of [Goldstein \(1983\)](#). As one can see in [Figure C.1](#), the flux tube is moving radially away from the Sun, i.e., in the x-direction, and centrally passes a spacecraft in the ecliptic plane. The magnetic field in this case is described by the components in the GSE coordinate system. In this situation, since the radial component  $B_x$  is zero in the whole MC, the minimum variance component is represented in the sketch by  $B_z^*$ . At the center of the flux tube, i.e., at the cloud's axis, the magnetic field is directed in the azimuthal (+y or East) direction. This is also the direction of intermediate variance, because  $B_y^*$  is zero at the cloud's outer boundaries (on the surface of the cylinder). Finally, the maximum change in the magnetic field direction would occur due to the south (S) to north (N) turning of the magnetic field vector, corresponding to the direction normal to the ecliptic ( $B_x^*$ ). In reality, the flux-tube axis may have any orientation relative to the ecliptic plane and to the radial direction i.e., the actual variance directions  $x^*$ ,  $y^*$ ,  $z^*$  usually differ from the solar ecliptic coordinate system in x, y, z. Whether the model is appropriate to describe the structure of MCs can be inferred from the results of MVA ([KLEIN; BURLAGA, 1982](#)) applied to measured data. In the case of a flux tube (magnetic cloud), the MVA has been used to describe the orientation (axis) of magnetic clouds at first order ([BURLAGA \*et al.\*, 1981](#); [KLEIN; BURLAGA, 1982](#); [BOTHMER; SCHWENN, 1998](#)).

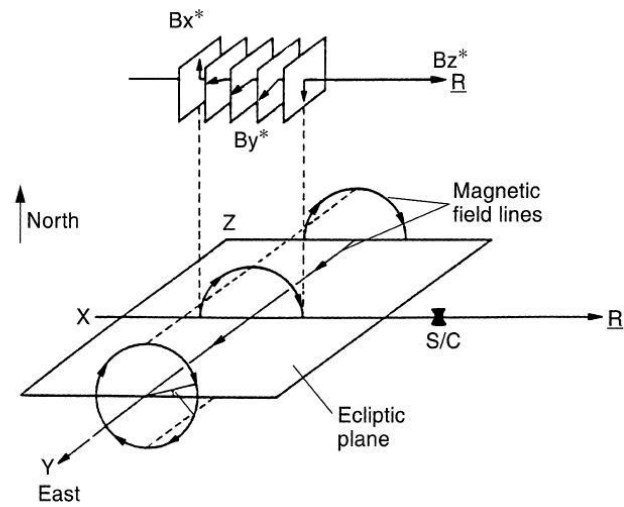


FIGURE C.1 - Representative sketch of a magnetic flux tube (approximation for a MC) traveling in the IP medium. Note that the original coordinate system is changed due to the application of the MVA technique, resulting in the components of maximum ( $B_x^*$ ), intermediate ( $B_y^*$ ), and minimum ( $B_z^*$ ) variance of the magnetic field.

SOURCE: Adapted from [Goldstein \(1983\)](#).

When observed in the maximum variance plane, a magnetic cloud is identified by the smooth rotation in the cloud magnetic field in form of an arc. Magnetic field normal components to this plane are almost constant ([BURLAGA et al., 1981](#); [KLEIN; BURLAGA, 1982](#); [BOTHMER; SCHWENN, 1998](#)). The magnetic field intermediate ( $B_2^* = B_y^*$ ) component corresponds to the orientation of the cloud axis, or its center ([BOTHMER; SCHWENN, 1998](#)). This is the way to determine when a cloud is being crossed by a satellite, however, the description for non-MC structures has not been developed so far.